

DTIC FILE COPY

FATIGUE AND FRACTURE OF TITANIUM ALUMINIDES

D.P. DeLuca
B.A. Cowles
F.K. Haake
K.P. Holland

AD-A226 737



United Technologies Corporation
Pratt & Whitney
Engineering Division
P.O. Box 109600
West Palm Beach, Florida 33410-9600

February 1990

Final Report for Period 1 July 1985 to 28 April 1989

Approved for Public Release; Distribution Is Unlimited

DTIC
ELECTE
SEP 12 1990
S D & D

DISTRIBUTION STATEMENT A

Approved for public release
Distribution Unlimited

Materials Laboratory
Wright Research and Development Center
Air Force Systems Command
Wright-Patterson Air Force Base, Ohio 45433-6533

90

**Best
Available
Copy**

NOTICE

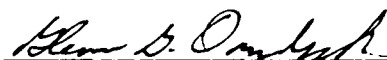
When government drawings, specifications, or other data are used for any purpose other than in connection with a definitely government-related procurement, the United States Government incurs no responsibility or any obligation whatsoever. The fact that the government may have formulated or in any way supplied the said drawings, specifications, or other data, is not to be regarded by implication, or otherwise in any manner construed, as licensing the holder, or any other person or corporation; or as conveying any rights or permission to manufacture, use, or sell any patented invention that may in any way be related thereto.

This report has been reviewed by the Office of Public Affairs (ASD/CPA) and is releasable to the National Technical Information Service (NTIS). At NTIS, it will be available to the general public, including foreign nations.

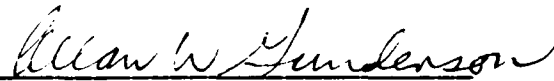
This technical report has been reviewed and is approved for publication.



MONICA A. STUCKE, WRDC/MLLN
FOR THE COMMANDER



GLENN G. ORMBREK
Technical Area Manager, Actg
Materials Behavior Branch
Metals and Ceramics Division



ALLAN W. GUNDERSON
Actg Branch Chief
Materials Behavior Branch
Metals and Ceramics Division

If your address has changed, if you wish to be removed from our mailing list, or if the addressee is no longer employed by your organization, please notify WRDC/MLLN, Wright-Patterson AFB OH 45433-6533 to help us maintain a current mailing list.

Copies of this report should not be returned unless return is required by security considerations, contractual obligations, or notice on a specific document.

				Form Approved OMB No. 0704-0188			
1a. REPORT SECURITY CLASSIFICATION Unclassified				1b. RESTRICTIVE MARKINGS None			
2a. SECURITY CLASSIFICATION AUTHORITY None				3. DISTRIBUTION/AVAILABILITY OF REPORT Approved For Public Release. Distribution is Unlimited.			
2b. DECLASSIFICATION/DOWNGRADING SCHEDULE N/A							
4. PERFORMING ORGANIZATION REPORT NUMBER(S) P&W/ED/FR-20781				5. MONITORING ORGANIZATION REPORT NUMBER(S) WRDC-TR-89-4136			
6a. NAME OF PERFORMING ORGANIZATION United Technologies Corporation Pratt & Whitney/Engineering Division			6b. OFFICE SYMBOL (If applicable)		7a. NAME OF MONITORING ORGANIZATION Wright Research and Development Center Materials Laboratory		
6c. ADDRESS (City, State, and ZIP Code) P.O. Box 109600 West Palm Beach, FL 33410-9600				7b. ADDRESS (City, State, and ZIP Code) Wright-Patterson AFB, OH 45433-6533			
8a. NAME OF FUNDING/SPONSORING ORGANIZATION			8b. OFFICE SYMBOL (If applicable)		9. PROCUREMENT INSTRUMENT IDENTIFICATION NUMBER F33615-85-C-5029		
8c. ADDRESS (City, State, and ZIP Code)				10. SOURCE OF FUNDING NOS.			
				PROGRAM ELEMENT NO. 62102F	PROJECT NO. 2420	TASK NO. 01	WORK UNIT ACCESSION NO. 64
11. TITLE (Include Security Classification) Fatigue and Fracture of Titanium Aluminides							
12. PERSONAL AUTHOR(S) D. P. DeLuca, B. A. Cowles, F. K. Haake, K. P. Holland							
13a. TYPE OF REPORT Final		13b. TIME COVERED FROM 07/01/85 TO 04/28/89		14. DATE OF REPORT (Year, Month, Day) February 1990		15. PAGE COUNT 271	
16. SUPPLEMENTARY NOTATION							
17. COSATI CODES			18. SUBJECT TERMS (Continue on reverse if necessary and identify by block number) Thermal Mechanical Fatigue Titanium Aluminide Crack Initiation Life Prediction Fatigue Crack Growth				
FIELD	GROUP	SUB. GR.					
19. ABSTRACT (Continue on reverse if necessary and identify by block number)							
<p>Two titanium aluminide alloys, Ti-24Al-11Nb and Ti-25Al-10Nb-3V-1Mo, were the subject of this program. A thermal processing and microstructure optimization study followed by monotonic and cyclic property testing was conducted.</p> <p>The program consisted of five tasks:</p> <p><i>Task I, Process Optimization</i>, examined isothermal forgings produced above and below the beta transus temperature. A beta forging followed by a fan air cool (arrived at from a cooling rate study) was chosen. An optimum stabilization and age cycle was developed after evaluating six temperature combination variations. Both alloys received the optimized forge/heat treat processing and basic mechanical properties were determined for both.</p> <p><i>Task II, Fatigue Crack Initiation</i>, determined smooth and notched low and high cycle fatigue behavior as a function of temperature, stress ratio, strain range, and frequency/dwell cycle. The application of hysteretic energy as the correlative damage parameter in a life prediction model was evaluated. The effects of hot salt stress corrosion, protective coatings and mechanical preconditioning were also investigated.</p>							
20. DISTRIBUTION/AVAILABILITY OF ABSTRACT <input checked="" type="checkbox"/> UNCLASSIFIED/UNLIMITED <input type="checkbox"/> SAME AS RPT. ... DTIC USERS				21. ABSTRACT SECURITY CLASSIFICATION Unclassified			
22a. NAME OF RESPONSIBLE INDIVIDUAL Monica A. Stucke			22b. TELEPHONE (Include Area Code) (513) 255-1353		22c. OFFICE SYMBOL WRDC/MLLN		

19. Abstract (Continued)

Task III, Fatigue Crack Propagation, determined near threshold stress intensity crack growth rates and fatigue crack growth propagation as a function of temperature, frequency, and stress ratio. An interpolative model of crack propagation as a function of stress ratio was developed.

Task IV, Thermal Mechanical Fatigue, evaluated the TMF life of both alloys as a function of stress, cycle type (in-phase versus out-of-phase) stress ratio, and the effects of hot salt stress corrosion. An incremental inelastic strain measurement technique was employed in the development of a hysteretic energy based life prediction model.

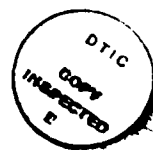
Task V, Fracture Mechanisms, consisted of extensive metallographic and fractographic analysis of the micro- and macrostructure of the alloys through all phases of the program. Characteristic fracture modes in monotonic and cyclic failures, typical fatigue origins, coating/substrate relationship, and thermal/environmental effects were documented.

FOREWORD

This work was performed under U.S. Air Force Contract F33615-85-C-5029, "Fatigue and Fracture of Titanium Aluminides." The sponsoring agency was the Materials Laboratory, Wright Research and Development Center (WRDC), Wright-Patterson Air Force Base, Dayton, OH. The U.S. Air Force program monitor was M.A. Stucke. The program was conducted at the Materials Engineering Laboratories, Pratt & Whitney, West Palm Beach, FL. The principal investigator for the program was D.P. DeLuca. The P&W program manager was B.A. Cowles reporting to M.C. VanWanderham. Florida Atlantic University, Boca Raton, FL, was subcontracted to perform part of the threshold testing. That testing was directed by Dr. G.C. Salivar. J.E. Heine was instrumental in conducting the thermal mechanical fatigue (TMF) testing. The authors would also like to acknowledge the contribution of J.W. Fischer for high cycle fatigue (HCF) testing and the technicians of the Fracture Mechanics, High Cycle Fatigue, Low Cycle Fatigue and Thermal Mechanical Fatigue groups at P&W for their part in conducting the testing for this program.

TABLE OF CONTENTS

<i>Section</i>	<i>Page</i>
I INTRODUCTION	1
II TECHNICAL PROGRAM PLAN AND RESULTS	2
1. Overview and Summary of Approach	2
2. Task I — Process Optimization	2
a. Summary	2
b. Technical Approach	2
c. Discussion of Results	6
3. Task II — Fatigue Crack Initiation	7
a. Summary	7
b. Technical Approach	7
c. Results	8
d. Discussion of Results	11
4. Task III — Fatigue Crack Propagation	14
a. Summary	14
b. Technical Approach	14
c. Results	17
d. Discussion of Results	19
5. Task IV — Thermal Mechanical Fatigue (TMF)	21
a. Summary	21
b. Technical Approach	21
c. Results	22
d. Discussion of Results	22
6. Task V — Fracture Mechanisms	23
a. Summary	23
b. Technical Approach	23
III. CONCLUSIONS AND RECOMMENDATIONS	26
1. Task I — Process Optimization	26
2. Task II — Fatigue Crack Initiation	26
3. Task III — Fatigue Crack Propagation	27
4. Task IV — Thermal Mechanical Fatigue	27
5. Task V — Fracture Mechanisms	27
REFERENCES	247



Distribution /	
Availability Codes	
Dist	Avail and/or Special
A-1	

LIST OF ILLUSTRATIONS

<i>Figure</i>		<i>Page</i>
1	As-Received Microstructure of Rotary-Forged Ti-25Al-10Nb-3V-1Mo — Equiaxed and Elongated Alpha-2 (Large White Phase) in a Transformed Beta Matrix Indicating Final Working Below the Beta Transus	51
2	Transformed Beta Structure of Ti-24Al-11Nb Exhibiting Minimal Work Below Beta Transus Followed by Slow Cooling from Reduction to Barstock	52
3	Photomicrographs of Alpha-2/Beta Forged Ti-25Al-10Nb-3V-1Mo Alloy — Beta Transus Determination (Pre-Beta Transus)	53
4	Photomicrographs of Alpha-2/Beta Forged Ti-25Al-10Nb-3V-1Mo Alloy — Beta Transus Determination	54
5	Selection of Beta Anneal Cooling Rate and Stabilization Cycle	55
6	Tower Cooling Fixture for Cooling Rate Response Study	56
7	Strip Chart From Cooling Rate Study	57
8	Sections From Ti-25Al-10Nb-3V-1Mo Cooling Rate Study, Cooled at Various Rates From the Beta + 23.6°C (1132°C) Annealing Temperature	58
9	Sections From Ti-25Al-10Nb-3V-1Mo Cooling Rate Study, Cooled at Various Rates From the Beta + 23.6°C (1132°C) Annealing Temperature (Continued)	59
10	Photomicrographs of Alpha-2/Beta Forged Ti-25Al-10Nb-3V-1Mo, Candidate No.3 From Heat Treatment Optimization Study — Solutioned at 1163°C (2125°F)/1 Hour, Cooled to 816°C (1500°F), and Held for ½ Hour, Air Cooled, and Aged for 8 Hours at 593°C (1100°F), Air Cooled	60
11	Pancake Appearance Typical for Both Alloys	61
12	Planar Fracture Surface With Material Flaking Off Ahead of Wire EDM Cut in As-Forged (Beta) Ti-24Al-11Nb Pancake	61
13	Schematic Diagram of EDM Wire Path and Pancake Fracture. Pancake Fractured When Wire Cut Reached Pancake Center	62
14	Shallow Crack in Ti-24Al-11Nb Pancake Section Resulting From Abrasive Cutoff. Crack Path Illustrates Mechanism by Which Material is Allowed to Flake From Fracture Surfaces.	63

LIST OF ILLUSTRATIONS (Continued)

<i>Figure</i>		<i>Page</i>
16	Secondary Cracking Along Gage Section of 650°C (1200°F) Tensile Specimen. Note: Subsurface Crack Along Prior Beta Grain Boundary (Right) Material is Ti-25Al-10Nb-3V-1Mo Candidate 3 (Alpha-2/Beta Forged)	65
17	Microstructure of Ti-24Al-11Nb Beta Forged and Fully Heat Treated ..	66
18	Microstructure of Ti-25Al-10Nb-3V-1Mo Beta Forged and Fully Heat Treated	67
19	Stabilization and Age Study Strength Results, Smooth Tensile Specimen Data for Ti-25Al-10Nb-3V-1Mo	68
20	Stabilization and Age Study Ductility Results, Smooth Tensile Specimen Data for Ti-25Al-10Nb-3V-1Mo	69
21	Stabilization and Age Study Strength Results, Post-Creep — Smooth Tensile Specimen Data for Ti-25Al-10Nb-3V-1Mo	70
22	Stabilization and Age Study Ductility Results, Post-Creep — Smooth Tensile Specimen Data for Ti-25Al-10Nb-3V-1Mo	71
23	0.2 Percent Yield Strength Versus Temperature for Ti-25Al-10Nb-3V-1Mo and Ti-24Al-11Nb	72
24	Ultimate Tensile Strength Versus Temperature for Ti-25Al-10Nb-3V-1Mo and Ti-24Al-11Nb	72
25	Elongation Versus Temperature for Ti-25Al-10Nb-3V-1Mo and Ti-24Al-11Nb	73
26	Reduction of Area Versus Temperature for Ti-25Al-10Nb-3V-1Mo and Ti-24Al-11Nb	73
27	Impact Strength Versus Temperature	74
28	Fracture Toughness for Ti-25Al-10Nb-3V-1Mo, Candidate 4	74
29	Specimen Orientations With Respect to Pancake Geometry and Macrostructure/Crack Propagation Relationships for Ti-25Al-10Nb-3V-1Mo	75
30	Ti-24Al-11Nb Fracture Toughness Screening Test Results	76
31	Ti-24Al-11Nb Rupture Model	77
32	Ti-24Al-11Nb 0.5 Percent Creep Model	77
33	Ti-25Al-10Nb-3V-1Mo Rupture Model	78

LIST OF ILLUSTRATIONS (Continued)

Figure		Page
34	Ti-25Al-10Nb-3V-1Mo 0.5 Percent Creep Model	78
35	Dynamic Modulus Versus Temperature	79
36	Ti-25Al-10Nb-3V-1Mo Notched Impact Fractures	80
37	Alpha-2/Beta Forged and Beta Annealed Ti-25Al-10Nb-3V-1Mo. Equiaxed Prior Beta Grain Structure at 316°C (600°F) Showing Predominately Transgranular Cleavage (Left) and at 650°C (1200°F), Mixed Inter/Transgranular Fracture (Right) From Toughness Specimens	81
38	Macro Views From 204°C (400°F) Left, and 316°C (600°F) Right, of Ti-24Al-11Nb Fracture Toughness Tests. Note Loose Flakes on Surfaces	82
39	Groups of Prior Beta Grains can be Lifted (or Drop) From Fracture Surfaces of Ti-24Al-11Nb and Ti-25Al-10Nb-3V-1Mo. This is Typical of Monotonic and Cyclic Fractures	83
40	Ti-24Al-11Nb Fracture Toughness Specimens From Left to Right 316°C (600°F) and 427°C (800°F) Tests. Deep Furrowing is Visible (Left).	84
41	Room Temperature Fracture Toughness Surface From Ti-24Al-11Nb ...	85
42	Intermediate and High Magnification Views of Fracture Surface From Ti-24Al-11Nb at Room Temperature. Note Ductile Tearing Surrounding Quasi-Cleavage Areas	85
43	Ti-24Al-11Nb Tensile Fractures Exhibiting a Transition in Fracture Mode From 204°C (400°F) on Left and 427°C (800°F) on Right. Secondary Cracking is Present Along Gage Section on Right There is None on Left.	86
44	Tensile Fractures at (From Left) 204°, 427°, and 650°C (400°, 800°, and 1200°F). Note Extensive Cracking Along Gage Section of Ti-25Al-10Nb-3V-1Mo	87
45	Beta Forged Ti-25Al-10Nb-3V-1Mo With 816°C/593°C (1500°F/1100°F) Stabilization/Age Cycle. Failed 650°C (1200°F) Tensile Specimen. Internal and Secondary Cracks Visible at Left of Photograph (b) (Arrow) and Along Gage Surface (Bracket).	88
46	Left, Extensive Secondary Cracking in Ti-24Al-11Nb Creep Test, 230 Hours at 650°C/207 MPa (1200°F/30 ksi). Right, Oxygen Embrittlement in Section Through Ti-25Al-10Nb-3V-1Mo Creep Specimen, 234 Hours at 650°C/310 MPa (1200°F/45 ksi). Ti-24Al-11Nb Sections are Identical to Ti-25Al-10Nb-3V-1Mo.	89

LIST OF ILLUSTRATIONS (Continued)

Figure		Page
47	Details of Surface Oxide, Oxygen Embrittlement Layer, and Crack Propagating into Substrate of Ti-25Al-10Nb-3V-1Mo Creep Specimen. Test Conducted at 650°C/310 MPa (1200°F/45 ksi) for 234 Hours.	90
48	Smooth LCF Specimen, $K_t = 1.0$	90
49	Fully Reversed Strain Cycle, $R_e = -1.0$	91
50	All Tensile Strain Cycle, $R_e = 0$	91
51	All Tensile Strain Cycle With Peak Strain Dwell	92
52	Notched LCF Specimen, $K_t = 2.18$	93
53	Smooth HCF Specimen, $K_t = 1.0$	94
54	Notched HCF Specimen, $K_t = 2.16$	94
55	Mean Stress Effects of Smooth LCF on Ti-24Al-11Nb at 25°C (77°F) .	95
56	Mean Stress Effects of Smooth LCF on Ti-24Al-11Nb at 427°C (800°F)	95
57	Mean Stress Effects of Smooth LCF on Ti-24Al-11Nb at 650°C (1200°F)	96
58	Mean Stress Effects of Smooth LCF on Ti-25Al-10Nb-3V-1Mo at 25°C (77°F)	96
59	Mean Stress Effects of Smooth LCF on Ti-25Al-10Nb-3V-1Mo at 427°C (800°F)	97
60	Mean Stress Effects of Smooth LCF on Ti-25Al-10Nb-3V-1Mo at 650°C (1200°F)	97
61	Comparison of Ti-24Al-11Nb Versus Ti-25Al-10Nb-3V-1Mo, Smooth LCF at 25°C (77°F), $R_e = 0$	98
62	Comparison of Ti-24Al-11Nb Versus Ti-25Al-10Nb-3V-1Mo, Smooth LCF at 427°C (800°F), $R_e = 0$	98
63	Comparison of Ti-24Al-11Nb Versus Ti-25Al-10Nb-3V-1Mo, Smooth LCF at 650°C (1200°F), $R_e = 0$	99
64	Comparison of Ti-24Al-11Nb Versus Ti-25Al-10Nb-3V-1Mo, Smooth LCF at 25°C (77°F), $R_e = -1.0$	99
65	Comparison of Ti-24Al-11Nb Versus Ti-25Al-10Nb-3V-1Mo, Smooth LCF at 427°C (800°F), $R_e = -1.0$	100

LIST OF ILLUSTRATIONS (Continued)

<i>Figure</i>		<i>Page</i>
66	Comparison of Ti-24Al-11Nb Versus Ti-25Al-10Nb-3V-1Mo, Smooth LCF at 650°C (1200°F), $R_e = -1.0$	100
67	Inelastic Strain Versus Cyclic Stress Range, Ti-25Al-10Nb-3V-1Mo at 26°C (80°F), 0.17 Hz	101
68	Inelastic Strain Versus Cyclic Stress Range, Ti-25Al-10Nb-3V-1Mo at 427°C (800°F), 0.17 Hz	101
69	Inelastic Strain Versus Cyclic Stress Range, Ti-25Al-10Nb-3V-1Mo at 650°C (1200°F), 0.17 Hz	102
70	Inelastic Strain Versus Cyclic Stress Range, Ti-24Al-11Nb at 26°C (80°F)	102
71	Inelastic Strain Versus Cyclic Stress Range, Ti-24Al-11Nb at 427°C (800°F)	103
72	Inelastic Strain Versus Cyclic Stress Range, Ti-24Al-11Nb at 650°C (1200°F)	103
73	Hysteretic Energy Versus Life, Smooth LCF of Ti-24Al-11Nb	104
74	Hysteretic Energy Versus Life, Smooth LCF of Ti-25Al-10Nb-3V-1Mo ..	104
75	Hysteretic Energy Versus Life, Smooth LCF, Ti-25Al-10Nb-3V-1Mo and Ti-24Al-11Nb	105
76	Actual Versus Predicted Life, Ti-25Al-10Nb-3V-1Mo and Ti-24Al-11Nb	105
77	Actual Versus Predicted Life, Ti-25Al-10Nb-3V-1Mo	106
78	Actual Versus Predicted Life, Ti-24Al-11Nb	106
79	Ti-25Al-10Nb-3V-1Mo Notched LCF Effects of Temperature	107
80	Ti-25Al-10Nb-3V-1Mo Notched LCF TiN Coated	107
81	Ti-24Al-11Nb Notched LCF Effects of Temperature	108
82	Ti-24Al-11Nb Notched LCF Effects of Coating	108
83	Ti-24Al-11Nb Notched LCF Effects of Hot Salt Stress Corrosion	109
84	Effects of Temperature on Ti-24Al-11Nb, Smooth HCF at $R = -1$, $K_t = 1.0$	109
85	Effects of Temperature on Ti-24Al-11Nb, Smooth HCF at $R = 0.05$, $K_t = 1.0$	110

LIST OF ILLUSTRATIONS (Continued)

Figure		Page
86	Effects of Temperature on Ti-24Al-11Nb, Notched HCF at $R = 0.05$, $K_t = 2.16$	110
87	Effects of Coating on Ti-24Al-11Nb, Smooth HCF at $R = 0.05$, $K_t = 1.0$	111
88	Effects of Prestressing on Ti-24Al-11Nb, Notched HCF at $R = 0.05$, $K_t = 2.16$	111
89	Effects of Temperature on Ti-25Al-10Nb-3V-1Mo, Smooth HCF at $R = -1$, $K_t = 1.0$	112
90	Effects of Temperature on Ti-25Al-10Nb-3V-1Mo, Notched HCF at $R = 0.05$, $K_t = 2.16$	113
91	Smooth HCF, Ti-25Al-10Nb-3V-1Mo Versus Ti-24Al-11Nb at $R = -1$, $K_t = 1.0$	113
92	Notched LCF, Ti-25Al-10Nb-3V-1Mo Versus Ti-24Al-11Nb at $R = 0.05$, $K_t = 2.16$	114
93	Smooth HCF, Ti-25Al-10Nb-3V-1Mo Versus Ti-24Al-11Nb at $R = -1$, $K_t = 1.0$	114
94	Notched HCF of Ti-25Al-10Nb-3V-1Mo	115
95	Significant Inelastic Strain Observed in 26°C (80°F) Ti-24Al-11Nb Strain Controlled LCF Test. Conditions: $\Delta\epsilon_t = 1.2$ Percent, Initial $\Delta\epsilon_i = 0.24$ Percent, Initial $\sigma_{\max} = 627$ MPa (91 ksi).	116
96	Cyclic Hardening Observed With Ti-24Al-11Nb at 427°C , $R = -1.0$, $\Delta\epsilon_t = 1$ Percent	117
97	Mean Stress Relaxation and Cyclic Hardening Observed in Ti-24Al-11Nb at 427°C , $R = 0.0$, $\Delta\epsilon_t = 0.8$ Percent	118
98	Fracture Surface Edge (Upper Right in Both Photographs) of LCF Specimen Tested at 650°C (1200°F) Showing Oxide Spalling and Secondary Cracking at Scale Cracking in Ti-25Al-10Nb-3V-1Mo	119
99	SEM Examination of Oxide and Sublayers (From Previous Figure) Showing Cracking Perpendicular to (a) and Parallel With (b) Stress Axis	120
100	Vickers Hardness of Oxygen Embrittled Surface Layer and Substrate Below in Ti-25Al-10Nb-3V-1Mo LCF Specimen Tested at 650°C (1200°F)	121
101	Remaining Life, Notched LCF Ti-24Al-11Nb at 427°C (800°F)	121

LIST OF ILLUSTRATIONS (Continued)

<i>Figure</i>		<i>Page</i>
102	Remaining Life, Notched LCF Ti-25Al-10Nb-3V-1Mo at 427°C (800°F)	122
103	Room Temperature LCF Origin (White Arrow) and Arrest Mark (Black Arrows, Probably Critical Crack Depth) From Notched LCF Test of Ti-24Al-11Nb	123
104	Critical Crack Depths are Visible in 650°C (1200°F, Left) and 427°C (800°F) Ti-24Al-11Nb Notched LCF Fractures. Dotted Line is Just Beyond Crack Front.	124
105	Remaining Life, Notched LCF Ti-24Al-11Nb at 26°C (80°F)	125
106	Surface Layer at Origin (Top) and Early Appearance of Oxide Scale Craze (Bottom) on Specimen From Previous Figure	126
107	Notch Appearance of Specimen in Previous Figure at "Overstress" Final Failure Side Showing Brittle Cracking of Surface Layer	127
108	Notched LCF Coated Specimens	128
109	Ti-25Al-10Nb-3V-1Mo/TiN Coating Nodules	129
110	Compact Type CT Specimen	130
111	Effects of Closure on Stress Intensity Range and Commonly Recognized Closure Mechanisms	131
112	Effects of Temperature, Ti-24Al-11Nb at R = 0.1, 20 Hz	132
113	Effects of Temperature, Ti-25Al-10Nb-3V-1Mo at R = 0.1, 20 Hz	133
114	Effects of Temperature, Ti-24Al-11Nb at R = 0.1, 120-Second Dwell	134
115	Effects of Temperature, Ti-24Al-11Nb at R = 0.1, 0.17 Hz	135
116	Effects of Temperature, Ti-25Al-10Nb-3V-1Mo, at R = 0.1, 0.17 Hz	136
117	Effects of Temperature, Ti-24Al-11Nb at R = 0.7	137
118	Effects of Temperature, Ti-25Al-10Nb-3V-1Mo, at R = 0.7, 0.17 Hz	138
119	Effects of Stress Ratio, Ti-24Al-11Nb, 26°C (80°F)	139
120	Effects of Stress Ratio, Ti-25Al-10Nb-3V-1Mo, 26°C (80°F), 0.17 Hz ...	140
121	Stress Ratio Model Coefficient for Constant C1 Versus Stress Ratio ...	141
122	Stress Ratio Model Coefficient for Constant C2 Versus Stress Ratio ...	142

LIST OF ILLUSTRATIONS (Continued)

<i>Figure</i>		<i>Page</i>
123	Stress Ratio Model Coefficient for Constant C3 Versus Stress Ratio ...	143
124	Stress Ratio Model Coefficient for Constant C4 Versus Stress Ratio ...	144
125	Stress Ratio Model Demonstration for Ti-24Al-11Nb at 427°C (800°F) and 0.17 Hz	145
126	Effects of Stress Ratio on Ti-25Al-10Nb-3V-1Mo at 427°C (800°F) and 0.17 Hz	146
127	Effects of Stress Ratio on Ti-24Al-11Nb at 650°C (1200°F) and 0.17 Hz	147
128	Effects of Stress Ratio on Ti-25Al-10Nb-3V-1Mo at 650°C (1200°F) and 0.17 Hz	148
129	Effects of Frequency on Ti-24Al-11Nb at 26°C (80°F), R = 0.1	149
130	Effects of Frequency on Ti-25Al-10Nb-3V-1Mo at 26°C (80°F), R = 0.1	150
131	Effects of Frequency on Ti-24Al-11Nb at 427°C (800°F), R = 0.1	151
132	Effects of Frequency on Ti-25Al-10Nb-3V-1Mo at 427°C (800°F), R = 0.1	152
133	Effects of Frequency on Ti-24Al-11Nb at 650°C (1200°F), R = 0.1	153
134	Effects of Frequency on Ti-25Al-10Nb-3V-1Mo at 650°C (1200°F), R = 0.1	154
135	Alloy Comparison at R = 0.1, 20 Hz, and 26°C (80°F)	155
136	Alloy Comparison at R = 0.1, 0.17 Hz, and 26°C (80°F)	156
137	Alloy Comparison at R = 0.7 and 26°C (80°F)	157
138	Alloy Comparison at R = 0.1, 20 Hz, and 427°C (800°F)	158
139	Alloy Comparison at R = 0.1, 0.17 Hz, and 427°C (800°F)	159
140	Alloy Comparison at R = 0.7, 0.17 Hz, and 427°C (800°F)	160
141	Alloy Comparison at R = 0.1, 20 Hz, and 650°C (1200°F)	161
142	Alloy Comparison at R = 0.1, 20 Hz, and 650°C (1200°F)	162
143	Alloy Comparison at R = 0.7, 0.17 Hz, and 650°C (1200°F)	163

LIST OF ILLUSTRATIONS (Continued)

<i>Figure</i>		<i>Page</i>
144	Threshold Crack Growth Rate Material Comparison, Ti-24Al-11Nb Versus Ti-25Al-10Nb-3V-1Mo at 26°C (80°F), R = 0.1, and 20 Hz	164
145	Threshold Crack Growth Rate Material Comparison, Ti-24Al-11Nb Versus Ti-25Al-10Nb-3V-1Mo at 26°C (80°F), R = 0.7, and 20 Hz	165
146	Threshold Crack Growth Rate Material Comparison, Ti-24Al-11Nb Versus Ti-25Al-10Nb-3V-1Mo at 650°C (1200°F), R = 0.1, and 20 Hz ..	166
147	Threshold Crack Growth Rate Material Comparison, Ti-24Al-11Nb Versus Ti-25Al-10Nb-3V-1Mo at 650°C (1200°F), R = 0.7, and 20 Hz ..	167
148	Threshold Crack Growth Rate Temperature Comparison, Ti-24Al-11Nb at R = 0.1 and 20 Hz	168
149	Threshold Crack Growth Rate Temperature Comparison, Ti-24Al-11Nb at R = 0.7 and 20 Hz	169
150	Threshold Crack Growth Rate Temperature Comparison, Ti-25Al-10Nb-3V-1Mo at R = 0.1 and 20 Hz	170
151	Threshold Crack Growth Rate Temperature Comparison, Ti-25Al-10Nb-3V-1Mo at R = 0.7 and 20 Hz	171
152	Threshold Crack Growth Rate Stress Ratio Effect, Ti-24Al-11Nb at 26°C (80°F) and 20 Hz	172
153	Threshold Crack Growth Rate Stress Ratio Effect, Ti-24Al-11Nb at 427°C (800°F) and 20 Hz	173
154	Threshold Crack Growth Rate Stress Ratio Effect, Ti-24Al-11Nb at 650°C (1200°F) and 20 Hz	174
155	Threshold Crack Growth Rate Stress Ratio Effect, Ti-25Al-10Nb-3V-1Mo at 26°C (80°F) and 20 Hz	175
156	Threshold Crack Growth Rate Stress Ratio Effect, Ti-25Al-10Nb-3V-1Mo at 650°C (1200°F) and 20 Hz	176
157	Threshold Crack Growth Rate Stress Ratio Comparison After Closure Correction, Ti-24Al-11Nb at 26°C (80°F) and 20 Hz	177
158	Threshold Crack Growth Rate Stress Ratio Comparison After Closure Correction, Ti-24Al-11Nb at 427°C (800°F) and 20 Hz	178
159	Threshold Crack Growth Rate Stress Ratio Comparison After Closure Correction, Ti-24Al-11Nb at 650°C (1200°F) and 20 Hz	179

LIST OF ILLUSTRATIONS (Continued)

<i>Figure</i>		<i>Page</i>
160	Threshold Crack Growth Rate Stress Ratio Comparison After Closure, Ti-25Al-10Nb-3V-1Mo at 26°C (80°F) and 20 Hz	180
161	Threshold Crack Growth Rate Stress Ratio Comparison After Closure, Ti-25Al-10Nb-3V-1Mo at 650°C (1200°F) and 20 Hz	181
162	Effect of Crack Length on Near Threshold Crack Growth Rates, Ti-25Al-10Nb-3V-1Mo at 26°C (80°F) and 20 Hz	182
163	Effect of Crack Length on Closure-Corrected Crack Growth Rates in the Near Threshold Region, Ti-25Al-10Nb-3V-1Mo at 26°C (80°F), R = 0.1, and 20 Hz	183
164	Comparison of Crack Growth Rates From K-Decreasing and Constant-Load Tests, Ti-24Al-11Nb at 26°C (80°F), R = 0.1, and 20 Hz	184
165	Comparison of Crack Growth Rates From K-Decreasing and Constant-Load Tests, Ti-24Al-11Nb at 26°C (80°F), R = 0.7, and 20 Hz	185
166	Comparison of Crack Growth Rates From K-Decreasing and Constant-Load Tests, Ti-24Al-11Nb at 650°C (1200°F), R = 0.1, and 20 Hz	186
167	Comparison of Crack Growth Rates From K-Decreasing and Constant Load Tests, Ti-24Al-11Nb at 650°C (1200°F), R = 0.7, and 20 Hz	187
168	Load Control TMF Specimen	188
169	Out-of-Phase Cycle (Type I) with (a) R = -1.0 and (b) R = 0.0	189
170	In-Phase Cycle (Type II) with R = -1.0	190
171	Load Control TMF Results of Ti-24Al-11Nb at 0.5 cpm and 38° to 650°C (Strain Ratio = R and Salted = Hot Salt Stress Corrosion Test)	190
172	Load Control TMF Results of Ti-25Al-10Nb-3V-1Mo at 0.5 cpm and 38° to 650°C (Strain Ratio = R)	191
173	Ti-24Al-11Nb Versus Ti-25Al-10Nb-3V-1Mo, Load Control TMF Results (Type I Cycle, 0.5 cpm, 38° to 650°C, and Strain Ratio = -1.0)	191
174	Load Control TMF Results of Ti-24Al-11Nb for Type I Cycle Versus Type II Cycle (0.5 cpm, 38° to 650°C, and Strain Ratio = -1.0)	192
175	Effects of HSSC on Ti-24Al-11Nb for Type I Cycle (0.5 cpm, 38° to 650°C, and Strain Ratio = -1.0)	192
176	Hysteretic Energy Versus Cycles to Failure for Type I Cycle (0.5 cpm, 38° to 650°C, and Strain Ratio Varied)	193

LIST OF ILLUSTRATIONS (Continued)

<i>Figure</i>		<i>Page</i>
177	Actual Life Versus Predicted Life	193
178	Detail of HSSC Fracture from Ti-24Al-11Nb TMF. Note Secondary Cracking on Gage Section Sides in Photograph at Left	194
179	Oxygen Embrittlement Layer (Arrows) After 0.5 Hours at 650°C (1200°F) in Ti-24Al-11Nb LCF Test. Note Secondary Cracking	195
180	Secondary LCF Cracks in Ti-24Al-11Nb Seen in Cross-Section Near Origin (Top). Left is 427°C (800°F), Right is 650°C (1200°F).	196
181	Secondary Crack on Outer Diameter of Gage Section, Ti-24Al-11Nb, LCF. Structure Revealed by Test Environment, 427°C (800°F) Air. There Seems to be No Obvious Relationship Between Crack and Microstructure.	197
182	Isolated Heavy Concentrations of Grain Boundary Alpha-2 in Ti-24Al-11Nb	198
183	Microstructure of Ti-25Al-10Nb-3V-1Mo Showing Grain Boundary Alpha-2 and Preferential Alignment of Widmanstatten Structure Along Prior Beta Grain Boundary	199
184	(a) Fractographic Appearance of Preferentially Aligned Widmanstatten Structure Along Prior Beta Grain Boundary With Probable Grain Boundary Alpha-2 (b) Enlargement of (a) Showing Cracked Oxide Scale and Sublayer Beneath for Ti-25Al-10Nb-3V-1Mo	200
185	Pronounced Linear Oxide Craze and Associated Multiple Secondary Cracks Perpendicular to Strain Axis on Ti-25Al-10Nb-3V-1Mo Smooth LCF Specimen Seen in Previous Figure	201
186	Low Cycle Fatigue (LCF) Fractures Produced at 650°C (1200°F) Exhibiting Internal (a) and Surface (b) Fatigue Origins for Ti-25Al-10Nb-3V-1Mo	202
187	Void at Fatigue Origin in Ti-25Al-10Nb-3V-1Mo Smooth LCF Specimen Tested at 650°C (1200°F)	203
188	Ti-24Al-11Nb LCF Origins at Grain Boundary Alpha-2	204
189	Room Temperature Strain Control LCF Origin in Ti-25Al-10Nb-3V-1Mo at a Prior Beta Grain Boundary	205
190	427°C (800°F) Strain Control LCF Origin at Prior Beta Grain Boundary in Ti-24Al-11Nb	206
191	650°C (1200°F) Strain Control LCF Origin at Probable Alpha-2 Platelets in Ti-24Al-11Nb	207

LIST OF ILLUSTRATIONS (Continued)

<i>Figure</i>		<i>Page</i>
192	High Cycle Fatigue (HCF) Origin in 427°C (800°F) Notched Ti-24Al-11Nb Specimen	208
193	Subsurface LCF Origin in Ti-24Al-11Nb 650°C (1200°F) Dwell Test. There Appears to be Fine Porosity Present.	209
194	Fatigue Striations on Ti-24Al-11Nb LCF Specimens at 427°C (800°F). Left is 0.17 Hz, R = -1.0; Right is R = 0, 120-Second Peak Strain Dwell Cycle.	210
195	Notched LCF Fracture Surface (a) and Notch Appearance (b) at Origin, Ti-25Al-10Nb-3V-1Mo Tested at 650°C (1200°F)	211
196	Documentation of Crack Aspect Ratio in Ti-24Al-11Nb 427°C (800°F) Notched LCF Test	212
197	Prestressed Ti-24Al-11Nb Notched LCF 26°C (80°F) Test (Nf = 46,524 cycles). Photographs Show Material Flaking From Surface and Critical Crack Depth.	213
198	Ti-24Al-11Nb Notched LCF Origin, 650°C (1200°F). Unusual Texture at Notch May Be Alpha-2 Platelet.	214
199	Left, Multiple Surface Crack Initiations in Coated Ti-24Al-11Nb 650°C (1200°F) Notched LCF. Center, Same as Left But With HSSC From ASTM Sea Salt (Visible in Notches). Right, Ti-25Al-10Nb-3V-1Mo Notched LCF, Titanium Nitride Coated Plus HSSC, Surface Origins in 427°C (800°F) LCF Test.	215
200	Subsurface HCF Origin in Ti-25Al-10Nb-3V-1Mo at 650°C (1200°F), R = -1.0 at Possible Void	216
201	Room Temperature HCF Origin at Surface Connected Prior Beta Grain Boundary in Ti-24Al-11Nb. Edge is Smeared.	217
202	Room Temperature HCF Origin in Ti-24Al-11Nb. Streaks are Probably Prior Beta Grain Boundaries.	218
203	Subsurface HCF Origin in Ti-24Al-11Nb at 650°C (1200°F)	219
204	Near Surface HCF Origin in Ti-25Al-10Nb-3V-1Mo at 650°C (1200°F) Appears to be Prior Beta Grain Boundary Junction	220
205	Notched HCF Origin at Alpha Platelet in 427°C (800°F) Ti-24Al-11Nb Specimen	221
206	From Left, Macro Views of Room Temperature, 427°C (800°F) and 650°C (1200°F) Fracture Surfaces From Ti-24Al-11Nb 20 Hz Crack Growth Tests	222

LIST OF ILLUSTRATIONS (Continued)

<i>Figure</i>		<i>Page</i>
207	Ti-25Al-10Nb-3V-1Mo Room Temperature Crack Growth Fractures — Orientations "c" (Left) and "b" (Right) Described in Figure 29	223
208	Macro Views of 0.17 Hz Crack Growth Test Specimens (Ti-24Al-11Nb). From Left: Room Temperature, 427°C (800°F), and 650°C (1200°F). Grain Pullout Decreases as Temperature Increases.	224
209	Room Temperature 20 Hz Crack Growth Surface of Ti-24Al-11Nb at Low and High Magnifications	225
210	Room Temperature 0.17 Hz Crack Growth Surface of Ti-24Al-11Nb at Low and High Magnifications	226
211	427°C (800°F) Crack Growth Surface of Ti-24Al-11Nb at 20 Hz	227
212	427°C (800°F) Crack Growth Surface of Ti-24Al-11Nb at 0.17 Hz	228
213	Low and High Magnifications of 650°C (1200°F) Ti-24Al-11Nb Crack Growth Surface at 20 Hz	229
214	Crack Growth Fracture Surface of Ti-24Al-11Nb at 650°C (1200°F) and 0.17 Hz	230
215	Macro Views of Ti-25Al-10Nb-3V-1Mo Crack Growth Specimen Surfaces. From Left to Right: Room Temperature, 427°C (800°F), and 650°C (1200°F).	231
216	Furrowed Crack Propagation Surface on Ti-25Al-10Nb-3V-1Mo Compact Tension Specimen Tested at Room Temperature and 20 Hz. Feathery Cleavage Predominates.	232
217	Ti-25Al-10Nb-3V-1Mo at 427°C (800°F) Crack Growth Specimen Exhibits Deep Furrowing Resulting From Branching Crack Front and Resultant Material Ejection	233
218	Ti-25Al-10Nb-3V-1Mo Crack Growth Specimen Tested at 650°C (1200°F) and 0.17 Hz. Extensive Secondary Cracking Results in Exfoliation of Large Pieces of Material.	234
219	Fracture Faces From Ti-25Al-10Nb-3V-1Mo TMF Specimens. Left is Type I (Out-of-Phase). Right is Type II (In-Phase).	235
220	Ti-25Al-10Nb-3V-1Mo In-Phase TMF Test Showing Extensive Oxide Scale Spalling and Rumpling	236
221	Ti-24Al-11Nb In-Phase TMF Fracture at Outside of Gage Surface (Left). Dark Surface Layer is Oxygen Diffusion (Right).	237

LIST OF ILLUSTRATIONS (Continued)

<i>Figure</i>		<i>Page</i>
222	Ti-24Al-11Nb Out-of-Phase TMF Fracture Surface and Side of Gage Showing Secondary Cracking Near Origin	238
223	Ti-24Al-11Nb In-Phase Thermal Mechanical Fatigue Fracture Surfaces Showing Surface Connected Prior Beta Grain Boundary and Oxygen Diffused Surface Layer	239
224	Ti-24Al-11Nb TMF Type II HSSC Showing Multiple Surface Origins .	240
225	Ti-24Al-11Nb Out-of-Phase TMF Fracture Resulting From HSSC	241
226	Hot Salt Stress Corrosion (HSSC) TMF Origin in Ti-24Al-11Nb (In-Phase Cycle)	242
227	Section Through HSSC TMF of Ti-24Al-11Nb Showing Secondary Cracking	243
228	(110) Pole Figure for Beta Phase of Ti-25Al-10Nb-3V-1Mo Pancake in Radial Direction	244
229	(0002) Pole Figure for Alpha-2 Phase of Ti-25Al-10Nb-3V-1Mo Pancake in Radial Direction	245
230	Relationship of Pancake to Pole Figures	246

LIST OF TABLES

<i>Table</i>		<i>Page</i>
1	Candidate Heat Treatments for Optimum Property Screening Tests	29
2	Alloy Chemistry (Weight Percent for Ti-25Al-10Nb-3V-1Mo (a/o))	30
3	Alloy Chemistry (Weight Percent for Ti-24Al-11Nb (a/o))	30
4	Ti-25Al-10Nb-3V-1Mo Isothermal Alpha-2 Plus Beta Forging Parameters	30
5	Candidate 3 (Alpha-2 Plus Beta Forging), Ti-25Al-10Nb-3V-1Mo Heat Treatment	30
6	Grain Size From Ti 24Al-11Nb Barstock	30
7	Grain Size From Beta Forgings	30
8	Heat Treatment Optimization Study Room Temperature Tensile Test Results, Ti-25Al-10Nb-3V-1Mo	31
9	Heat Treatment Optimization Study Room Temperature Post-Creep Exposure Tensile Test Results, Ti-25Al-10Nb-3V-1Mo	32
10	Candidate 3, Ti-25Al-10Nb-3V-1Mo Notched Charpy Impact Results ...	32
11	Candidate 3, Ti-25Al-10Nb-3V-1Mo Tensile Results	33
12	Candidate 3, Ti-25Al-10Nb-3V-1Mo Fracture Toughness Precracked Compact Tension Specimens	33
13	Candidate 3, Ti-25Al-10Nb-3V-1Mo Creep Results Conditions 650°C (1200°F), 379 MPa (55 ksi)	33
14	Ti-25Al-10Nb-3V-1Mo Candidate 4 Tensile Test Results	33
15	Ti-24Al-11Nb Tensile Test Results	34
16	Candidate 4, Ti-25Al-10Nb-3V-1Mo Notched Charpy Impact Versus Temperature	34
17	Notched Charpy Impact Versus Temperature Ti-24Al-11Nb	34
18	Candidate 4, Ti-25Al-10Nb-3V-1Mo Fracture Toughness	35
19	Fracture Toughness for Ti-24Al-11Nb	35
20	Ti-24Al-11Nb a/o Creep Results	35
21	Candidate 4, Ti-25Al-10Nb-3V-1Mo a/o Creep Results	36

LIST OF TABLES (Continued)

<i>Table</i>		<i>Page</i>
22	Modulus of Elasticity Versus Temperature	37
23	Smooth LCF for Ti-24Al-11Nb a/o Controlled Axial Strain, Frequency = 0.17Hz (10 cpm)	38
24	Smooth LCF for Ti-24Al-11Nb a/o Controlled Axial Strain, Frequency = 0.17Hz (10 cpm)	39
25	Smooth LCF for Ti-24Al-11Nb a/o Controlled Axial Strain, Frequency = 0.17Hz (10 cpm)	40
26	Smooth LCF for Ti-25Al-10Nb-3V-1Mo a/o Controlled Axial Strain, Frequency = 0.17Hz (10 CPM)	41
27	Regression Fit Indicators For Strain Versus Life Plots	42
28	Regression Fit Indicators For Energy Versus Life Plots	42
29	Candidate 4, Ti-25Al-10Nb-3V-1Mo Notched Low Cycle Fatigue (Frequency = 0.17 Hz (10 cpm), R = 0.5, Kt = 2.18)	43
30	Notched LCF for Ti-24Al-11Nb (Frequency = 0.17 Hz (10 cpm), R = 0.05, Kt = 2.18)	44
31	Notched LCF for Ti-24Al-11Nb (Frequency = 0.17 Hz (10 cpm), R = 0.05, Kt = 2.18)	44
32	Smooth Axial High Cycle Fatigue Results for Ti-24Al-11Nb	45
33	Notched Axial High Cycle Fatigue Results for Ti-24Al-11Nb	45
34	Smooth and Notched Axial High Cycle Fatigue Results for Ti-25Al-10Nb-3V-1Mo	46
35	Regression Analysis Summary For Axial High Cycle Fatigue Results ...	46
36	Regression Analysis Summary for HCF Mean Lines	47
37	Load-Controlled TMF Results for Ti-24Al-11Nb	48
38	Load-Controlled TMF Results for Ti-25Al-10Nb-3V-1Mo	49
39	Hysteretic Energy Results-Load Controlled TMF	50

I. INTRODUCTION

Future tactical aircraft engine designs depend heavily on advanced materials technology to meet thrust-to-weight and durability goals. Several types of materials currently under development are candidates for use in these advanced engines, including intermetallic titanium aluminides. Titanium aluminide alloys offer low density, high specific strength, and elevated temperature capabilities. If the materials are used in major structural and rotating components, these properties could significantly increase engine thrust-to-weight ratio.

Monolithic titanium aluminides are currently being evaluated for static components where they offer strength and stiffness advantages at temperatures above conventional titanium alloy capability. Since their specific strength and stiffness are competitive with nickel alloys up to 650°C or beyond, use of the titanium aluminides could significantly reduce weights as compared to nickel structures. In addition, titanium aluminides are much less susceptible to combustion than conventional titanium alloys and can therefore be considered for rotating components with higher operating temperatures than current titanium alloys permit.

Primary limitations of titanium aluminides have been low ductility at low temperatures and uncertainty about fatigue and fracture capability. Early work associated with alloy and process development concentrated on basic mechanical properties. The fatigue and fracture mechanics behavior, and limitations imposed by low ductility, must be thoroughly evaluated and understood before titanium aluminides can be given serious consideration for rotating component applications.

This program's objective was to provide an understanding of the fatigue and fracture behavior of monolithic Ti_3Al alloys. The program consisted of five tasks addressing:

- Potential improvements in the fatigue and fracture capability of the selected alloy by optimizing forging and heat treatment conditions to provide the best balance of strength, ductility, toughness, creep, and impact resistance. The process optimization, conducted on the Ti-25Al-10Nb-3V-1Mo, examined isothermal forgings above and below the beta transus. An optimum stabilization and age cycle was developed after evaluating six temperature combination variations. Both alloys received the optimized forge/heat treat process and basic mechanical property screening.
- Applicability of current life prediction and data analysis models to the material. The ability of conventional fatigue and fracture analysis tools and methods to predict the effects of a wide array of variables with these materials is of great importance. The use of these tools was investigated in low cycle fatigue (LCF), high cycle fatigue (HCF), thermal mechanical fatigue (TMF), and crack propagation testing. Variables included temperature, cycle type (frequency/dwell), stress, strain, stress intensity, and R-ratio. The application of hysteretic energy in a fatigue life prediction model and the hyperbolic sine model for crack propagation was addressed.
- The effects of low ductility on fatigue and fracture properties, including thermal mechanical fatigue capability and changes in this behavior as temperature and ductility increase. Low temperature/low ductility presents a particular problem from an out-of-phase TMF cycle standpoint. Notched fatigue behavior at low temperature results in large inelastic surface strains. The roles that these conditions play in the cyclic behavior is of critical importance. Smooth and notched isothermal LCF and HCF testing and TMF testing employing in-phase and out-of-phase cycle types were among those employed to address these questions.

These objectives were met under this program.

II. TECHNICAL PROGRAM PLAN AND RESULTS

1. OVERVIEW AND SUMMARY OF APPROACH

The investigation was conducted as a five-task program with a 45-month technical effort directed toward characterizing fatigue and fracture behavior of monolithic Ti_3Al alloys.

Task I included a study of candidate processing/heat treatment variations to optimize microstructure and mechanical properties for improved fatigue and damage tolerance. The optimization plan included a direct comparison of candidate forging and heat-treatment conditions determined under this task with results of other U.S. Air Force contracts performed by Pratt & Whitney (P&W) Commercial Engine Business, East Hartford, Connecticut. Based on a balance of properties and microstructural features, the optimum processing conditions for the alloy were selected. Details and results of that study are shown in the Task I discussion.

A substantial experimental program and associated analytical effort emphasized fatigue and fracture behavior. In Tasks II and III, fatigue crack initiation and propagation behavior were evaluated over a range of temperatures, frequencies, and stress ratios, spanning potential service conditions for the material including the low temperature, low ductility area. The initiation behavior study also included waveshape effects (dwell) and spanned the high cycle fatigue (HCF) and low cycle fatigue (LCF) regimes. The crack propagation evaluation included threshold behavior, temperature, stress ratio, and frequency effects. Use of the hyperbolic sine model (SINH) provided a mathematical model of the crack growth behavior over a portion of the range of conditions evaluated. Thermal mechanical fatigue (TMF) behavior for different phase cycles and stress ratios was included in Task IV. Finally, in Task V extensive metallography and fractography was used to understand the mechanisms of initiation and propagation.

2. TASK I — PROCESS OPTIMIZATION

a. Summary

Initial development work on Ti_3Al alloys under previous U.S. Air Force contracts concentrated on obtaining an acceptable overall balance of properties, including good elevated temperature creep strength, and finite, although still small, low-temperature ductility. Two of the most promising compositions are Ti-24Al-11Nb a/o and Ti-25Al-10Nb-3V-1Mo a/o.* Both of these alloys were studied in this program although initially only one alloy, Ti-24Al-11Nb, was to be studied.

A forging and heat treatment study was conducted using the Ti-25Al-10Nb-3V-1Mo alloy. This evaluation consisted of a two-part study — the first part to select candidate processes, the second part to perform screening tests. The key process elements addressed were the forging temperature, the beta anneal cooling rate and the stabilization and age cycle. Processing details are discussed later. The optimum Ti-25Al-10Nb-3V-1Mo process was applied to the Ti-24Al-11Nb material and both alloys received preliminary characterization.

b. Technical Approach

The best process/property combination previously achieved for Ti-25Al-10Nb-3V-1Mo was from AFWAL-TR-82-4086, "R&D On Composition And Processing Of Titanium Aluminide Alloys For Turbine Engines" (Reference 1). Process elements from that program are shown as candidate in Table 1. In that program, the material was forged from cast ingot. There, it was

* All references to alloy composition are on the basis of atomic percent unless otherwise stated.

noted that while heat treatment of alpha-2 base alloys can be used to produce quite a large variation in properties; the best ductility at low temperatures and the best creep-rupture capability is produced by a beta solution treatment. Throughout the development of these materials, it has also been felt that toughness, if not independent of ductility, may in fact be positively related.

The cooling rate from the beta phase field has also been shown to be of crucial importance. By controlling the rate to give a fine Widmanstatten structure, the best property balance is achieved. A fine prior beta grain size was noted to be associated with longer fatigue lives as well as good tensile ductility and that creep lives were better with an elongated (and coarser) prior beta grain morphology. That study also indicated that the additional working introduced by redundant ingot upset forging broke up the cast structure resulting in a much finer uniform grain size.

In the Ti-24Al-11Nb alloy, a similar relationship between microstructure strength and ductility was seen in "Research to Conduct an Analytical Investigation of Alloys," AFML-TR-78-18. There, it was observed that a rapid (12°C/sec) cooling rate results in a partially transformed structure with a high room temperature yield strength and finite but low ductility. Intermediate cooling rates (3.3°C/sec) result in a Widmanstatten structure with good ductility and a strength level greater than 689.5 MPa (100 ksi). Slow cooling rates (1°C/sec) give a colony-type structure with the associated low strength and ductility. This cooling rate-to-microstructure relationship was also shown in "Production of Titanium Aluminide Products," AFWAL-TR-4050.

Based on these assumptions, wrought barstock would be isothermally forged above and below the beta transus, a cooling rate from the beta field capable of producing a fine Widmanstatten structure would be determined, and an effort would be made to obtain a fine prior beta grain structure by direct stabilization from the beta forge cycle, eliminating a beta solution cycle. The other two Ti-25Al-10Nb-3V-1Mo process variants in the table show the optimized beta anneal cooling method and the results of the stabilization/age cycles from those portions of the process study. From the screening study on these three variants, the best process (Candidate 4) was selected and applied to pancake forgings of both alloys. The cyclic characterization in Tasks II through V was divided to allocate 75 percent of the testing effort to Ti-24Al-11Nb and 25 percent to Ti-25Al-10Nb-3V-1Mo.

(1) Material

The Ti-25Al-10Nb-3V-1Mo material was obtained as 15.6 cm (6.125 in.) diameter barstock. The "as-received" microstructure is shown in Figure 1. This material had been triple vacuum melted and cast into a 14-inch diameter ingot at Timet's Henderson, Nevada facility and then converted to barstock at their Toronto, Ohio mill. The conversion process entails rotary forging into an octagonal cross-section high in the alpha-beta temperature range. The reduced barstock was subsequently lathe turned into round barstock. The 430 kg (950 lb) ingot yielded 234 kg (516 lb) of finished barstock. The Ti-24Al-11Nb was produced in a similar manner, however, reduction was to 20 cm (8.5 in.) diameter. The Ti-24Al-11Nb barstock microstructure is shown in Figure 2.

Alloy chemistry is shown in Tables 2 and 3. A beta transus determination was conducted on the Ti-25Al-10Nb-3V-1Mo upon receipt. The study consisted of microstructural review (Figures 3 and 4) of specimens water quenched from ascending temperatures starting at 1038°C (1900°F). The beta transus was found to be between 1099°C (2010°F) and 1104°C (2020°F).

The approximate beta transus for the Ti-24Al-11Nb was known since numerous Timed heats with similar elemental analysis have been found to possess beta transus between 1121°C (2050°F) and 1132°C (2070°F).

(2) Process Application/Selection Procedure

Initially, a full-sized Ti-25Al-10Nb-3V-1Mo pancake was isothermally alpha-2 beta forged. The forging details are shown in Table 4. This pancake was cut in half and one-half of the forging was given the "Candidate 3" heat treatment. That heat treatment is described in detail in Table 5. The remaining half was set aside to provide material for the cooling rate and stabilization cycle study described in Figure 5, and for the Candidate 2 variant once the optimum parameters had been determined.

The cooling rate study was conducted using the "tower" fixture and strip specimen shown in Figure 6. The tower fixture was fabricated from a titanium alloy with similar thermal conductivity. A strip of the subject alloy was inserted into the slot in the fixture, thermocouples were placed into the indicated holes, and the assembly was wired together. The thermocouples were routed to a strip recorder. The tower assembly was placed in a furnace and heated to the beta forging temperature, 1150°C (2100°F), and soaked for 30 minutes. The assembly was then withdrawn from the furnace and allowed to air cool. The resultant microstructures and cooling rate curves are shown in Figures 7 through 10.

The cooling rate that produced the desired fine acicular alpha-2 plus beta Widmanstatten microstructure was found to exist between 158° and 129°C (285° to 233°F) per minute. Based upon the comparative section thermal masses, it was determined that an optimum cooling rate for the 28.6 mm (1.125 in.) thick pancakes could be obtained with an air cool. A fan air cool was employed for the Ti-24Al-11Nb forgings since they were produced at a slightly greater thickness for specimen accommodation.

(3) Forgings

All of the pancake forgings were produced in a 2.67-MN (300-ton) press with open dies under true isothermal conditions. A Ti-24Al-11Nb pancake forging typical of both Ti-25Al-10Nb-3V-1Mo and Ti-24Al-11Nb is shown in Figure 11. No cracking occurred during the forging of any of the pancakes; however, pancakes did crack from residual stresses during sectioning by both wire EDM (Figures 12 and 13) and abrasive cut-off wheel machining (Figure 14). The pancakes were in the as-forged condition. A cross-section showing the macrostructure of a beta forged and stabilization/age Ti-25Al-10Nb-3V-1Mo pancake (Candidate 4) is shown in Figure 15. The presence of extremely elongated prior beta grains in the radial direction of the pancake revealed the flow pattern resulting from forging. Since no subsequent beta solution was applied, this structure was not allowed to recrystallize and grow to the equiaxed prior beta structure seen in Figure 16 from the Candidate 3 forging (beta annealed after alpha-2/beta forging). Grain size and comments on the microstructures are given in Tables 6 and 7. The degree of upset for the Ti-24Al-11Nb forgings was 72 percent; the upset for the Ti-25Al-10Nb-3V-1Mo forgings was 86 percent.

The fully heat treated microstructures are shown in Figures 17 and 18. Typical features for both Ti-24Al-11Nb and Ti-25Al-10Nb-3V-1Mo microstructures are the fine basket weave of white acicular alpha-2 platelets and the dark beta phase preferentially aligned along prior beta grain boundaries with grain boundary alpha-2 phase present and some larger alpha-2 platelets oriented normal to the viewing plane.

(4) Stabilization/Age Study

A study was conducted to identify an optimum stabilization and age cycle combination. Based on P&W experience with alpha-2 aluminides and current practice with conventional beta-processed titanium alloys, a matrix of two solution temperatures was established. Advantage would be taken of the observed correlation of hardness and room-temperature yield strength in

identifying which cycle combination provided optimum strength. Ti-25Al-10Nb-3V-1Mo test bars were fabricated and 816°C (1500°F) and 871°C (1600°F) 30-minute stabilization cycles were applied. Eight-hour age cycles were subsequently applied at 47°C (100°F) intervals between 593°C (1100°F) and 704°C (1300°F). A microstructural review augmented with a microhardness survey was then conducted. The results of this study were inconclusive and consequently pieces of material large enough to provide limited numbers of tensile specimens were subjected to the same thermal process matrix. Room temperature strength and ductility test results for each stabilization/age combination are reported in Table 8 and shown in comparison in Figures 19 and 20. The 816°C (1500°F) 30-minute stabilization — 593°C (1100°F) 8-hour age cycle appears to offer the best combination of room temperature strength and ductility. Post-creep tensile stability was determined by exposure of tensile specimens to 379 MPa (55 ksi), 650°C (1200°F) creep conditions to 0.5 creep and then down-loaded to 138 MPa (20 ksi) and given a further 100 hours of exposure. Specimens were then removed from test and room temperature strength and ductility were rechecked. The post-creep tensile results are shown in Table 9. Post-creep ductility at room temperature decreased for all of the stabilization cycles evaluated. Post-creep results are shown graphically in Figures 21 and 22.

(5) Screening Test Results

The various thermal cycle combinations were screened for tensile strength, ductility, and suspended creep/tensile stability. Based upon these results, an 815°C (1500°F)/30-minute stabilization — 593°C (1100°F)/8-hour age cycle applied to beta forged material appeared to provide an optimum combination of strength and ductility. This eliminated the need to screen a "Candidate 2", since applying the indicated stabilization/age cycle to the alpha-2/beta forged material would have been a duplication of the heat treatment screened in the "Candidate 3" testing. The beta forged material with the same stabilization/age cycle exhibited similar strength and greater ductility. Screening test results for "Candidate 3" are shown in Tables 10 through 13.

Tensile ductility data obtained are similar to, and in some cases higher than, those observed in the previous Air Force Wright Aeronautical Laboratories (AFWAL) program (Reference 1) from which the Candidate 3 heat treatment was developed. Room temperature Charpy notched impact strength was minimal (less than 2.0 joules). Both 0.2 percent yield strength and ultimate strength were 1) to 20 percent lower than expected (probably due to a somewhat coarser Widmanstätten structure).

Fracture toughness was similar to that previously observed, while creep capability was poor compared to previous results (Reference 1) reflecting the reduced strength. Creep tests were conducted at 379 MPa (55 ksi) to provide a direct comparison with the work done in the previous program.

Strength and ductility versus temperature for the optimized Ti-25Al-10Nb-3V-1Mo alloy, "Candidate 4" and the Ti-24Al-11Nb alloy (Candidate 1) is reported in Tables 14 and 15 and Figures 23 through 26. The strength for the Ti-24Al-11Nb material was lower than the Ti-25Al-10Nb-3V-1Mo alloy as expected. Ductility for the Ti-24Al-11Nb was only slightly lower than the Ti-25Al-10Nb-3V-1Mo. Since the alloys were both beta forged from wrought barstock with similar upsets and subsequently, received identical heat treatments, the effects of composition on mechanical properties can be clearly seen. The higher aluminum content and the increased amount of beta stabilizers in the Ti-25Al-10Nb-3V-1Mo alloy results in superior strength.

A comparison of notched Charpy impact strength for the two alloys is shown in Figure 27. Although similar up to 205°C (400°F), above that temperature the Ti-24Al-11Nb material has a clear advantage. Results are listed in Tables 16 and 17.

Fracture toughness versus temperature for the Ti-25Al-10Nb-3V-1Mo Candidate 4 alloy is shown in Figure 28. Since the macrostructure resulting from the absence of a beta anneal cycle

appears highly directional, supplemental tests to look at the three extremes in macrostructure versus crack propagation direction were conducted. The orientations are described in Figure 29. No difference was seen at the condition examined. Tabulated results are shown in Table 18.

Fracture toughness results for the Ti-24Al-11Nb are shown in Table 19 and Figure 30. Since the Ti-24Al-11Nb macrostructure was similar to the Ti-25Al-10Nb-3V-1Mo alloy, orientation was not addressed. Creep behavior is shown in Tables 20 and 21 for the two alloys. Rupture, Figure 31, and 0.5 percent creep, Figure 32, for the Ti-24Al-11Nb are plotted as a function of stress and temperature. Figures 33 and 34 show the Ti-25Al-10Nb-3V-1Mo results plotted. Dynamic elastic modulus versus temperature was determined for both alloys and is shown in Figure 35 and Table 22.

c. Discussion of Results

The limited determination of mechanical properties obtained by the screening tests provided a good overview of the alloys' monotonic capabilities. In addition, insight into the relationship between macrostructure, microstructure, environmental effects, and failure modes were gained.

Notched Charpy impact strength is less than 5 joules below 427°C for the Ti-25Al-10Nb-3V-1Mo alpha-2/beta forged/solutioned (equiaxed) structure. This is also true for the beta processed Ti-25Al-10Nb-3V-1Mo with the markedly different prior beta grain morphology seen in Figure 36; in both cases, microstructure is similar. Prior beta grain structure appears to have no effect on impact strength.

There is a significant strength advantage for the Ti-25Al-10Nb-3V-1Mo over Ti-24Al-11Nb at room temperature but there is minimal difference in impact strength. At 427°C, the high ductility of Ti-24Al-11Nb compared to Ti-25Al-10Nb-3V-1Mo is manifested in a large impact advantage over Ti-25Al-10Nb-3V-1Mo. Fracture toughness also appears to be independent of prior beta grain morphology as seen in the Candidate 4 testing where extremes in orientation were tested showing little difference. The Candidate 3 structure undergoes the transition in fracture mode between 316° and 650°C and is shown in Figure 37. The 650°C test specimen exhibiting necking was not plane strain, and the data were not used.

The alpha-2/beta forged material has an advantage in toughness over the beta forging at low and elevated temperatures. Its yield strength is higher and its ductility lower versus the beta material. Strength is not the determining factor since the Ti-24Al-11Nb is significantly weaker yet has better toughness with less room temperature ductility than the Ti-25Al-10Nb-3V-1Mo beta forged material.

The Ti-24Al-11Nb and Ti-25Al-10Nb-3V-1Mo creep and rupture curves are a result of response surface models. They predict creep and rupture life based on the test stress and temperature (both independent variables) as opposed to Larson-Miller which confuses the dependent variable, life, with an independent variable, temperature to predict life. The response surface models have been shown to better predict creep life than Larson-Miller for these and similar titanium alloys as well as Ni-base alloys due to a smaller standard error for the model (Reference 2). The standard error for one Ni-base alloy (PWA 1422) was reduced by more than a factor of two through the use of response surface modeling.

Fracture surfaces at various temperatures are shown for the beta forged structure in Figures 38 through 42. A common occurrence with both alloys is the flaking of material from fracture surfaces. In Figure 39, pieces of this material were picked from a fracture and examined to determine if they were individual grains. This was done with the beta and alpha-2/beta forged material and in both cases, the results indicate transgranular cracks around multiple grains of

material with no apparent predisposition to grain boundary cracking. This condition leaves a furrowed appearance on some fractures. This is seen in Figure 40. Figures 41 and 42 show details of Ti-24Al-11Nb toughness fractures, a mixture of ductile tearing and quasi-cleavage.

Tensile results for both alloys show a decrease in yield and ultimate strength between room temperature and 204°C. Yield strength continues to drop after that. But, both alloys exhibit a pronounced peak in ultimate strength and ductility at 427°C. At room temperature, fractures appear brittle (Figure 43) but begin to show a more ductile appearance at 204°C. Secondary cracking along gage section sides occurs above room temperature (Figures 44 and 45) and is extensive at 427°C. Internal cracks have also been detected, but no repeated association with prior beta grain boundaries has been noted. Creep specimens experience extensive secondary cracking and although cracks appear to be associated with circumferential grind marks, similar cracks form on LCF specimens highly polished in the axial direction.

As expected, the higher strength of the Ti-25Al-10Nb-3V-1Mo resulted in a distinct advantage in creep/stress rupture over the Ti-24Al-11Nb. Both alloys exhibit oxygen embrittlement indicating the need for protective coatings. Sectioned creep specimens are shown in Figures 46 and 47 and exhibit a distinct layer of oxygen embrittlement and secondary cracks as in tensile tests (where thermal exposure is minimal). The hardness of the layer has been measured and is HV 856 compared to HV 393.3 for the unembrittled material.

3. TASK II — FATIGUE CRACK INITIATION

a. Summary

The program was structured to provide an understanding of the more important variables that will affect the general fatigue crack initiation and propagation of advanced titanium aluminide alloys. The variables that were addressed include the effects of temperature, frequency, stress-ratio, waveshape, and stress concentration in both the LCF and HCF regimes. Additional testing involved the effects of hot salt stress corrosion (HSSC), protective coatings, and the effects of prestressing.

b. Technical Approach

Smooth and notched HCF and LCF testing was conducted at three temperatures chosen to span expected service temperatures that may result in fatigue crack initiation in engine components. These temperatures range from ambient conditions at engine startup to above 650°C. The three temperatures shown in the tables (26°, 427°, and 650°C) cover this range and were chosen to allow any temperature-dependent fracture mechanism transitions to occur.

As shown in Figure 48, smooth LCF testing used the specimen that has a round cross-sectional area, a cylindrical gage section and a K_t of 1.0. Specimen testing was done in either an axial strain control-strain feedback or load (stress) controlled mode as noted in the tables of results. Specimen axial strains were measured and controlled by means of a dual proximity probe extensometer system mechanically attached to the gage section. Test loads were monitored and controlled by commercial tension-compression flat load cells. Strain, as sensed by the extensometer system, was recorded on the X-axis of an X-Y recorder, and load (sensed by the load cell) was recorded on the Y-axis; thus providing material hysteresis loops as desired during the cyclic life of the specimen.

Both fully reversed strain cycling to eliminate mean stress and mean strain effects, and an all tensile strain cycle demonstrating strain and stress ratio effects were employed and are described in Figures 49 and 50. Strain ranges were selected to produce S-N curves over a range of 1,000 to 50,000 cycles. These tests were conducted at a frequency of 0.17 Hz (10 cpm) with a

sawtooth waveform. An additional waveform possessing a 120-second peak strain hold time (Figure 51) was also employed to quantify creep and stress relaxation behavior of the alloy.

The LCF notch tests used the double-edge notch specimen, shown in Figure 52, which has a rectangular cross-sectional area and a K_t of 2.18 on the two opposite notches. The specimens were load cycled to failure with periodic inspections to determine life to detectable surface cracking. Three inspection methods were used for crack detection: visual inspections using high intensity light and a traveling microscope, fluorescent penetrant inspection (FPI), and acetate film replication (used for a permanent record of relevant indications).

The HCF cracking in compressor components is generally due to high frequency resonant excitation of the structure. Smooth, $K_t = 1$, tests were run at $R = 0.0$ as well as $R = -1.0$ and at a cyclic frequency of 30 Hz. The S-N curves were established for both conditions. The maximum HCF stress level was chosen to provide a comparison with the lowest LCF level for frequency effect determination. The effects of coating and prestressing were also examined. The smooth and notched HCF specimens used are shown in Figures 53 and 54.

c. Results

Isothermal strain controlled LCF test results for Ti-24Al-11Nb at room temperature are shown in Table 23 and plotted in Figure 55 for total strain range versus life. The plot shows a comparison of the $R = 0$ versus $R = -1.0$ and shows lower life per expectation for the higher mean stress ($R = 0$) test condition. Included in the data are two tests run with American Society for Testing and Materials (ASTM) sea salt applied to the gage sections. These were run to augment the HSSC testing being conducted with notched LCF and TMF specimens. The tests were run without the 650°C pre-exposure given to room temperature notched LCF tests where a marked life debit was seen. The tests were conducted to determine if the salt exposure alone would lead to a debit in fatigue life.

Results from Ti-24Al-11Nb tests conducted at 427°C are listed in Table 24 and are plotted in Figure 56. The plot shows little effect due to strain ratio compared to room temperature results. Mean stress differences between cycle type are smaller than those seen at room temperature, hence the smaller life difference. The curves were drawn for each R separately so that later temperature and alloy comparisons could be made with data deleted for clarity. This shows curves to cross in some cases due to the decrease in R effects at higher strains and data scatter. Since mean stress decreases with increasing strain range for the all-tensile strain cycle, the mean stress debit is most prominent at the lower strain levels. At the higher strains, the lives for the two cycle types converge.

Also shown is the effect of a 120-second peak strain dwell cycle where a life penalty is seen. Minimal creep at this temperature results in limited stress relaxation. The 650°C results are shown in Table 25 and plotted in Figure 57. The 120-second dwell cycle has allowed the initially positive mean stress associated with the $R = 0$ cycle to stress relax to a negative mean stress resulting in higher life than the nondwell cycle.

Results for strain control testing of Ti-25Al-10Nb-3V-1Mo are shown in Table 26 for room temperature, 427°C, and 650°C.

The data are plotted in Figure 58 for room temperature comparing stress ratios. The fully reversed strain cycle exhibits higher life. Thread failures were a problem at this condition and an increase to the next standard thread size was made for subsequent tests. Results for strain control testing of Ti-25Al-10Nb-3V-1Mo are shown at 427°C for $R = -1$ and $R = 0$ in Figure 59. Again, a mean stress effect appears as in the 650°C results shown in Figure 60.

Figures 61 through 63 compare the two alloys for $R = 0$ at room temperature, 427°C, and 650°C respectively. The comparisons are shown with the least squares fit mean lines only; the data points (shown in the previous figures) have been deleted for clarity. The apparent reversal at 427°C, $R = 0$ is probably due an artifact of data variability. The limited number of tests precludes resolution of small differences and behavior is probably quite similar at this condition. The curve fit parameters for the regressions are shown in Table 27. The same comparisons are drawn for the fully reversed ($R = -1$) cycle in Figures 64 through 66.

(1) Hysteretic Energy Damage Modeling

In an attempt to further consolidate LCF life, an alternative method of characterizing cyclic damage was employed. In this approach, the damage occurring in the cycle is assumed to be related to the amount of energy dissipated as the material undergoes hysteresis. The energy in a particular hysteresis loop may be approximated by the product of the tensile portion of the cyclic stress range and the inelastic strain range:

$$\Delta W = (\sigma_t)(\Delta \epsilon_i)$$

where ΔW is the hysteretic energy damage parameter, σ_t is the tensile portion of the cyclic stress range, and $\Delta \epsilon_i$ is the inelastic strain range. The relationship is independent of strain ratio. The damage parameter is then assumed to be related to LCF life by the equation:

$$N_f = A(\Delta W)^B$$

where A and B are regressed constants.

The relationship was calculated from the hysteresis loops obtained at 50 percent of the life for each test.

Inelastic strain versus cyclic stress range for Ti-25Al-10Nb-3V-1Mo is shown in Figures 67 through 69 for the three test temperatures, and Figures 70 through 72 show the same relationship for Ti-24Al-11Nb. These plots provided the inelastic strains used in the hysteretic energy calculations. Hysteretic energy versus life plots pooling the three test temperatures and two strain ratios are shown in Figure 73 for Ti-24Al-11Nb and Figure 74 for Ti-25Al-10Nb-3V-1Mo. The results for the two alloys are pooled in Figure 75. Fit parameters for the regressions are shown in Table 28. The actual lives versus the predicted lives for both alloys are shown in Figure 76 and individually for each alloy in Figures 77 and 78.

(2) Notched LCF Testing

The effects of stress and temperature on notched fatigue crack initiation were investigated in testing conducted with both alloys at room temperature, 427°C, and 650°C. In addition to the baseline testing, several other areas of interest were studied.

Notched LCF results for Ti-25Al-10Nb-3V-1Mo are shown in Table 29 and Figure 79. Life at 427°C is similar to room temperature life. Life at 650°C is much lower, consistent with alloy strength versus temperature. Usually, other than smooth-area fracture mechanics limitations, the stress concentration areas are of most concern from a fatigue and fracture life standpoint. Notch areas in low ductility materials are usually limited in the amount of inelastic deformation that can be tolerated, which limits even the nominal (smooth area) stresses that can be applied. Most of the plastic deformation occurs on the initial service cycle; subsequent cycles are usually nearly elastic, even in the most severe stress concentrations. Local overstressing was evaluated

using an overstress cycle, performed at 427°C where the material ductility is higher and can withstand more plastic deformation without damage. This method was expected to result in deep-set compressive residual stresses at the root of the notch. The overstress cycle has been successfully used to enhance crack growth life behavior when applied by sleeve coldworking (same local stress-strain effect) and is currently in use for F100 engine Ti-6Al-2Sn-4Zr-6Mo disks, applied as a cryogenic overspeed spin cycle.

Two supplemental tests employing a single overstress cycle at 517 MPa and 427°C were conducted. The concentrated surface stress was 1127 MPa. Two overload cycles, one at a 0.17 Hz ramp rate with a 60-second dwell at peak stress and the other without the dwell, were tried. At this temperature, ductility is a maximum, however, since an LCF benefit was not realized, the severity of the overstress cycle may have been insufficient to produce the desired effect.

Elevated temperature tests exhibit a surface layer of oxygen embrittlement. This fact and the knowledge that aluminides suffer from hot salt stress corrosion (HSSC) at least as severely as conventional titanium alloys indicate the need to investigate the use of protective coatings. Consequently, testing was conducted with both alloys in coated and uncoated conditions to investigate the effects of high-temperature oxidation and resistance to HSSC.

Ti-25Al-10Nb-3V-1Mo tests were conducted at 26° and 427°C with a TiN coating applied by physical vapor deposition. Its ductility was expected to be high at 427°C, close to its maximum service temperature, minimizing any coating associated life effect. However, a debit was seen. The TiN coated life was not further debited by HSSC. Tests were run with and without HSSC and were preceded by a 1-hour, 650°C thermal exposure cycle before testing. Results are shown in Figure 80.

Notched LCF results for Ti-24Al-11Nb are listed in Table 30 showing estimated life to 0.8 mm surface crack length and failure. Figure 81 shows the effects of temperature. Least squares fit regressed mean lines are shown for each temperature. Lives at room temperature and 427°C are similar; however, a significant drop in life is seen above 650°C.

The effects of mechanically introduced compressive residual stresses appear negligible even though the overstress cycle was increased to 620.6 MPa for five cycles at 427°C based on the Ti-25Al-10Nb-3V-1Mo results. A group of specimens was coated with an alumina forming aluminum slurry coating. Alumina coatings have been proposed (Reference 3) for use with titanium and are the object of study by various laboratory groups at Pratt & Whitney. The coating can be applied by spray techniques and is appropriate for use in applications requiring the coating of large areas such as metal matrix composite sheet.

The coating application involved a 2-hour diffusion cycle at 760°C. Since the temperature is higher than the alloy's age temperature (650°C), tests on uncoated specimens that had received the thermal cycle alone were run in addition to coated specimens. The results seen in Figure 82 show a life penalty for both the coated material and the material with the diffusion cycle alone.

The HSSC results from the Ti-25Al-10Nb-3V-1Mo work were augmented with further testing on Ti-24Al-11Nb. The HSSC effects were evaluated at room temperature (with the 1-hour 650°C pre-exposure cycle) and in testing at 650°C. Both conditions showed greatly reduced life. Two alumina coated specimens received an application of the salt solution and pre-exposure cycle and were subsequently tested at room temperature. Coated LCF life was further debited by HSSC. Life was degraded as severely as uncoated HSSC results. Results are shown in Table 31 and Figure 83.

(3) High Cycle Fatigue (HCF) Testing

High cycle fatigue (HCF) in compressor components is generally due to high frequency resonant excitation of the structure. Primary HCF testing was conducted at two temperatures: 25°C where ductility is at a minimum and strength is highest, and 650°C where the reverse is true. Smooth tests were run at $R = -1.0$ and $R = 0.05$ as well as at a cyclic frequency of 30 Hz. The S-N curves were established for both conditions. The higher HCF stress levels were chosen to provide a direct comparison with the lowest LCF levels for a frequency effect determination. Supplementary tests evaluated an additional temperature (427°C) and the effects of warm prestressing employing the same technique used in the notched LCF Ti-24Al-11Nb testing. In addition, the alumina forming coating was evaluated with Ti-24Al-11Nb smooth tests.

Smooth axial HCF results for Ti-24Al-11Nb testing at room temperature and 650°C are shown in Table 32. Notched results are shown in Table 33. The effects of temperature for smooth $R = -1.0$ testing is shown in Figure 84 where little difference is seen. A similar comparison for $R = 0.05$ is shown in Figure 85 where a significant life debit is seen for 650°C. Figure 86 shows notched results for $R = 0.05$ as a function of temperature. Insufficient data at 427°C negated the ability to provide a regressed mean life curve as was done in all other cases. The 427°C curve is estimated. The effect on HCF life resulting from the alumina coating evaluated in notched LCF testing was examined at room temperature and is shown in Figure 87. A large life penalty is seen at the relatively high test stress. The 620.6 MPa five cycle/0.17 Hz prestress cycle (conducted at 427°C) that was used in LCF testing was also tried in HCF. The results, shown in Figure 88, indicate a significant improvement in the notched HCF life resulting from the overstress cycle.

The HCF results for Ti-25Al-10Nb-3V-1Mo in Table 34 show notched and smooth data at room temperature and 650°C. The effects of temperature are shown for $R = -1$ smooth testing in Figure 89. A temperature comparison for the notched data is shown in Figure 90. Less effect exists than that noted in Ti-24Al-11Nb testing.

The two alloys are compared in Figure 91 at 25°C where a large life advantage is present for the stronger alloy. Little difference exists for the notched alloy comparison in Figure 92. Comparisons are also drawn at 650°C for smooth and notched results in Figures 93 and 94.

Regression results for ten million cycle run-out fatigue strength are shown in Table 35. Mean life curve regression fit indicators are shown in Table 36.

d. Discussion of Results

(1) Smooth Controlled Strain Low Cycle Fatigue

Strain ratio comparisons showed that life was dependent upon mean stress and inelastic strain range consistent with conventional titanium alloys. Alloy comparisons showed the stronger Ti-25Al-10Nb-3V-1Mo to possess a life advantage in almost all cases. Initiation, 5 percent stress range drop equated to a 0.8 mm surface crack, was obtained by a strip chart on load and indicated generally negligible life between initiation and failure. The expectation that limited room temperature ductility would be accompanied by poor controlled strain LCF behavior at room temperature should be examined. Figure 95 shows a hysteresis loop from a room temperature test exhibiting significant inelastic strain contrary to the perception that aluminides are essentially "elastic" materials. The Ti-24Al-11Nb lives at 1 percent strain are scattered around 10,000 cycles for room temperature as well as 427°C where ductility is at a maximum. This is consistent with notched LCF results. Examination of the Ramberg Osgood (50 percent life) relationships for the two temperatures shows less inelastic strain for a given cyclic stress range at room temperature versus 427°C (26°C yield strength is much higher than 427°C).

This characteristic results in comparable hysteretic energy for the strain cycle at either temperature. The fully reversed cycle at 0.8 percent strain is similar and the same appears true for Ti-25Al-10Nb-3V-1Mo at 1 percent and 1.5 percent. Another observation, pertinent to constitutive modeling, is the propensity for cyclic hardening and stress relaxation in strain control testing exhibited by both alloys. This is seen graphically in the 427°C fully reversed 1 percent strain cycle shown in Figure 96 where a 36 percent increase in cyclic stress range was accompanied by a 10× decrease in inelastic strain between the initial cycle and 50 percent life. In Figure 97, a 0.8 percent $R = 0.0$ cycle shows similar changes plus a reduction in mean stress. The mean stress drop is also seen in 26°C tests where a creep component is not present and would seem to be achieved by way of a stress range increase alone, with proportionately more compressive than tensile component increase. Peak strain dwell tests conducted at 427° and 650°C both demonstrate significant creep components; consequently, the mean stress drop noted in 427°C tests may be attributed to the combined effects of stress relaxation and cyclic hardening. At 650°C, stress relaxation due to creep resulted in $R = 0.0$ peak strain dwell tests outlasting similar non-dwell tests by relaxation to a negative mean stress. Several other observations regarding 650°C results are of note. Significant cyclic hardening was still present at 650°C. At this temperature, a 30 percent increase in cyclic stress range was not uncommon.

Tensile stability has been a point of concern with aluminides. Post-creep tensile tests indicated extreme loss of room temperature ductility resulting from exposure to stress and temperature. Still, lives comparable in some cases to those observed at lower temperatures were seen. This may be because much more ductility exists at 650°C than 26°C. An expectation might be that an out-of-phase TMF cycle would demonstrate the effects of tensile instability on fatigue behavior since thermal exposure is experienced in combination with excursions to maximum strain at near room temperature. Test results indicated otherwise, and are discussed in Task IV.

Environmental effects in the form of oxygen embrittlement were prominent in creep specimens tested at 538°C but were not observed in LCF specimens with more than 250 hours exposure at 427°C. An examination of a 650°C LCF test specimen with more than 400 hours exposure appears in Figures 97 through 99. The surface is heavily oxidized. Cracks in the oxide scale are visible on the gage surface as are the polishing marks perpendicular to the scale cracks demonstrating the lack of association between the two. The degree of oxide spalling is obvious and material has clearly exfoliated from the surface in some areas (Figure 98). The structure of the oxide scale is shown in cross-section in Figure 99 where multiple breeches in the scale are visible, some with cracks extending through the embrittled layer into the specimen. The mechanism by which exfoliation occurs can be seen as cracks forming beneath the oxides in the embrittled layer and run parallel to the surface. Relative microhardness of the layer is shown in Figure 100. The X-ray diffraction phase analysis showed the scale to be composed of rutile, titanium dioxide. Niobium aluminum spinel and niobium alloyed rutile were also suggested. The mechanism of crack formation in the oxide is important. For an outward growing scale such as niobium oxide, a crack in the scale is self healing. As cracks form, oxide scale continues to build outward on the surface and the crack is filled and closes with rutile. However, the formation of scale is by inward diffusion of oxygen into the substrate as opposed to outward migration of alloy constituents. Consequently, as cracks form in the scale through straining, they tend to propagate into the metal. An oxidation-fatigue interaction occurs as high plastic strains are continually experienced while the scale builds from thermal exposure.

(2) Notched Low Cycle Fatigue (LCF)

Notched LCF results showed generally the same temperature effect trends and alloy ranking seen in strain control testing. Remaining life from initiation to failure appears more significant for stress controlled notch versus smooth strain control conditions as seen in Figures 101 and 102. Representative samples showing critical crack depths for the three temperatures evaluated are shown in Figures 103 and 104 and show a considerable fraction of the cross-

sectional area cracks before failure. In addition, $a/2c$ aspect ratio can be seen to be approximately 0.5. The effects of prestressing were not evident in total life; however, some benefit does appear in crack growth. A comparison of remaining life for prestressed versus baseline is shown in Figure 105.

Environmental effects were also evident in notched testing. In Figure 106, the early stages of formation and cracking of the oxide scale can be seen in addition to the fractographic appearance of the embrittled layer along the edge of the failed specimen. Figure 107 shows the notch opposite the fatigued notch where overstress failure has occurred and is a graphic indication of the brittle nature of the oxygen diffused surface layer (0.013 mm deep in this case). The results of the coating experiments appeared to be partly successful in that the alumina former coated specimens tested at 650°C did not exhibit signs of oxygen diffusion beneath the coating (Figure 108). This statement cannot be made for the TiN coating since visible oxygen diffusion does not occur at the 427°C test temperature. The alumina former possessed the disadvantage of the 760°C diffusion cycle which is above the age cycle temperature. The TiN coating possesses a temperature limitation that the other coating does not. The TiN coating nodules appear to be detrimental from a fatigue initiation standpoint (Figure 109); however, application process modifications could mitigate this problem. The TiN did seem to become somewhat ductile at 427°C since the 25°C test exhibited a much greater life debit compared to baseline data. Hot salt stress corrosion still must be the final criteria of efficacy if the alloys are to be used in applications where salt might be encountered. The alumina former life was debited by the addition of HSSC. The TiN coated life was not decreased by the exposure to HSSC. Uncoated Ti-25Al-10Nb-3V-1Mo HSSC resistance was not tested so no baseline exists to provide a comparison. Further testing is needed in this area since the lower test temperature (427° versus 650°C) and lack of baseline precludes more accurate observations.

(3) High Cycle Fatigue (HCF)

Temperature effects were best resolved with smooth specimens in ($R = 0.05$) tests where the increase from 25° to 650°C was accompanied by a large decrease in HCF capability. Little temperature effect was seen with $R = -1.0$ tests since this cycle results in zero mean stress. Fatigue life is a function of mean stress and inelastic strain range. With no mean stress component, inelastic strain range (relatively small at the lower HCF stresses) is the chief factor in determining life. The difference in temperature effect for the two stress ratios indicates a significant stress ratio effect and agrees with LCF results. In the case of notched testing, the life effect due to temperature was less apparent than with smooth tests. The high plastic strains and the tendency for stress relaxation would allow notch conditions to relax to between the $R = 0.05$ cycle and the fully reversed cycle. As in smooth $R = -1.0$ tests, less temperature effect would result. The LCF tendency for grouping of 25°C with 427°C results and the debit seen at 650°C was detectable in HCF results but to a lesser extent. A comparison of HCF and LCF results indicated no life debit associated with higher test frequencies. The comparisons were drawn at $R = 0.05$ for notched tests at all three test temperatures and smooth tests at $R = -1.0$, 25°C, where some of the smooth LCF tests were run in stress control.

The effects of prestressing were evaluated at 427°C and a significant life benefit was found. The tests were conducted at low stresses. The LCF evaluations were conducted at high stresses. This would seem to be the key to why LCF initiation results were not impressive. The HCF coating evaluation agreed with the results obtained in notched LCF testing; a significant life penalty exists at 25°C. These results should be reconciled with the fact that engine representative stresses were not used and would be considerably lower. The true performance of a coating should be evaluated in reference to the run-out stress and examined from a Goodman diagram standpoint.

An effort was made to model the HCF data based on tensile hysteretic energy as proposed by Ostergren (Reference 4) with simplifications to represent the inelastic strain range (Reference

5). However, coefficients of correlation and standard estimates of error were poor. Hence, stress was used as the correlative parameter for regressions. The reason for the difficulties lie in not accounting for cyclic hardening in the technique used for estimating inelastic strain. The pronounced cyclic instability observed in controlled strain LCF testing must be accounted for in life modeling.

4. TASK III — FATIGUE CRACK PROPAGATION

a. Summary

Isothermal fatigue crack growth rate testing covered the same temperature range as in fatigue testing. The variables included temperature, stress ratio, dwell effect, frequency, and orientation. Crack growth rate tests, plus tests to establish threshold crack growth stress intensity were run. Several conditions were examined to investigate the crack growth behavior of cracks in the near-threshold region ($da/dN = 10^{-10}$ m (10^{-9} in.)/cycle).

The planned threshold test method was modified to allow the use of the compact tension test specimen and the provision for some of these tests to be conducted by Dr. Gary Salivar at Florida Atlantic University. The test technique, load shedding by "K" control, used the compact type, CT, specimen rather than the planned iterative bend specimen technique and provided crack closure data not afforded by the bend method. Experimental fatigue crack growth rate data was obtained using the CT specimen shown in Figure 110. The database was generated using the ASTM standard CT specimen. As in fatigue testing, test temperature range was chosen to represent the probable operating range of Ti_3Al in engine hardware.

b. Technical Approach

Isothermal crack growth rate testing was conducted per ASTM E647. The specimen used was the standard compact type. This type was chosen for the large amount of crack propagation data yielded. Test specimens were precracked using procedures outlined in ASTM Section E647. Precracking was performed at room temperature at a cyclic frequency of 20 Hz. This helped to maintain the crack propagation perpendicular to the loading direction. Cyclic tests were performed using isosceles triangular load waveforms. Specimen heating was provided by resistance clamshell furnaces having windows allowing observation of crack growth at the test temperature.

Using a traveling microscope, crack lengths were measured on both surfaces of the specimen at the mean test load. This procedure held the specimen rigid while increasing crack tip visibility. A high intensity light was used to provide oblique illumination to the crack and further increase crack visibility. In general, crack length measurements were taken at increments no larger than 0.25 mm (0.010 in.).

Monolithic Ti_3Al can be treated as a homogeneous isotropic continuum with respect to crack propagation. Combining this assumption with the deformation characteristics of Ti_3Al leads to the use of linear elastic fracture mechanics with stress intensity range (ΔK) as the correlative parameter for describing fatigue crack growth rates. The use of ΔK is also supported by previous testing at P&W. A fatigue crack growth rate model has been successfully developed for a Ti_3Al alloy similar to the alloys studied in this contract. That model described crack growth rates for cast Ti_3Al from 204° to 650°C (400° to 1200°F) for stress ratios of 0.1 to 0.7, and ΔK was used to correlate the data.

$$\log (da/dN) = C_1 \sinh (C_2(\log (\Delta K) + C_3)) + C_4 \quad (1)$$

where the coefficients have been shown to be functions of test frequency (References 6 and 7), stress ratio, and temperature (V, R, and T respectively).

$$\begin{aligned}C_1 &= \text{material constant} \\C_2 &= f_2 (v, R, T) \\C_3 &= f_2 (v, R, T) \\C_4 &= f_2 (v, R, T)\end{aligned}$$

The hyperbolic sine is defined as

$$y = \sinh (x) = \frac{e^x - e^{-x}}{2} \quad (2)$$

and when presented on Cartesian coordinates it exhibits the overall shape of typical da/dN versus ΔK plots obtained over several decades of crack growth rates.

In some gas turbine applications, crack growth data is needed at ΔK levels corresponding to extremely low growth rates. The threshold stress intensity, ΔK_{th} , is defined as that ΔK level where crack propagation ceases, at least for all practical purposes. The threshold stress intensity becomes significant when a relatively small crack is subjected to a high stress, for example in a disk bolthole, or when a component can accumulate a large number of cycles in a short time, such as a compressor blade subjected to vibrational loading. To investigate fatigue crack growth rates in the near threshold region, $da/dN=10^{-8}$ m/cycle, it is generally necessary to employ specialized test techniques. This section will review the test techniques used to obtain threshold information, and will discuss the results of that testing.

The test method used for determining ΔK_{th} is described in detail in ASTM E-647-88, Standard Test Method for Measurement of Fatigue Crack Growth Rates (Reference 8). In general, this method consists of establishing crack propagation at a relatively high rate and then continuously reducing the test loads to decrease the applied ΔK , thus reducing the crack growth rates. The specimen used for these tests is the CT specimen described earlier. Standard stress intensity solutions, size restrictions, and crack front curvature limitations are applicable. Precracking procedures are the same as those employed in standard crack growth rate testing.

The test consists of applying a decreasing stress intensity to the specimen to back down the da/dN , ΔK curve and approach the fatigue crack growth threshold. This is accomplished by decreasing the test load (load shedding) as the crack extends. The test is started by cycling at a ΔK and K_{max} level equal to or greater than the final level used during precracking. The load shedding can then be performed on a continuous basis under computer control. Care must be exercised in the selection of the rate of load shedding to ensure that the decrease in load does not result in retardation of crack growth rates. This would introduce error into the calculated crack growth rate behavior, which would result in an error in the determination of the fatigue crack growth threshold stress intensity, ΔK_{th} .

Another factor which must be taken into consideration is crack closure. Under some combinations of environment, geometry, and loading, a crack will remain closed during some portion of the fatigue cycle. This crack closure phenomenon is commonly observed, even for tension-tension cycles. Little or no additional damage accumulates at the crack tip during that portion of the cycle when the crack is closed. Thus, the applied stress intensity range, ΔK , is reduced to an effective stress intensity range, ΔK_{eff} , as shown in Figure 111. After Figure 111,

$$\Delta K = K_{\max} - K_{\min}$$

and,

$$\Delta K_{\text{eff}} = K_{\max} - K_{\text{cl}},$$

where, K_{cl} corresponds to the load level at which the crack closes.

Three general closure mechanisms are commonly recognized: oxide-induced, roughness-induced, and plasticity-induced closure. Those closure mechanisms are shown schematically in Figure 111. Oxide-induced closure can be explained simply. When an oxide layer or oxide debris is formed at the crack tip and reaches a thickness on the order of the crack-tip-opening-displacement, it can serve to prop the crack open at a load above the minimum. The effective stress intensity range is reduced accordingly. Roughness-induced closure occurs by a similar mechanism. Crack surface asperities combined with the minor Mode II (sliding) displacements intrinsic to Mode I crack opening can cause the crack to close before the minimum load is reached. Again, this mechanism is significant only when the scale of roughness is comparable to the crack-tip-opening-displacement. Plasticity-induced closure is related to the plastic deformation occurring at the crack tip. As the crack extends, the residual deformation from the plastic zone ahead of the crack produces a plastic wake along the flanks of the crack. Since the undeformed elastic material surrounding the crack restrains expansion in other directions, the majority of the residual deformation occurs perpendicular to the crack surface. As the crack closes, this expanded material comes into contact before the minimum load is reached, thus reducing the effective ΔK . Although these mechanisms differ considerably, they all have the effect of reducing the effective stress intensity range, thereby decreasing the observed crack growth rates.

The load shedding schedule used is developed in Reference 9:

$$\Delta K = \Delta K_0 \exp^{C(a-a_0)} \quad (3)$$

where the zero subscript indicates the initial values of the test and C is a constant which determines the rate of decrease of stress intensity range (load). This expression was derived by noting that in a K -decreasing test, the monotonic plastic zone size should decrease. It was then assumed that the rate of change in plastic zone size remains constant with increasing crack length. The constant C is defined as:

$$C = \frac{1}{K} \frac{dK}{da} \quad (4)$$

which is the normalized K -gradient. The value of C that is chosen depends on the material, the load ratio, R , and the environment. The constant, C , also should be chosen to obtain five da/dN , ΔK pairs of approximately equal spacing per decade of crack growth rate. In this program, C varied from -0.08 mm^{-1} to $-0.04.0 \text{ mm}^{-1}$.

Under computer control, the load is automatically decreased to reduce the stress intensity range, ΔK . The specimen compliance is monitored and used to provide an indication of crack length. The computer calculates the value of stress intensity range associated with the crack length and adjusts the load to reduce ΔK according to Equation (3). Several visual crack length measurements are taken over the course of the test to confirm and calibrate the compliance measurements. The specimen compliance is determined from load versus crack-mouth-opening-displacement records, as described in Reference 9.

Load shedding is continued until a minimum of five da/dN , ΔK pairs of approximately equal spacing are obtained between crack growth rates of 10^{-9} and 10^{-10} m/cycle. Linear regression is then used to obtain the best-fit line to the data in this region. The regressed line is used to calculate the ΔK value that corresponds to a crack growth rate of 10^{-10} m/cycle. This value of ΔK is used as the operational definition of fatigue crack growth threshold, ΔK_{th} . (This regression technique was not used for this contract for reasons detailed in the following discussion section.)

To check the validity of the data obtained from the K-decreasing tests, K-increasing tests were performed on several specimens after a determination of ΔK_{th} was made by the K-decreasing procedure. The data from the two methods should correspond, indicating that retardation effects are not present in the data obtained from the K-decreasing method and that the value of C chosen provides a valid test for the determination of ΔK_{th} .

c. Results

(1) Crack Growth Results

Ti-24Al-11Nb was tested at 26°C, 427°C and 650°C. The effects of temperature for a stress ratio of $R = 0.1$ and frequency of 20 Hz are shown in Figure 112. The 650°C condition exhibited the most rapid growth rate while the lower temperatures experienced a reversal at approximately 7MPa \sqrt{m} stress intensity after which 26°C growth exceeded 427°C growth. This ordering was effectively duplicated for Ti-25Al-10Nb-3V-1Mo and can be seen in Figure 113. The 26°C data also describe the effects of prior beta grain orientation resulting from the highly directional macrostructure previously described. The orientations were shown in Figure 29. Surprisingly little difference can be seen as was the case with fracture toughness testing. A comparison of 427°C and 650°C, 120-second peak load dwell test crack growth rates is shown in Figure 114 where the lower temperature poses a distinct advantage. Temperature effects are shown for Ti-24Al-11Nb and Ti-25Al-10Nb-3V-1Mo at the lower 0.17 Hz frequency in Figures 115 and 116 respectively. The ordering is unchanged from that seen at 20 Hz with the 650°C growth rate being the most rapid.

The 26°C curve in Figure 116 is a composite of both 0.17 Hz and 20 Hz results and, as is evident, no frequency effect exists. Consequently, the data were pooled. As in the 20 Hz results previously seen for both alloys, the crossover for the 26°C and 427°C data again occurs. This time the reversal takes place at approximately 2×10^{-4} m/cycle growth rate for both alloys.

Temperature effect for the highest mean stress condition tested, $R = 0.7$, is demonstrated in Figures 117 and 118 for Ti-24Al-11Nb and Ti-25Al-10Nb-3V-1Mo, respectively. The 650°C growth rate is most rapid while the 427°C and 26°C exhibit the same mixed behavior described in all previous cases. The ordering holds true for both alloys. Stress ratio effects for the two alloys appear in Figures 119 and 120 and show crack growth rate to be greatly accelerated with increasing mean stress in both cases.

Correlative parameters for the Ti-24Al-11Nb stress ratio model appear in Figures 121 through 124 for the coefficients C1 through C4 respectively; C1 is the material constant and C2 through C4 reflect functions of frequency, stress ratio, and temperature.

In Figure 125, the model is demonstrated for Ti-24Al-11Nb at 427°C and 0.17 Hz showing a minimum R^2 of 0.9677 and standard estimate of error of 0.0623. The model accurately fits the $R = 0.1$, 0.5 and 0.7 data.

Ti-25Al-10Nb-3V-1Mo stress ratio effects are shown in Figure 126 for 427°C at 0.17 Hz and show a similar convergence at the higher stress intensities as was seen for Ti-24Al-11Nb. The

650°C comparisons of $R = 0.1$ and $R = 0.7$ are shown in Figures 127 and 128 for the two alloys, and the ordering remains the same with the $R = 0.7$ crack growth rate exceeding that of the $R = 0.1$ stress ratio.

Frequency effects are shown for the two alloys at 26°C in Figures 129 and 130. At this temperature, neither alloy exhibits any effect due to frequency. Increasing frequency results in decreased growth rate at higher temperatures (427° and 650°C) for both alloys as seen in Figures 131 through 134. Alloy comparisons have been drawn at all temperatures, stress ratios, and frequencies, and appear in Figures 135 through 143. Ti-25Al-10Nb-3V-1Mo was generally faster in crack growth rate although in some cases, 650°C, 20 Hz, $R = 0.1$ or 26°C, $R = 0.7$ for example, differences were not significant. In one case, 427°C, $R = 0.7$, Ti-24Al-11Nb exhibited the more rapid growth. A discussion of these results follows.

(2) Threshold Results

Room temperature comparisons of threshold crack growth rate for the two alloys are shown in Figures 144 and 145 for $R = 0.1$ for $R = 0.7$, respectively. In both cases, Ti-25Al-10Nb-3V-1Mo exhibits the lower threshold value. No difference is seen between the two alloys at 650°C for $R = 0.1$ in Figure 146; however, Ti-25Al-10Nb-3V-1Mo does show a lower threshold at $R = 0.7$ in Figure 147 at 650°C. The parity at 650°C for $R = 0.1$ may be oxidation related. Ti-24Al-11Nb temperature effects on threshold behavior are seen in Figure 148 for $R = 0.1$ and Figure 149 for $R = 0.7$. The $R = 0.1$ data shows no grouping of 26° and 427°C data or the greatly reduced capability at 650°C as observed in fatigue testing. A reduction is seen in threshold value with increasing temperature. Ti-25Al-10Nb-3V-1Mo temperature effects on threshold growth appear in Figure 150 for $R = 0.1$ and Figure 151 for $R = 0.7$. In both cases, an increase in temperature has resulted in a decrease in threshold stress intensity.

Stress ratio effects on threshold crack growth for Ti-24Al-11Nb are shown in Figure 152 for 26°C, Figure 153 for 427°C, and Figure 154 for 650°C. In all three cases, the higher $R = 0.7$ stress ratio results in significantly lower threshold capability. The difference between $R = 0.7$ and $R = 0.1$ seems to decrease with increasing temperature. The same effect is seen in Figures 155 and 156 for Ti-25Al-10Nb-3V-1Mo at 26° and 650°C respectively.

The correction of threshold data for closure effects seen in Figure 157 has reduced the stress ratio effect previously noted for Ti-24Al-11Nb at 26°C. In Figure 158, closure correction has affected consolidation of 427°C stress ratio effects at lower stress intensities. Since this effect did not occur in closure corrected 650°C results (Figure 159), oxidation does not seem to be the explanation. Stress ratio consolidation was observed in the Ti-25Al-10Nb-3V-1Mo comparison (Figure 160) corrected for closure at room temperature and would indicate the existence of roughness-induced closure effects. Plasticity-induced effects should be minimal due to low ductility of the material at 26°C. Secondary cracking, however, is extensive and material exfoliation (common in these alloys) would lead to crack wedging.

The effects of correcting for closure at 650°C for Ti-25Al-10Nb-3V-1Mo are shown in Figure 161. As with Ti-24Al-11Nb, the effect has been a reduction in the $R = 0.1$ threshold stress intensity. The effect of crack length is shown in Figure 162 for Ti-25Al-10Nb-3V-1Mo at 26°C. The stress ratio is 0.1 and variability in closure correction exists since Figure 163 eliminates closure from the crack length comparison with significant effect on the long crack data. Constant load tests are run to detect any load history effects.

Little effect was observed resulting from decreasing stress intensity by load shedding compared to results obtained from constant load testing. The results at 26°C are shown for Ti-24Al-11Nb in Figure 164 for $R = 0.1$ and in Figure 165 for $R = 0.7$. The same comparisons are made in Figures 166 and 167 for $R = 0.1$ and 0.7, respectively, at 650°C where an effect appears at $R = 0.1$.

d. Discussion of Results

(1) Temperature Effects

The dependency of isothermal crack growth rate upon temperature was investigated at room temperature, 427°C, and 649°C. In general, $\Delta K_{\text{Threshold}}$ increased with decreasing temperature, and K_{Ic} was larger at elevated temperature than at room temperature. Temperature effects were more pronounced than is seen in more conventional materials, which is probably related to the large ductility increase between room temperature (6 percent) and 427° to 650°C (elongation greater than 20 percent). The room temperature crack growth curves are nearly vertical — characteristic of a brittle material.

At all conditions tested, Ti-25Al-10Nb-3V-1Mo generally had equal to or slightly higher crack growth rates than Ti-24Al-11Nb. The differences in crack growth rates were, in all cases, relatively small. The somewhat faster crack growth rates for Ti-25Al-10Nb-3V-1Mo are probably associated with higher strength and a finer microstructure.

Temperature comparisons generally indicate increasing crack growth rates with increasing temperature. The increase in crack growth rates are suspected to be related to increased oxidation at elevated temperatures. The slopes of the crack growth rate curves decrease with increasing temperature resulting in crossing of the curves in some instances. Flatter slopes at elevated temperatures are typical of higher ductility materials, and it is therefore assumed that the changes in slope are associated with the large increase in ductility with temperature shown in Figure 26. Further, if oxidation and ductility are seen as competing mechanisms in the process zone ahead of the crack (one increasing, and one decreasing the crack growth rates), smaller changes in slope and/or greater differences in crack growth rate with temperature at low frequencies would be expected, where the crack is open for longer periods allowing greater oxidation. A comparison of Figures 112, 114, and 115 shows this to be exactly the case.

(2) Frequency Effects

The effects of cyclic frequency upon isothermal crack propagation rate were studied at room temperature, 427°C, and 649°C. Stress ratio was held constant at $R = 0.1$ and frequencies of 20 Hz, 0.167 Hz, and 120-second peak load dwell were applied. As indicated by Figure 129, there is no frequency effect at room temperature between 20 and 0.17 Hz for $R=0.1$. By comparison, Figure 133 displays a large difference in crack growth rates for frequencies of 20 Hz, 0.17 Hz, and 120-second dwell cycles at 650°C, $R=0.1$. As mentioned previously, the increase in crack growth rates with decreasing frequency is thought to be mainly due to oxidation. This is supported by Figure 133, which shows drastically increasing crack growth rates with decreasing frequency at elevated temperature. At the limiting condition for these data, the 120-second dwell data is virtually vertical. Note, however, that these differences in crack growth rates occur at higher ΔK levels, above approximately $7 \text{ MPa}\sqrt{\text{m}}$. The data appear to converge at low ΔK levels.

(3) Stress Ratio Effects

Normal stress ratio effects were observed as indicated in the R comparison figures. The $\Delta K_{\text{Threshold}}$ decreased as R increased. There was a considerable increase in crack growth rates with increasing R . This is common behavior for R data in both magnitude and direction, and can probably be directly attributed to the effect of mean stress.

The results of near-threshold tests at room temperature and 650°C are included in Figures 152 and 154. These tests were conducted on separate CT specimens in a K -decreasing mode. All of the threshold tests were conducted at 20 Hz. Note that the threshold data display the same trends as the K -increasing data. This held true for the effects of temperature on crack growth and for the alloy comparisons discussed earlier.

(4) Crack Growth Interpolation Model

Initial plans were to generate a crack growth interpolation algorithm for Ti-24Al-11Nb. For conventional titaniums, the algorithm calculates hyperbolic sine coefficients (C_1 through C_4) for a set of crack growth test conditions. The hyperbolic sine curve relates da/dN to ΔK as described below.

$$\log (da/dN) = C_1 \sinh (C_2 (\log (\Delta K) + C_3)) + C_4$$

Coefficient $C_1 = 0.7$ for titanium alloys. The other hyperbolic sine coefficients are functions of test temperature, stress ratio, and frequency.

A material must exhibit a continuous transition in crack growth behavior over temperature to be modeled with a global interpolation algorithm. Ti-24Al-11Nb behaves like a conventional material at 427° and 650°C but is brittle at room temperature. This discontinuity precludes a single algorithm to describe its behavior completely. A partial model based on the results of tests conducted at 427°C, 0.17 Hz, and stress ratios of $R = 0.1, 0.5$, and 0.7 was developed. This algorithm provides sinh coefficients for test conditions of 427°C, 0.17 Hz, and any stress ratio between 0 and 1.

(5) ΔK_{th} Discussion

The near threshold decreasing-K testing displayed the same general trends as the baseline constant load tests for both materials. The most obvious of those trends are slower crack growth rates for Ti-24Al-11Nb than for Ti-25Al-10Nb-3V-1Mo, slightly reduced ΔK_{th} values at elevated temperatures for both materials, and a large stress ratio effect with the higher R tests showing much reduced crack growth rates. These results would be anticipated since the few constant load tests run in the near-threshold region agreed with the decreasing-K data.

Crack growth rates measured using constant load and decreasing-K tests were very nearly equal. Only a few of the sinh curves fit to the constant load data required revision to bring them into agreement with the decreasing-K data, and those revisions were minor.

The near threshold crack growth rate data displayed unusually steep slopes, particularly for high stress ratios. This behavior necessitated the use of relatively small K-gradients for controlling the load shedding rates. Even when using small K-gradients (-0.04 mm^{-1} (-1.0 in.^{-1}) as opposed to -0.06 to -0.08 mm^{-1} (-1.5 to -2.0 in.^{-1}) for conventional titanium alloys), it was often difficult to obtain the number of points per decade of crack growth rate recommended by ASTM standard. In several instances, it was also impractical to calculate an absolute value for ΔK_{th} based on a Paris equation fit to the near threshold data as detailed by ASTM. The slope of the threshold data was simply too near vertical to perform a numerical slope evaluation. Therefore, absolute ΔK_{th} values based on Paris equations are not tabulated for these data. If ΔK_{th} values are required, they can be obtained graphically with very little error.

Closure measurements were taken on all decreasing-K tests. Closure levels expressed as a percentage of maximum load were calculated based on deviation from linearity of the load-displacement curve. This technique is described in detail by Donald (Reference 10). For the purposes of this contract, the crack opening load was arbitrarily defined as the point where the slope of the load displacement curve deviated from a constant value by 8 percent. As indicated by the stress ratio comparisons presented previously, calculating ΔK_{eff} in this fashion did not consistently collapse the stress ratio data to a single curve, which is a common indicator of a successful closure measurement technique. Altering the closure levels by varying the definition of

crack opening load to a deviation of the slope of the load-displacement curve between 1 and 16 percent did not improve the behavior of the stress ratio data.

In general, the closure level increased with increasing crack lengths. However, this did not occur in a regular fashion. Often the crack opening loads changed abruptly. This behavior is illustrated in Figures 162 and 163. In those figures, the data from sequential decreasing-K tests on the same specimen are presented with and without closure correction. Specimen 4599T started at a crack length of approximately 9.8 mm, and 4599T2 started at a crack length of approximately 12.1 mm. As seen in the figures, the two specimens fall directly in line in terms of ΔK , and are widely separated when plotted versus ΔK_{eff} . In fact, at a crack length of about 14mm on 4599T, the closure level changes abruptly from 18 to 32 percent resulting in a separation of the ΔK_{eff} data on a single specimen.

The abrupt changes in closure level are directly related to the active closure mechanism. The most likely closure mechanism is a combination of roughness and oxidation-induced closure with the roughness mechanism being dominant. Figures 179 and 180 illustrate the mechanism resulting in roughness of the fracture surfaces with asperities well in excess of the observed crack opening displacements. In fact, it appears that entire groups of grains are separating from the fracture surface in a few areas. The roughness of the fracture surface is almost certainly attributable to the extreme bifurcation tendency observed. A considerable amount of oxidation was also present in the 650°C tests. It is improbable that a large degree of plasticity-induced closure was present due to the low ductility of the material and the minimal K levels. Further evaluation of the active closure mechanisms is beyond the scope of the contract.

The inability of these straightforward closure measurement techniques to collapse stress ratio data and the evidence of abrupt changes in closure levels indicates that a more sophisticated closure analysis would be required to successfully employ ΔK_{eff} in evaluating the threshold stress intensity for these materials. Until those techniques are evaluated, it is recommended that the near threshold data be used only in terms of ΔK .

5. TASK IV — THERMAL MECHANICAL FATIGUE (TMF)

a. Summary

Various effects on the TMF life of both titanium aluminide alloys were investigated. These effects included strain ratio, strain range, and cycle type. One of the alloys was also tested for the effect of hot-salt stress corrosion (HSSC). The test specimen used is shown in Figure 168 and is of hollow design.

Two strain ratios (minimum strain/maximum strain) were evaluated, $R = -1.0$ and 0.0 . This essentially tests the effect of mean stress. Various strain ranges were also tested for each cycle type. The two TMF cycle types are the out-of-phase or Type I cycle (Figure 169), and the in-phase or Type II cycle (Figure 170).

b. Technical Approach

The results of the TMF testing are presented in Tables 37 and 38, and Figures 171 and 172. A comparison of Ti-24Al-11Nb and Ti-25Al-10Nb-3V-1Mo is shown in Figure 173. The Ti-25Al-10Nb-3V-1Mo had generally longer TMF life than Ti-24Al-11Nb alloy. This difference in life is not very large and is within experimental scatter.

The effect of cycle type for both alloys was investigated. Type I life was similar to that observed for Type II cycles for Ti-25Al-10Nb-3V-1Mo. Type I results are compared to Type II results for Ti-24Al-11Nb in Figure 174. There is no significant difference between the TMF life

of the Type I cycle and the Type II cycle for this alloy either. The effect of strain ratio was also studied for both of the alloys. Each alloy was tested with a strain ratio of 0.0 and -1.0 using Type I cycles. The strain ratio of 0.0 resulted in higher mean stress. Due to control problems during testing, only one test of each alloy was tested at the strain ratio of 0.0. Both alloys exhibited decreased TMF lives for the strain ratio of 0.0 because of the increased mean stress. The effect of hotsalt corrosion on the primary alloy was also studied. As expected, the tests with salt on the alloy had significantly lower TMF lives than the unsalted tests (Figure 175).

The TMF data was also characterized using a hysteretic energy based model (References 11 and 12). The hysteretic energy of a material is based on the maximum tensile stress and the inelastic strain range. Determination of the inelastic strain for the TMF cycle is complicated by the variation of material constants with temperature. A technique developed in previous work (Reference 13) was used to determine the inelastic strain of the cycle. This method, called the "Incremented Inelastic Strain Technique," uses Ramberg-Osgood regressions of the inelastic strain at each temperature of the cycle. The TMF cycle is divided into legs; Type I and Type II cycles have two legs each. At each temperature increment of the leg, the inelastic strain is iterated from the Ramberg-Osgood regressions at that temperature. The inelastic strain is averaged over the leg and the strain is summed for all of the legs. The tensile stress for the hysteretic energy equation is measured directly from test data.

c. Results

The hysteretic energy results are shown in Figure 176 and Table 39. Correlation coefficients (R^2) greater than 0.80 indicate that the hysteretic energy model is reasonable for this material. The actual TMF life versus predicted life is presented in Figure 177.

d. Discussion of Results

Low room temperature ductility and post-creep ductility loss were expected to present a significant problem for fatigue capability, but isothermal LCF testing at both 26° and 650°C exhibited impressive lives under controlled strain conditions. Peak strain ranges for 650°C tests were similar to post-creep room temperature ductility maximums. An explanation lies in the fact that sufficient ductility exists at this temperature to prevent any negative impact of ductility loss on fatigue life. Ductility at 26°C (approximately 5 percent) provided a comfortable margin to conduct strain control tests at 1.5 percent $\Delta\epsilon_t$.

The loss of ductility at room temperature was expected to be most detrimental in an out-of-phase TMF cycle. In the Type I cycle, thermal exposure is repeatedly followed by maximum strain at nearly room temperature. This test would be expected to highlight the post-creep ductility loss problem, especially when compared to an in-phase cycle where tensile yielding is not encountered at low temperature, and peak strain occurs at 650°C where available ductility is adequate regardless of post-creep ductility loss. Minimal difference was observed. An explanation may lie in the high degree of cyclic hardening noted.

In the out-of-phase cycle, as ductility is lost through successive high temperature excursions, inelastic strain range is simultaneously lowered through cyclic hardening (recall that in isothermal tests a 10 × reduction in inelastic strain was observed). This would have the effect of nullifying the post-creep ductility loss. The need for further testing to address this effect is indicated.

Another interesting occurrence is the small difference observed in the alloy comparison in Figure 173. Both alloys would have experienced the same cyclic hardening and surface oxygen embrittlement. Thus, all other things being equal, the only remaining difference is a significant strength advantage for Ti-25Al-10Nb-3V-1Mo. Yet the life difference, especially at 0.8 percent

strain, is not impressive. The effects would seem to be related to cyclic stress and strain range instability, and reflects on the success of the hysteretic energy modeling technique. Since cyclic stabilization occurs as early as at 10 percent of life and hysteretic energy accounts for both inelastic strain range and mean stress, the model was able to deal with the extreme cyclic instability encountered.

As expected, hot-salt stress corrosion effects were quite severe. Extensive secondary cracking along gage section sides and heavy fracture surface oxidation, as seen in Figure 178, were common. A $20 \times$ life debit (approximately) was observed at 0.6 percent strain. These results, coupled with those obtained in isothermal LCF, point out the necessity of providing protection against HSSC.

6. TASK V — FRACTURE MECHANISMS

a. Summary

Representative specimens from all phases of the program were analyzed to gain insight into the mechanisms of fatigue crack initiation and crack propagation. In addition, a significant amount of analysis was conducted on specimens from the process development effort. Mechanical property test specimens (tensile, creep, toughness, and impact) were scrutinized to form a basis for an understanding of the effects of microstructure and processing on service and fracture behavior.

b. Technical Approach

Essentially no difference in fractographic details existed between the alloys. Hence, the observations apply to both alloys unless otherwise stated. From this work, the susceptibility of the alloys to oxygen embrittlement was observed and subsequently studied in greater detail. Also noted was the alloys tendency toward secondary cracking and branching leading to significant flaking and exfoliation of material from fracture surfaces. These events were seen in detail in Figure 179, where after only 30 minutes at 650°C, 0.0234mm of oxygen diffused layer has formed on an isothermal strain control LCF specimen. Also seen is the extent of secondary cracking and branching with no apparent interaction with alpha-2/beta platelet structure. In Figure 180, a 427°C specimen shows similar cracking and a 650°C specimen provides a good example of the mechanism that results in material loss from fracture surfaces. This effect probably plays a significant role in crack closure since very small particles of material are likely to be freed in the crack path to shift position and become "wedges." The lack of obvious crack interaction with microstructure is seen in Figure 181. Oxidation from the 427°C exposure during testing has revealed the Ti-24Al-11Nb microstructure. The secondary crack that formed on the gage surface allowed study without polishing or etching, which might have obscured a feature of interest. The gage section was examined directly on a metallograph. There does not appear to be a prior beta grain boundary at the area of origin nor does the surface propagation seem to be affected by the alpha-2 beta platelet structure. Typically, fatigue origins form at surface connected prior beta grain boundaries with significant amounts of grain boundary alpha-2 phase as seen in Figure 182. These areas are frequently marked by preferential alignment of the Widmanstatten structure, as seen in Figure 183. When observed fractographically, they appear as in Figure 184a. This characteristic structure aids in the identification of failure crack origins.

Figure 184b shows the fractographic appearance of an oxygen embrittled surface layer resulting from 650°C exposure. The circumferential cracks seen earlier in tensile and creep rupture testing appeared to be associated with grinding marks. In Figure 185, the surface effects of oxygen embrittlement are detailed. Here, the polishing marks are parallel to the stress axis, while oxide cracks form normal to the loading direction. After approximately 400 hours at 650°C, material has started to be ejected from the surface. The effect was not typical and 400 hours of

LCF exposure represents an extreme case. In Figure 186, the embrittled layer appears optically almost like a coating. The subsurface origin is detailed in Figure 187 and in spite of the materials conversion to barstock and the high degree of forging upset, appears to be a void. Optical views of grain boundary alpha-2 fatigue origins at 127° and 650°C are shown in Figure 188. A 26°C LCF origin at a surface connected prior beta grain boundary is shown in Figure 189. A second example at 427°C is shown in Figure 190.

Another type of origin occasionally found in fatigue failure appears in Figure 191. The shape and size of the features suggest alpha-2 platelets, perhaps favorably oriented to allow Stage I crystallographic cracking. A second example of this type of feature is seen in Figure 192. This example is from a notched HCF failure at 427°C. Figure 193 shows another example of a subsurface origin, this time exhibited by a 650°C, 120-second dwell test. Stereographic examination indicated the presence of porosity.

The occurrence of fatigue striations was seen only occasionally as shown in Figure 194. Propagation was by transgranular cleavage in general. No obvious intergranular propagation was present in fatigue fractures. An example of a notched LCF failure at 650°C is shown in Figure 195. A single point origin (nonspecific) is visible. Another example is shown in Figure 196, this time at 427°C and reveals the fatigue crack propagation aspect ratio (somewhat distorted due to specimen tilt). The notched specimen, shown in Figure 197, was prestressed at 427°C and run at 26°C. Bifurcation and flaking of material is seen. Fluorescent penetrant has marked the critical crack depth. A 650°C origin in Figure 198 shows an unusual texture at what may be an alpha-2 phase.

Investigations into the effects of coatings produced the multiple surface origins in both notches of the Ti-24Al-11Nb specimen (at 650°C) shown in Figure 199a. Metallography, seen earlier, showed no oxygen diffusion indicating that the alumina forming coating may be effective against oxygen embrittlement. Coating behavior in HSSC is seen in Figure 199b where multiple origins are present in both notches. Figure 199c shows a notched Ti-25Al-10Nb-3V-1Mo specimen coated with TiN and exposed to HSSC at 427°C. Continuous surface origin and (as in the two previous cases) extensive bifurcation has occurred.

High cycle fatigue (HCF) origins for the most part were similar to LCF initiation sites. Figure 200 shows a subsurface origin at a possible void detected in a 650°C HCF test. Figures 201 and 202 show surface connected prior beta grain boundaries in 26°C fatigue origins. A subsurface origin produced at 650°C in Ti-24Al-11Nb is shown in Figure 203. The area was heavily oxidized and could not be analyzed. Another 650°C HCF fracture is shown in Figure 204 at a prior beta grain boundary. Figure 205 shows a 427°C notched Ti-24Al-11Nb HCF failure with alpha-2/beta platelets prominent at the origin.

Crack growth specimen fracture surfaces are shown for the three test temperatures at 20 Hz for Ti-24Al-11Nb in Figure 206. The low magnification macro photos show the characteristic flaking of material most obvious here at 26°C but present at the higher temperature as well. This tendency results in strong closure effects due to surface roughness. The flaking was also noted for the equiaxed (beta solutioned) structure described earlier in fracture toughness and impact screening tests. The prior beta grain structure is apparent as elongated grains in the direction of crack propagation. The silver markings are areas of grain boundary alpha-2 in many cases. The different prior beta grain morphology presented by the two specimen orientations, shown in Figure 207, did not have an effect in either fracture toughness tests or crack propagation tests. This and the fact that the predominant fracture mode in fatigue and crack growth tests was by transgranular cleavage suggests that prior beta grain size does not play an important role in cyclic behavior as is assumed.

In Figure 208, the 26°, 427°, and 650°C fractures were produced at 0.17 Hz. The fractures appear similar to 20 Hz fractures with the characteristic flaking of material again present.

Scanning electron microscope (SEM) views of the 20 Hz and 0.17 Hz fractures, in Figures 209 and 210, show little difference due to frequency. Both fractures show secondary cracking and a pseudo-cleavage appearance with small amounts of ductility. The 427°C textures, in Figures 211 and 212, show a more ductile appearance but at 650°C (Figures 213 and 214), the fracture surface seems more brittle. This is probably due to the tendency for oxidation at this temperature. Ti-25Al-10Nb-3V-1Mo fractures at 26°, 427° and 650°C are shown in Figure 215 at low magnification and appear similar to those described for Ti-24Al-11Nb. The SEM examination reveals differences associated with the finer Widmanstätten structure (Figures 216 and 217) and higher 26°C ductility as some ductility is apparent in Figure 216. Pieces of material can be seen nearly parted from the fracture surface. The 650°C fracture, shown in Figure 218, exhibits exfoliation of material through bifurcation, extensive secondary cracking, and significant amounts of oxidation. The oxidation effect at 650°C has been observed previously (Reference 14) with vacuum testing resulting in increased evidence of ductility in fractographic studies.

Thermal mechanical fatigue (TMF) fractures produced with Type I out-of-phase and Type II in-phase cycles are shown in Figure 219. The out-of-phase fracture shows a single origin and little oxidation due to the crack opening only at the low temperature end of the cycle. The in-phase fracture appears more like 650°C isothermal failures with heavy oxidation. Inside diameter origins are seen in spite of the argon passing through the specimen for cooling purposes. Enough oxygen is present for embrittlement to occur. An example of surface oxidation is shown in Figure 220 where scale can be seen rumpling and spalling. In Figure 221, a typical in-phase TMF failure origin area is shown with an oxygen diffused layer that is indicated by arrows. An out-of-phase fracture is shown in Figure 222. The side of the gage section exhibits extensive secondary cracking. The origin appears to be oxide-related and no point source is apparent. In Figure 223, an in-phase TMF origin at a surface connected prior beta grain boundary is shown intersecting the dark oxygen embrittled layer at the outside diameter of the specimen.

Hot salt stress corrosion tests were run on Ti-24Al-11Nb with in-phase and out-of-phase test cycles. The effects of HSSC with a Type II cycle resulting in maximum load at 650°C are evident in Figure 224 where gross attack has occurred. Multiple outside diameter surface origins appear and extensive secondary cracking has taken place in one of the spots where the salt solution was applied. Further examination of HSSC TMF fractures are shown in Figures 225 and 226. Both fractures show secondary cracking and oxide films. Figure 226 exhibits an intergranular appearance. However, sectioning through secondary cracks in the gage section (Figure 227) shows cracks to be transgranular.

Late in the program, X-ray diffraction was conducted to examine crystallographic texture. In retrospect, some specimens could have been oriented to maximize the texture effect. Figures 228 and 229 show pole figures for the beta forged Ti-25Al-10Nb-3V-1Mo with the radial direction represented at the center and the pancake normal at the 0 degree position. Figure 228 shows the preferred orientation of the (110) planes of the beta-phase which implies a strong (100) fiber texture in the normal direction of the pancake. The 'blotchy' concentrations of contours indicate the presence of large grains. Figure 229 shows that the (0002) planes of the alpha-2 phase has the same orientations as the (110) beta-phase planes, which is the result of habit plane transformation. A schematic showing the orientation of the pancake in relation to the pole figures is shown in Figure 230.

III. CONCLUSIONS AND RECOMMENDATIONS

1. TASK I — PROCESS OPTIMIZATION

Optimum mechanical properties were obtained with isothermal beta forgings. The desired microstructure, a fine Widmanstätten structure, was produced by air cooling from the forging temperature for Ti-25Al-10Nb-3V-1Mo. The Ti-24Al-11Nb required a fan air cool, and the Widmanstätten structure was still not as fine as that achieved in Ti-25Al-10Nb-3V-1Mo. Prior beta grain size was similar for both alloys. No subsequent solution cycle was applied, and little effect on properties was observed with various stabilization and age cycles.

The directional microstructure resulting from the absence of a solution cycle did not appear to be a negative factor. Post creep exposure ductility loss indicates equilibrium was not reached with Ti-25Al-10Nb-3V-1Mo. Further work is needed in this area.

Both alloys exhibit a pronounced tendency toward the development of an oxygen embrittled surface layer starting at 538°C. Ti-25Al-10Nb-3V-1Mo was stronger and more ductile than Ti-24Al-11Nb and possessed better creep capability. Impact resistance and toughness for the two alloys were similar. Prior beta grain morphology did not effect toughness at 26°C when various orientations were tested.

2. TASK II — FATIGUE CRACK INITIATION

Controlled strain testing showed life to be dependent upon mean stress and inelastic strain range. The stronger Ti-25Al-10Nb-3V-1Mo exhibited generally better LCF capability than the Ti-24Al-11Nb. Negligible remaining life from initiation was observed in smooth strain control LCF. Extreme cyclic hardening and stress relaxation was observed with both alloys. Cyclic stability was achieved at 10 to 20 percent of total life. Future work should include tensile strength and ductility assessment after cyclic stabilization has been reached. Low temperature ductility was not a life limiting factor. Tests conducted at 1 percent total strain range exhibited room temperature lives similar to those observed at 427°C where ductility is high. Dwell tests at 427° and 650°C experienced significant stress relaxation to mean stresses at and below zero respectively. Extreme surface oxidation was observed, yet specimens exhibited LCF lives greater than 10^5 cycles (despite oxygen embrittlement). Hysteretic energy damage modeling was employed and successfully consolidated at all temperatures and strain ratios for both alloys.

Notched LCF results showed little difference between 26° and 427°C lives; however, 650°C capability was considerably reduced. Ti-25Al-10Nb-3V-1Mo capability was greater than Ti-24Al-11Nb. Remaining life from 0.8 mm surface crack length was generally lower than 10 percent of total life. The effects of warm prestressing were inconclusive and, judging from HCF results, may have been resolved if the 26°C tests were conducted at a lower stress level. Further work on the effects of compressive residual stresses is needed.

The evaluation of an alumina forming coating, resulted in a fatigue debit at 26° and 650°C; however, oxygen diffusion into the substrate (Ti-24Al-11Nb) seems to be inhibited. The coating did not provide protection against HSSC. The evaluation of TiN PVD coating also resulted in a debit in life; however, TiN life was not further decreased by exposure to HSSC. Further testing should be done in this respect since the evaluation was conducted at 427°C for the TiN/Ti-25Al-10Nb-3V-1Mo system. Future work should examine both coating and alloy systems and HSSC resistance in more detail.

Smooth HCF life was found to decrease with increasing temperature dependent upon mean stress, i.e., $R = 0.05$ showed a large temperature effect while $R = -1$ did not. *Notched HCF* results (all run at $R = 0.05$) show little difference in 10^7 cycle fatigue strength for 26° versus 650°C due

to local stress relaxation in the notch at 650°C. Low cycle fatigue (LCF) versus HCF comparisons showed no frequency effect. Warm prestressing was found to be effective with HCF tests run at 427°C. Ti-24Al-11Nb coated with an alumina forming coating exhibited more than an order of magnitude life debit at 26°C. Hysteretic energy modeling using inelastic strain estimations was not successful due to the material's cyclic instability. Mean fatigue strengths for Ti-25Al-10Nb-3V-1Mo were 10 to 50 percent higher, depending on conditions, than those observed for Ti-24Al-11Nb.

3. TASK III — FATIGUE CRACK PROPAGATION

Room temperature crack growth behavior was typical for that of a brittle material. Plots of da/dN versus ΔK were very steep and growth was rapid. Orientation effects with respect to upset were not present. In general Ti-25Al-10Nb-3V-1Mo exhibited higher crack growth rates. In some cases differences were minimal. Temperature effects were more pronounced than those observed in conventional titanium alloys. Threshold stress intensity decreased with increasing temperature while toughness increased. A frequency effect was not seen at 26°C but growth rate did increase with decreasing frequency at 427° and 650°C. Crack growth rate increased with increasing stress ratio for a given ΔK . The materials' discontinuous transition in crack growth behavior with increasing temperature precluded modeling with a global interpolation algorithm. A partial model based on the condition where data from three stress ratios was available was constructed. The 427°C model exhibited satisfactory predicted versus actual results.

Near threshold crack growth rate testing Ti-24Al-11Nb demonstrated consistently higher threshold stress intensities than Ti-25Al-10Nb-3V-1Mo, except at 650°C, $R = 0.1$ where they are approximately equal. Ti-24Al-11Nb and Ti-25Al-10Nb-3V-1Mo both exhibited lower threshold stress intensities at elevated temperatures. There was no apparent difference in ΔK_{th} at 427°C and 650°C for Ti-24Al-11Nb. Both Ti-24Al-11Nb and Ti-25Al-10Nb-3V-1Mo displayed a strong correlation between stress ratio and ΔK_{th} , with higher stress ratios resulting in lower ΔK_{th} . Standard closure measurement techniques do not appear to be directly applicable to these materials. The techniques employed did not collapse stress ratio trends consistently, nor did they account for the abrupt changes in closure level. It appears that this difficulty is due to the closure mechanisms, the unusual microstructures, or some combination of both. The decreasing-K near threshold crack growth rates agreed well with the constant load data and necessitated only minor changes in the baseline crack growth rate models. An area of future work should be to examine the relationship of oxygen diffusion rate compared to crack tip advance rate in the near threshold regime versus more rapid crack growth.

4. TASK IV — THERMAL MECHANICAL FATIGUE

Ti-25Al-10Nb-3V-1Mo exhibited better TMF capability than Ti-24Al-11Nb. Cycle type did not effect TMF life. Type I (in-phase) lives were similar to Type II (out-of-phase) lives. Hot salt stress corrosion is stress dependent. Hot salt stress corrosion (HSSC) reduced Type I TMF life by more than an order of magnitude. Type II life experienced a greater debit for HSSC than Type I cycling. Hysteretic energy modeling produced satisfactory results. Further testing is needed to understand the relationship of post-creep ductility loss and simultaneous cyclic hardening.

5. TASK V — FRACTURE MECHANISMS

Both alloys develop brittle, oxygen diffused surface layers above 538°C. This layer is prone to cracking perpendicular and parallel to the direction of applied load. Surface scale develops and with prolonged exposure, exfoliation of the oxygen diffused layer occurs. Both alloys demonstrated a pronounced tendency for crack propagation through the development of multiple ancillary cracks. This condition does not appear to be associated with prior beta grain structure.

Crack closure effects attributable to surface roughness result. The condition is seen in monotonic as well as cyclic fractures at all temperatures. Fatigue crack initiation was most frequently observed in the surface connected prior beta grain boundary alpha-2 phase. These features can frequently be recognized by preferential alignment of the Widmanstatten structure along the boundary. The alpha-2 phase appears as a distinct silver streak at the boundary. Subsurface origins were observed occasionally. No obvious differences prevailed between LCF, HCF, or TMF tests. Both alloys exhibited crack propagation predominantly by transgranular cleavage. The two coatings evaluated exhibited multiple fatigue crack origins. The alumina former showed evidence of crack initiation at the coating/substrate interface. The TiN coating cracks appeared to initiate at nodules in the coating. Prior beta grain orientation did not effect 26°C toughness or crack growth in the highly directional microstructure. The specimen orientations examined did not reveal any effect resulting from the strong (001) fiber texture observed in X-ray diffraction.

TABLE 1. Candidate Heat Treatments for Optimum Property Screening Tests

Alloy	Ti-24Al-11Nb (a/o)	Ti-25Al-10Nb-3V-1Mo (a/o)			
Heat-Treatment	Candidate Processes				
Cycle	1	2	3*	4	
Forging Temp	1150°C (2100°F)	1037°C (1900°F)	1037°C (1900°F)	1150°C (2100°F)	
Cooling Rate	Fan Air Cool	-	-	Air Cool	
Annealing Temp	-	1150°C (2100°F)	1150°C (2100°F)	-	
Cooling Rate	-	Air Cool	Fluidized Bed	-	
Stabilization	815°C (1500°F)/0.5 hr	815°C (1500°F)/0.5 hr	815°C (1500°F)/0.5 hr	815°C (1500°F)/0.5 hr	
Age	593°C (1100°F)/8 hrs	593°C (1100°F)/8 hrs	593°C (1100°F)/8 hrs	593°C (1100°F)/8 hrs	



Constitutes
75% of
Task II-V
Testing



Result
Candidate 4
Identified As
Best Process from
Screening Tests
(25% of
Task II-V
Testing)

TABLE 2. Alloy Chemistry (Weight Percent for Ti-25Al-10Nb-3V-1Mo (a/o))

		Al	Nb	V	Mo	Fe	O ₂
Heat V-6474	Top	13.8	18.4	3.14	1.95	0.11	0.073
	Bottom	13.8	18.5	3.14	1.93	0.10	0.073

TABLE 3. Alloy Chemistry (Weight Percent for Ti-24Al-11Nb (a/o))

		Ingot				
		Al	Nb	Fe	O ₂	N
V-6629	Top	13.5	21.0	0.037	0.058	0.003
	Bottom	13.6	21.0	0.040	0.054	0.004

TABLE 4. Ti-25Al-10Nb-3V-1Mo Isothermal Alpha-2 Plus Beta Forging Parameters

Forging Temperature - 1038°C (1900°F), Soak Time 0.5 hr
Strain Rate - 0.1 sec ⁻¹
Atmosphere - Inert
Initial Dia - 156 mm (6.125 in.)
Final Dia - 406 mm (16 in.)
Initial Height - 229 mm (9 in.), Final Height - 31.8 mm (1.25 in.)

TABLE 5. Candidate 3 (Alpha-2 Plus Beta Forging), Ti-25Al-10Nb-3V-1Mo Heat Treatment

1150°C (2100°F) 1 hr, Fluidized Bed - Air Atmosphere
815°C (1500°F) 0.5 hr, Fluidized Bed - Air Atmosphere
Air Cool to Room Temp
593°C (1100°F), 8 hr Air

TABLE 6. Grain Size From Ti-24Al-11Nb Barstock

• Barstock as Received — Grain Size Obtained at Two Positions on Flat Top-Surface of Billet, at Rim and Mid-radius Positions — Macro Grain Size: ⁽¹⁾
Mid-radius — Predominantly M-10.5 to M-12.0, Occasionally M-10.0
Rim — Predominantly M-12.5 to M-13.0, Occasionally M-10.0
Note: ⁽¹⁾ M-10 = 1.1 mm
M-10.5 = 0.95 mm
M-12 = 0.56 mm
M-12.5 = 0.47 mm
M-13 = 0.40 mm

TABLE 7. Grain Size From Beta Forgings

Ti-25Al-10Nb-3V-1Mo	
• Elongated (Flattened) Prior Beta Grains, ASTM Macro 7, Average Dia 3.2 mm (0.125 in.)	
• Normal to Upset, Macro 10.5, Average Height 0.94 mm (0.037 in.)	
• Fine Acicular Alpha-2 + Beta Widmanstatten With Grain Boundary Alpha-2	
Ti-24Al-11Nb	
• Elongated (Flattened) Prior Beta Grains, ASTM Macro 7, Average Dia 3.2 mm (0.125 in.)	
• Normal to Upset, Macro 10, Average Height 1.1 mm (0.44 in.)	
• Fine Acicular Alpha-2 + Beta Widmanstatten With Grain Boundary Alpha-2	

TABLE 8. Heat Treatment Optimization Study Room Temperature Tensile Test Results,
Ti-25Al-10Nb-3V-1Mo

S/N	Stabilization/ Age Cycle	0.2% Yield Strength		Ultimate Strength		Ductility	
		MPa	(ksi)	MPa	(ksi)	% EL	% RA
1	A	682.6	(99.0)	906.0	(131.4)	3.3	4.4 ⁽¹⁾
2	A	716.4	(103.9)	915.7	(132.8)	3.3	6.5
3	B	661.2	(95.9)	877.0	(127.2)	4.0	3.8
4	B	680.5	(98.7)	894.3	(129.7)	3.3	6.3
5	C	692.3	(100.4)	852.9	(123.7)	2.7	3.8
6	C Thread Failure	—	—	—	—	—	—
7	D	692.9	(100.5)	883.9	(128.2)	2.4	2.6
8	D	655.7	(95.1)	819.8	(118.9)	1.6	4.3
9	E	700.5	(101.6)	788.1	(114.3)	0.6	1.3
10	E	659.8	(95.7)	799.8	(116.0)	1.6	3.8
11	F	674.3	(97.8)	830.2	(120.4)	1.6	5.9
12	F	681.9	(98.9)	866.1	(125.6)	2.4	5.1

Stabilization/Age Cycles

A, B, and C = 816°C (1500°F)/0.5 hr

Plus

A = 593°C (1100°F)

B = 694°C (1200°F)

C = 704°C (1300°F)

D, E, and F = 871°C (1600°F)/0.5 hr

Plus

D = 593°C (1100°F)

E = 649°C (1200°F)

F = 704°C (1300°F)

⁽¹⁾Failed out of gage.

TABLE 9. Heat Treatment Optimization Study Room Temperature Post-Creep Exposure Tensile Test Results, Ti-25Al-10Nb-3V-1Mo

S/N	Stabilization/ Age Cycle	0.2% Yield Strength		Ultimate Strength		Ductility	
		MPa	(ksi)	MPa	(ksi)	% EL	% RA
1	A	692.2	(100.4)	790.8	(114.7)	1.3	0.6
2	A	Thread Failure					
3	B	719.8	(104.4)	787.4	(114.2)	0.5	0.6
4	B	Thread Failure					
5	C	730.9	(106.0)	834.3	(121.0)	1.4	0.6
6	C	688.8	(99.9)	761.9	110.5	0.9	0.6
1	D	688.1	(>99.8)	(1)	—		
2	D	680.5	(98.7)	(2)	(107.4)	1.3	0.7
3	E	657.1	(>95.3)	(1)	—		
4	E	697.8	(101.2)	(3)	—	1.3	1.9
5	F	748.8	(108.6)	835.0	(121.1)	0.7	3.8
6	F	724.0	(105.0)	748.1	(108.5)	1.3	2.9

Stabilization/Age Cycles

Creep Exposure

A, B, and C = 816°C (1500°F)/0.5 hr
 Plus 8 hr at:
 A = 593°C (1100°F)
 B = 694°C (1200°F)
 C = 704°C (1300°F)

All Received 379 MPa (55 ksi) to
 0.5% Creep Followed By 100 hrs
 Exposure at 138 MPa (20 ksi)
 at 649°C (1200°F)

D, E, and F = 871°C (1600°F)/0.5 hr
 Plus 8 hr at:
 D = 593°C (1100°F)
 E = 649°C (1200°F)
 F = 704°C (1300°F)

- (1) Radius failure prior to yield.
 (2) Radius failure.
 (3) Failed at yield.

TABLE 10. Candidate 3, Ti-25Al-10Nb-3V-1Mo Notched Charpy Impact Results

S/N	Temperature		Impact Strength	
	°C	(°F)	Joules	(ft-lb)
1	26	(79)	0.68	(0.5)
2	26	(79)	1.36	(1.0)
3	650	(1200)	35.2	(26.0)
4	650	(1200)	38.0	(28.0)

TABLE 11. Candidate 3, Ti-25Al-10Nb-3V-1Mo Tensile Results

S/N	Temperature		0.2% Yield Strength		Ultimate Strength		%EL	%RA
	°C	(°F)	MPa	(ksi)	MPa	(ksi)		
1	26	(79)	720.5	(104.5)	817.1	(118.5)	1.3	3.7
2	26	(79)	771.6	(111.9)	889.4	(129.0)	2.7	3.2
3	650	(1200)	468.9	(68.0)	650.2	(94.3)	13.3	23.1
4	650	(1200)	552.3	(80.1)	690.9	(100.2)	9.3	16.9

TABLE 12. Candidate 3, Ti-25Al-10Nb-3V-1Mo Fracture Toughness Precracked Compact Tension Specimens

S/N	Test Temperature		K _{IC}	
	°C	(°F)	MPa \sqrt{m}	(ksi $\sqrt{in.}$)
1	RT	—	21.3	(19.4)
2	RT	—	21.2	(18.3)
3	315°C	(600°F)	31.5	(28.6)
4	427°C	(800°F)	52.8	(48.0)

TABLE 13. Candidate 3, Ti 25Al-10Nb-3V-1Mo Creep Results Conditions 650°C (1200°F), 379 MPa (55 ksi)

S/N	0.1% (hr)	0.2% (hr)	0.5% (hr)	1% (hr)	Rupture (hr)	% EL	% RA
1	0.1	0.2	1.7	9.1	68.3	4.43	12.36
2	0	0.2	1.4	7.7	68.8	5.08	9.73

TABLE 14. Ti-25Al-10Nb-3V-1Mo Candidate 4 Tensile Test Results

S/N	Temperature		0.2% Yield Strength		Ultimate Strength		Ductility	
	°C	(°F)	MPa	(ksi)	MPa	(ksi)	%EL	%RA
26	26	(79)	682.6	(99.0)	906.0	(131.4)	3.3	4.4
26	26	(79)	716.4	(103.9)	915.7	(132.8)	3.3	6.5
204	204	(400)	544.3	(80.4)	882.6	(128.0)	7.1	12.7
204	204	(400)	516.4	(74.9)	886.7	(125.7)	7.7	11.3
427	427	(800)	508.2	(73.7)	959.1	(139.1)	23.0	26.5
427	427	(800)	499.9	(72.5)	928.0	(134.6)	20.6	28.6
538	538	(1000)	472.3	(68.5)	803.9	(116.6)	12.8	23.5
538	538	(1000)	429.6	(62.3)	775.7	(112.5)	12.5	22.5
650	650	(1200)	432.3	(62.7)	690.9	(100.2)	13.3	22.2
650	650	(1200)	—	—	717.8	(104.1)	9.3	22.4

TABLE 15. Ti-24Al-11Nb Tensile Test Results

<i>Temperature</i>		<i>0.2% Yield Strength</i>		<i>Ultimate Strength</i>		<i>Ductility</i>	
<i>°C</i>	<i>(°F)</i>	<i>MPa</i>	<i>(ksi)</i>	<i>MPa</i>	<i>(ksi)</i>	<i>%EL</i>	<i>%RA</i>
26	(79)	523.3	(75.9)	677.8	(98.3)	1.8	5.3
26	(79)	494.4	(71.7)	663.3	(96.2)	2.3	3.2
204	(400)	368.9	(53.5)	638.3	(92.7)	5.5	8.2
204	(400)	344.8	(50.0)	624.7	(90.6)	7.8	11.6
427	(800)	297.2	(43.1)	756.4	(109.7)	27.3	34.9
427	(800)	311.7	(45.2)	732.2	(106.2)	31.9	45.2
538	(1000)	274.4	(39.8)	590.2	(85.6)	21.1	29.2
538	(1000)	264.8	(38.4)	573.2	(83.2)	22.3	39.2
650	(1200)	255.0	(37.0)	463.3	(67.2)	17.4	45.3
650	(1200)	251.7	(36.5)	466.1	(67.6)	21.8	42.6

TABLE 16. Candidate 4, Ti-25Al-10Nb-3V-1Mo Notched Charpy Impact Versus Temperature

<i>Temperature</i>		<i>Impact Strength</i>	
<i>°C</i>	<i>(°F)</i>	<i>Joules</i>	<i>(ft-lb)</i>
26	(79)	2.7	(2.0)
26	(79)	2.7	(1.9)
26	(79)	2.3	(1.7)
204	(400)	3.8	(2.8)
204	(400)	3.5	(2.6)
427	(800)	6.1	(4.5)
427	(800)	6.0	(4.4)
650	(1200)	20.4	(15.0)
650	(1200)	25.2	(18.5)

TABLE 17. Notched Charpy Impact Versus Temperature Ti-24Al-11Nb

<i>Temperature</i>		<i>Impact Strength</i>	
<i>°C</i>	<i>(°F)</i>	<i>Joules</i>	<i>(ft-lb)</i>
26	(79)	1.4	(1.0)
26	(79)	1.4	(1.0)
26	(79)	1.8	(1.3)
204	(400)	3.9	(2.9)
204	(400)	4.6	(3.4)
427	(800)	3.8	(2.8)
427	(800)	14.2	(10.5)
427	(800)	17.3	(12.8)
427	(800)	15.6	(11.4)
650	(1200)	35.1	(26.0)
650	(1200)	32.4	(24.0)
650	(1200)	33.8	(25.0)

TABLE 18. Candidate 4, Ti-25Al-10Nb-3V-1Mo Fracture Toughness

Test		Toughness		Orientation ⁽¹⁾
Temperature				
°C	(°F)	MPa \sqrt{m}	(ksi $\sqrt{in.}$)	
26	(77)	16.39	(14.9)	
26	(77)	14.63	(13.3)	a
26	(77)	16.17	(14.7)	b
26	(77)	15.18	(13.8)	b
26	(77)	16.06	(14.6)	c
316	(600)	35.42	(32.2)	c ⁽²⁾
427	(800)	42.57	(38.7)	c ⁽²⁾
538	(1000)	62.81	(57.1)	c ^(2, 3)

⁽¹⁾ Orientations are described in Figure 29.⁽²⁾ Estimated value.⁽³⁾ Test attempted, not plane strained.

TABLE 19. Fracture Toughness for Ti-24Al-11Nb

Test		Toughness	
Temperature			
°C	(°F)	MPa \sqrt{m}	(ksi $\sqrt{in.}$)
26	(77)	18.6	(16.9)
26	(77)	20.7	(18.8)
205	(400)	32.8	(29.8)
205	(400)	31.2	(28.4)
315	(600)	55.0	(50.0) ⁽¹⁾
315	(600)	51.3	(46.7) ⁽¹⁾
427	(800)	—	— ⁽²⁾
427	(800)	—	— ⁽²⁾

⁽¹⁾ Estimated value.⁽²⁾ Test attempted, not plane strained.

TABLE 20. Ti-24Al-11Nb a/o Creep Results

Stress		Temperature		0.1%	0.2%	0.5%	1.0%	Rupture	%EL	%RA
MPa	(ksi)	°C	(°F)	(hr)	(hr)	(hr)	(hr)	(hr)		
207.0	(30.0)	650	(1200)	0.1	0.5	6.1	27.4	544.7	12.5	14.2
207.0	(30.0)	650	(1200)	0.1	0.4	4.6	22.3	448.2	8.9	14.1
172.0	(25.0)	540	(1000)	31.1	117.1	769.5	—	> 1317.1 ⁽¹⁾	0.81	—
172.0	(25.0)	540	(1000)	33.1	126.6	812.1	—	> 1212.5 ⁽¹⁾	0.79	—
138.0	(20.0)	590	(1100)	6.1	28.9	372.4	—	> 789.3 ⁽¹⁾	0.81	—
138.0	(20.0)	590	(1100)	5.3	24.4	311.4	—	> 707.4 ⁽¹⁾	0.84	—
137.9	20.0	605	(1125)	—	178.0	550.0	—	—	—	—
137.9	20.0	605	(1125)	—	206.0	524.0	—	—	—	—
137.9	20.0	650	(1200)	—	23.0	175.0	—	—	—	—
137.9	20.0	650	(1200)	—	43.0	179.0	—	—	—	—

⁽¹⁾ Not ruptured, tests suspended.

TABLE 21. Candidate 4, Ti-25Al-10Nb-3V-1Mo a/o Creep Results

<i>Stress</i>		<i>Temperature</i>		<i>0.1%</i>	<i>0.2%</i>	<i>0.5%</i>	<i>1.0%</i>	<i>Rupture</i>	<i>%EL</i>	<i>%RA</i>
<i>MPa</i>	<i>(ksi)</i>	<i>(°C)</i>	<i>(°F)</i>	<i>(hr)</i>	<i>(hr)</i>	<i>(hr)</i>	<i>(hr)</i>	<i>(hr)</i>		
380.0	(55.0)	650	(1200)	<0.1	0.1	1.2	4.0	60.4	7.3	13.1
380.0	(55.0)	650	(1200)	<0.1	<0.1	0.5	3.8	47.8	7.4	14.8
414.0	(60.0)	590	(1100)	<0.1	0.1	1.5	8.3	293.6	6.9	18.4
448.0	(65.0)	540	(1000)	—	3.5	32.8	160.3	1437.0	3.4	5.5
310.0	(45.0)	650	(1200)	0.1	0.4	3.0	15.6	233.9	7.1	7.9
380.0	(55.0)	540	(1000)	0.1	127.5	387.0	1292.5	2863.9 ⁽¹⁾	— ⁽²⁾	— ⁽²⁾
345.0	(50.0)	590	(1100)	0.6	2.0	13.8	70.7	818.4	4.5	— ⁽³⁾

⁽¹⁾Did not rupture — suspended.⁽²⁾Discontinued.⁽³⁾Ruptured in radius.

TABLE 22. Modulus of Elasticity Versus Temperature

<i>Ti-24Al-11Nb</i>			
°C	Temperature	GPa	Modulus
	°F		PSI X 10 ⁶
21.11	70	106.180	15.4
93.33	200	104.801	15.2
204.44	400	102.733	14.9
315.56	600	100.664	14.6
426.67	800	97.906	14.2
537.78	1000	95.148	13.8
648.89	1200	91.011	13.2
760.00	1400	86.185	12.5
887.78	1630	81.359	11.8
926.67	1700	79.980	11.6
982.22	1800	77.911	11.3
1037.78	1900	76.532	11.1
1093.33	2000	75.153	10.9
<i>Ti-25Al-10Nb-3V-1Mo</i>			
22.78	73	100.664	14.6
93.33	200	99.285	14.4
204.44	400	97.906	14.2
315.56	600	95.148	13.8
426.67	800	93.080	13.5
537.78	1000	89.632	13.0
648.89	1200	86.185	12.5
760.00	1400	82.738	12.0
871.11	1600	78.601	11.4
926.67	1700	76.532	11.1
982.22	1800	74.464	10.8
1037.78	1900	68.948	10.0

TABLE 23. Smooth LCF for Ti-24Al-11Nb a/o Controlled Axial Strain, Frequency = 0.17Hz (10 cpm)

Strain, %	Temperature °C (°F)	Inelastic Strain, N=1	Mean Stress			Stress Range			Cycles to 5% σ Drop	Cycles to Failure					
			%N=1		50% Life	N=1		50% Life							
			MPa	ksi	MPa	ksi	MPa	ksi							
Strain Ratio = -1.0															
0.0	1.50	26	(77)	0.475	0.275	-32.4	(-4.7)	-47.6	(-6.9)	1065.3	(154.5)	1258.3	(182.5)	N/A	130
0.0	1.00	26	(77)	0.137	0.02	0.0	(0.0)	2.1	(0.31)	841.9	(122.1)	967.4	(140.3)	N/A	18,022
0.0	1.00	26	(77)	0.090	0.025	3.45	(0.5)	35.2	(5.1)	909.5	(131.9)	1005.3	(145.8)	N/A	8,953
0.0	0.80	26	(77)	0.02	<0.01	-2.8	(-0.4)	-26.9	(-3.9)	807.4	(117.1)	827.4	(120.0)	N/A	119,786
Strain Ratio = 0															
0.60	1.20	26	(77)	0.240	0.100	134.4	(19.5)	103.4	(15.0)	972.2	(141.0)	1105.9	(160.4)	1,406	1,418
0.50	1.00	26	(77)	0.135	0.03	185.5	(26.9)	173.0	(25.1)	859.8	(124.7)	914.3	(132.6)	N/A	5,268
0.50	1.00	26	(77)	0.15	0.035	135.1	(19.6)	99.3	(14.4)	805.3	(116.8)	889.4	(129.7)	N/A	5,690
0.40	0.80	26	(77)	0.075	0.017	207.5	30.1	191.7	(27.8)	698.5	(101.3)	728.8	(105.7)	11,640	11,647
0.40	0.80	26	(77)	0.07	0.015	167.5	(24.3)	124.8	(18.1)	694.3	(100.7)	773.6	(112.2)	23,180	23,183 **
Salted															
0.00	1.0 Eq.	26	(77)			0.0				965.3	(140)			17,572	
0.00	1.0 Eq.	26	(77)							965.3	(140)			7,648	

**Failure associated with extensometer contact
Eq. = Run in load control at equivalent stress

**Failure associated with extensometer contact
Eq. = Run in load control at equivalent stress

TABLE 24. Smooth LCF for Ti-24Al-11Nb a/o Controlled Axial Strain, Frequency = 0.17Hz (10 cpm)

Strain, %		Temperature		Inelastic Strain,		Mean Stress				Stress Range				Cycles to 5% σ Drop		Cycles to Failure	
Mean	Range	$^{\circ}\text{C}$	$^{\circ}\text{F}$	$N=1$	50% Life	% $N=1$	ksi	MPa	ksi	MPa	ksi	MPa	ksi	σ			
Strain Ratio = 0																	
0.75	1.50	427	(800)	0.664	0.188	227.9	(11.1)	88.3	(4.3)	772.9	(112.1)	1182.5	(171.5)	2,640		2,697	
0.50	1.00	427	(800)	0.325	0.068	124.8	(18.1)	75.8	(11.0)	616.4	(89.4)	859.1	(124.6)	6,224		6,322	
0.50	1.00	427	(800)	0.275	0.035	17.2	(5.5)	35.2	(5.1)	678.5	(98.4)	831.5	(120.6)	10,645		10,673	
0.40	0.80	427	(800)	0.185	<0.010	80.6	(11.7)	35.8	(5.2)	520.6	(75.5)	718.4	(104.2)	46,060		46,797	
Strain Ratio = -1.0																	
0.0	1.50	427	(800)	0.610	0.093	-21.4	(-3.1)	-29.6	(-4.3)	795.0	(115.3)	1222.5	(177.3)	1,660		1,667	
0.0	1.00	427	(800)	0.306	0.028	-22.8	(-3.3)	-26.9	(-3.9)	651.6	(94.5)	910.8	(132.1)	11,900		11,964	
0.0	1.00	427	(800)	0.265	0.025	-5.5	(-0.8)	-4.1	(-0.6)	652.9	(94.7)	886.7	(128.6)	7,447		7,650	
0.0	0.80	427	(800)	0.150	<0.010	-49.7	(-7.2)	-31.0	(-4.5)	567.4	(82.3)	728.8	(105.7)	—		17,936	
2 Minute Dwell Tests																	
0.75	1.50	427	(800)	0.605	0.290	39.3	(5.7)	13.8	(2.0)	815.0	(118.2)	1147.3	(166.4)	775		829	
0.50	1.00	427	(800)	0.038*	0.020*	75.2	(10.9)	11.0	(1.6)	673.6	(97.7)	812.2	(117.8)	3,758		4320	

*Creep component.

TABLE 25. Smooth LCF for Ti-24Al-11Nb a/o Controlled Axial Strain, Frequency = 0.17Hz (10 cpm)

Strain, %	Temperature °C	Temperature (°F)	Inelastic Strain,		Mean Stress				Stress Range				Cycles to 5% σ Drop	Cycles to Failure			
			N=1	50% Life	%N=1	ksi	MPa	ksi	MPa	ksi	MPa	50% Life					
Strain Ratio = 0																	
0.50	1.00	650	(1200)	0.254	0.19	—	61.4	(8.9)	20.7	(3.0)	—	592.3	(85.9)	736.4	(106.8)	475	489
0.50	1.00	650	(1200)	—	—	—	—	—	—	—	—	—	—	—	—	549	648
0.375	0.75	650	(1200)	0.175	0.015	—	126.8	(18.4)	126.9	(5.5)	—	467.5	(67.8)	604.7	(18.7)	8,373	8,439
0.375	0.75	650	(1200)	0.165	0.035	—	52.4	(7.6)	23.4	(3.4)	—	471.6	(68.2)	568.8	(82.5)	2,117	2,378
0.30	0.60	650	(1200)	0.100	0.025	—	67.6	(9.8)	37.1	(5.4)	—	455.1	(66.0)	497.8	(72.2)	260,480	261,094
Strain Ratio = -1.0																	
0.0	1.40	650	(1200)	0.500	0.265	—	0.0	(0.0)	-4.1	(-0.6)	—	715.0	(103.7)	893.6	(129.6)	218	262 ¹
0.0	1.00	650	(1200)	0.300	0.186	—	-2.8	(-0.4)	-13.1	(-1.9)	—	620.6	(90.0)	796.4	(115.5)	2,811	2,857 ¹
0.0	1.00	650	(1200)	0.26	0.10	—	-6.2	(-0.9)	-3.4	(-0.5)	—	614.3	(89.1)	732.9	(106.3)	1,366	1,482
0.0	0.80	650	(1200)	0.17	0.055	—	-1.4	(-0.2)	3.4	(0.5)	—	542.3	(78.7)	615.0	(89.2)	11,598	11,987 ¹
0.0	0.80	650	(1200)	0.15	0.05	—	-0.7	(-0.1)	0.7	(0.1)	—	512.3	(74.3)	606.1	(87.9)	6,395	6,515 ¹
0.0	0.70	650	(1200)	0.06	0.015	—	0.28	(0.04)	-13.1	(-1.9)	—	526.8	(76.4)	533.7	(77.4)	28,055 ²	28,055 ²
Dwell Tests																	
0.5	1.00	650	(1200)	0.262	0.130	—	29.1	(4.22)	82.7	(-12.0)	—	631.6	91.6	745.3	(108.1)	940	1,057
				0.068*	0.052*	—	—	—	—	—	—	—	—	—	—	—	—
0.375	0.75	650	(1200)	0.125	0.056	—	23.3	(3.38)	-23.3	(-13.8)	—	526.8	(76.4)	596.4	(86.5)	7,195	7,268
				0.042*	0.026*	—	—	—	—	—	—	—	—	—	—	—	—
*Creep component. ¹Failure associated with extensometer contact ²Did not fail unloaded																	

*Creep component.

¹Failure associated with extensometer contact

²Did not fail, unloaded

TABLE 26. Smooth LCF for Ti-25Al-10Nb-3V-1Mo a/o Controlled Axial Strain, Frequency = 0.17Hz (10 CPM)

Strain, %	Temperature °C	Temperature (°F)	Inelastic Strain, N=1	Mean Stress				Stress Range				Cycles to 5% σ Drop	Cycles to Failure	
				%N=1	MPa	ksi	50% Life	N=1	MPa	ksi	50% Life			
Strain Ratio = 0														
0.50	650	(1200)	0.12	0.06	114.4	(16.6)	82.0	(11.9)	736.4	(106.8)	789.5	(114.5)	1,215	1,280
0.375	650	(1200)	0.05	<0.01	166.2	(24.1)	112.4	(16.3)	489.5	(71.0)	661.2	(95.9)	—	481,886 ⁽¹⁾
Strain Ratio = 1.0														
0.0	650	(1200)	0.40	0.25	-13.8	(-2.0)	120.0	(17.4)	940.5	(136.4)	1139.7	(165.3)	520	572
0.0	650	(1200)	0.10	0.03	(0.0)	(0.0)	20.7	(-3.0)	759.1	(110.1)	794.3	(115.2)	21,3968	214,157
Strain Ratio = 0.0														
0.75	427	(800)	0.25	0.19	229.6	(33.3)	80.0	(11.6)	1061.8	(154.0)	1218.3	(176.7)	710	712 ⁽⁴⁾
0.75	427	(800)	0.41	0.15	689.5	(14.4)	689.5	(27.4)	689.5	(123.4)	689.5	(149.3)	1,800	1,890
0.50	427	(800)	0.12	0.04	140.0	(20.3)	162.0	(23.5)	684.0	(99.2)	732.2	(106.2)	4,650	4,696 ⁽²⁾
Strain Ratio = 1.0														
0.0	427	(800)	0.35	0.15	-4.14	(-0.6)	(0.0)	(0.0)	1021.8	(148.2)	1171.5	(169.9)	2,621	2,627 ⁽²⁾
0.00	427	(800)	0.09	<0.01	-6.2	(-0.9)	20.0	(2.9)	896.33	(130.0)	965.3	(140.0)	—	25,0041 ⁽¹⁾
Strain Ratio = 0.0														
0.5	26	(77)	0.07	0.05	308.9	(44.8)	N/A	N/A	941.8	(136.6)	N/A	N/A	460	466 ^(5,8)
0.375	26	(77)			273.7	(39.7)	N/A	N/A	729.5	(105.8)	N/A	N/A		9,137 ^(3,6)
0.375	26	(77)	0.025	N/A	196.5	(28.5)	N/A	N/A	714.3	(103.6)	N/A	N/A	<19000	19,197 ⁽²⁾
0.375	26	(77)	0.025	<0.01	213.1	(30.9)	204.7	(29.7)	619.2	(89.8)	610.2	(88.5)		197,000 ⁽¹⁾
Strain Ratio = 1.0														
0.0	26	(77)	0.06	<0.01	44.1	(6.4)	53.1	(7.7)	819.8	(118.9)	852.2	(123.6)		129,283 ^(3,7)
0.0	26	(77)	0.02	<0.01	(0.30)	(0.30)	—			(152.4)	—			12,262 ^(3,8)
0.0	26	(77)	0.17	0.09	9.0	(1.3)	43.4	(6.3)	1078.4	(156.4)	1205.2	(174.8)	3,400	3,418 ⁽⁹⁾
0.0	26	(77)	0.22	0.12	8.3	(-1.2)	15.2	(2.2)	1370.7	(198.8)	1482.4	(215.0)	2,070	2,083 ⁽¹⁾

⁽¹⁾Did not fail — no N/5%.

⁽²⁾Failure associated with extensometer contact.

⁽³⁾Thread failure — no N/5%.

⁽⁴⁾250,041 previous cycles at 1%.

⁽⁵⁾Not used in regression.

⁽⁶⁾Run in stress control.

⁽⁷⁾Had 197,000 previous cycles at 0.75%.

⁽⁸⁾Extensometer slip occurred.

⁽⁹⁾N/5% estimated.

⁽¹⁾Did not fail — no N/5%.

⁽²⁾Failure associated with extensometer contact.

⁽³⁾Thread failure — no N/5%.

⁽⁴⁾250,041 previous cycles at 1%.

⁽⁵⁾Not used in regression.

⁽⁶⁾Run in stress control.

⁽⁷⁾Had 197,000 previous cycles at 0.75%.

⁽⁸⁾Extensometer slip occurred.

⁽⁹⁾N/5% estimated.

TABLE 27. Regression Fit Indicators For Strain Versus Life Plots

	<i>Temperature</i>		<i>Stress Ratio</i>	<i>R²</i>	<i>Standard Error of Estimate</i>
	<i>°C</i>	<i>(°F)</i>			
Ti-24Al-11Nb	26	79	R = 0.0	0.9288	0.0582
			R = -1.0	0.9288	0.0519
	427	800	R = 0.0	0.8508	0.1211
			R = -1.0	0.8553	0.3109
	650	1200	R = 0.0	0.9699	0.0833
			R = -1.0	0.8868	0.5543
Ti-25Al-10Nb-3V-1Mo	26	79	R = 0.0*	0.9879	0.0231
			R = -1.0	0.7323	0.2998
	427	800	R = 0.0		
			R = -1.0*		
	650	1200	R = 0.0*		
			R = -1.0*		

*Insufficient data for regression.

TABLE 28. Regression Fit Indicators For Energy Versus Life Plots

	<i>Temperature Stress Ratios</i>	<i>R²</i>	<i>Standard Error of Estimate</i>
Ti-24Al-11Nb	All Data Pooled	0.9295	1.0379
Ti-25Al-10Nb-3V-1Mo	All Data Pooled	0.6881	4.9681
Ti-24Al-11Nb and Ti-25Al-10Nb-3V-1Mo	Both Alloys Pooled	0.7011	9.2915

TABLE 29. Candidate 4, Ti-25Al-10Nb-3V-1Mo Notched Low Cycle Fatigue
(Frequency = 0.17 Hz (10 cpm), R = 0.5, K_t = 2.18)

Nominal Stress		Temperature		Life Cycles to 0.8 mm (1/32 in.) Crack	Cycles to Failure
MPa	(ksi)	°C	(°F)		
275.8	40	650	(1200)	83,759	83,469
310.3	45	650	(1200)	38,650	39,448
344.8	50	650	(1200)	1,223	1,248
310.3	45	427	(800)	*	100,009 ⁽¹⁾
379.2	55	427	(800)	*	160,000 ⁽¹⁾
379.2	65	427	(800)	*	44,778 ⁽²⁾
379.2	65	427	(800)	144,500	144,663
379.2	65	26	(77)	126,250	126,390
517.1	75	26	(77)	*	29,008

Mechanically Conditioned Prior to Test

517.1	75	26	(77)	*	18,225 ⁽³⁾
517.1	75	26	(77)	*	8,578 ⁽⁴⁾

Coated and HSSC

379.2	65	26	(77)	TiN ⁽⁵⁾	586
379.2	65	427	(800)	TiN ⁽⁵⁾	4,445
379.2	65	427	(800)	TiN + HSSC ⁽⁶⁾	4,475

* = No crack found

⁽¹⁾ = Uploaded

⁽²⁾ = Thread failure

⁽³⁾ = Conditioned at 427°C (800°F)/517.1 MPa (75 ksi)/120 second
peak load dwell, one cycle

⁽⁴⁾ = Conditioned at 427°C (800°F)/517.1 MPa (75 ksi)/0.17 Hz
(10 cpm), one cycle

⁽⁵⁾ = Coated with TiN

⁽⁶⁾ = ASTM sea salt + 650°C (1200°F)/1-hour pretest thermal
cycle

TABLE 30. Notched LCF for Ti-24Al-11Nb
(Frequency = 0.17 Hz (10 cpm), R = 0.05, K_t = 2.18)

Nominal Stress		Temperature		0.8 mm Crack	Cycles to	
MPa	(ksi)	°C	(°F)		Failure	Comments
206.8	30	650	(1200)	2,000	2,976	1
206.8	30	650	(1200)	2,800	5,176	1
379.2	55	26	(77)	700	746	1
379.2	55	26	(77)	2,000	2,072	1
379.2	55	26	(77)	9,400	9,978	2
379.2	55	26	(77)	5,000	5,301	2
310.3	45	26	(77)	133,940	142,712	3
310.3	45	26	(77)	44,000	46,524	3
310.3	45	26	(77)	8,300	8,365	4
310.3	45	26	(77)	152,000	160,309	4
379.2	55	26	(77)	27,800	29,335	4
379.2	55	26	(77)	24,700	26,004	4
310.3	45	427	(800)	53,000	55,270	4
310.3	45	427	(800)	100,000	106,009	4
379.2	55	427	(800)	36,000	38,342	4
379.2	55	427	(800)	7,700	8,178	4
275.8	40	650	(1200)	14,000	15,225	4
275.8	40	650	(1200)	3,460	3,642	4
206.9	30	650	(1200)	31,100	33,062	4
275.8	30	650	(1200)	52,000	52,899	4

1 - Aluminum slurry coating

2 - Baseline (uncoated) + coating diffusion cycle

3 - Prestressed, conditioned at 427°C (800°F)/620.6 MPa
(90 ksi)/0.17 Hz (10 cpm), 5 cycles

4 - Baseline, not coated

TABLE 31. Notched LCF for Ti-24Al-11Nb
(Frequency = 0.17 Hz (10 cpm), R = 0.05, K_t = 2.18)

Nominal Stress		Temperature		Surface Treatment	Cycles to Failure
MPa	(ksi)	°C	(°F)		
137.9	30	650	(1200)	HSSC ⁽¹⁾	53,500 dnf uploaded
206.8	30	650	(1200)	HSSC ⁽¹⁾	2,694
206.8	30	650	(1200)	HSSC ⁽¹⁾	2,371
379.2	55	26	(77)	HSSC ⁽¹⁾	172
379.2	55	26	(77)	HSSC ⁽¹⁾	416
379.2	55	26	(77)	HSSC/COATED ⁽²⁾	259
379.2	55	26	(77)	HSSC/COATED ⁽²⁾	191

⁽¹⁾HSSC = ASTM sea salt + 650°C (1200°F)/1hr pre-test thermal cycle.

⁽²⁾HSSC/Coated = ASTM sea salt applied to COATED specimens + thermal cycle, (Coated with aluminum slurry).

TABLE 32. Smooth Axial High Cycle Fatigue Results for Ti-24Al-11Nb

K_t	"R" Ratio	Temperature		Maximum Stress		Cycles to Failure	Remarks
		°C	(°F)	MPa	(ksi)		
1.0	0.05	26	(77)	551.6	(80)	1.07E5	
1.0	0.05	26	(77)	517.1	(75)	2.70E5	
1.0	0.05	26	(77)	482.7	(70)	2.18E6	
1.0	0.05	26	(77)	448.2	(65)	9.66E6	
1.0	0.05	26	(77)	448.2	(65)	1.00E7	Did Not Fail
1.0	-1	26	(77)	482.7	(70)	3.08E4	
1.0	-1	26	(77)	448.2	(65)	2.79E4	
1.0	-1	26	(77)	379.2	(55)	5.32E4	
1.0	-1	26	(77)	344.8	(50)	1.40E5	
1.0	-1	26	(77)	310.3	(45)	1.00E7	Did Not Fail
1.0	0.05	650	(1200)	413.7	(60)	9.70E5	
1.0	0.05	650	(1200)	379.2	(55)	1.09E6	
1.0	0.05	650	(1200)	379.2	(55)	3.67E6	
1.0	0.05	650	(1200)	344.8	(50)	1.00E7	Did Not Fail
1.0	0.05	650	(1200)	310.3	(45) ⁽¹⁾	1.00E7	Did Not Fail
1.0	-1	650	(1200)	413.7	(60)	2.96E4	
1.0	-1	650	(1200)	413.7	(60)	2.67E5	
1.0	-1	650	(1200)	344.8	(50)	4.70E5	
1.0	-1	650	(1200)	310.3	(45)	2.10E6	
1.0	-1	650	(1200)	275.8	(40)	1.00E7	Did Not Fail

⁽¹⁾Not used in regression analysis

TABLE 33. Notched Axial High Cycle Fatigue Results for Ti-24Al-11Nb

K_t	"R" Ratio	Temperature		Maximum Stress		Cycles to Failure	Remarks
		°C	(°F)	MPa	(ksi)		
2.16	0.05	26	(77)	379.2	(55)	2.27E4	
2.16	0.05	26	(77)	344.8	(50)	3.04E4	
2.16	0.05	26	(77)	310.3	(45)	8.70E6	
2.16	0.05	26	(77)	275.8	(40)	1.06E6	
2.16	0.05	26	(77)	275.8	(40)	2.80E6	Did Not Fail
2.16	0.05	26	(77)	241.3	(35)	1.00E7	Did Not Fail
2.16	0.05	650	(1200)	310.3	(45)	1.46E4	
2.16	0.05	650	(1200)	275.8	(40)	2.93E6	
2.16	0.05	650	(1200)	241.3	(35)	1.00E7	Did Not Fail
2.16	0.05	650	(1200)	206.9	(30) ⁽¹⁾	1.00E7	Did Not Fail
2.16	0.05	427	(800)	344.8	(50)	2.18E4	
2.16	0.05	427	(800)	310.3	(45)	1.09E6	
2.16	0.05	427	(800)	344.8	(50) ⁽²⁾	1.00E7	Did Not Fail
2.16	0.05	427	(800)	310.3	(45) ⁽²⁾	1.00E7	Did Not Fail

⁽¹⁾Not used in regression analysis⁽²⁾Prestressed at: 620 MPa (90 ksi) (max), 427°C (800°F), R = 0.05, 0.17 Hz (10 cpm), 5 to 7 cycles.

TABLE 34. Smooth and Notched Axial High Cycle Fatigue Results for Ti-25Al-10Nb-3V-1Mo

K_t	"R" Ratio	Temperature		Maximum Stress		Cycles to Failure	Remarks
		°C	(°F)	MPa	(ksi)		
1.0	-1	26	(77)	517.1	(75)	3.23E4	
1.0	-1	26	(77)	482.7	(70)	1.98E5	
1.0	-1	26	(77)	448.2	(65) ⁽¹⁾	3.22E6	Thread Failure
1.0	-1	26	(77)	448.2	(65)	6.90E6	
1.0	-1	26	(77)	448.2	(65)	1.00E7	Did Not Fail
1.0	-1	26	(77)	413.7	(60)	1.00E7	Did Not Fail
1.0	-1	650	(1200)	517.1	(75)	3.00E5	
1.0	-1	650	(1200)	448.2	(65)	1.07E6	
1.0	-1	650	(1200)	448.2	(65)	3.86E6	
1.0	-1	650	(1200)	413.7	(60)	1.00E7	Did Not Fail
1.0	-1	650	(1200)	310.3	(45) ⁽¹⁾	1.00E7	Did Not Fail
2.16	0.05	26	(77)	310.3	(45)	1.70E5	
2.16	0.05	26	(77)	275.8	(40)	1.00E7	Did Not Fail
2.16	0.05	650	(1200)	344.8	(50)	8.20E3	
2.16	0.05	650	(1200)	310.3	(45)	7.79E5	
2.16	0.05	650	(1200)	275.8	(40)	1.00E7	Did Not Fail

⁽¹⁾Not used in regression analysis

TABLE 35. Regression Analysis Summary For Axial High Cycle Fatigue Results

Condition	Alloy Ti-24Al-11Nb	10 ⁷ Cycle Fatigue Strength MPa (ksi)		
		Mean	Min	(-97.5%)
R = 0.05, 25°C (77°F), $K_t = 1.0$	448.2	(65.0)	435.1	(63.1)
R = 1.0, 25°C (77°F), $K_t = 1.0$	281.3	(40.8)	219.3	(31.8)
R = 0.05, 650°C (1200°F), $K_t = 1.0$	353.7	(51.3)	299.2	(43.4)
R = 1.0, 650°C (1200°F), $K_t = 1.0$	275.1	(39.9)	228.9	(33.2)
R = 0.05, 25°C (77°F), $K_t = 2.16$	250.3	(36.3)	193.1	(28.0)
R = 0.05, 650°C (1200°F), $K_t = 2.16$	247.5	(35.9)	—	(1)
R = 0.05, 427°C (800°F), $K_t = 2.16$	—	(1)	—	(1)
Alloy - Ti-25Al-10Nb-3V-1Mo				
R = -1.0, 25°C (77°F), $K_t = 1.0$	429.6	(62.3)	382.0	(55.4)
R = -1.0, 25°C (77°F), $K_t = 1.0$	429.6	(62.3)	382.0	(55.4)
R = 0.05, 25°C (77°F), $K_t = 2.16$	275.8	(40.0)	—	(1)
R = 0.05, 650°C (1200°F), $K_t = 2.16$	279.2	(40.5)	—	(1)

(1) Insufficient data to calculate mean or minimum life

TABLE 36. Regression Analysis Summary for HCF Mean Lines

	<i>Temperature</i>		<i>Stress Ratio</i>	<i>R</i> ²	<i>Standard Error of Estimate</i>
	<i>°C</i>	<i>(°F)</i>			
Ti-24Al-11Nb					
Smooth	26	79	R = 0.05	0.9902	0.1029
			R = -1.0	0.7502	0.6145
	650	1200	R = 0.05	0.8075	0.7164
			R = -1.0	0.8722	0.3933
Notched	26	79	R = 0.05	0.6736	0.7544
	427	800	R = 0.05*		
	650	1200	R = 0.05	0.8354	0.8648
Ti-25Al-10Nb-3V-1Mo					
Smooth	26	79	R = 0.05	0.9902	0.1029
			R = -1.0	0.8442	0.5264
	650	1200	R = 0.05		
			R = -1.0	0.8740	0.2883
Smooth	26	79	R = 0.05*		
			R = -1.0	0.9879	0.0231
	427	800	R = 0.05	0.7323	0.2998
			R = -1.0		
	650	1200	R = 0.05	0.9501	0.4940
			R = -1.0		

*Insufficient data for regression

TABLE 37. Load-Controlled TMF Results for Ti-24Al-11Nb
38° to 650°C (100° to 1200°F)

Strain Ratio	Strain Range %	Half Life Stress		Frequency cpm	Cycle Type ⁽¹⁾	Cycles to Failure
		Maximum MPa (ksi)	Minimum MPa (ksi)			
-1.0	0.6	408.4 (59.2)	-152.4 (-22.1)	1.0	I	9095 ⁽²⁾
-1.0	0.8	472.3 (68.5)	-271.7 (-39.4)	0.5	I	1948 ⁽²⁾
-1.0	0.6	427.5 (62.0)	-143.4 (-20.8)	0.5	I	20690
-1.0	1.0	593.6 (86.1)	-330.3 (-47.9)	0.5	I	201
-1.0	0.8	517.8 (75.1)	-231.7 (-33.6)	0.5	I	1933
-1.0	0.8	242.0 (35.1)	-504.0 (-73.1)	0.5	II	776
-1.0	0.6	148.9 (21.6)	-422.0 (-61.2)	0.5	II	2466 ⁽³⁾
-1.0	1.0	336.5 (48.8)	-604.7 (-87.7)	0.5	II	369
0.0	0.5	443.0 (62.8)	-26.0 (-3.77)	0.5	I	12383

Hot Salt Stress Corrosion (HSSC) Tests ⁽⁴⁾

-1.0	0.6	344.1 (49.9)	-215.8 (-31.3)	0.5	I	1145
-1.0	0.4	228.9 (33.2)	-124.8 (-18.1)	0.5	I	34126 ⁽³⁾
-1.0	0.8	446.1 (67.6)	-287.5 (-41.7)	0.5	I	397
-1.0	1.6	237.9 (34.5)	-326.1 (-47.3)	0.5	II	59
-1.0	0.6	227.5 (33.0)	-329.6 (-47.8)	0.5	II	421
-1.0	0.8	308.9 (44.8)	-436.4 (-63.3)	0.5	II	33

⁽¹⁾ I = Out-of-Phase II = In-Phase

⁽²⁾ Thread failure, not used in hysteretic energy analysis

⁽³⁾ Did not fail — Test suspended. Data used in
hysteretic energy analysis

⁽⁴⁾ HSSC data not used in hysteretic energy analysis

TABLE 38. Load-Controlled TMF Results for Ti-25Al-10Nb-3V-1Mo
38° to 650°C (100° to 1200°F)

Strain Ratio	Strain Range %	Half Life Stress		Frequency cpm	Cycle Type ⁽¹⁾	Cycles to Failure
		Maximum MPa (ksi)	Minimum MPa (ksi)			
-1.0	0.6	399.9 (58.0)	-200.6 (-29.1)	1.0	I	36796 ⁽²⁾
-1.0	0.8	614.3 (89.1)	-186.2 (-27.0)	0.5	I	2677 ⁽²⁾
-1.0	1.0	703.3 (102.0)	-286.1 (-41.5)	0.5	I	767
-1.0	1.2	408.2 (59.2)	-768.1 (-111.4)	0.5	II	461
-1.0	1.0	88.9 (12.9)	-885.3 (-128.4)	0.5	II	20173 ⁽²⁾
0.0	0.65	619.8 (89.9)	-25.4 (-3.69)	0.5	I	2542

⁽¹⁾ I = Out-of-Phase II = In-Phase

⁽²⁾ Did not fail — Test suspended. Data used in
hysteretic energy analysis

TABLE 39. Hysteretic Energy Results-Load Controlled TMF

<i>Inelastic Strain %</i>	<i>Tensile Stress MPa (ksi)</i>	<i>Hysteretic Energy MPa (ksi)</i>
<i>Ti-24Al-11Nb:</i>		
$N_f = A(\Delta W)^B$, $A = 61660$, $B = -1.362$, $R^2 = 0.845$		
1.262E-02	427.5 (62.0)	5.3921 (0.782)
1.057E-01	593.6 (81.6)	34.474 (9.105)
4.325E-02	517.8 (75.1)	22.408 (3.250)
4.325E-02	242.0 (35.1)	10.466 (1.518)
1.262E-02	148.9 (35.1)	1.882 (0.273)
1.057E-01	336.5 (48.8)	35.543 (5.155)
5.614E-03	433.0 (62.8)	2.427 (0.352)
<i>Ti-25Al-10Nb-3V-1Mo:</i>		
$N_f = A(\Delta W)^B$, $A = 83370$, $B = -1.227$, $R^2 = 0.824$		
6.381E-03	399.9 (58.0)	2.551 (0.370)
2.652E-02	614.3 (89.2)	16.299 (2.364)
7.457E-02	703.3 (102.1)	52.463 (7.609)
1.598E-01	408.2 (59.2)	65.177 (9.453)
7.457E-02	88.9 (12.8)	6.605 (0.958)
9.537E-03	619.8 (89.9)	5.909 (0.857)

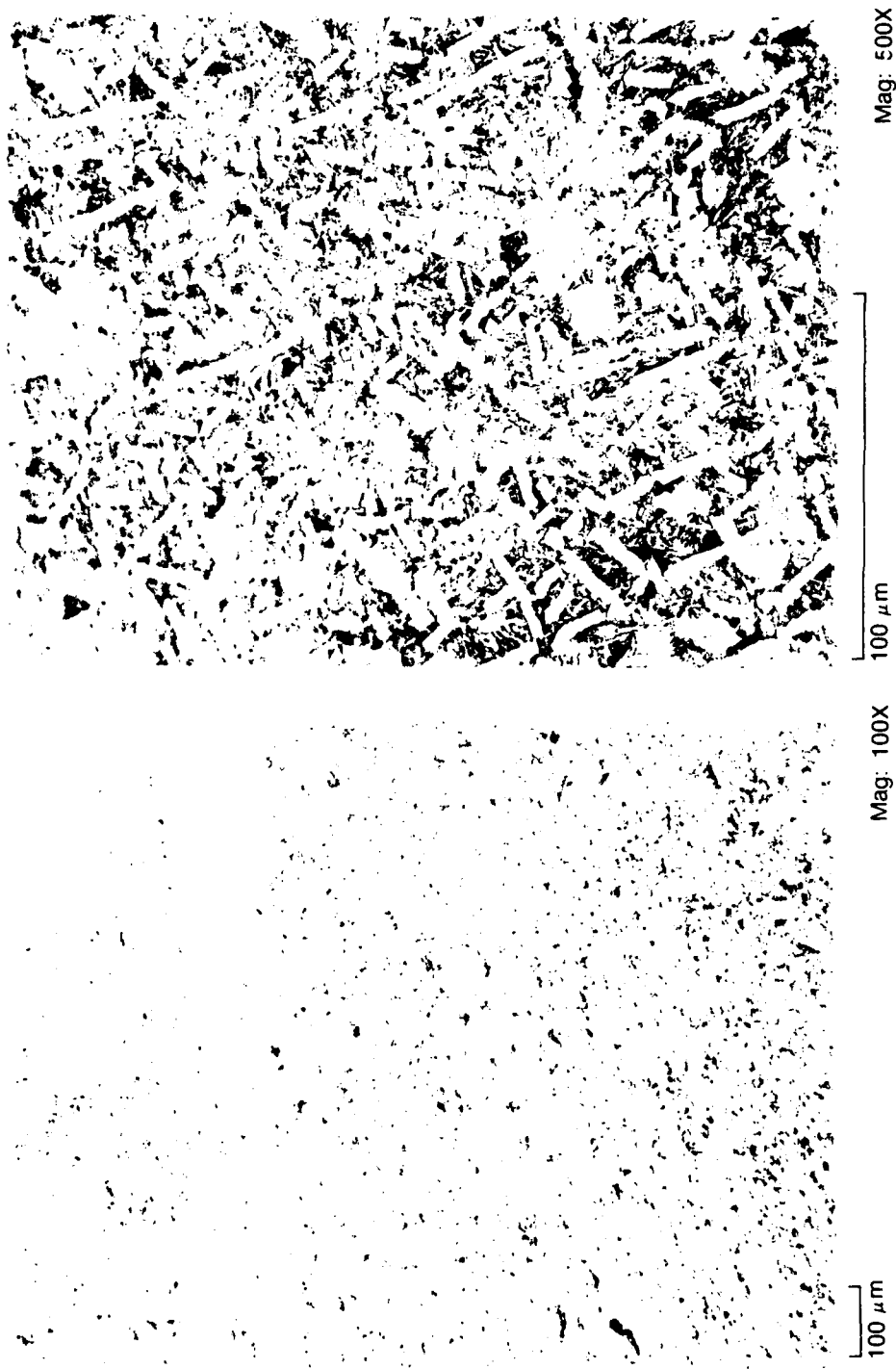
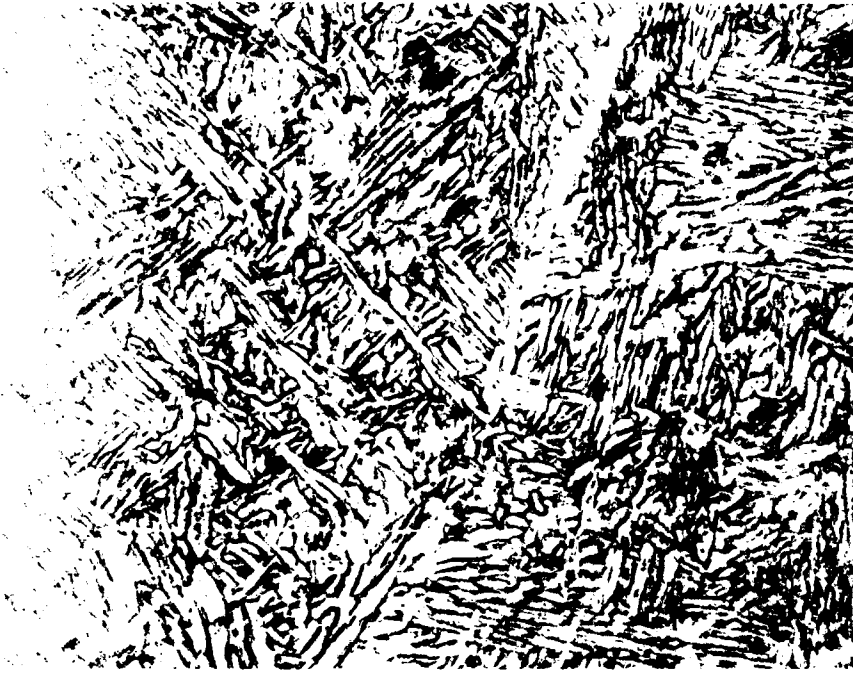
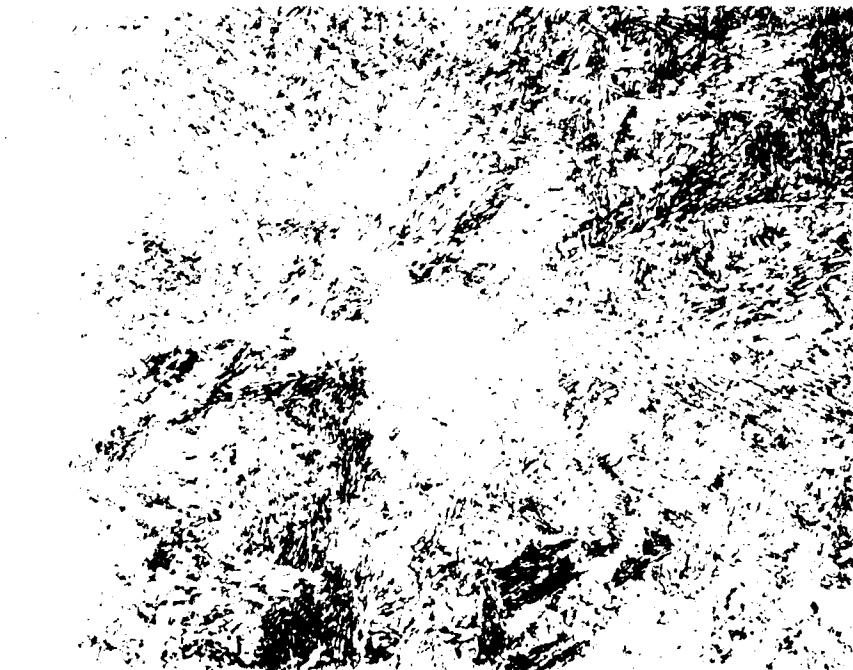


Figure 1. As-Received Microstructure of Rotary-Forged Ti-25Al-10Nb-3V-1Mo — Equiaxed and Elongated Alpha-2 (Large White Phase) in a Transformed Beta Matrix Indicating Final Working Below the Beta Transus

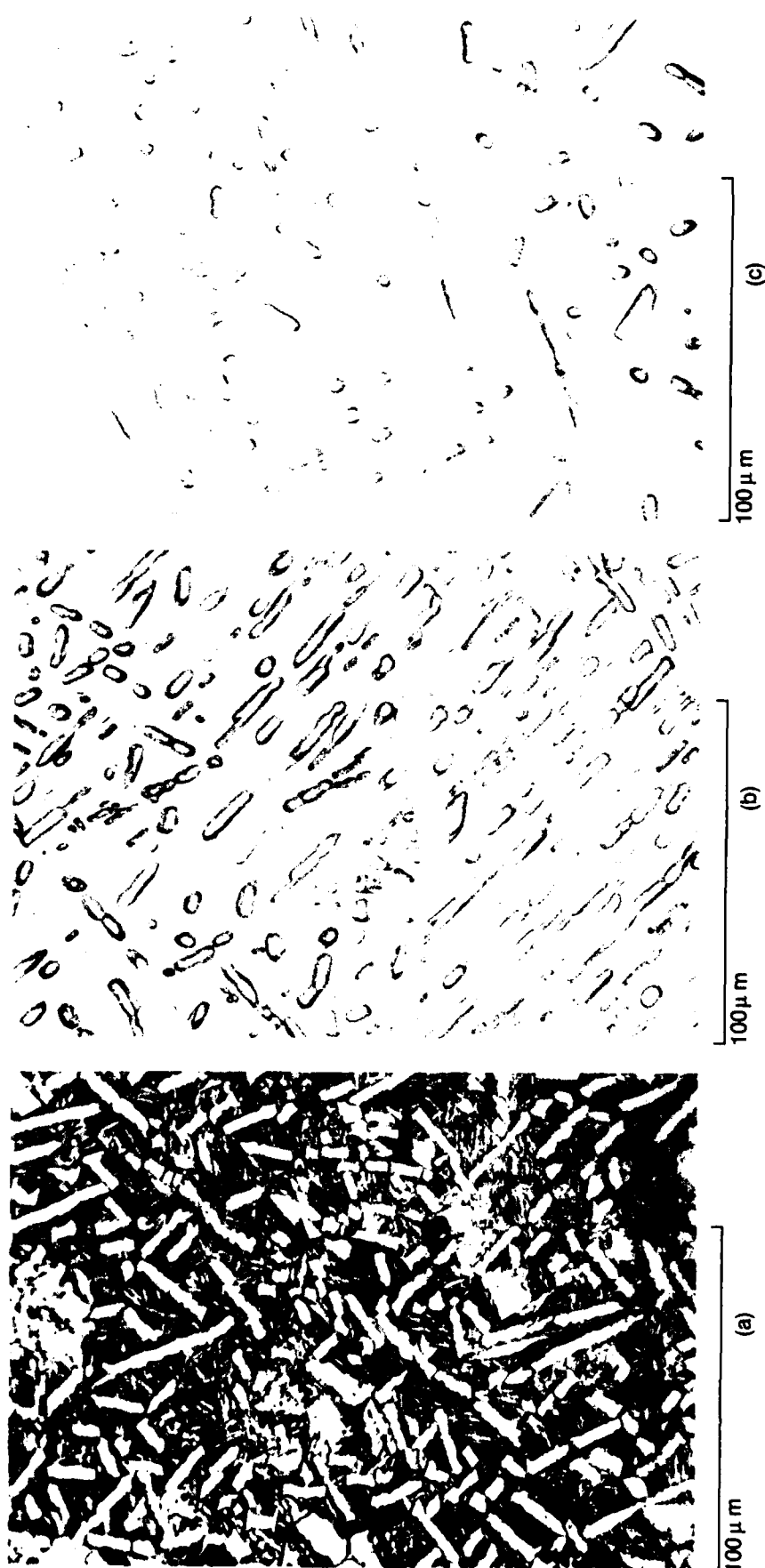


100 μm



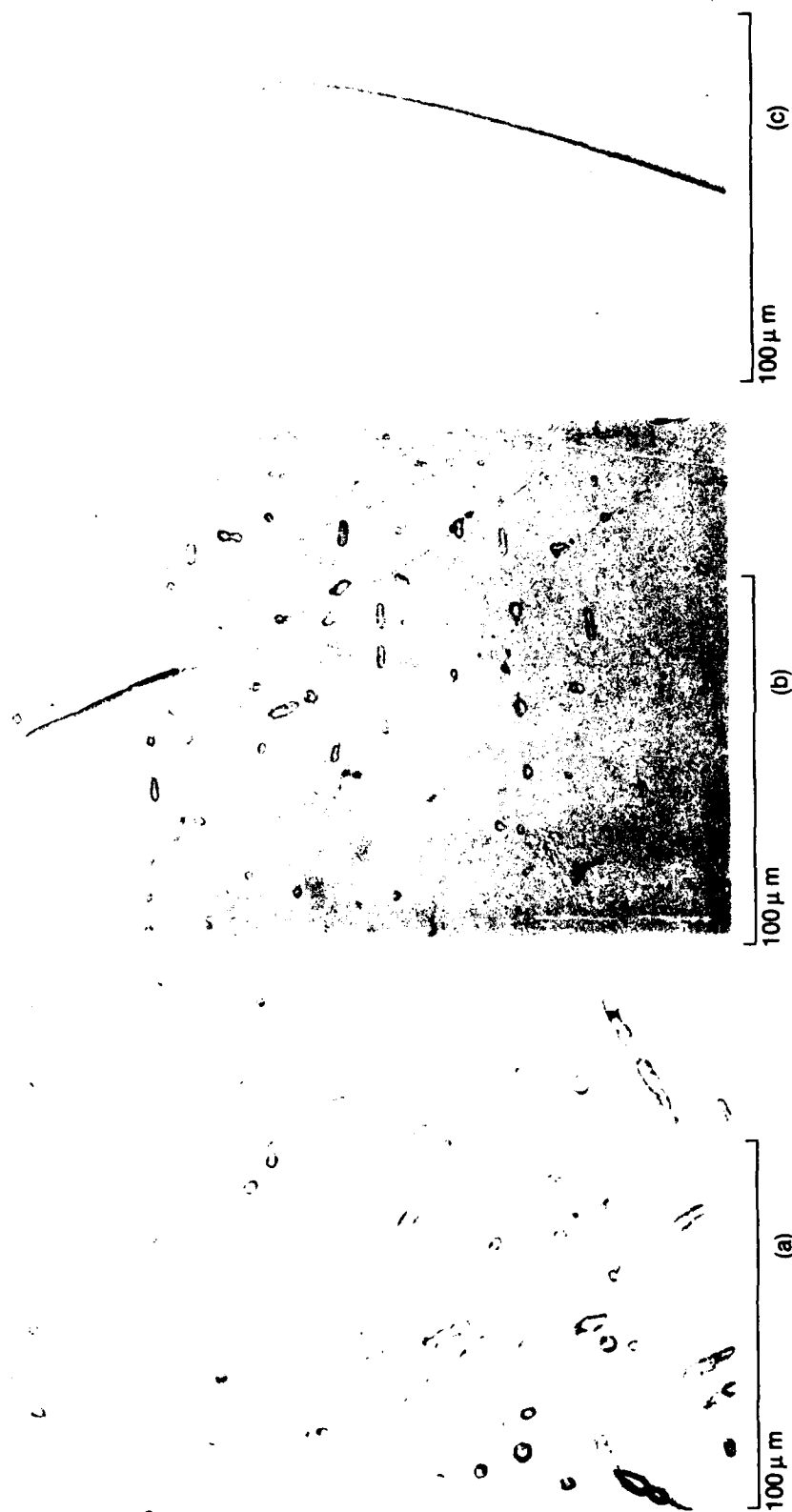
100 μm

Figure 2. Transformed Beta Structure of Ti-24Al-11Nb Exhibiting Martensitic Work Before Beta Transus (Left) and by Slow Cooling from Reduction to Beta-peak



- (a) As-forged microstructure consisting of equiaxed and elongated alpha grains in a transformed beta (fine acicular alpha-2 + beta) matrix resulting from air cooling from the forging temperature.
- (b) 1038°C (1900°F)/1/2 hr/water quench
- (c) 1066°C (1950°F)/1/2 hr/water quench. Higher temperature produced less primary alpha-2.

Figure 3. Photomicrographs of Alpha-2/Beta Forged Ti-25Al-10Nb-3V-1Mo Alloy — Beta Transus Determination (Pre-Beta Transus)



- (a) 1093°C (2000°F)/1/2 hr/water quench exhibiting fewer primary alpha grains as the β -transus is approached.
- (b) 1099°C (2010°F)/1/2 hr/water quench showing very few primary alpha-2 grains, indicating that the β -transus temperature is close.
- (c) 1104°C (2020°F)/1/2 hr/water quench consisting entirely of alpha-2 with no remaining primary alpha-2, indicating that the β -transus has been reached.

Figure 4. Photomicrographs of Alpha-2/Beta Forged Ti-25Al-10Nb-3V-1Mo Alloy — Beta Transus Determination

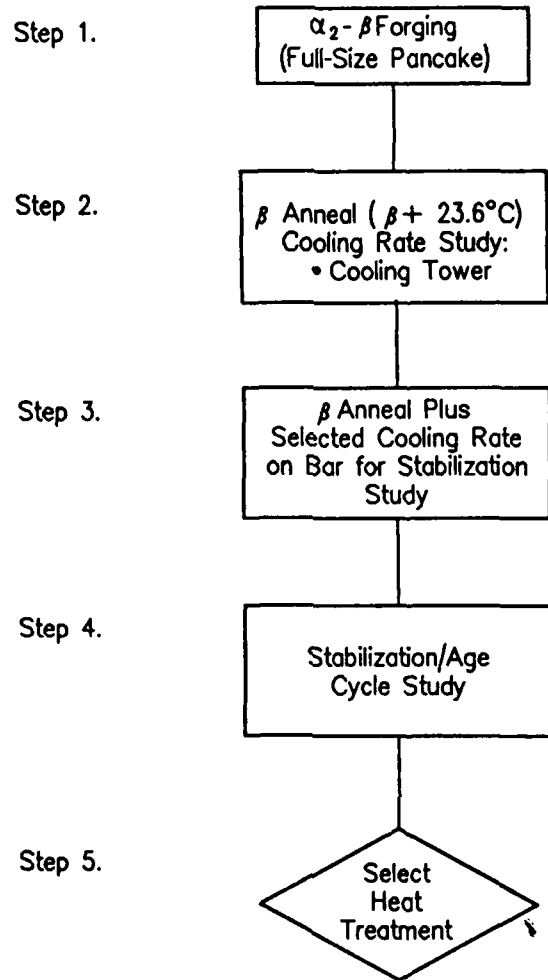


Figure 5. Selection of Beta Anneal Cooling Rate and Stabilization Cycle

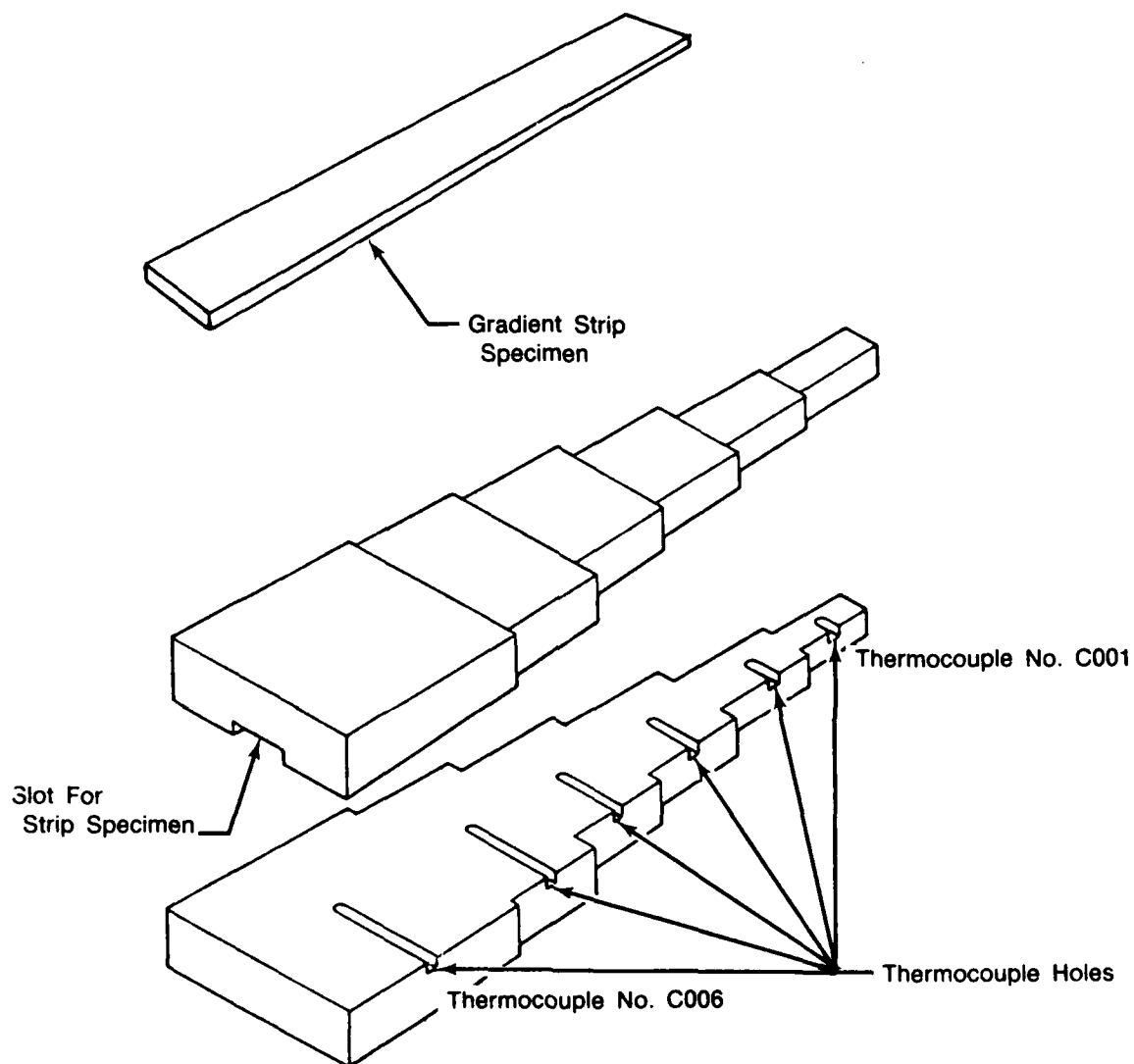


Figure 6. Tower Cooling Fixture for Cooling Rate Response Study

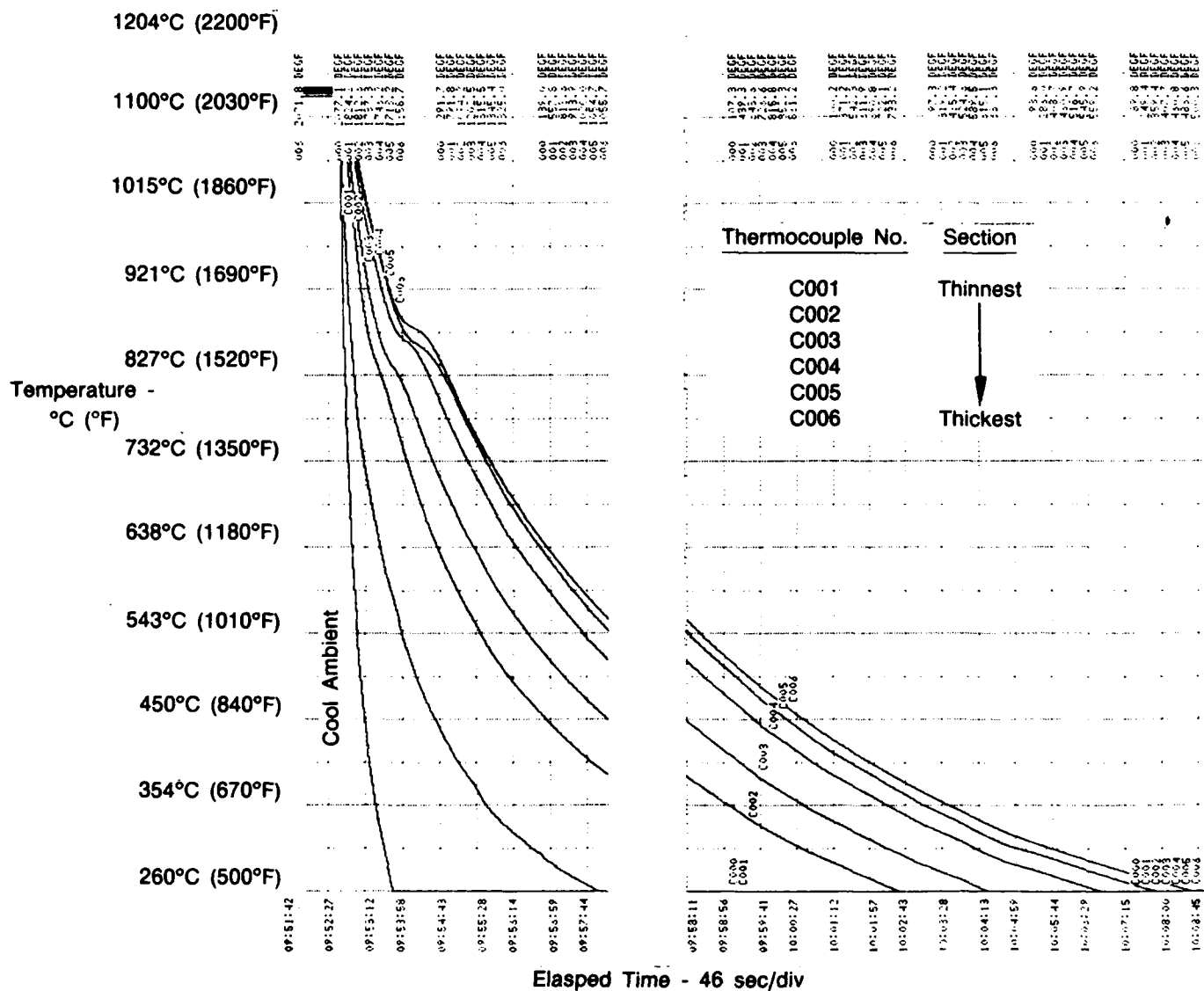
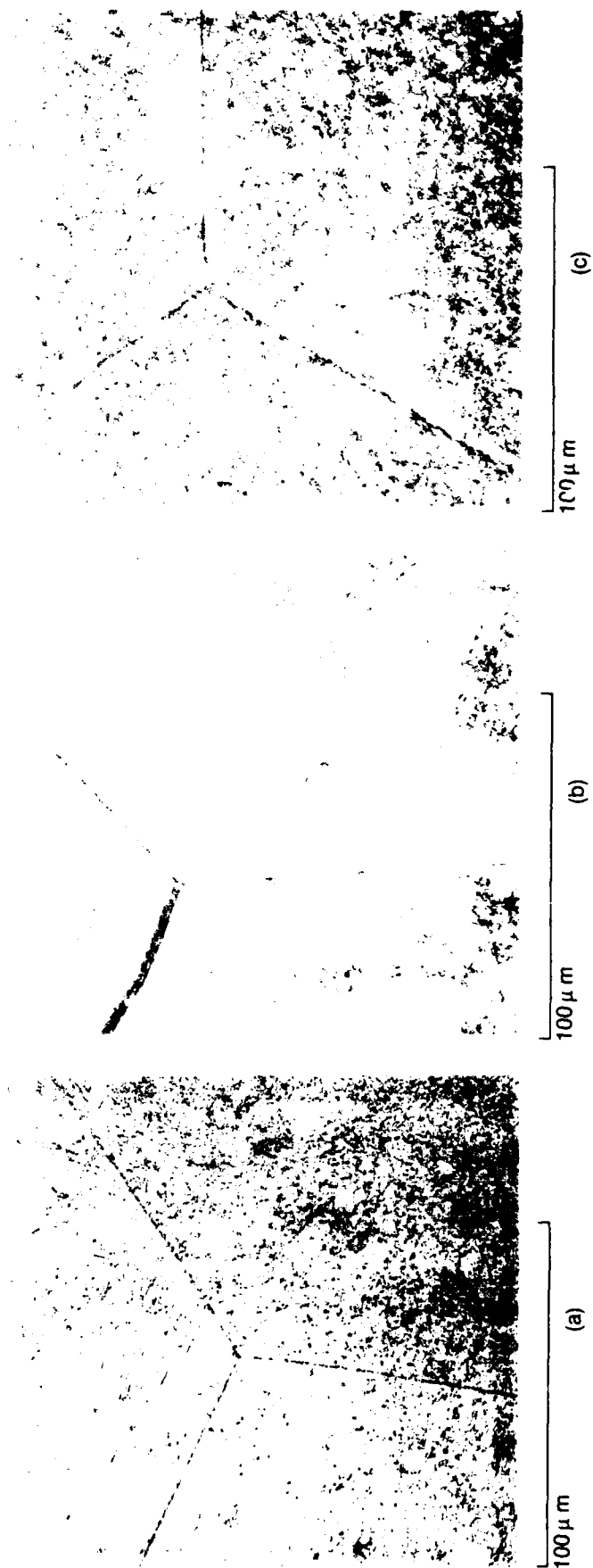


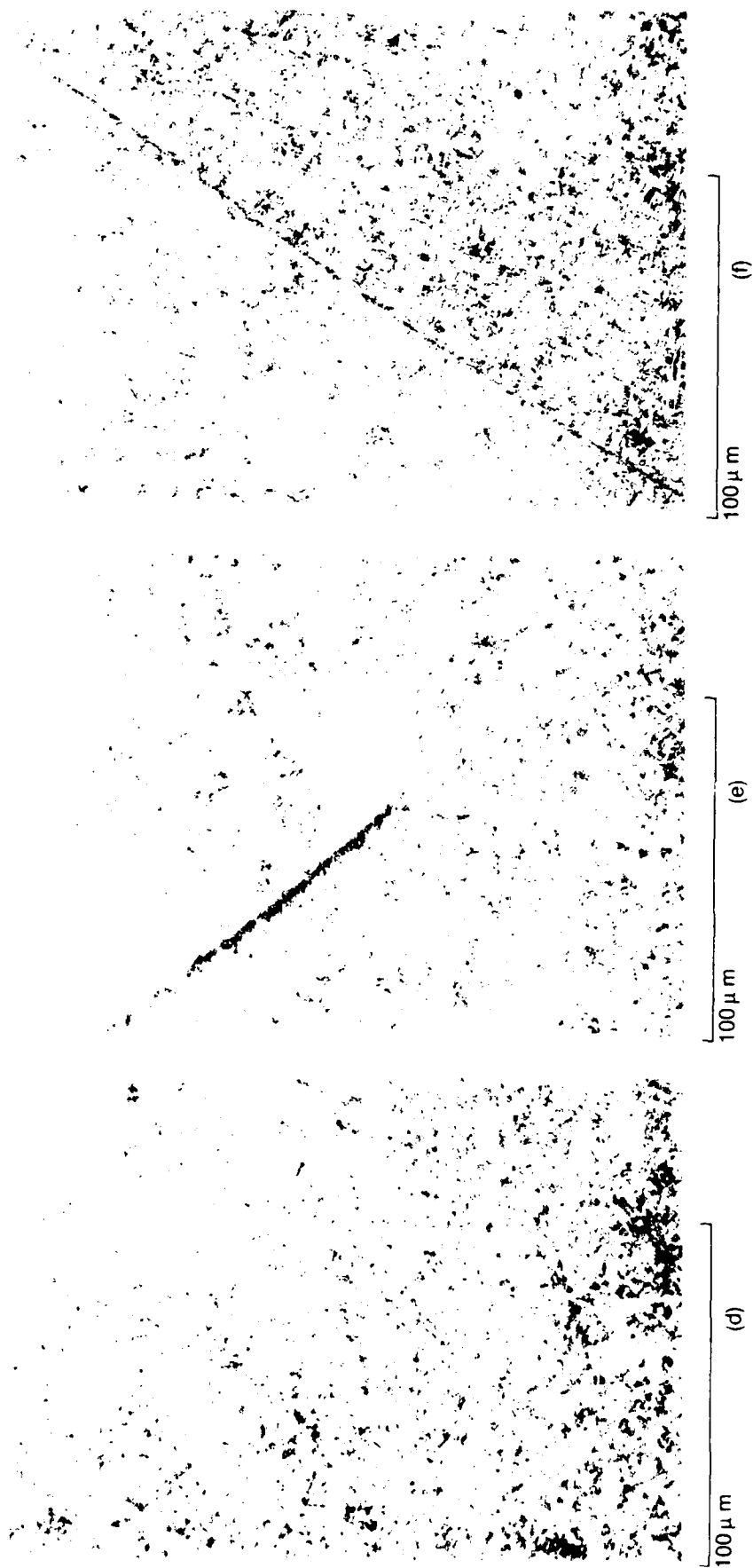
Figure 7. Strip Chart From Cooling Rate Study



Rate of cooling decreases from Sections 1 to 6:

- (a) Section 1 (TC No. C001) - Only small amounts of the desired transformation product (fine acicular alpha-2 + beta) was produced, indicating that cooling was too rapid.
- (b) Section 2 (TC No. C002) - Some partial transformation (dark areas).
- (c) Section 3 (TC No. C003) - Nearly complete transformation.

Figure 4. Sections From Ti-25Al-10Nb-3V-1Mo Cooling Rate Study, Cooled at Various Rates From the Beta + 23.6°C (4132°C) Annealing Temperature



(d) Section 4 (TC No. C004) - } Each Section exhibits preferred microstructure - fine acicular alpha-2 (white needles) and beta.
 (e) Section 5 (TC No. C005) - }
 (f) Section 6 (TC No. C006) - }

Figure 9 Sections From Ti-25Al-10Nb-3V-1.5Mo Cooling Rate Study, Cooled at Various Rates From the Beta + 23.6 °C (1132 °C) Annealing Temperature (Continued)



100 μ m



100 μ m



100 μ m

Figure 10 Photomicrographs of Alpha-2/Beta Forged Ti-25Al-10Nb-3V-1Mo, Candidate No.3 From Heat Treatment Optimization Study -- Solutioned at 1163°C (2125°F)/1 Hour, Cooled to 816°C (1500°F), and Held for 1/2 Hour, Air Cooled, and Aged for 8 Hours at 593°C (1100°F), Air Cooled

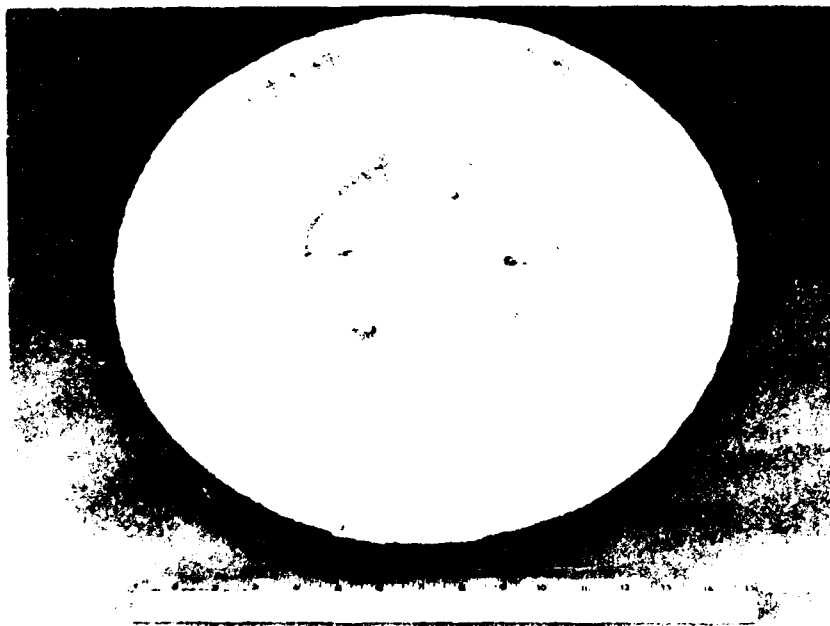


Figure 11. Pancake Appearance Typical for Both Alloys

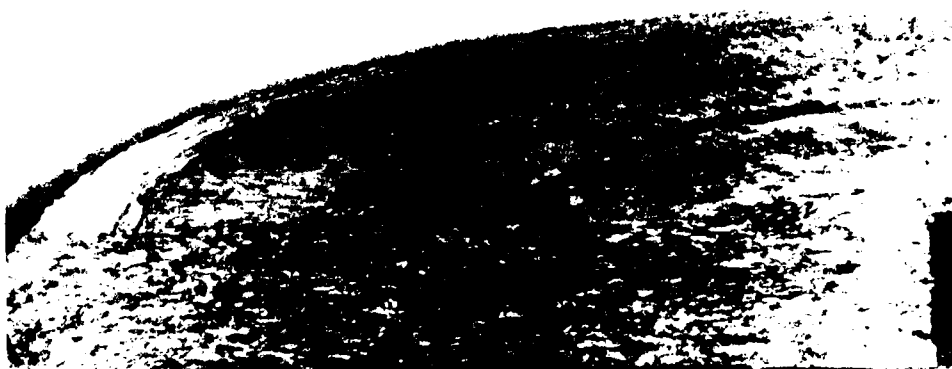


Figure 12. Planar Fracture Surface With Material Flaking Off Ahead of Wire EDM Cut in As Forged (Beta) Ti-24Al-11Nb Pancake

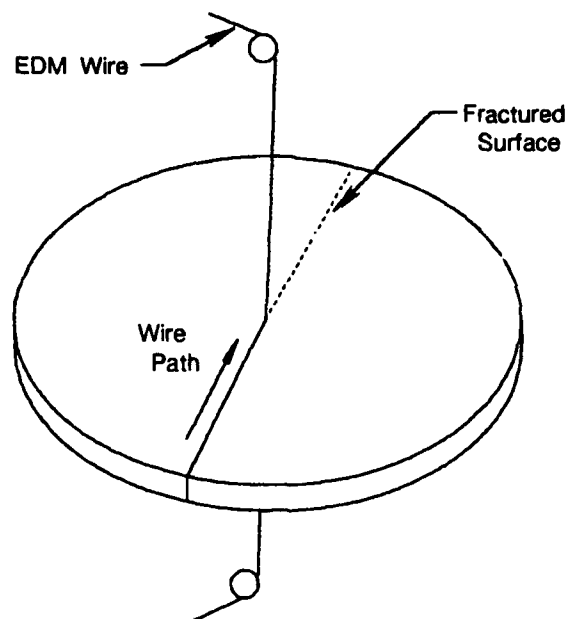


Figure 13. Schematic Diagram of EDM Wire Path and Pancake Fracture. Pancake Fractured When Wire Cut Reached Pancake Center



Figure 14. Shallow Crack in Ti-24Al-11Nb Pancake Section Resulting From Abrasive Cutoff. Crack Path Illustrates Mechanism by Which Material is Allowed to Flake From Fracture Surfaces.



1 cm

Mag: 1X

Figure 15. Cross-Section (Macroetched) of a 16-Inch Diameter Beta Forged Ti-25Al-10Nb-3V-1Mo Pancake From Near Center (Left) to Outer Diameter (Right)

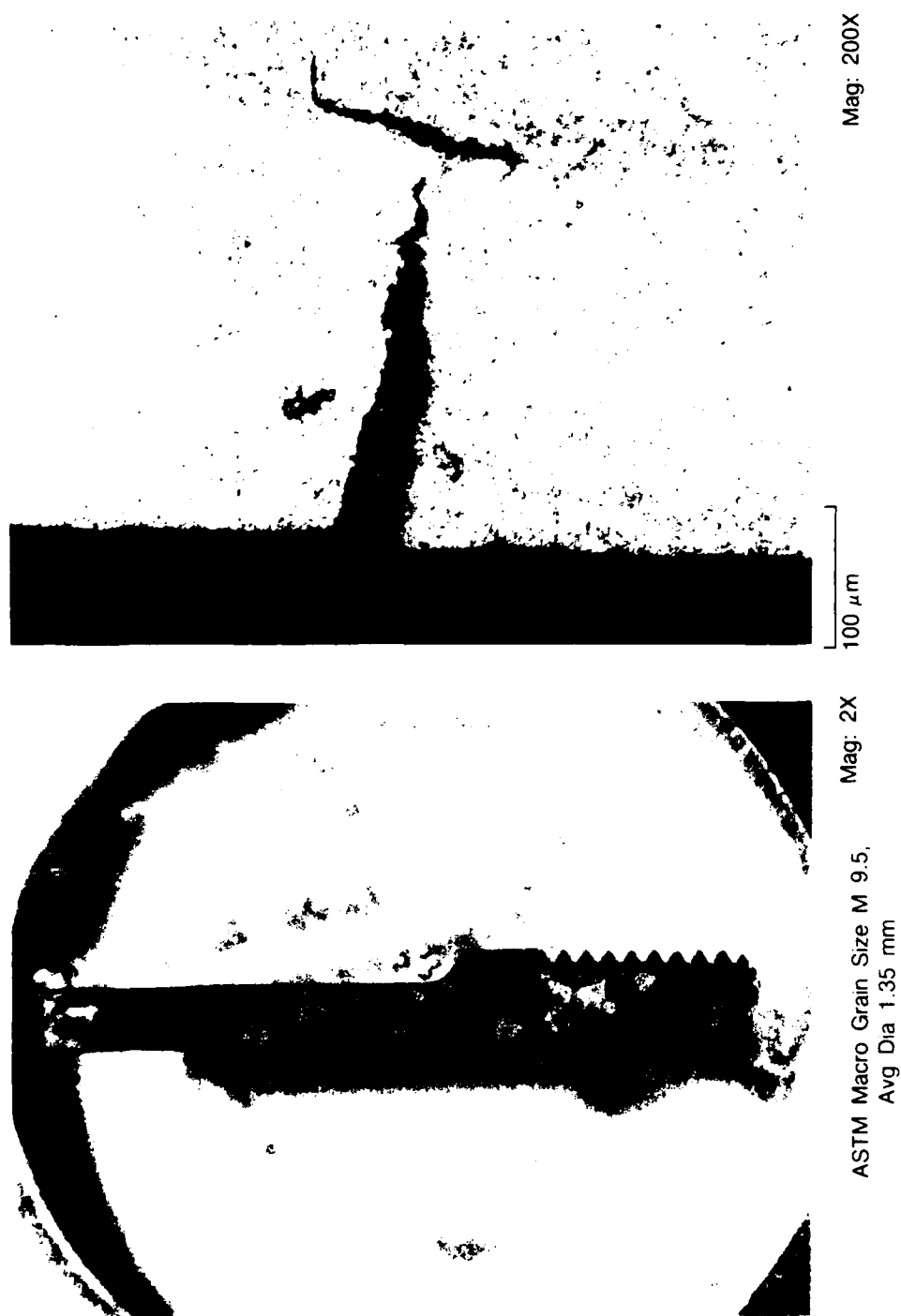
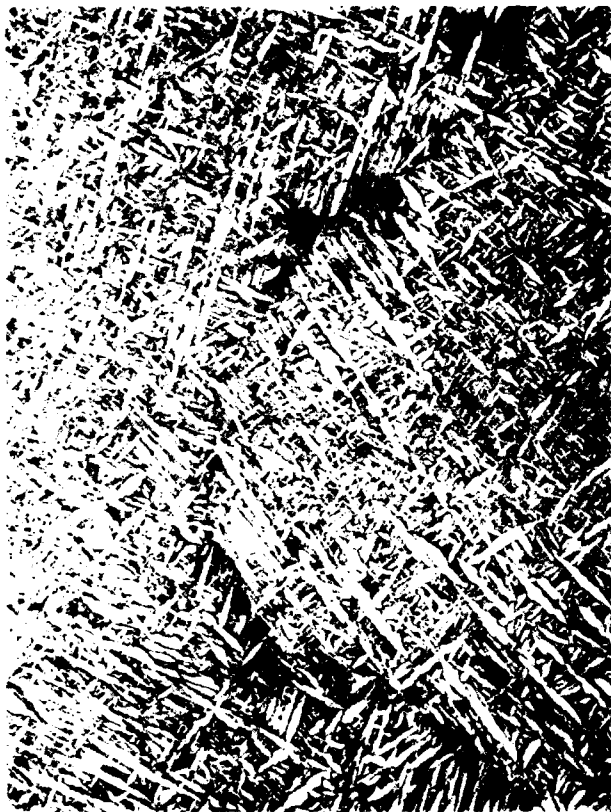


Figure 16. Secondary Cracking Along Gage Section of 650°C (1200°F) Tensile Specimen.
 Note: Subsurface Crack Along Prior Beta Grain Boundary (Right) Material is Ti-25Al-10Nb-3V-1Mo Candidate 3 (Alpha-2/Beta Forged)

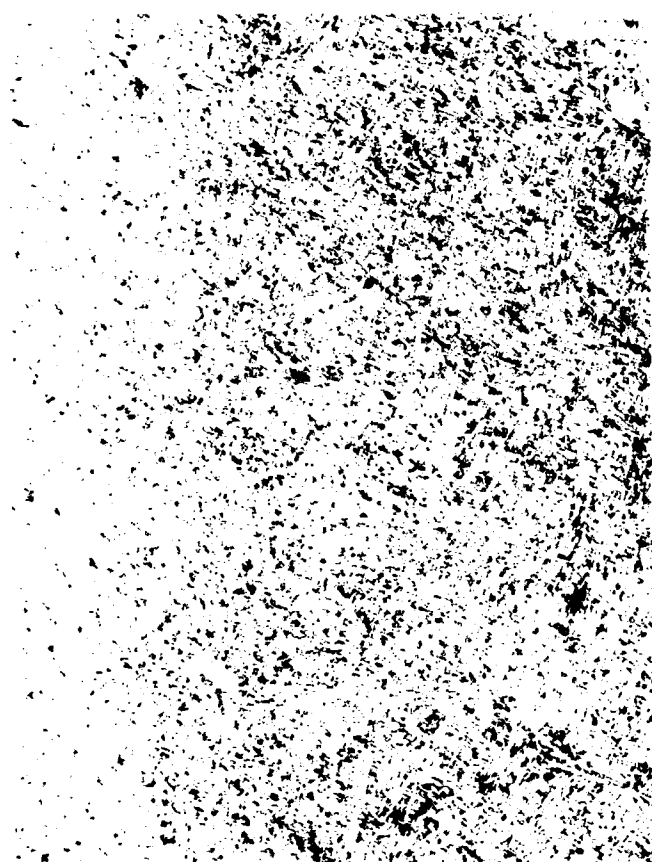


100 μ m



100 μ m

Figure 17. Microstructure of Ti-24Al-11Nb Beta Forged and Fully Heat Treated

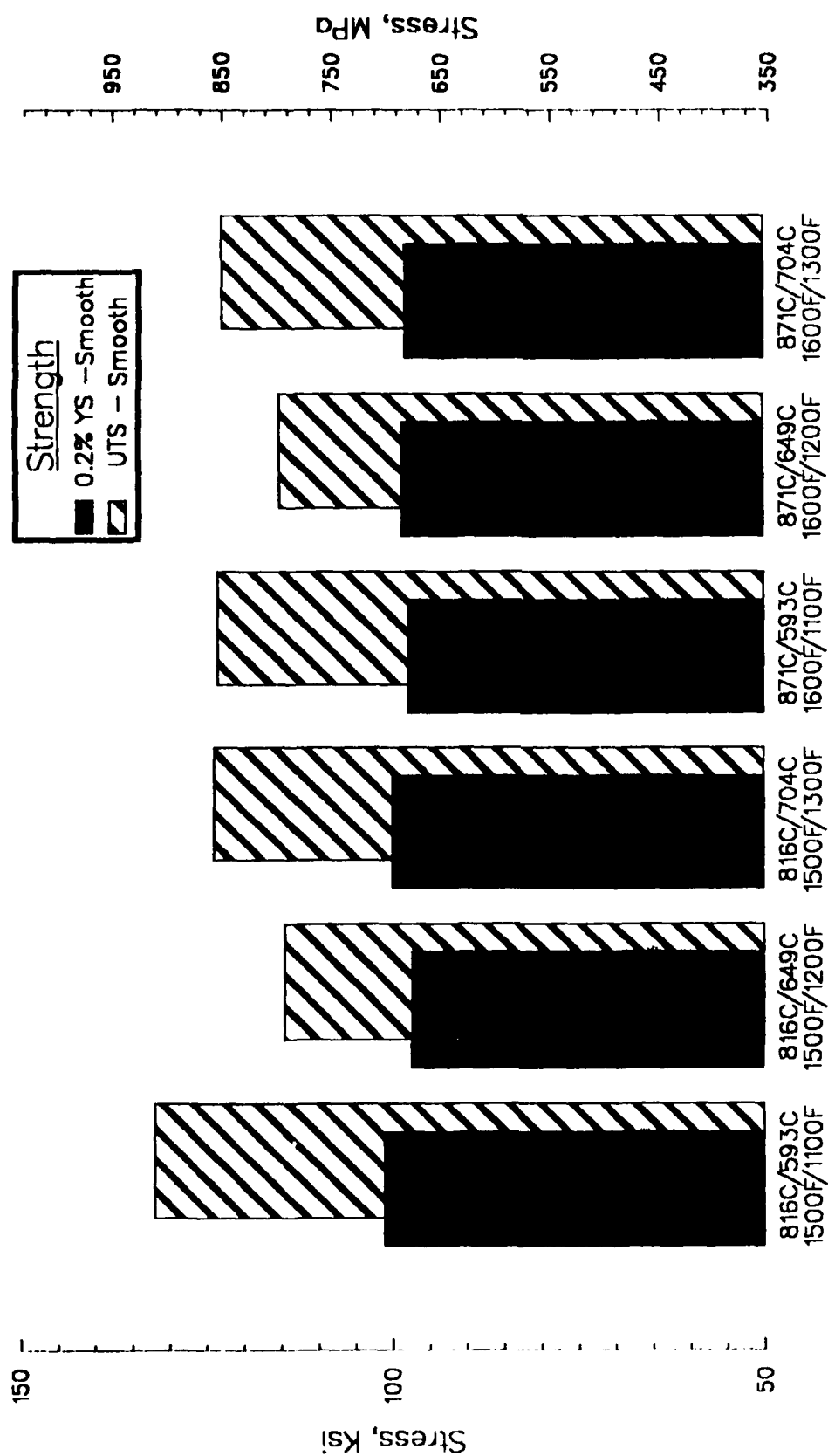


100 μ m



100 μ m

Figure 18. Microstructure of Ti-25Al-10Nb-3V-1Mo Beta Forged and Fully Heat Treated



.5hr Stabilization/8hr Age
Cycles

Figure 19. Stabilization and Age Study Strength Results, Smooth Tensile Specimen Data for Ti-25Al-10Nb-3V-1Mo

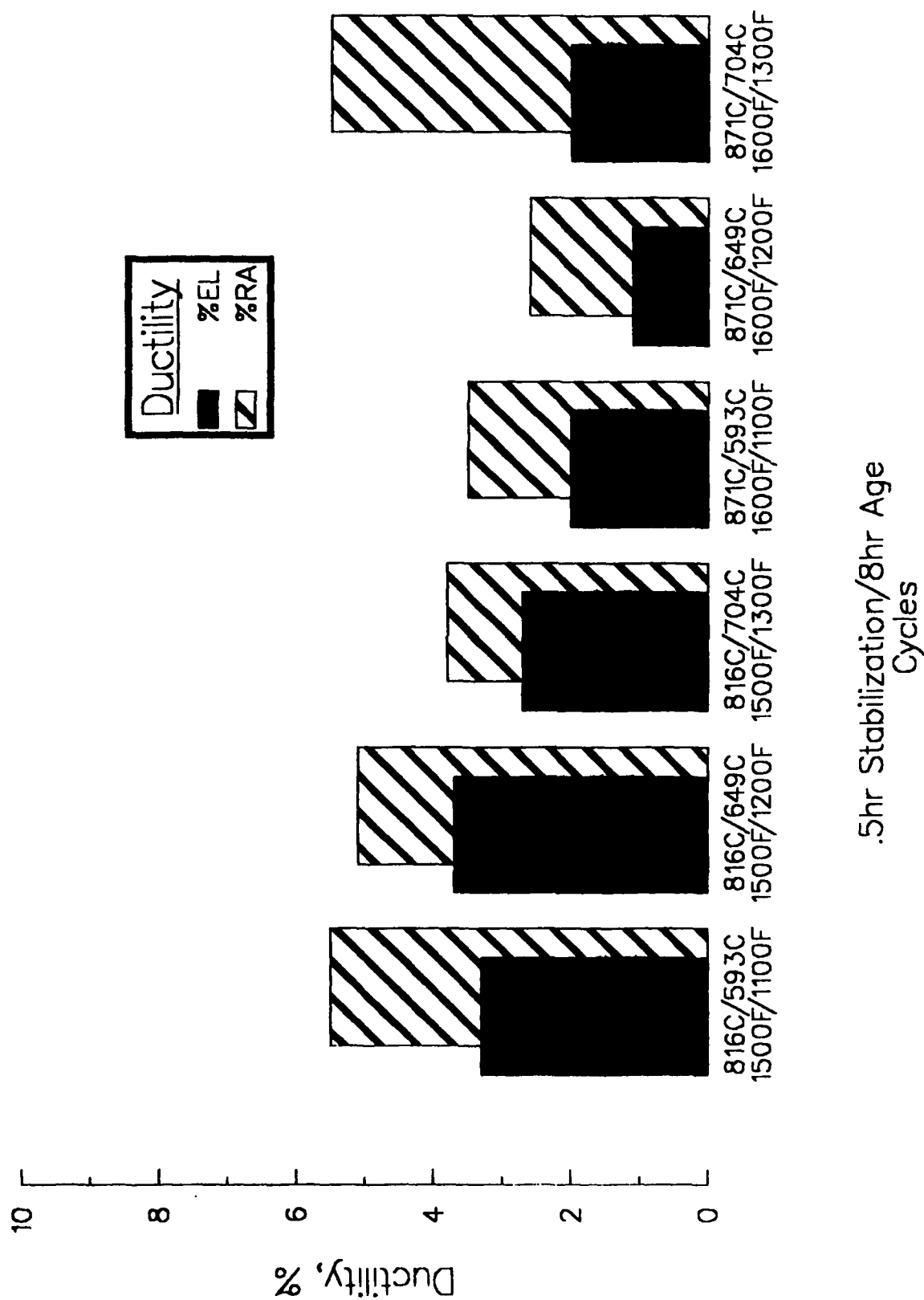
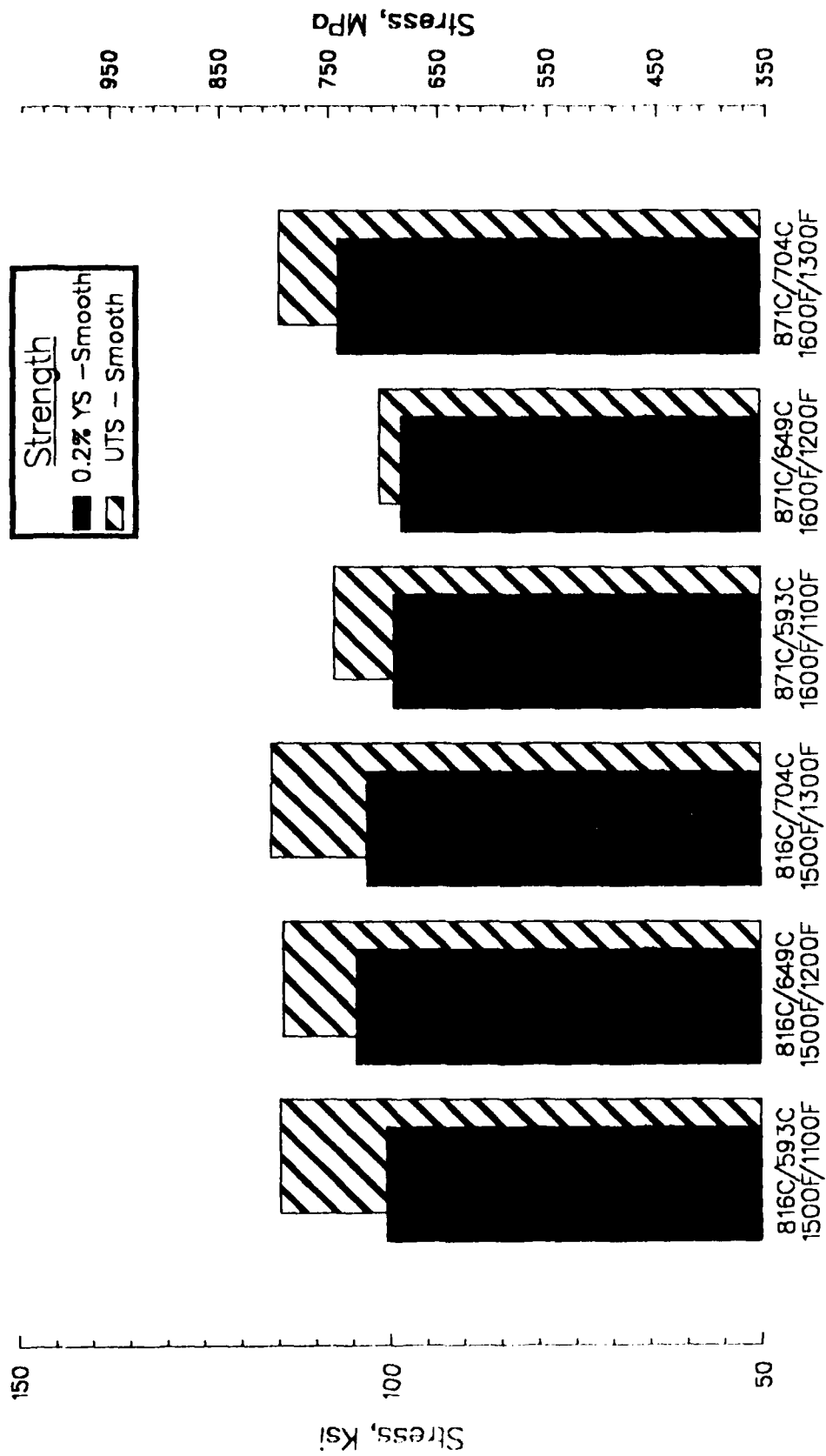


Figure 20. Stabilization and Age Study Ductility Results, Smooth Tensile Specimen Data for Ti-25Al-10Nb-3V-1Mo



.5hr Stabilization/8hr Age
Cycles

Figure 21. Stabilization and Age Study Strength Results, Post-Creep — Smooth Tensile Specimen Data for Ti-25Al-10Nb-3V-1Mo

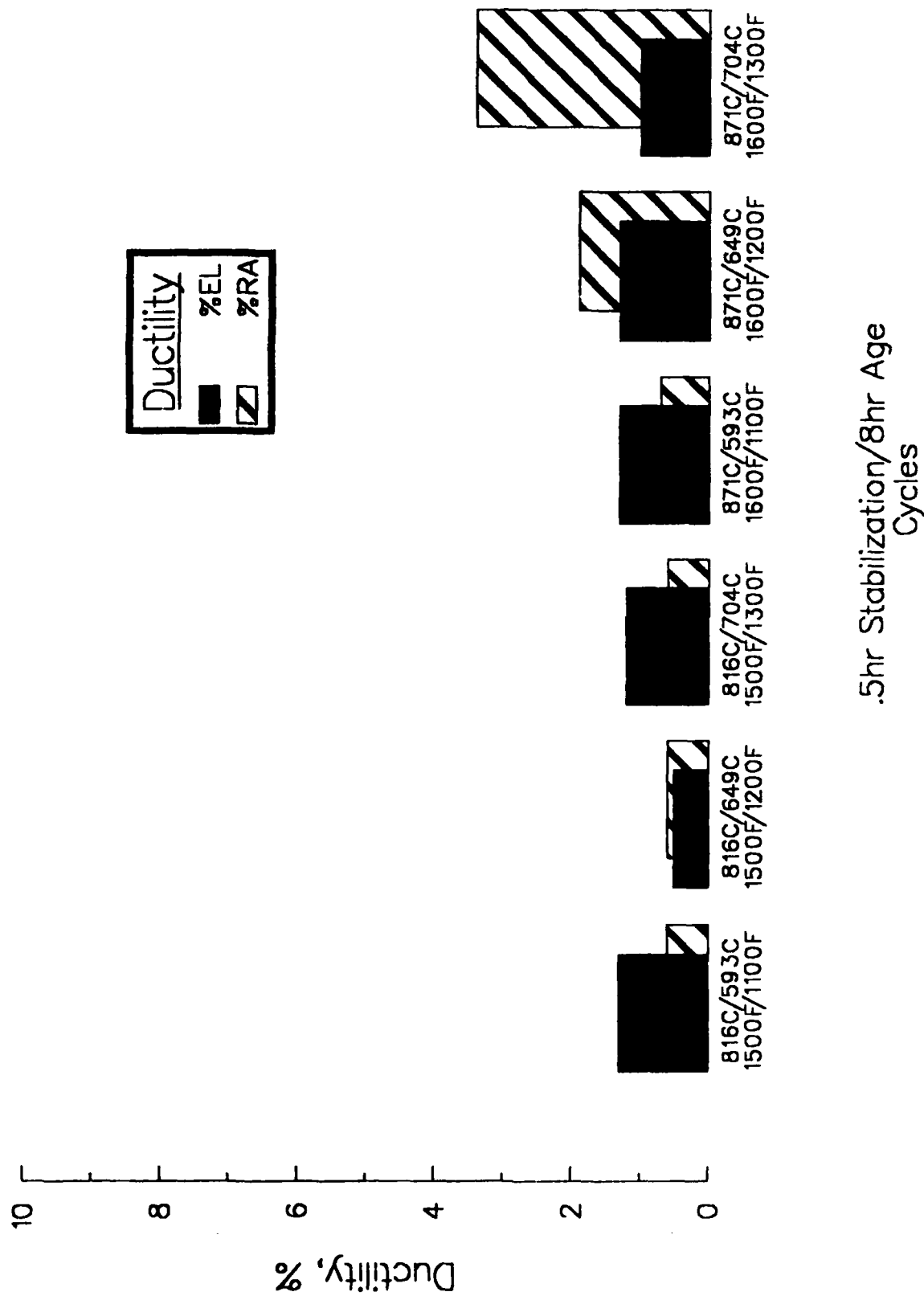


Figure 22. Stabilization and Age Study Ductility Results, Post-Creep — Smooth Tensile Specimen Data for Ti-25Al-10Nb-3V-1Mo

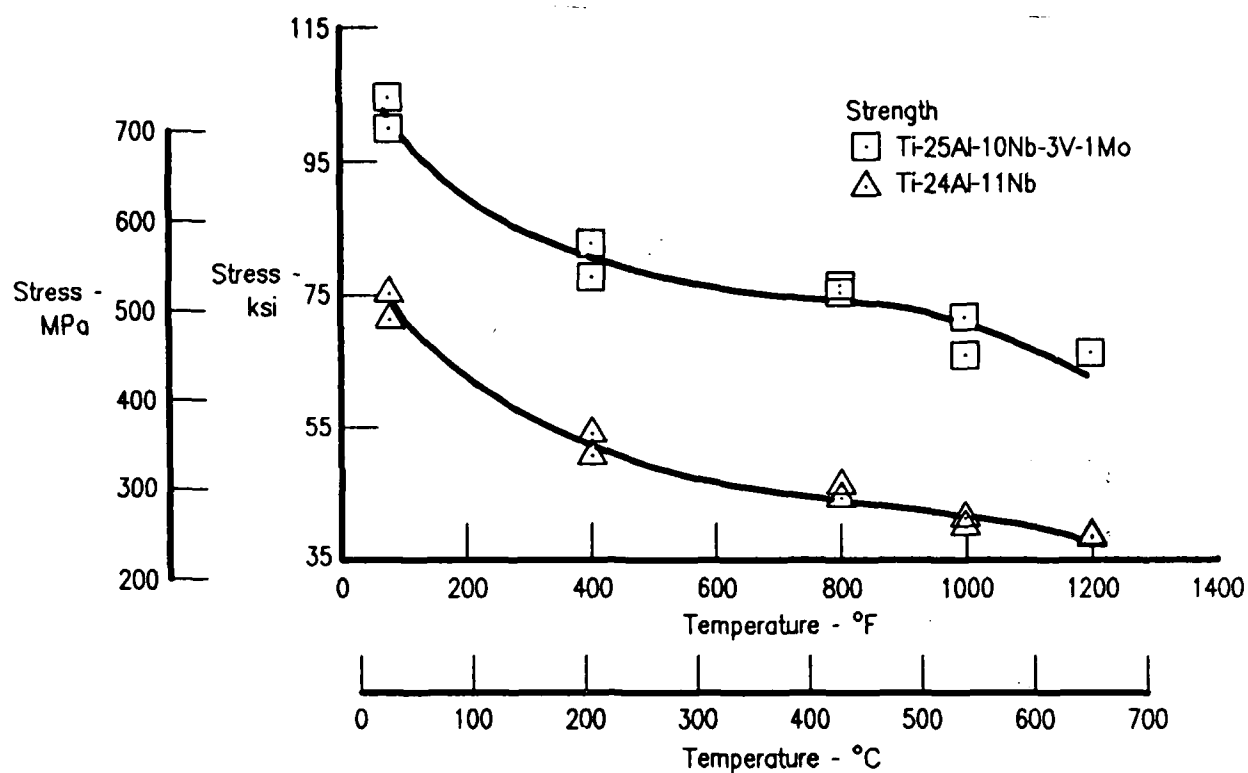


Figure 23. 0.2 Percent Yield Strength Versus Temperature for Ti-25Al-10Nb-3V-1Mo and Ti-24Al-11Nb

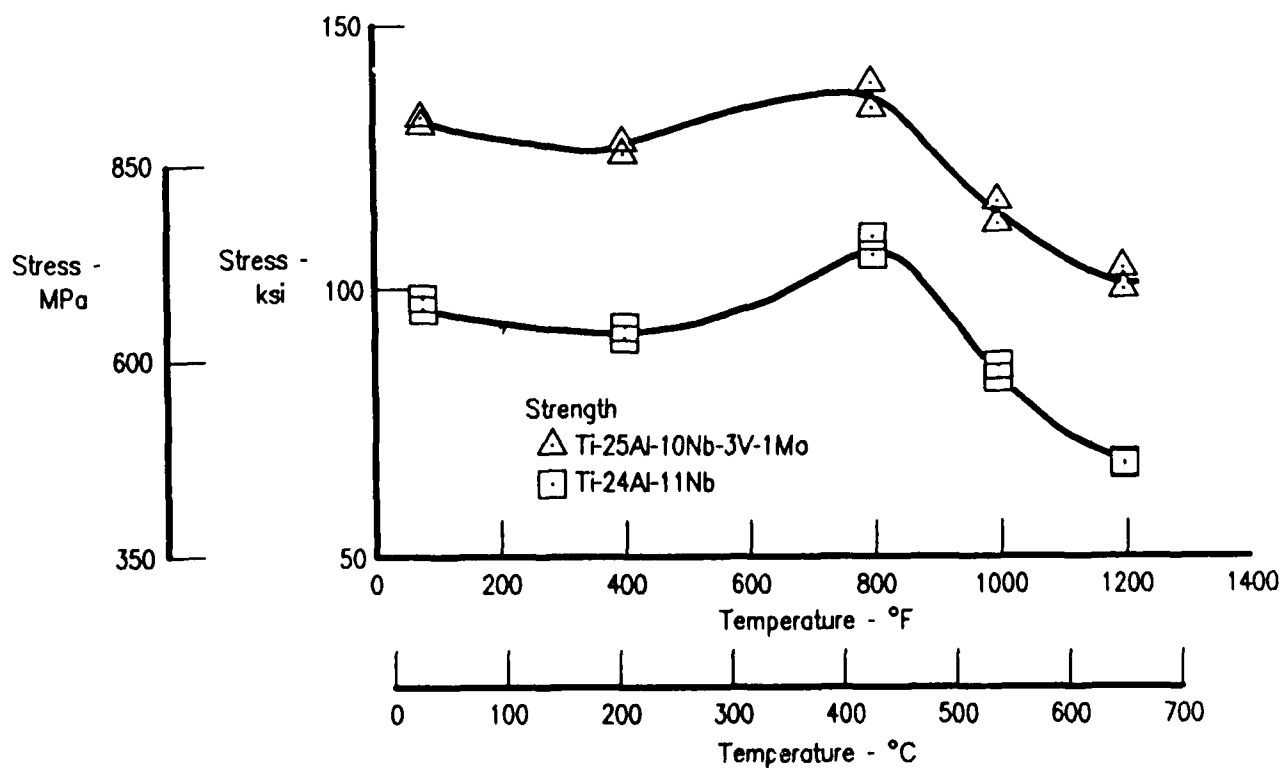


Figure 24. Ultimate Tensile Strength Versus Temperature for Ti-25Al-10Nb-3V-1Mo and Ti-24Al-11Nb

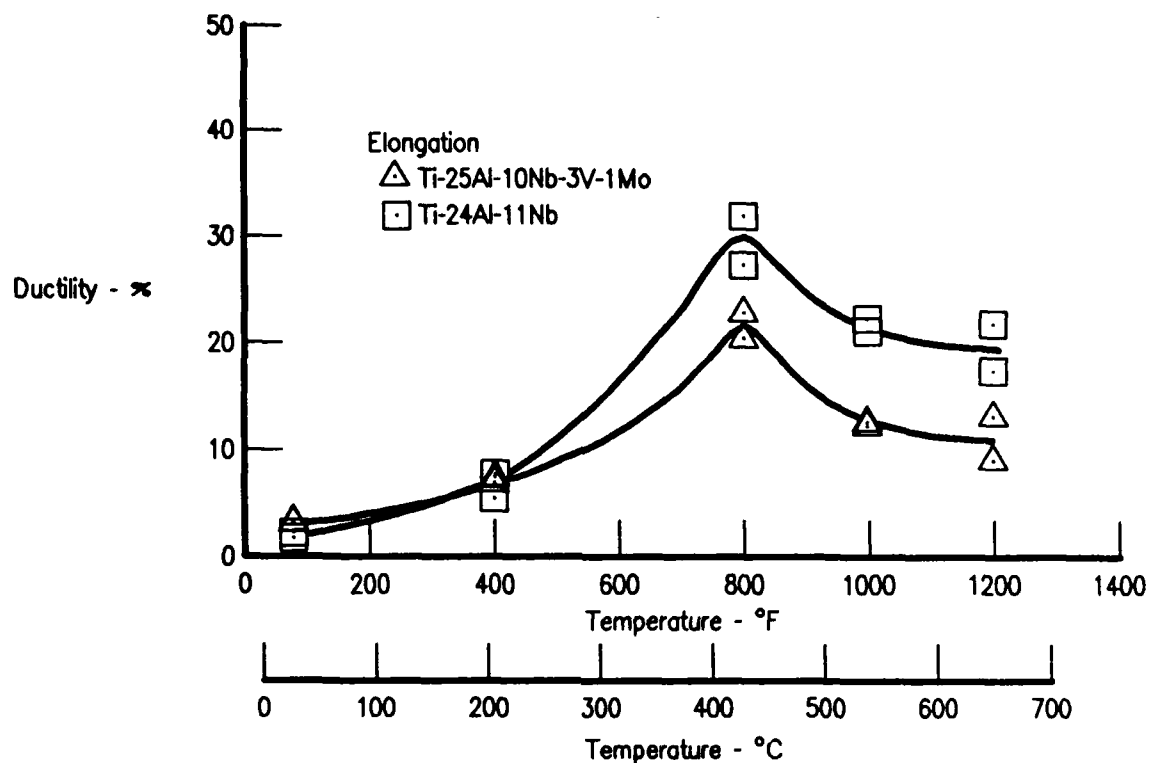


Figure 25. Elongation Versus Temperature for Ti-25Al-10Nb-3V-1Mo and Ti-24Al-11Nb

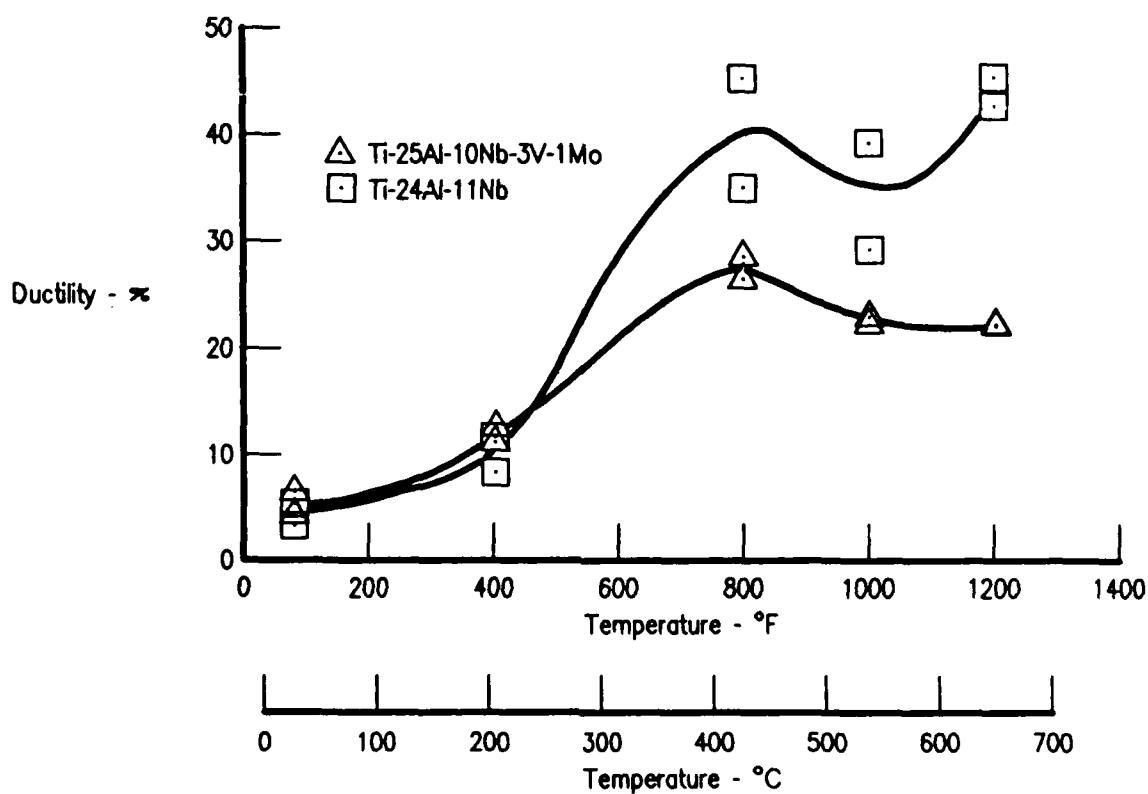


Figure 26. Reduction of Area Versus Temperature for Ti-25Al-10Nb-3V-1Mo and Ti-24Al-11Nb

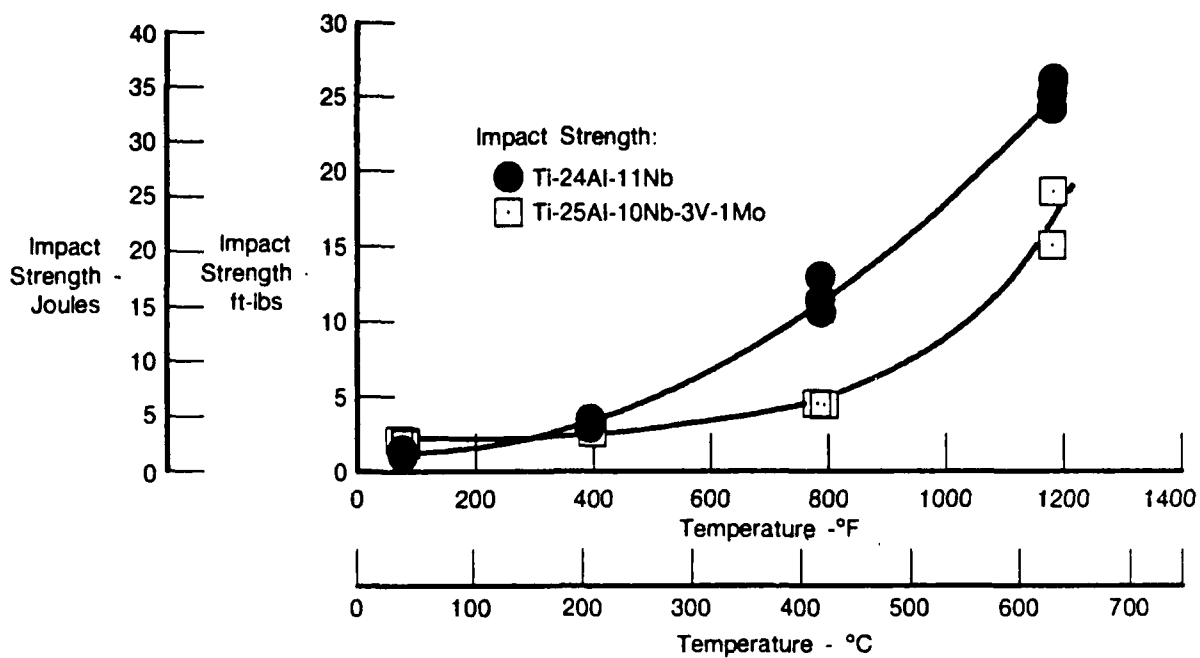


Figure 27. Impact Strength Versus Temperature

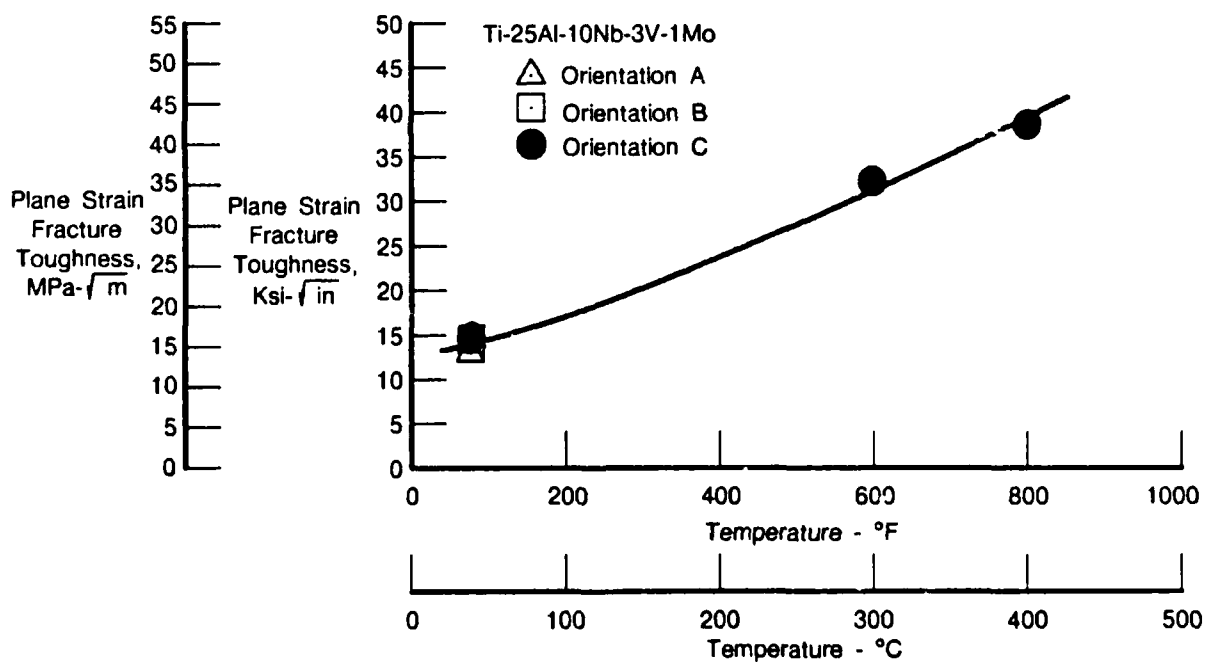
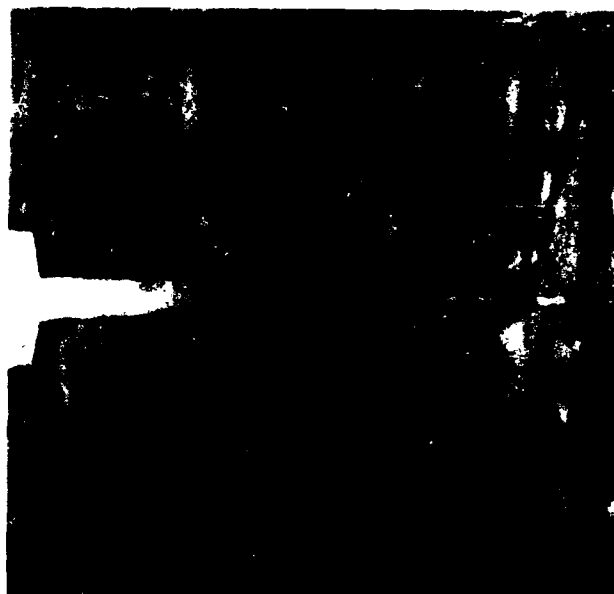


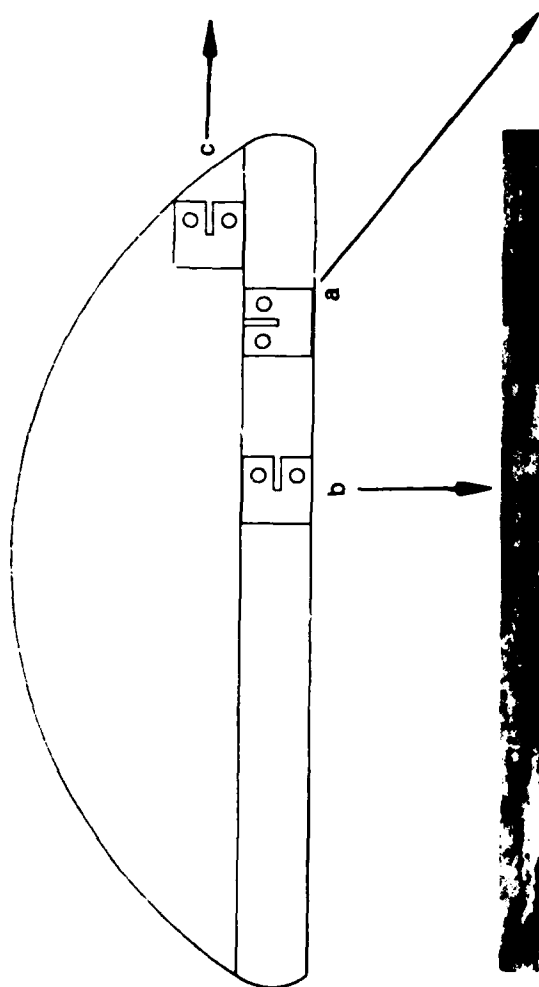
Figure 28. Fracture Toughness for Ti-25Al-10Nb-3V-1Mo, Candidate 4



Mag: 1.5X



Mag: 3.5X



Mag: 3.5X

Figure 29. Specimen Orientations With Respect to Pancake Geometry/Crack Propagation Relationships for Ti-25Al-10Nb-3V-1Mo

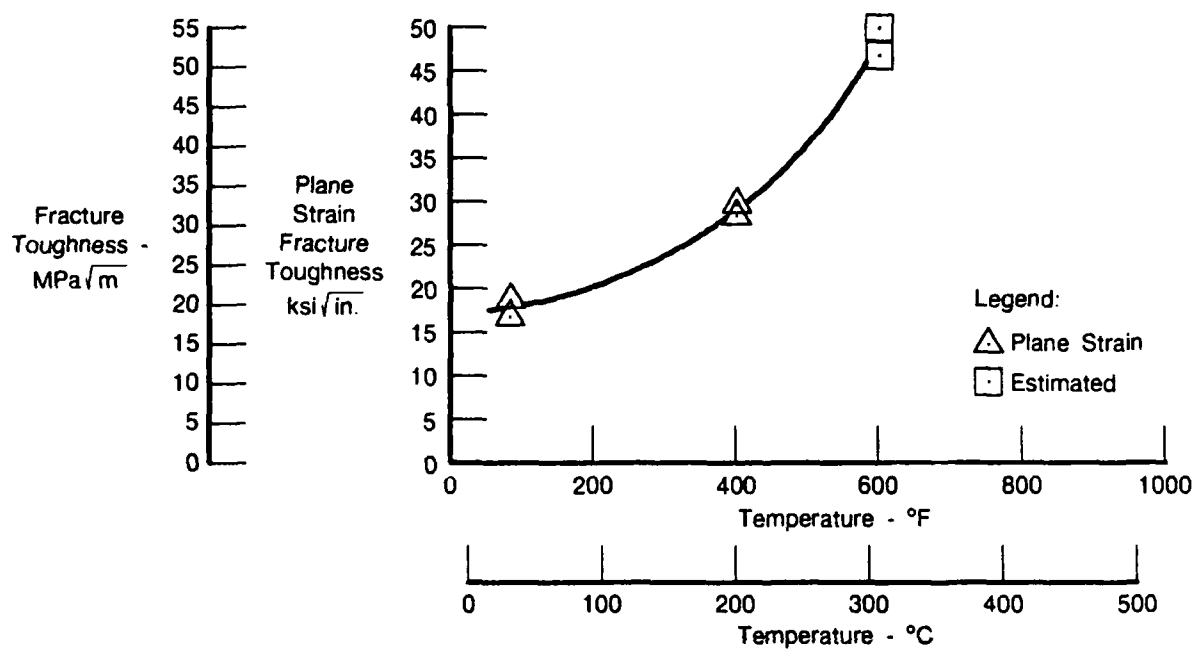


Figure 30. Ti-24Al-11Nb Fracture Toughness Screening Test Results

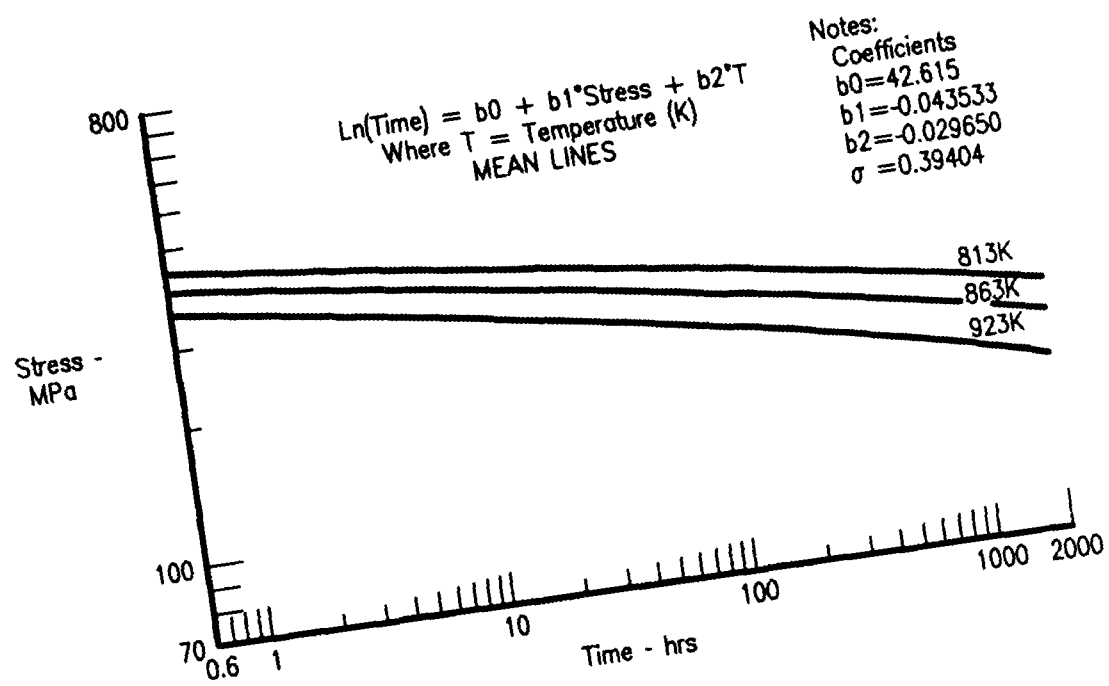


Figure 31. Ti-24Al-11Nb Rupture Model

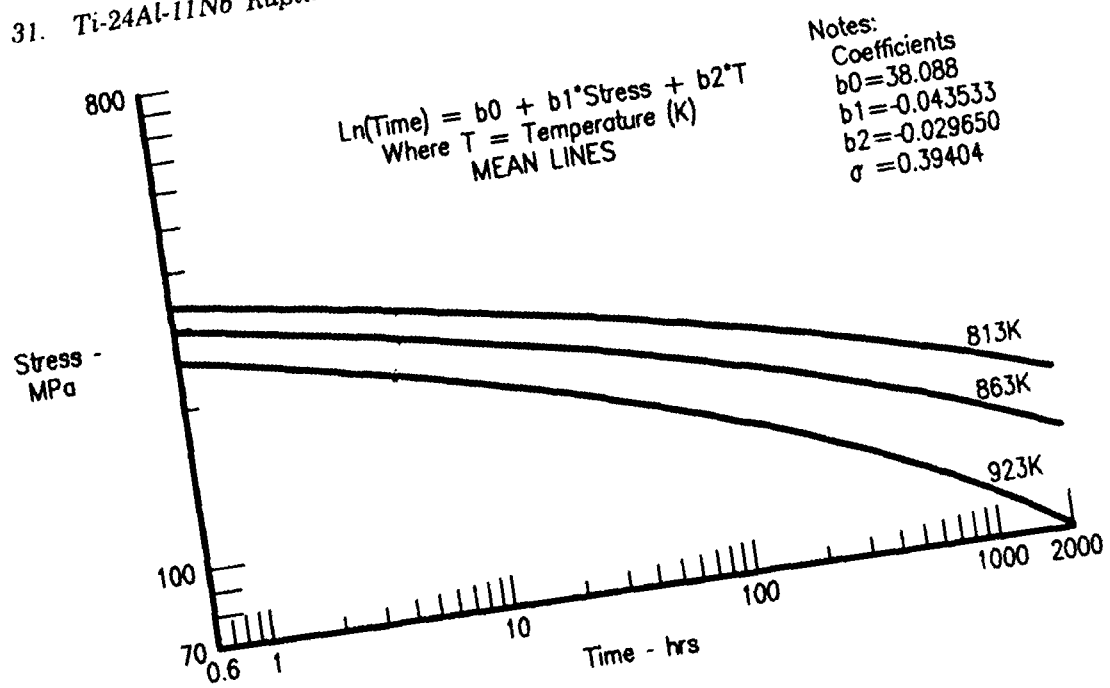


Figure 32. Ti-24Al-11Nb 0.5 Percent Creep Model

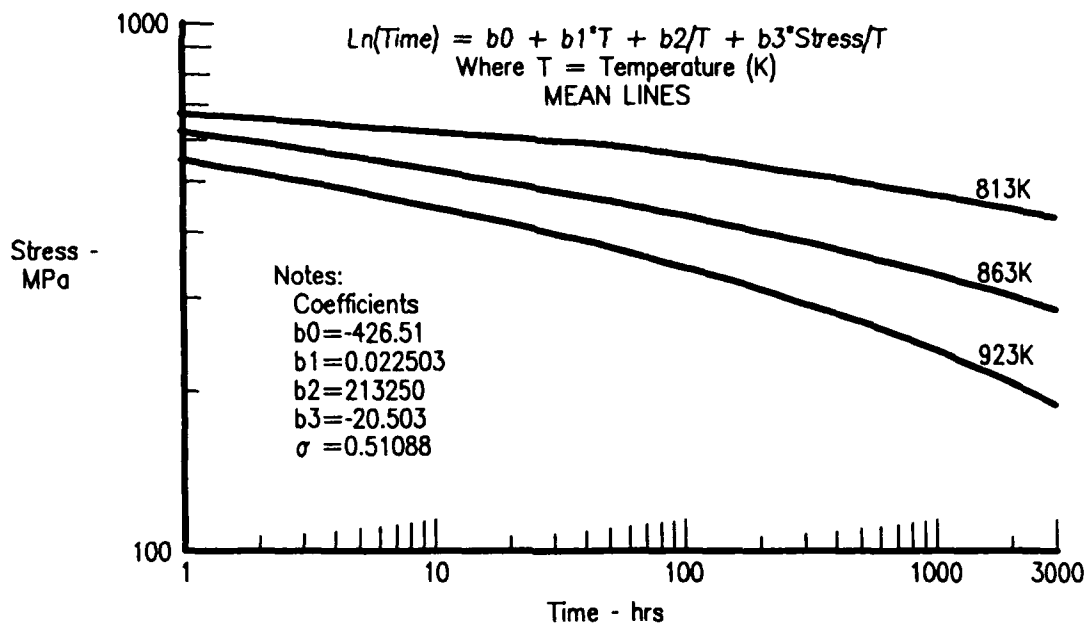


Figure 33. Ti-25Al-10Nb-3V-1Mo Rupture Model

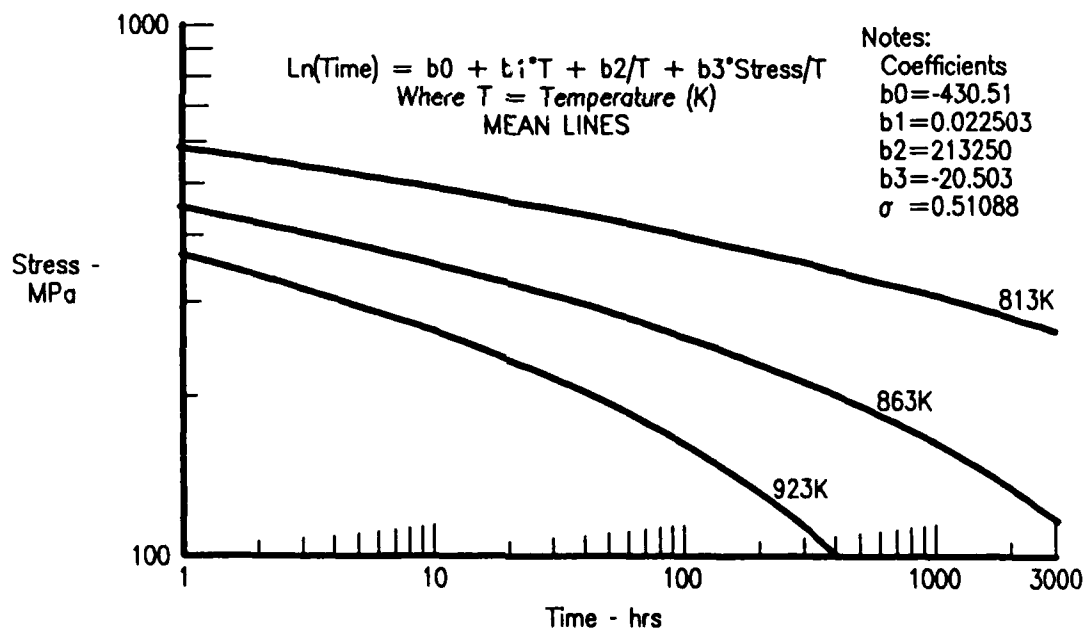


Figure 34. Ti-25Al-10Nb-3V-1Mo 0.5 Percent Creep Model

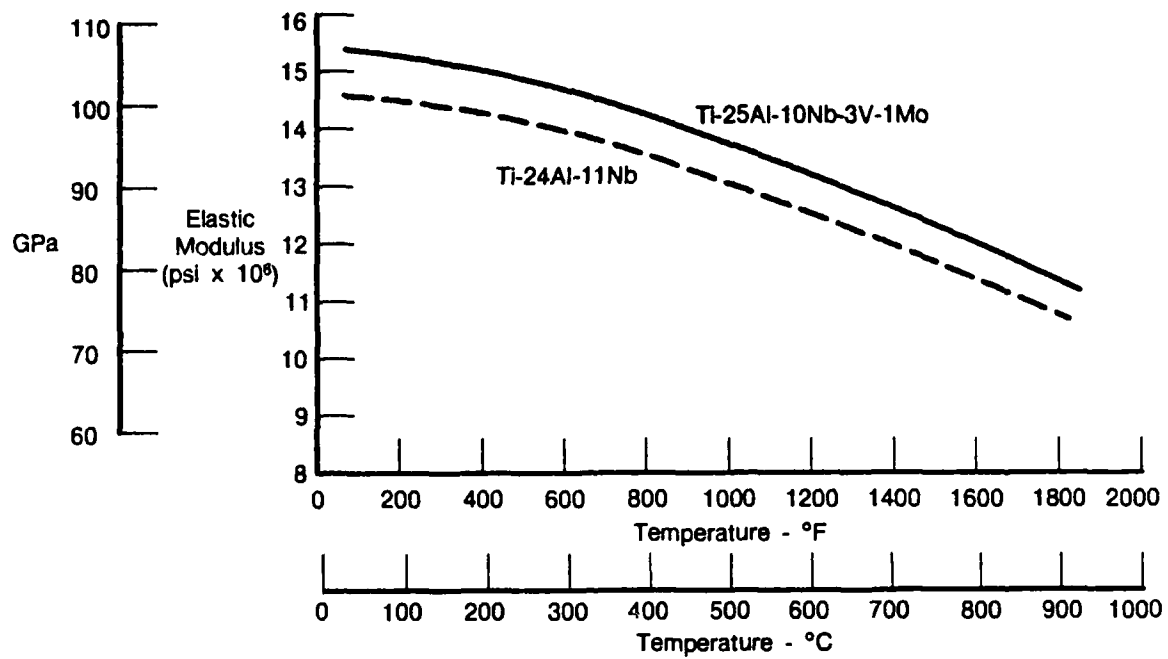


Figure 35. Dynamic Modulus Versus Temperature



Candidate 4
Beta Forged
No Beta Anneal



Candidate 3
Alpha-2-Beta Forged
Plus Beta Anneal

Figure 36. Ti-25Al-10Nb-3V-1Mo Notched Impact Fractures



10mm

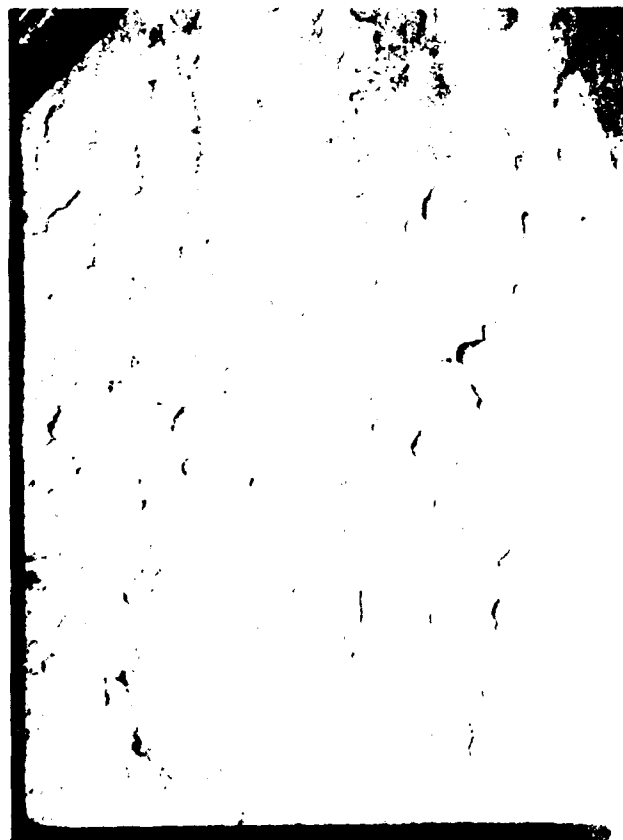


10mm

Fig. 17 Alpha 2/Beta Forged and Beta Annealed Ti-25Al-10Nb-3V-1Mo Equiaxed Prior Beta Grain Structure at 316°C (600°F) Showing Predominantly Transgranular Cleavage (Left) and at 650°C (1200°F), Mixed Inter/Transgranular Fracture (Right) From Toughness Specimens



1mm



1mm

Figure 38. Macro Views From 204°C (400°F) Left, and 316°C (600°F) Right, of Ti-24Al-11Nb Fracture Toughness Tests. Note Loose Flakes on Surfaces

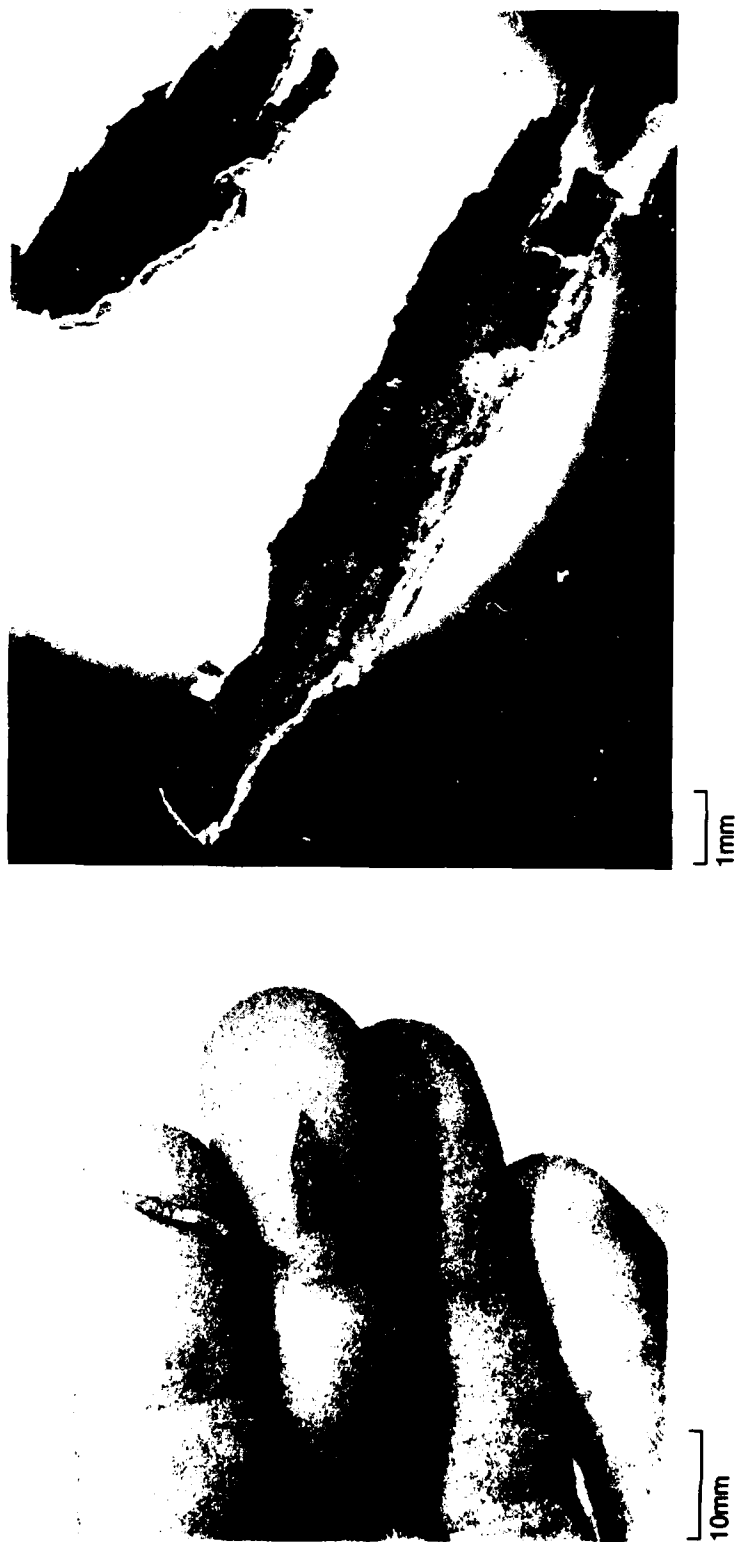


Figure 39. Groups of Prior Beta Grains can be Lifted (or Drop) From Fracture Surfaces of Ti-24Al-11Nb and Ti-25Al-10Nb-3V-1Mo. This is Typical of Monotonic and Cyclic Fractures.



1mm



1mm

Figure 40. Ti-24Al-11Nb Fracture Toughness Specimens From Left to Right 316°C (600°F) and 427°C (800°F) Tests. Deep Furrowing is Visible (Left)

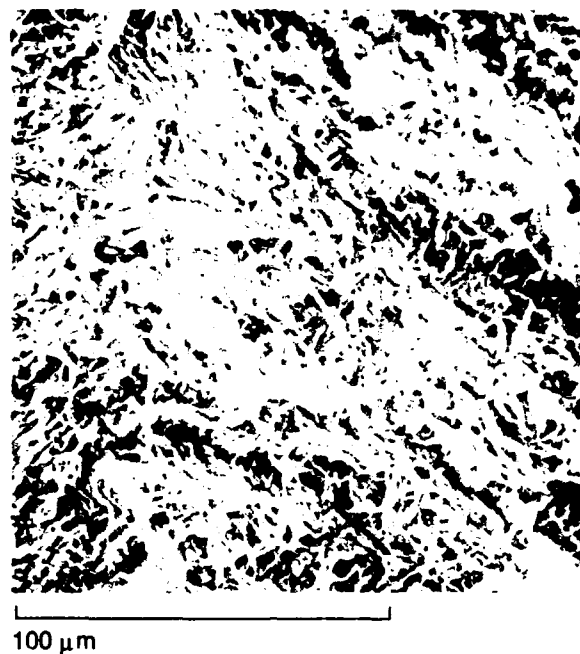


Figure 41. Room Temperature Fracture Toughness Surface From Ti-24Al-11Nb

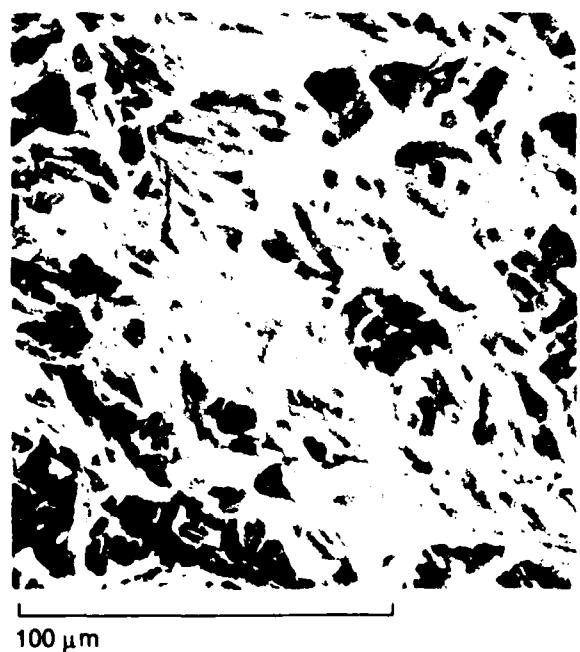


Figure 42. Intermediate and High Magnification Views of Fracture Surface From Ti-24Al-11Nb at Room Temperature. Note Ductile Tearing Surrounding Quasi-Cleavage Areas

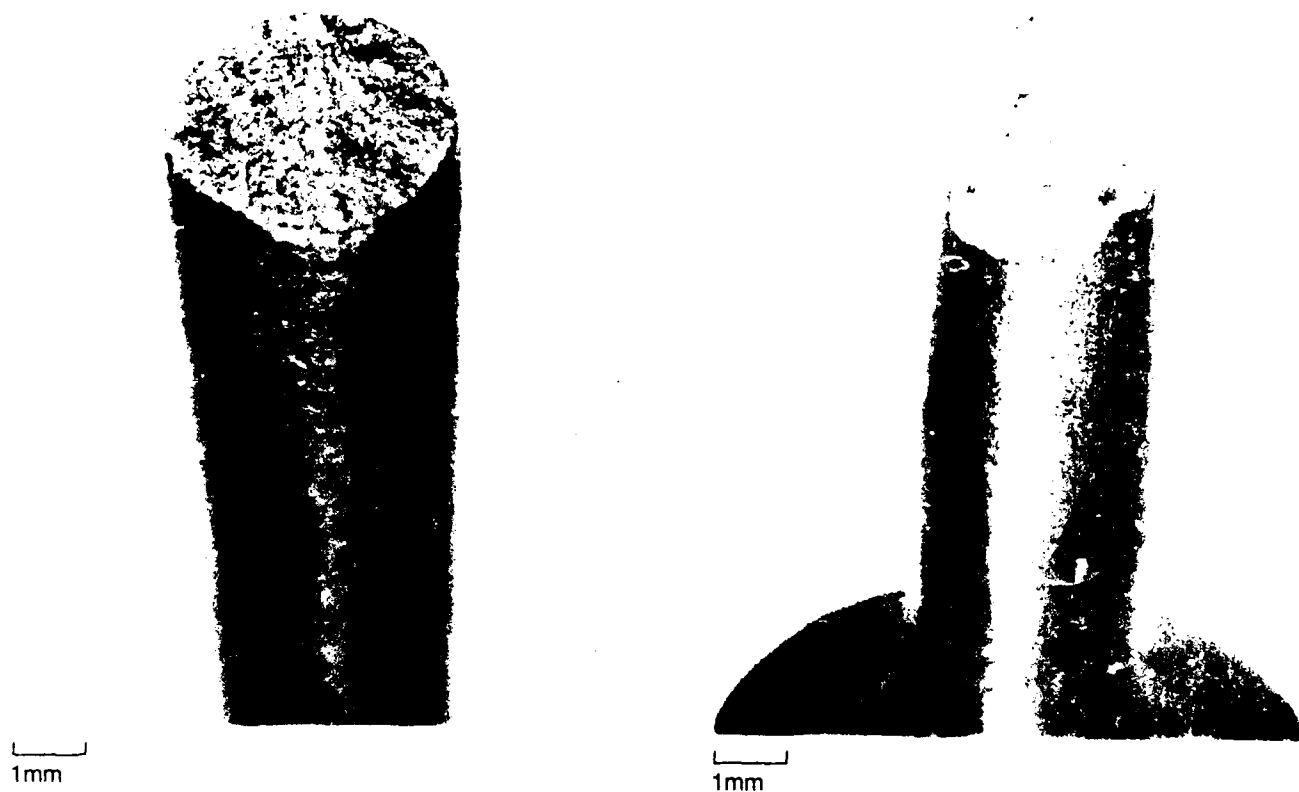


Figure 43. Ti-24Al-11Nb Tensile Fractures Exhibiting a Transition in Fracture Mode From 204°C (400°F) on Left and 427°C (800°F) on Right. Secondary Cracking is Present Along Gage Section on Right. There is None on Left

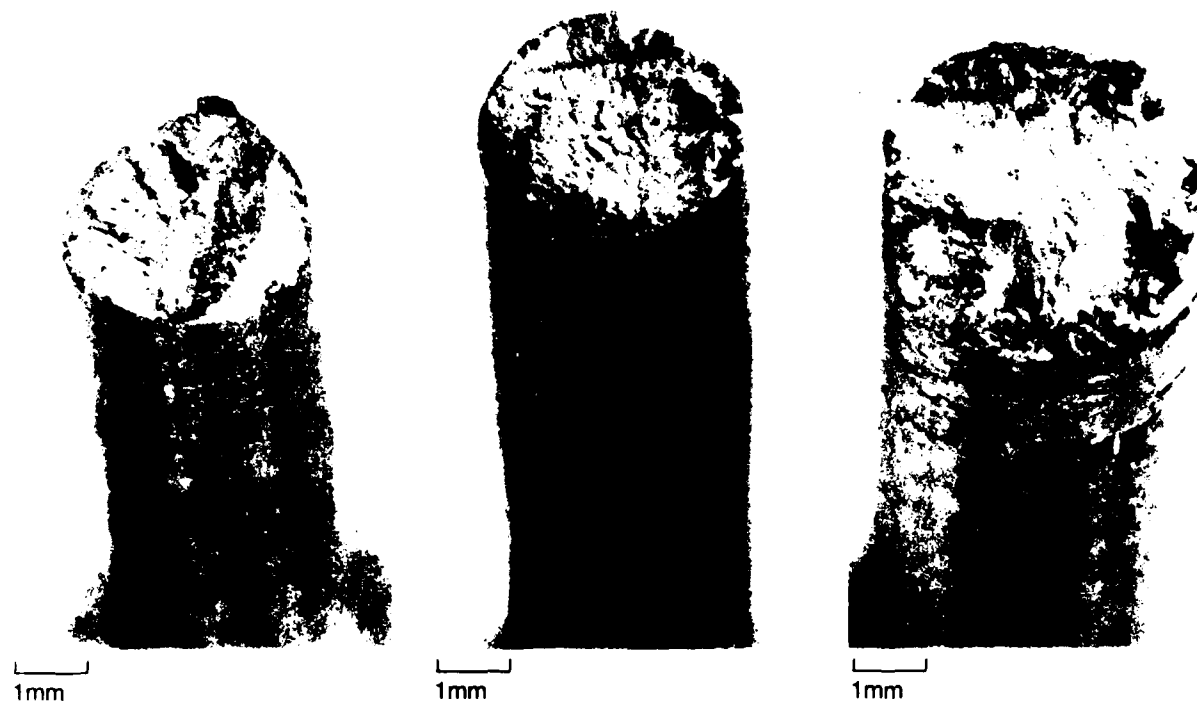


Figure 44. Tensile Fractures at (From Left) 204°, 427°, and 650°C (400°, 800°, and 1200°F). Note Extensive Cracking Along Gage Section of Ti-25Al-10Nb-3V-1Mo

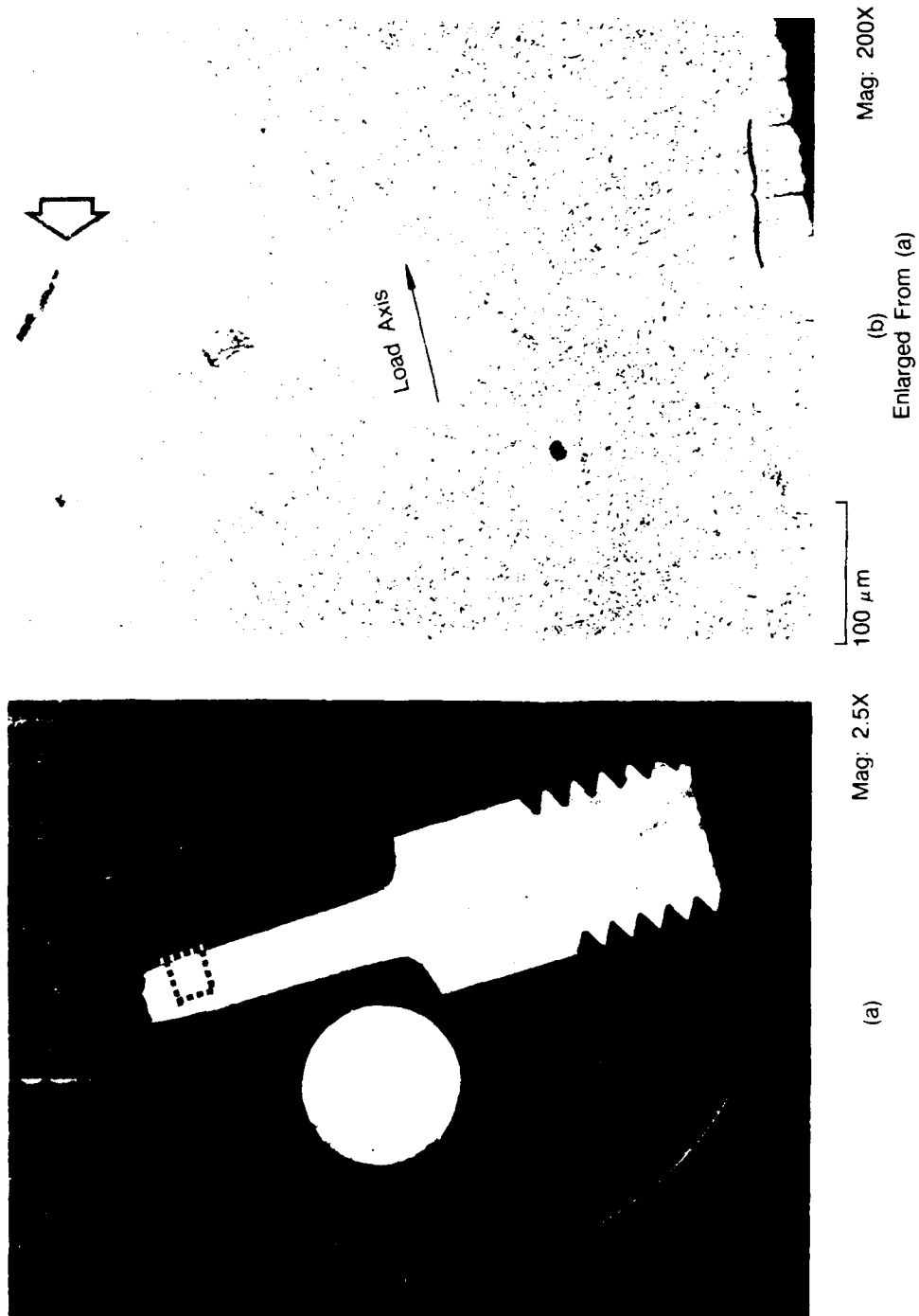


Figure 45. Beta Forged Ti-25Al-10Nb-3V-1Mo With 816°C/593°C (1500°F/1100°F) Stabilization/Age Cycle. Failed 650°C (1200°F) Tensile Specimen. Internal and Secondary Cracks Visible at Left of Photograph (b) (Arrow) and Along Gage Surface (Bracket)

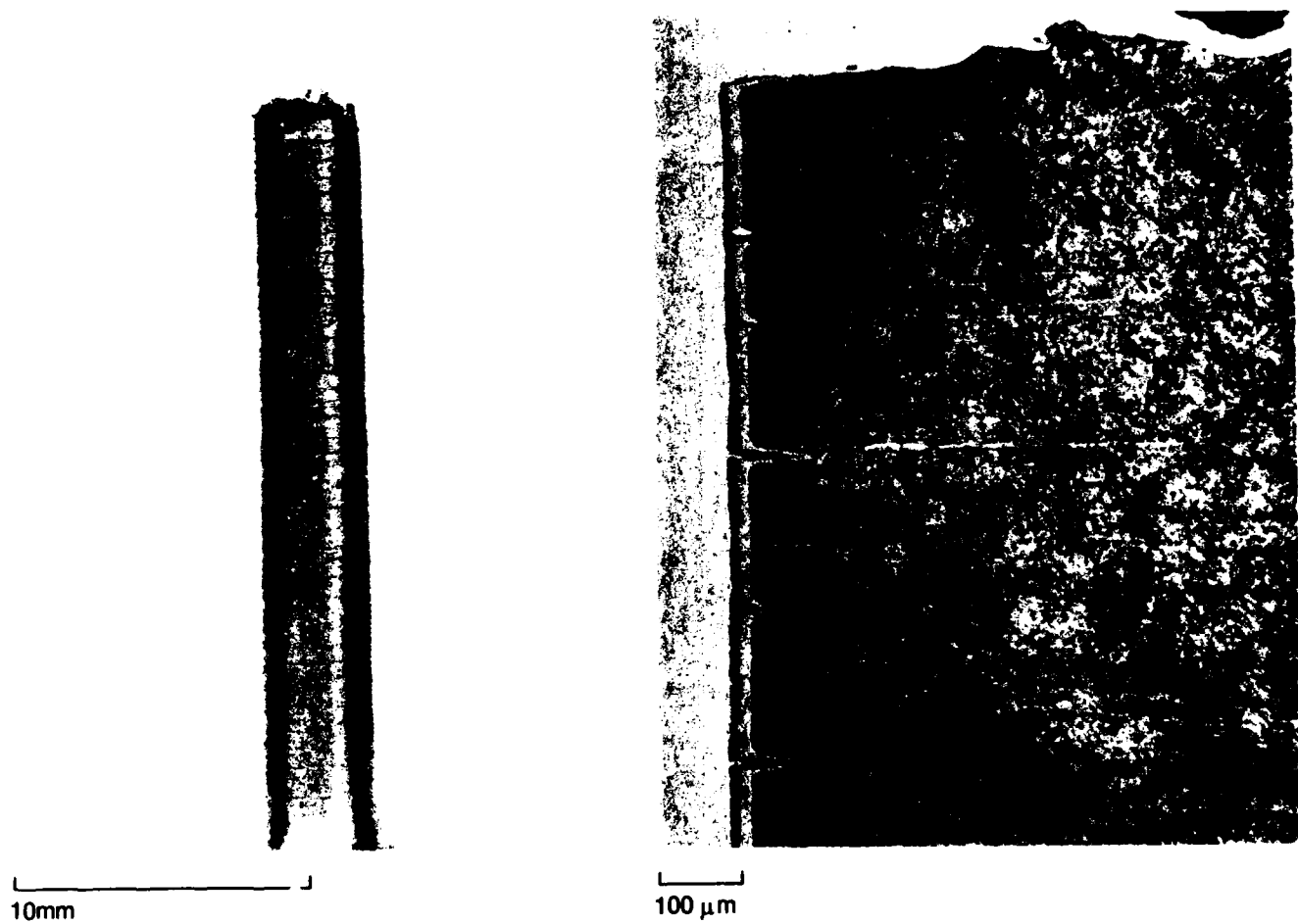


Figure 46. Left, Extensive Secondary Cracking in Ti-24Al-11Nb Creep Test, 230 Hours at 650°C/207 MPa (1200°F/30 ksi). Right, Oxygen Embrittlement in Section Through Ti-25Al-10Nb-3V-1Mo Creep Specimen, 234 Hours at 650°C/310 MPa (1200°F/45 ksi). Ti-24Al-11Nb Sections are Identical to Ti-25Al-10Nb-3V-1Mo

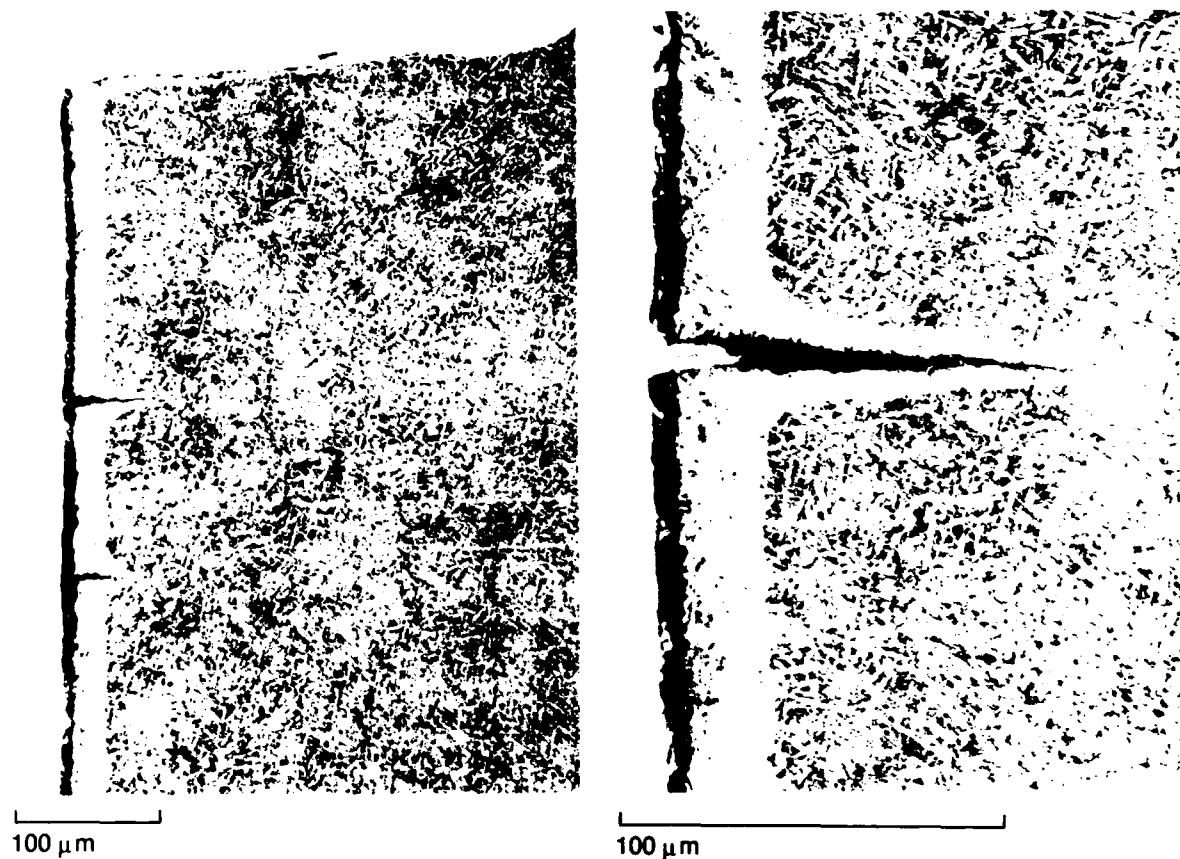
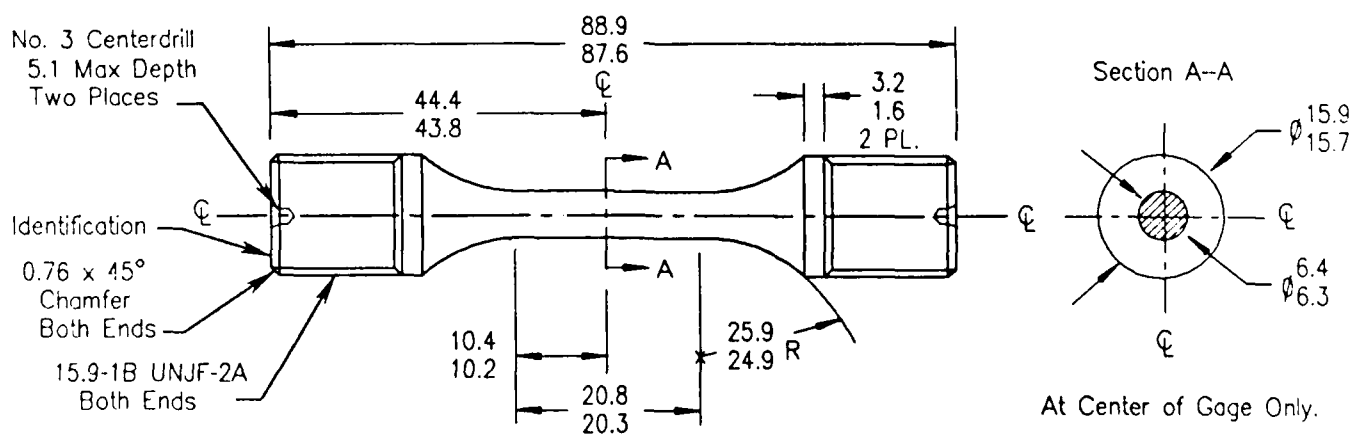


Figure 47. Details of Surface Oxide, Oxygen Embrittlement Layer, and Crack Propagating into Substrate of Ti-25Al-10Nb-3V-1Mo Creep Specimen. Test Conducted at 650°C/310 MPa (1200°F/45 KSI) for 234 Hours



Note: All Dimensions Are in mm.

Figure 48. Smooth LCF Specimen, $K_t = 1.0$

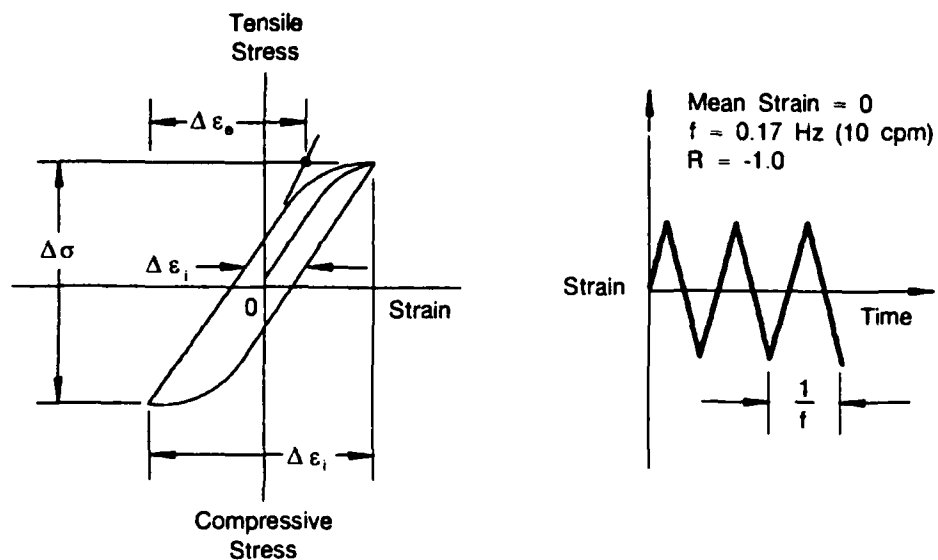


Figure 49. Fully Reversed Strain Cycle, $R_\epsilon = -1.0$

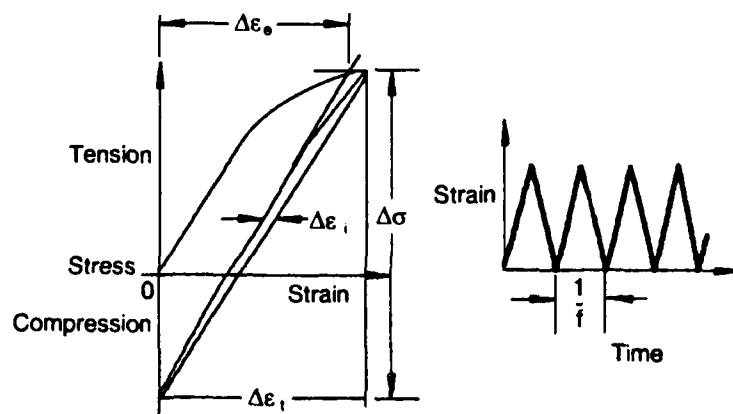


Figure 50. All Tensile Strain Cycle, $R_\epsilon = 0$

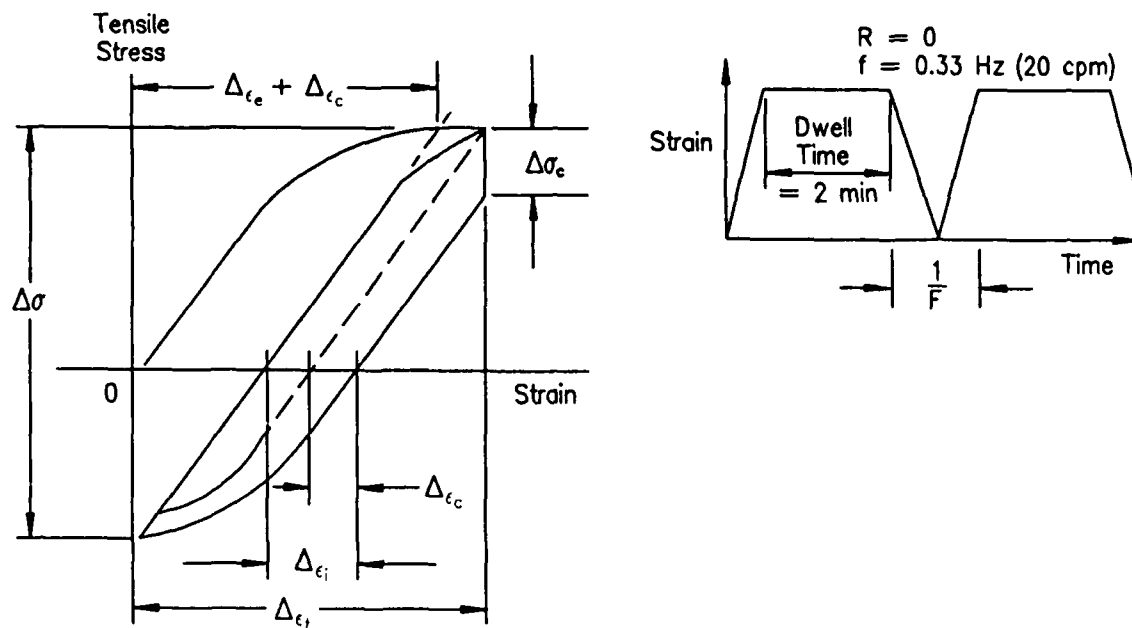
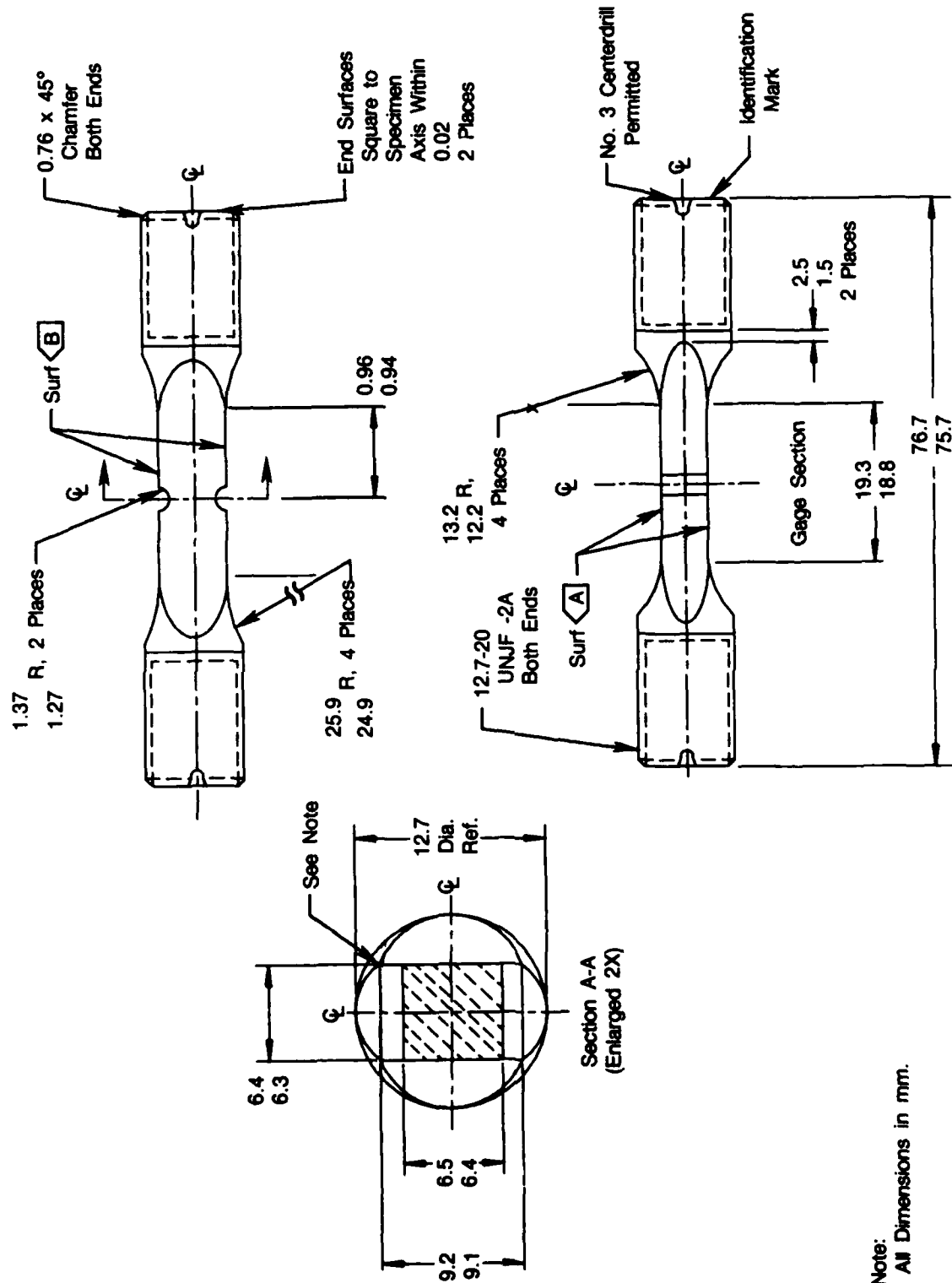


Figure 51. All Tensile Strain Cycle With Peak Strain Dwell



Note:
All Dimensions in mm.

Figure 52. Notched LCF Specimen, $K_t = 2.18$

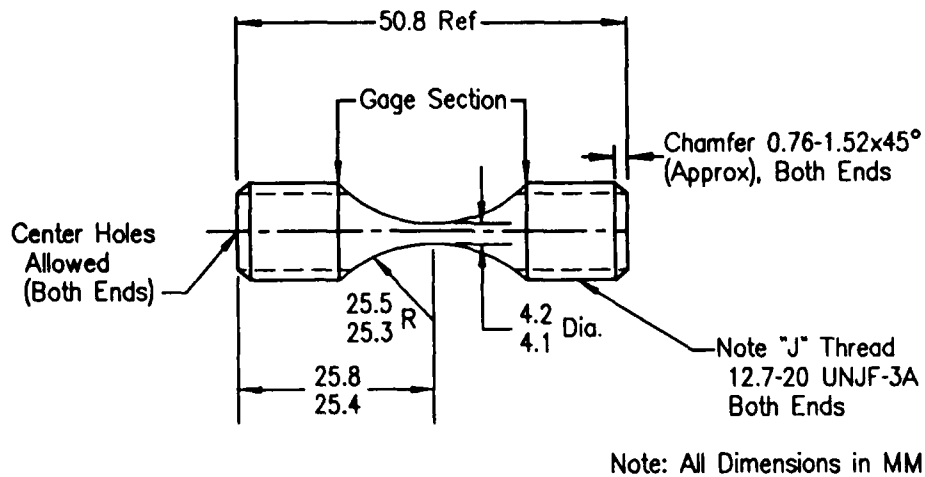


Figure 53. Smooth HCF Specimen, $K_t = 1.0$

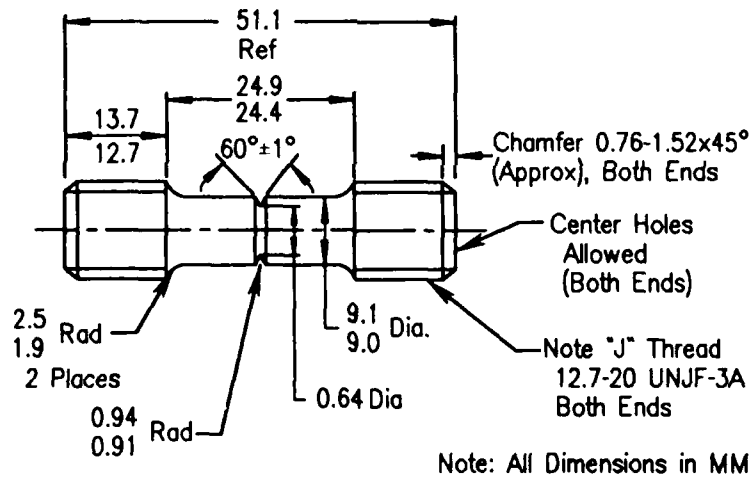


Figure 54. Notched HCF Specimen, $K_t = 2.16$

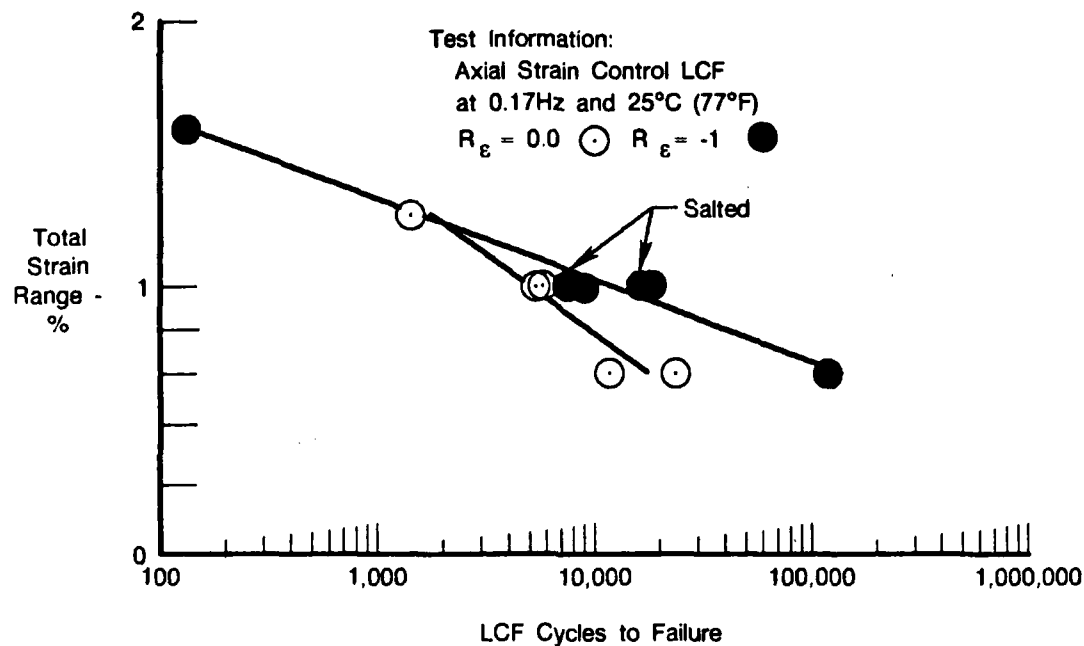


Figure 55. Mean Stress Effects of Smooth LCF on Ti-24Al-11Nb at 25°C (77°F)

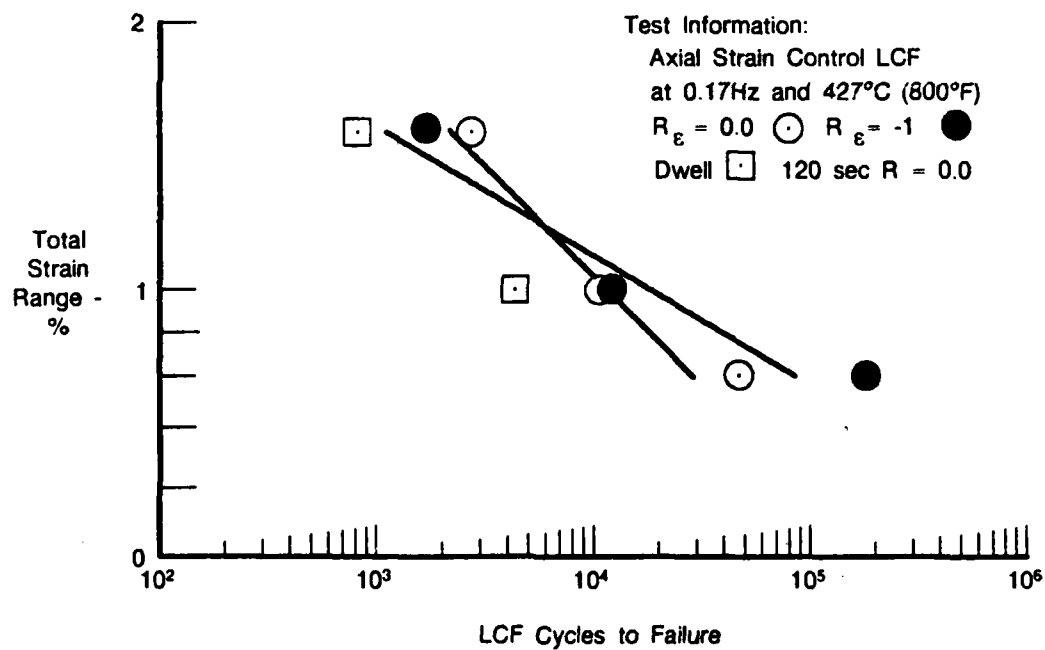


Figure 56. Mean Stress Effects of Smooth LCF on Ti-24Al-11Nb at 427°C (800°F)

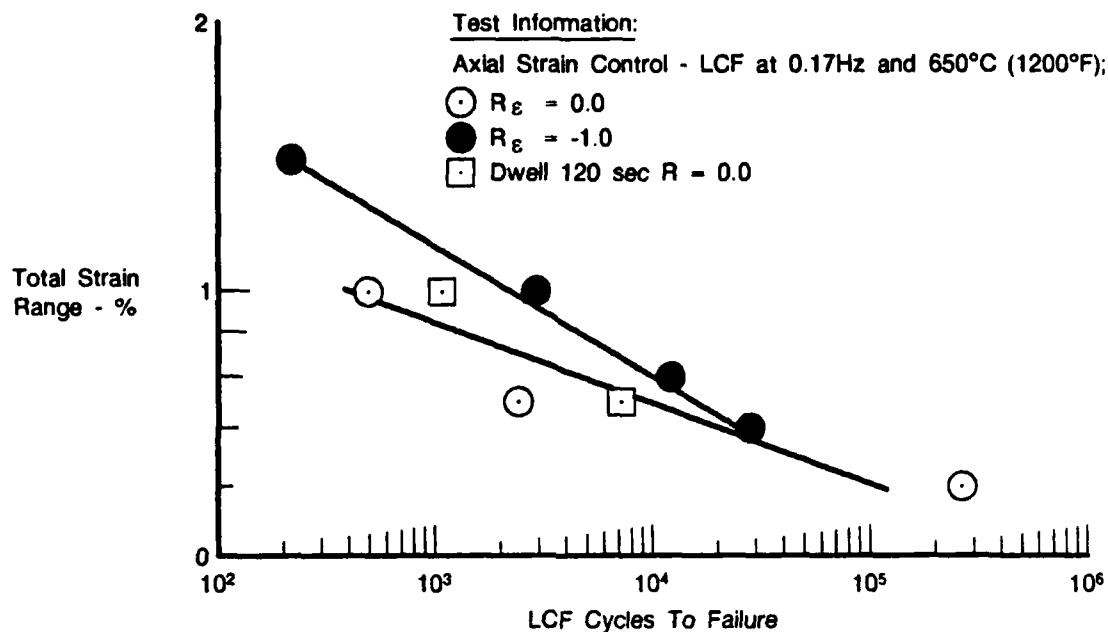


Figure 57. Mean Stress Effects of Smooth LCF on Ti-24Al-11Nb at 650°C (1200°F)

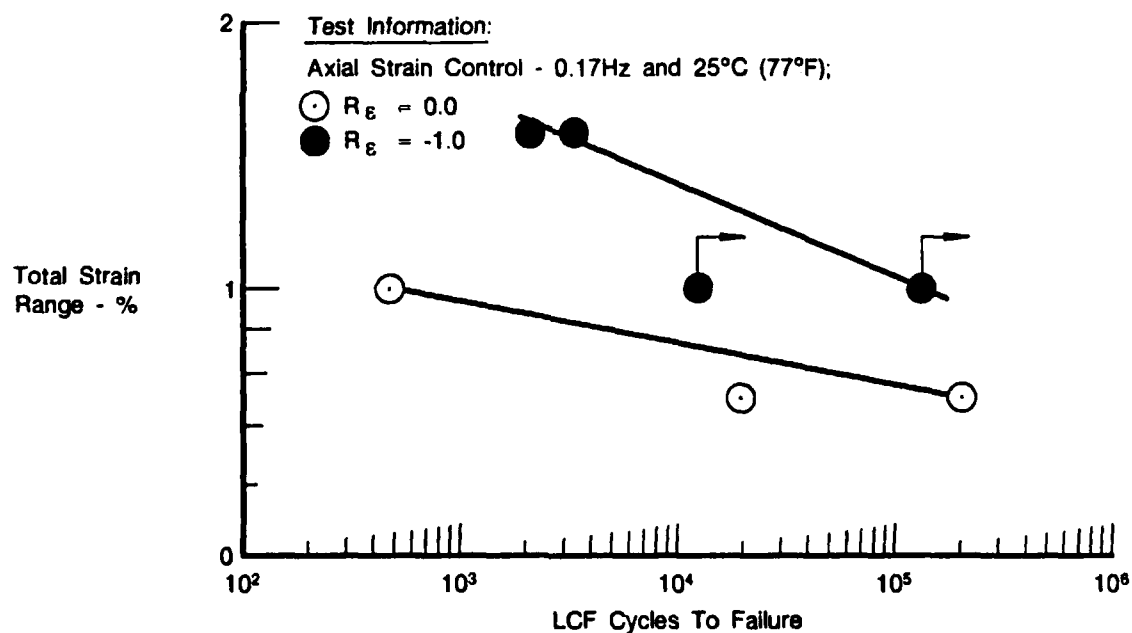


Figure 58. Mean Stress Effects of Smooth LCF on Ti-25Al-10Nb-3V-1Mo at 25°C (77°F)

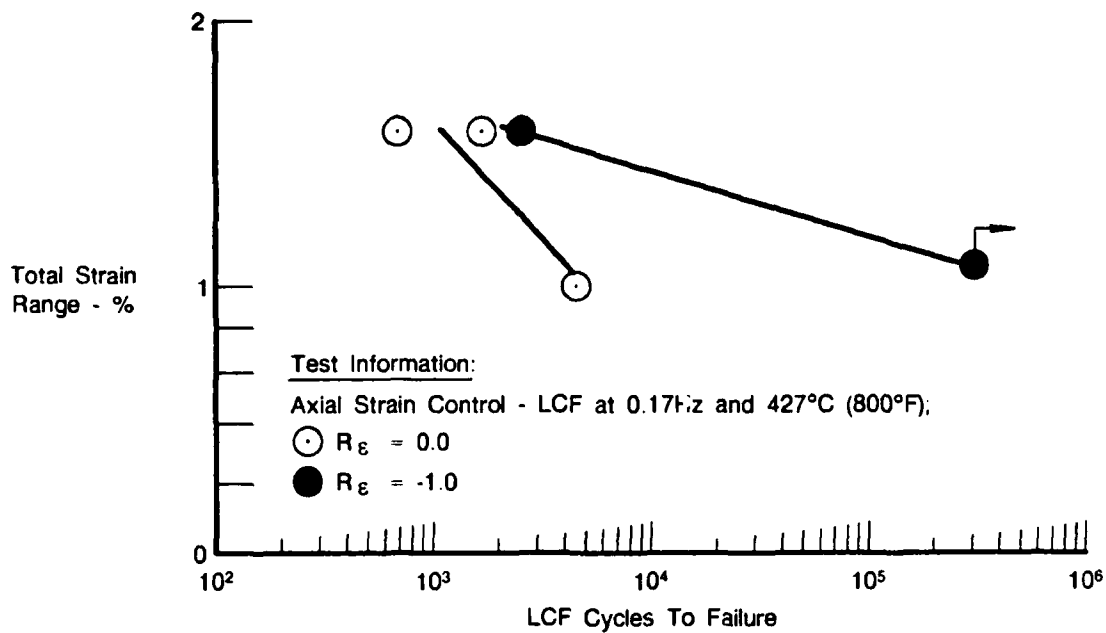


Figure 59. Mean Stress Effects of Smooth LCF on Ti-25Al-10Nb-3V-1Mo at 427°C (800°F)

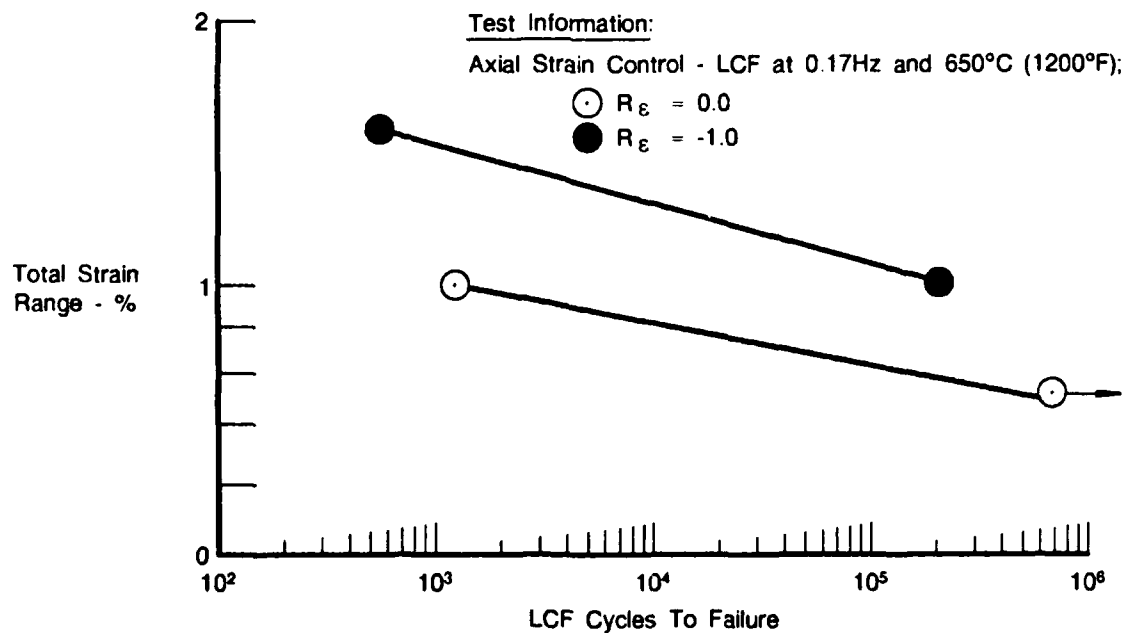


Figure 60. Mean Stress Effects of Smooth LCF on Ti-25Al-10Nb-3V-1Mo at 650°C (1200°F)

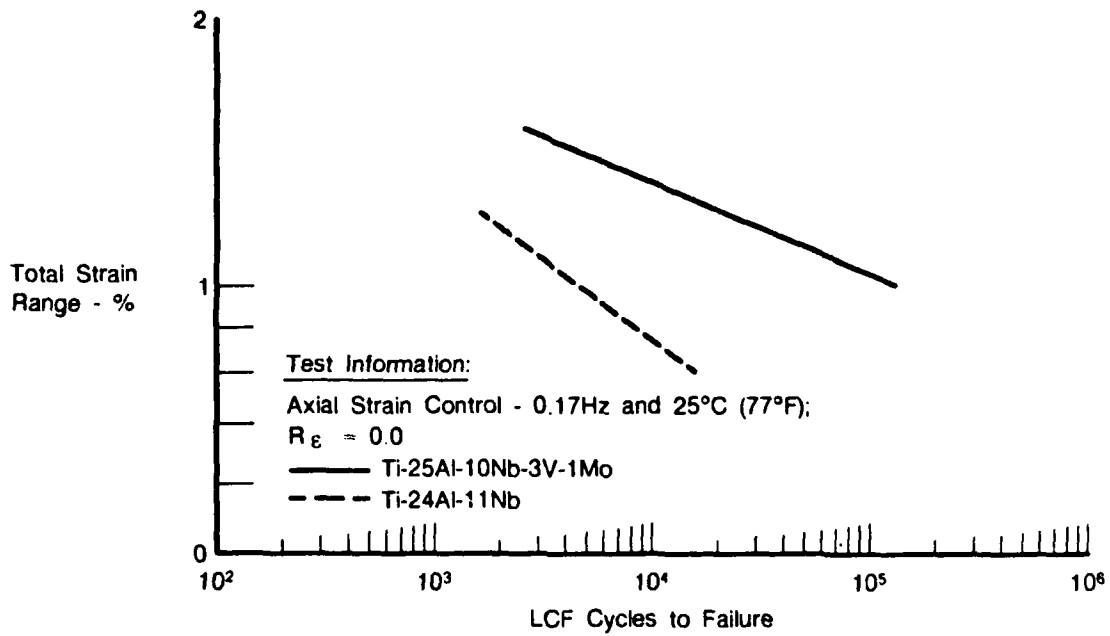


Figure 61. Comparison of Ti-24Al-11Nb Versus Ti-25Al-10Nb-3V-1Mo, Smooth LCF at 25°C (77°F), $R_\epsilon = 0$

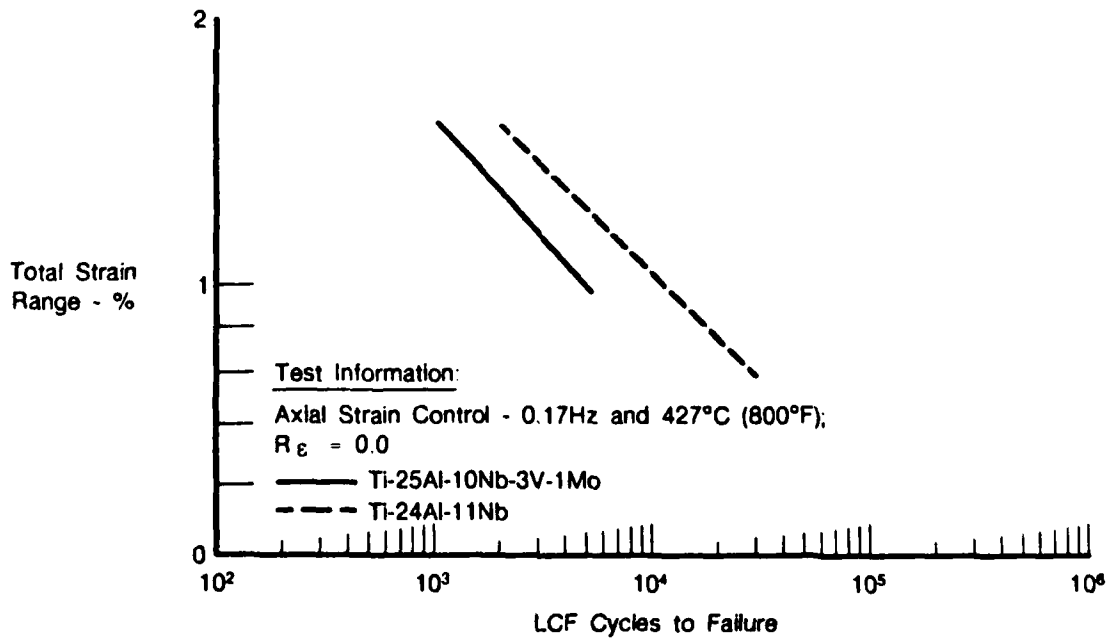


Figure 62. Comparison of Ti-24Al-11Nb Versus Ti-25Al-10Nb-3V-1Mo, Smooth LCF at 427°C (800°F), $R_\epsilon = 0$

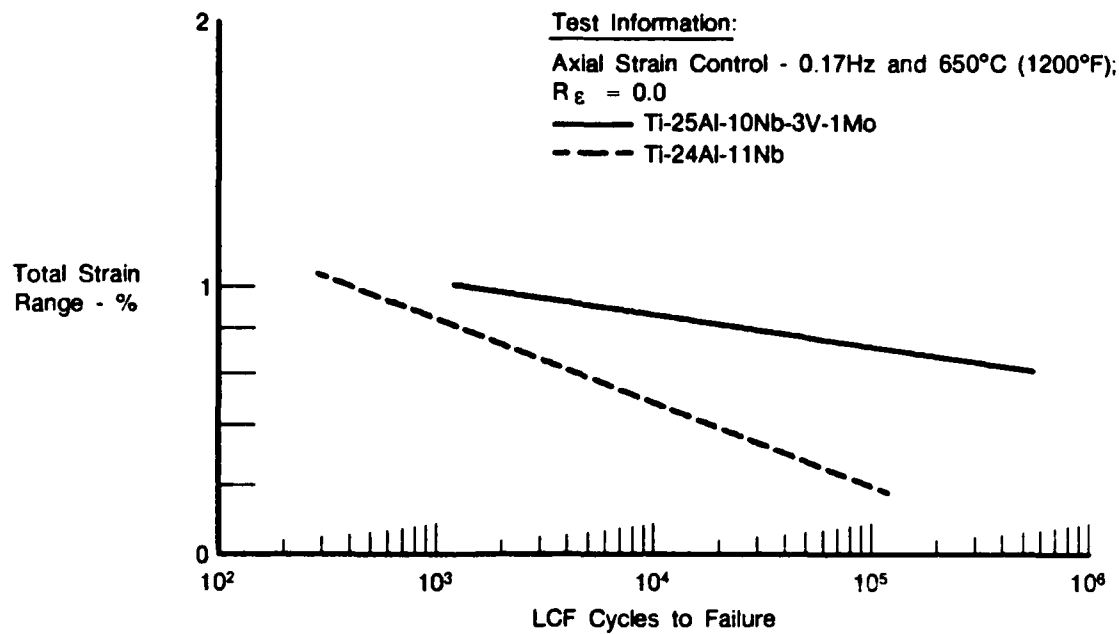


Figure 63. Comparison of Ti-24Al-11Nb Versus Ti-25Al-10Nb-3V-1Mo, Smooth LCF at 650°C (1200°F), $R_\epsilon = 0$

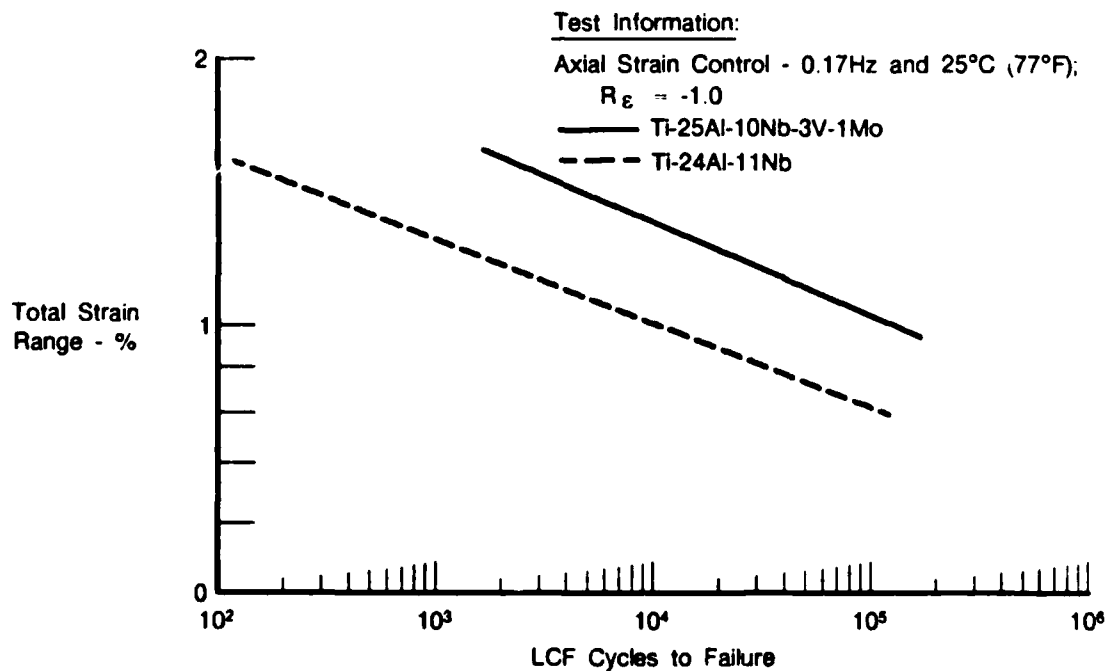


Figure 64. Comparison of Ti-24Al-11Nb Versus Ti-25Al-10Nb-3V-1Mo, Smooth LCF at 25°C (77°F), $R_\epsilon = -1.0$

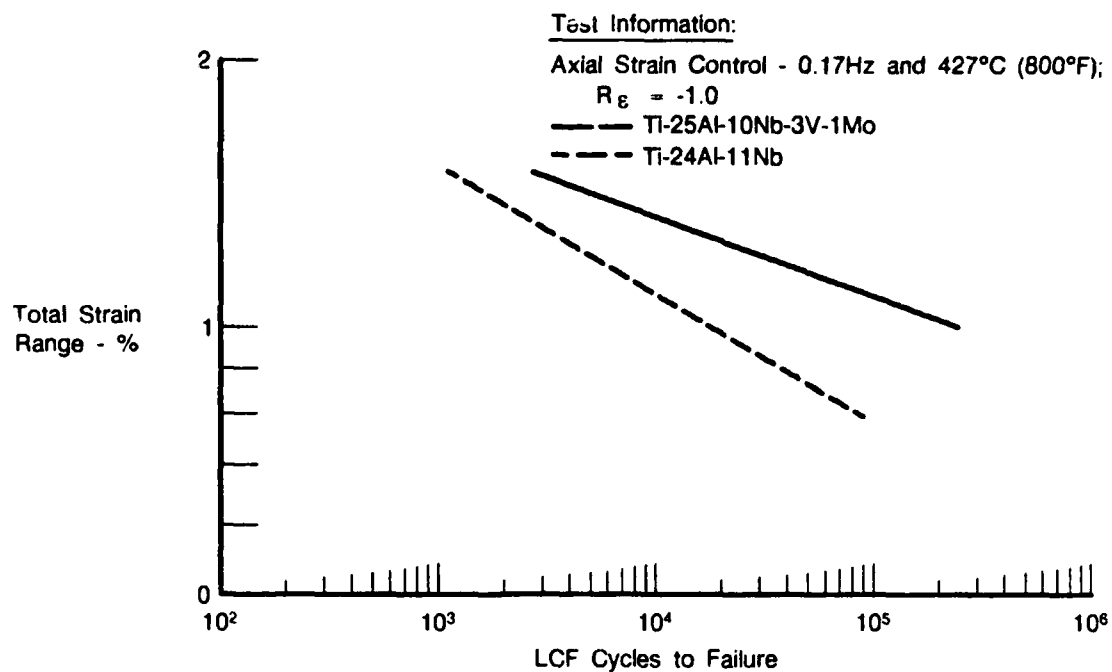


Figure 65. Comparison of Ti-24Al-11Nb Versus Ti-25Al-10Nb-3V-1Mo, Smooth LCF at 427°C (800°F), $R_\epsilon = -1.0$

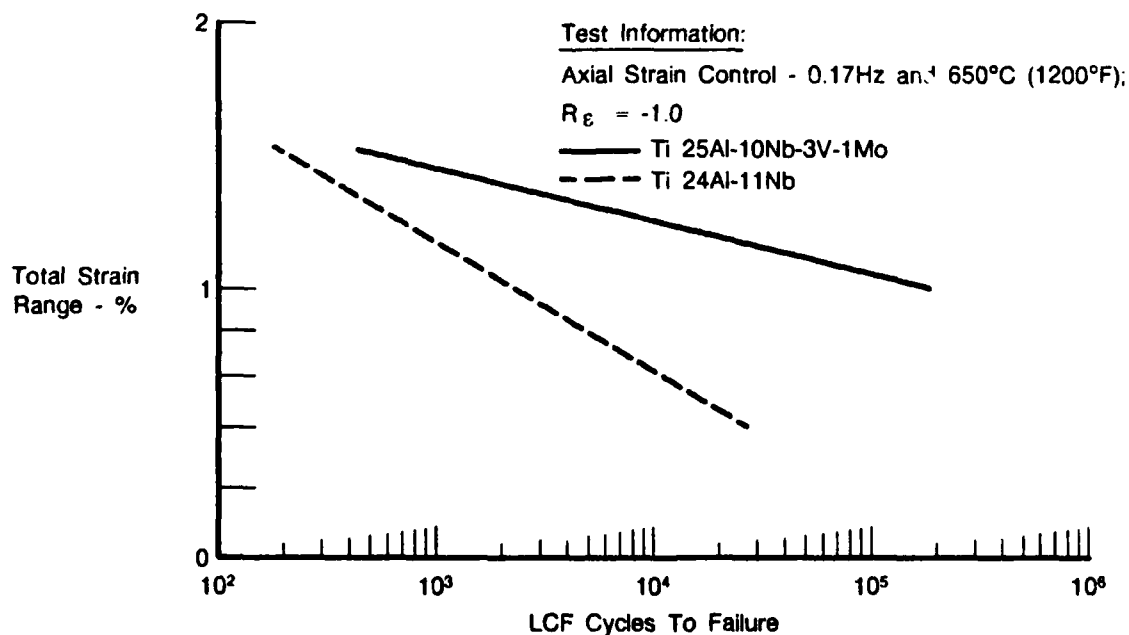


Figure 66. Comparison of Ti-24Al-11Nb Versus Ti-25Al-10Nb-3V-1Mo, Smooth LCF at 650°C (1200°F), $R_\epsilon = -1.0$

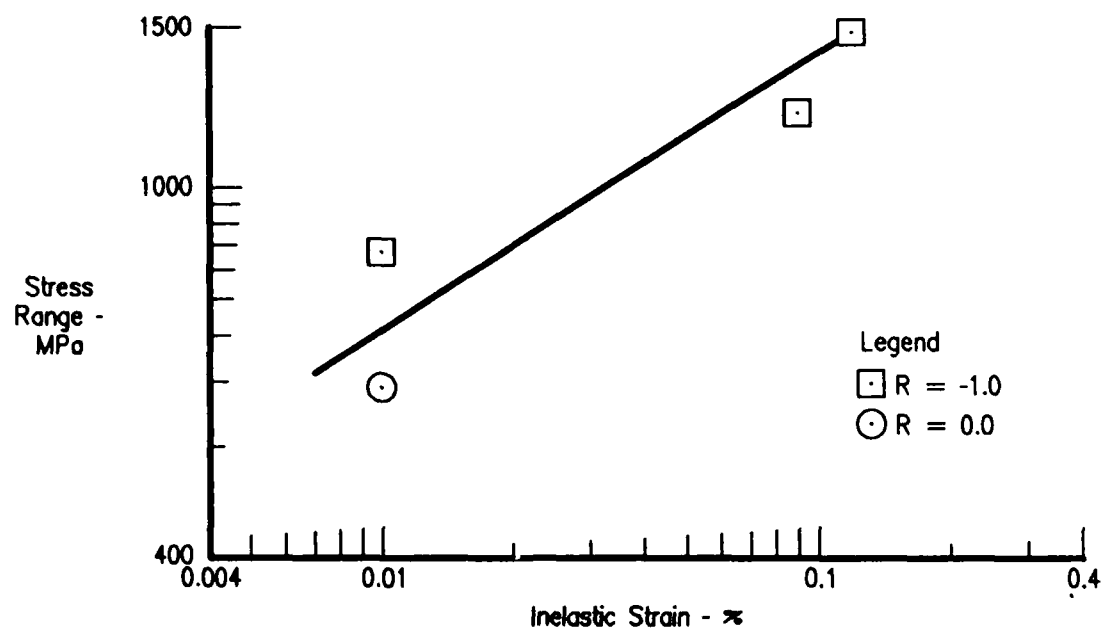


Figure 67. Inelastic Strain Versus Cyclic Stress Range, Ti-25Al-10Nb-3V-1Mo at 26°C (80°F), 0.17 Hz

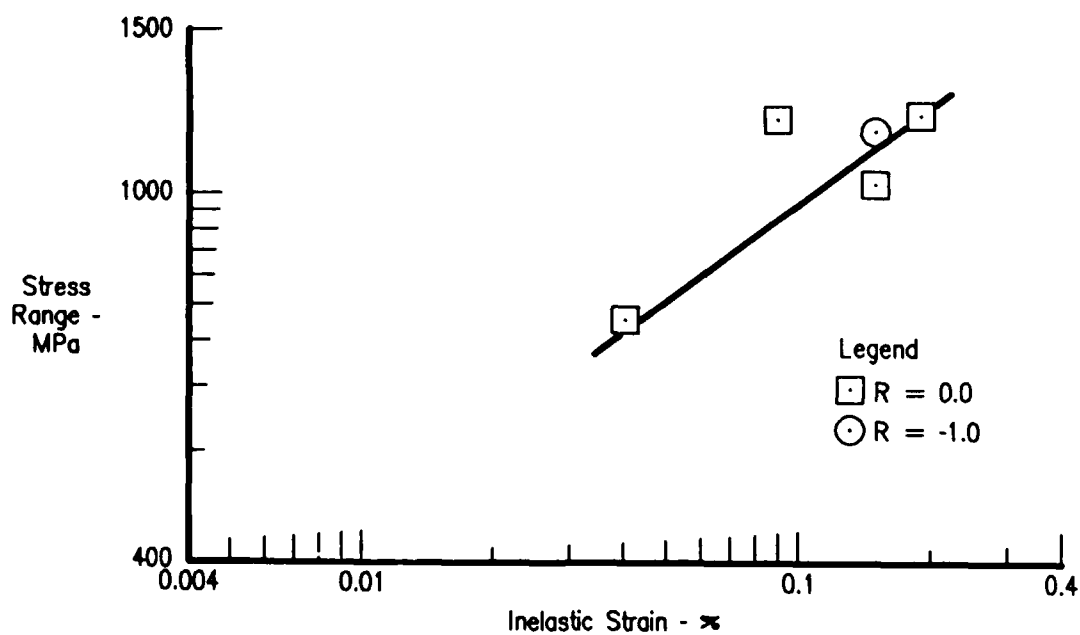


Figure 68. Inelastic Strain Versus Cyclic Stress Range, Ti-25Al-10Nb-3V-1Mo at 427°C (800°F), 0.17 Hz

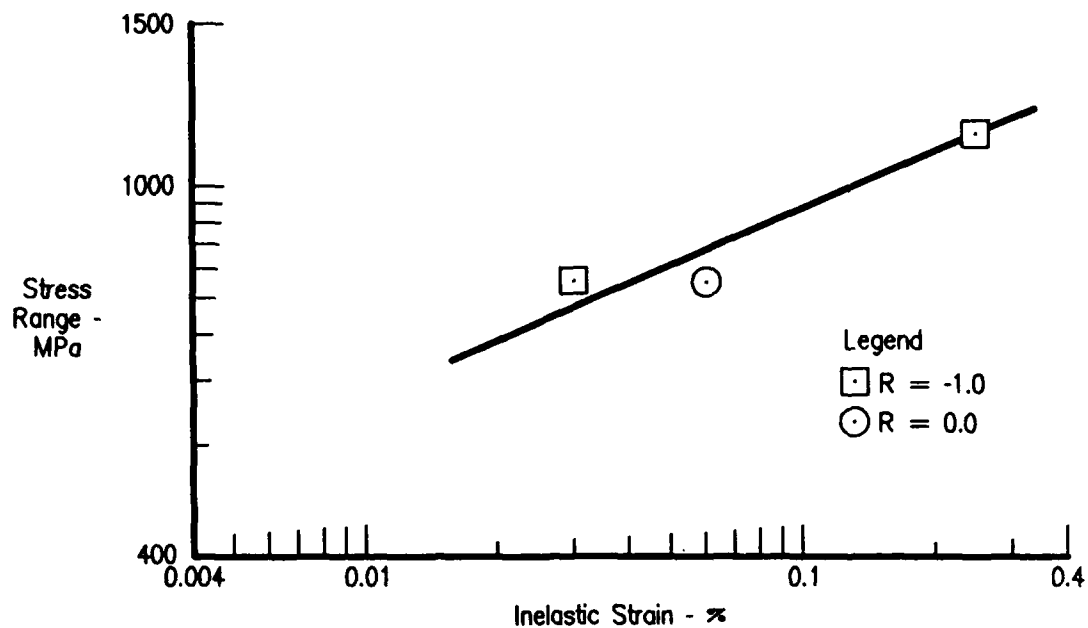


Figure 69. Inelastic Strain Versus Cyclic Stress Range, Ti-25Al-10Nb-3V-1Mo at 650°C (1200°F), 0.17 Hz

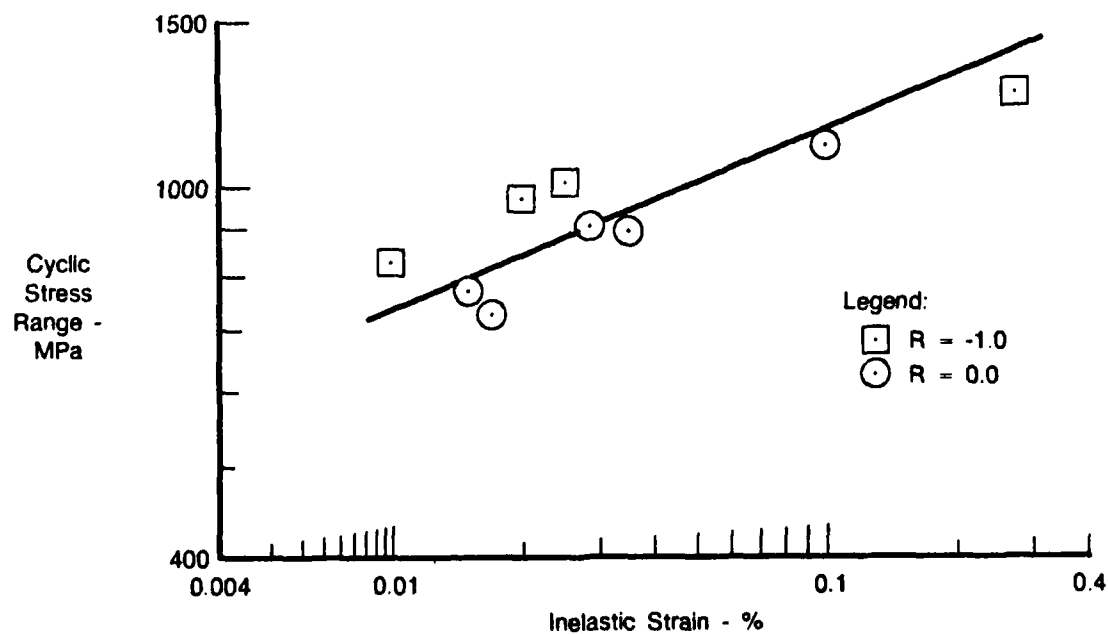


Figure 70. Inelastic Strain Versus Cyclic Stress Range, Ti-24Al-11Nb at 26°C (80°F)

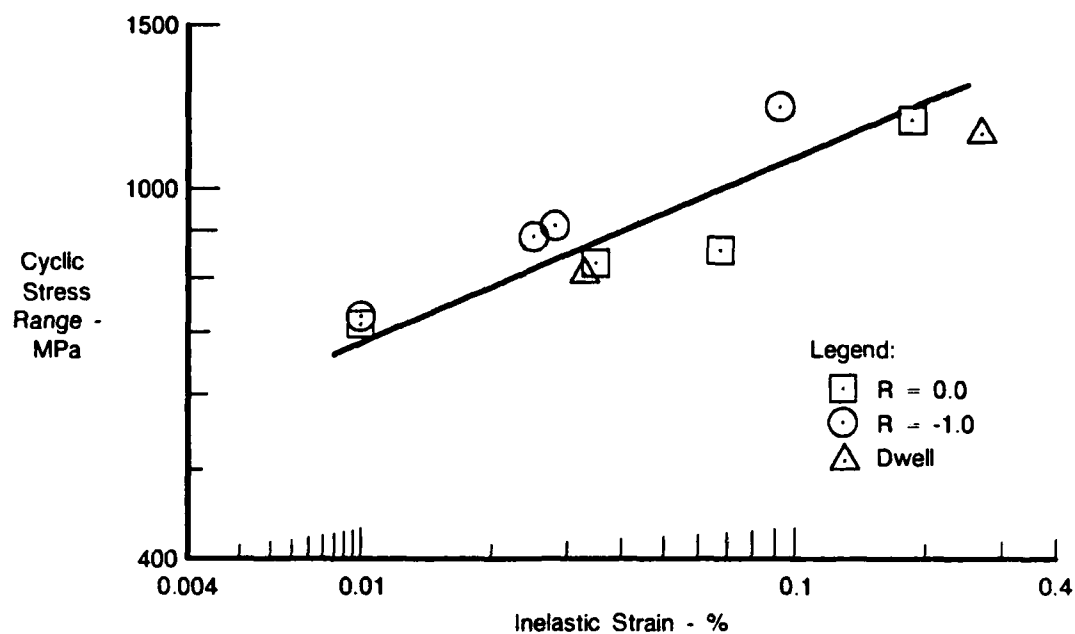


Figure 71. Inelastic Strain Versus Cyclic Stress Range, Ti-24Al-11Nb at 427°C (800°F)

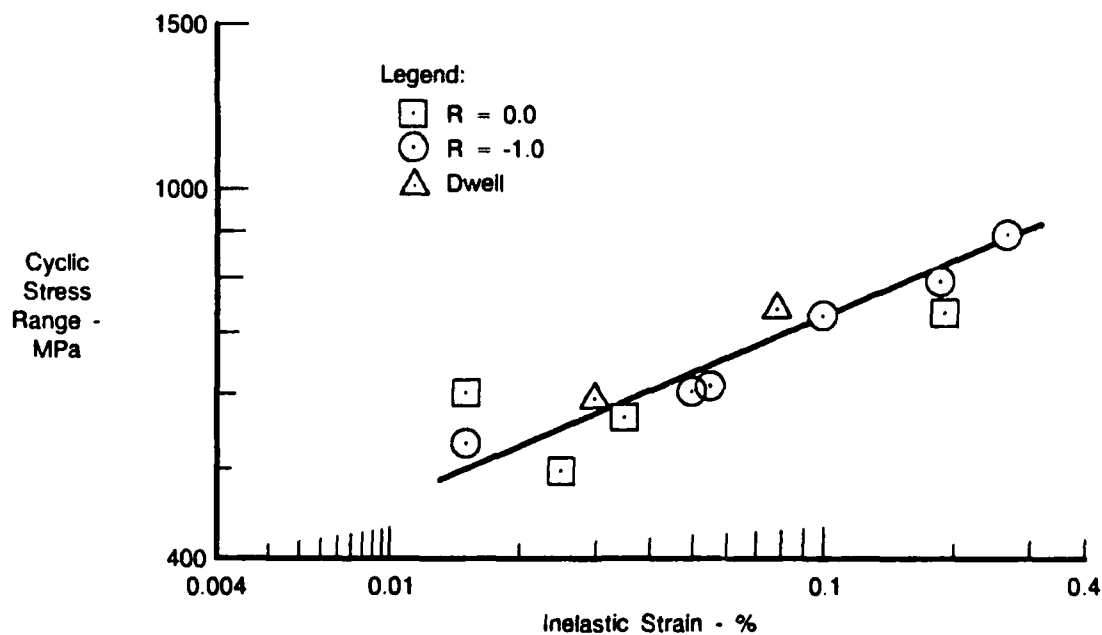


Figure 72. Inelastic Strain Versus Cyclic Stress Range, Ti-24Al-11Nb at 650°C (1200°F)

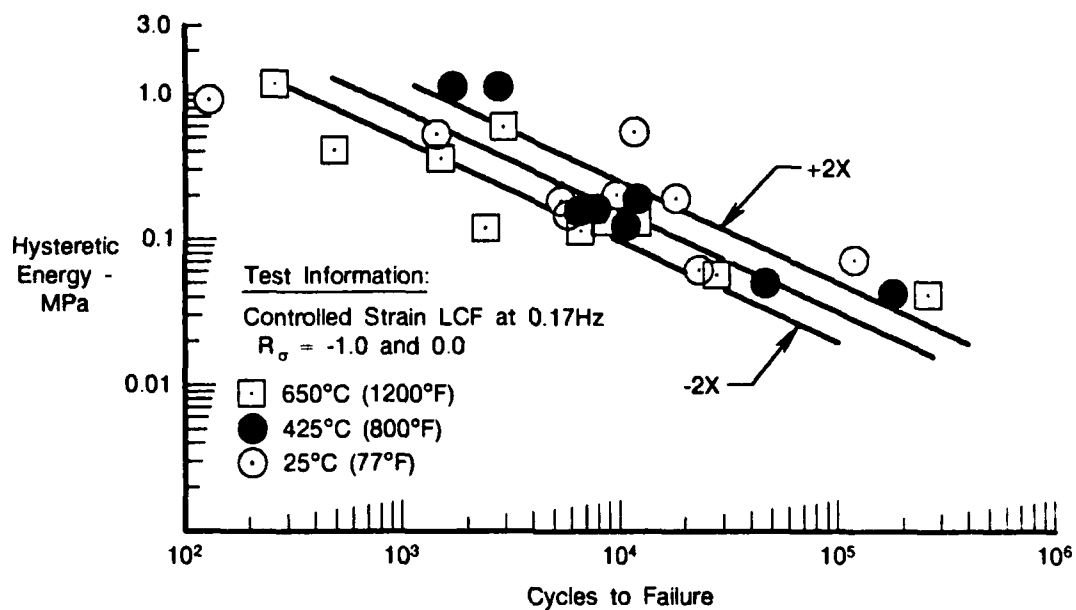


Figure 73. Hysteretic Energy Versus Life, Smooth LCF of Ti-24Al-11Nb

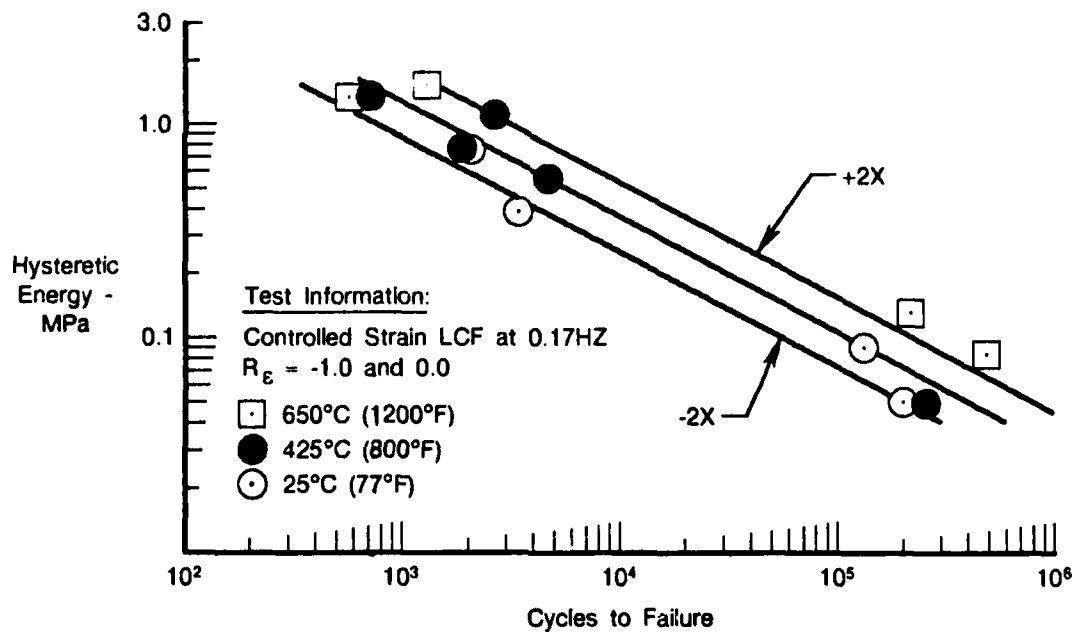


Figure 74. Hysteretic Energy Versus Life, Smooth LCF of Ti-25Al-10Nb-3V-1Mo

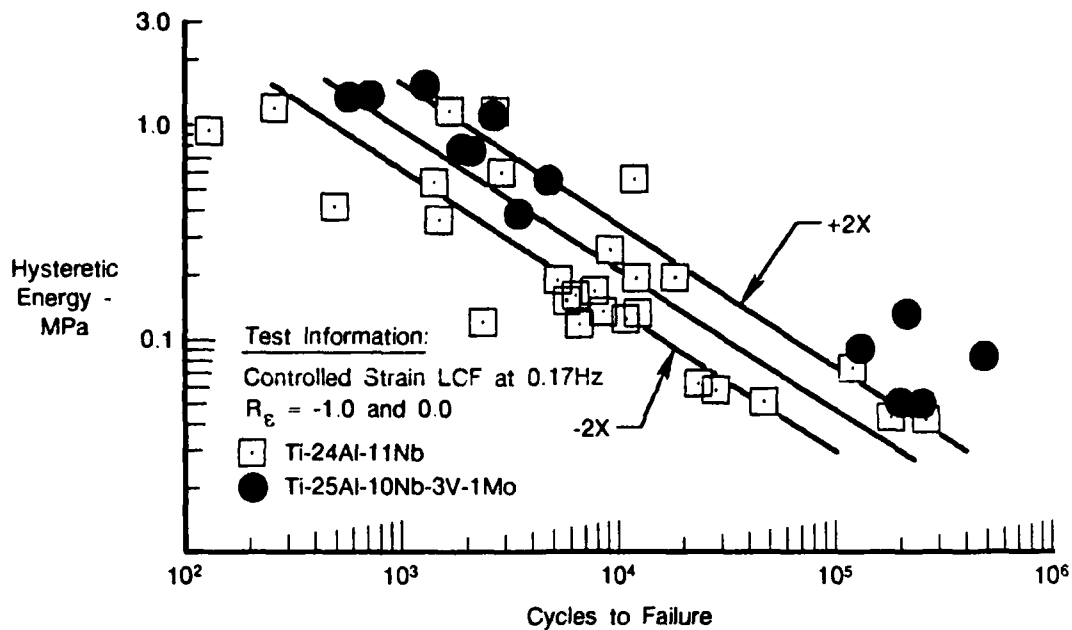


Figure 75. Hysteretic Energy Versus Life, Smooth LCF, Ti-25Al-10Nb-3V-1Mo and Ti-24Al-11Nb

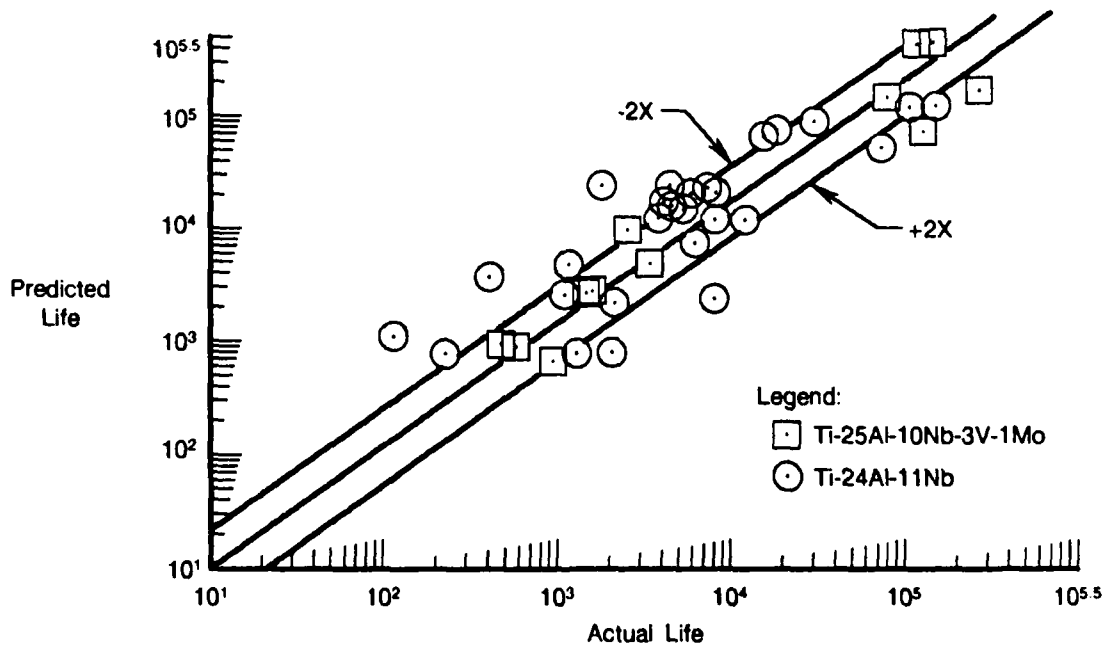


Figure 76. Actual Versus Predicted Life, Ti-25Al-10Nb-3V-1Mo and Ti-24Al-11Nb

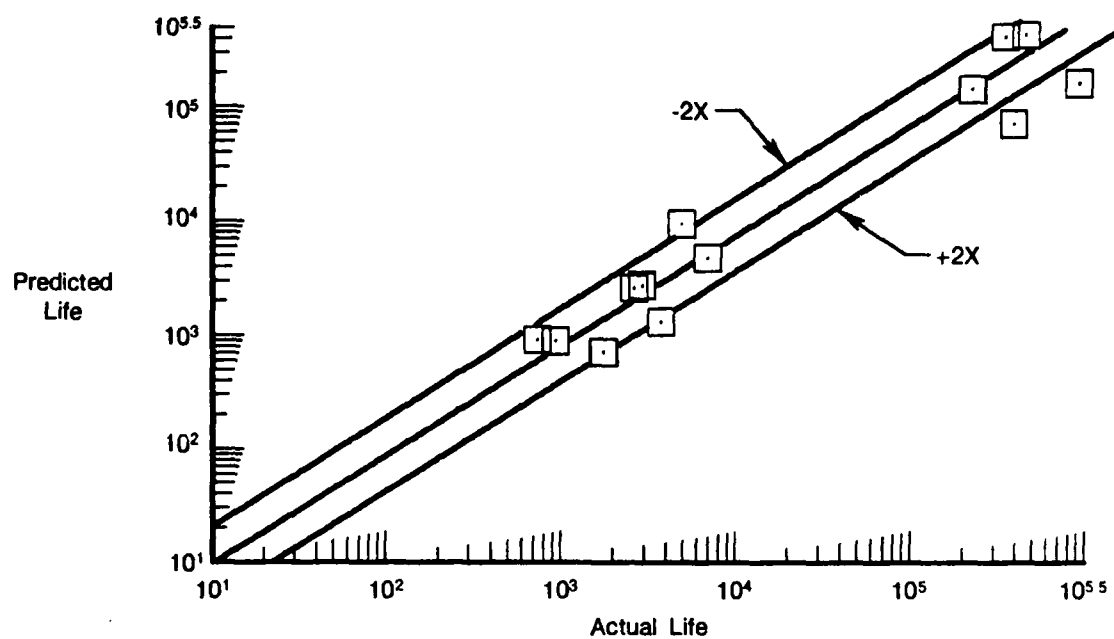


Figure 77. Actual Versus Predicted Life, Ti-25Al-10Nb-3V-1Mo

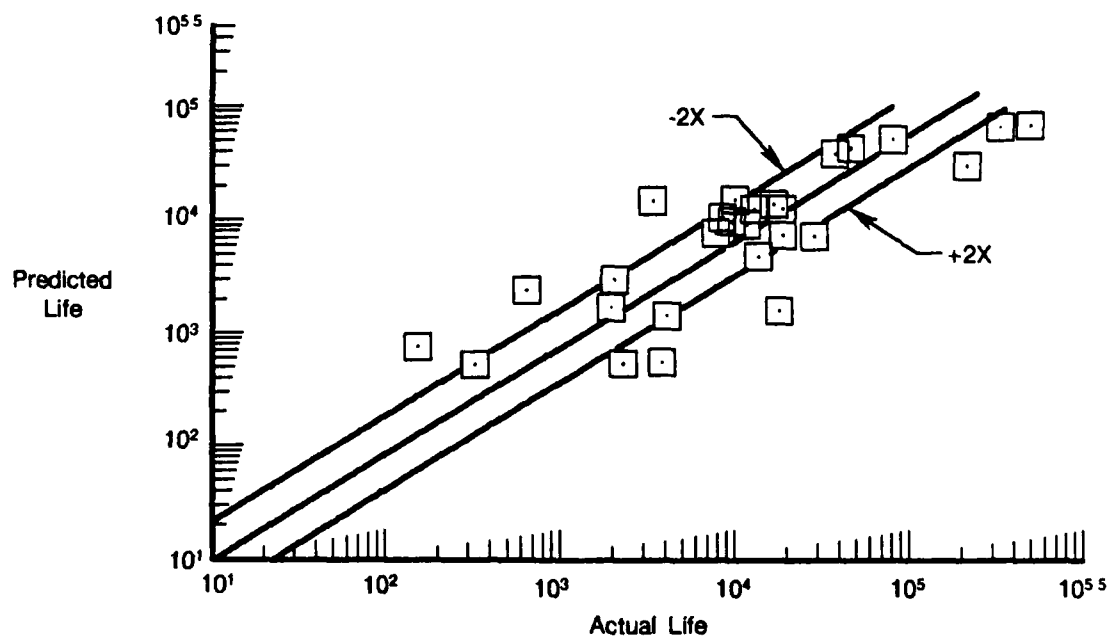


Figure 78. Actual Versus Predicted Life, Ti-24Al-11Nb

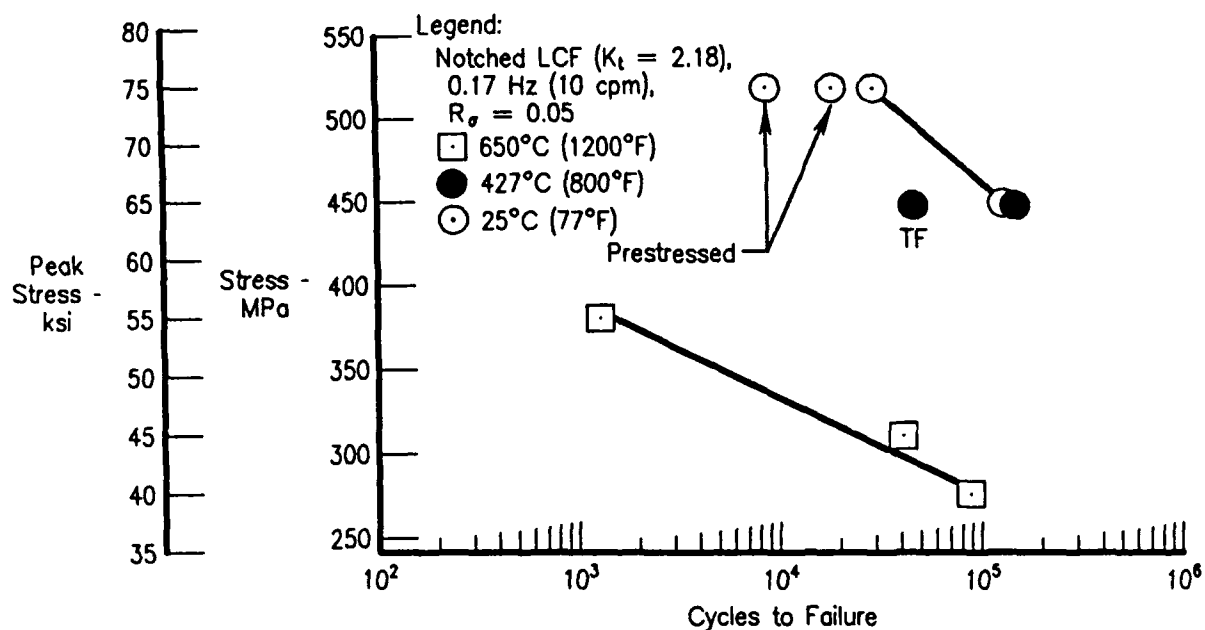


Figure 79. Ti-25Al-10Nb-3V-1Mo Notched LCF Effects of Temperature

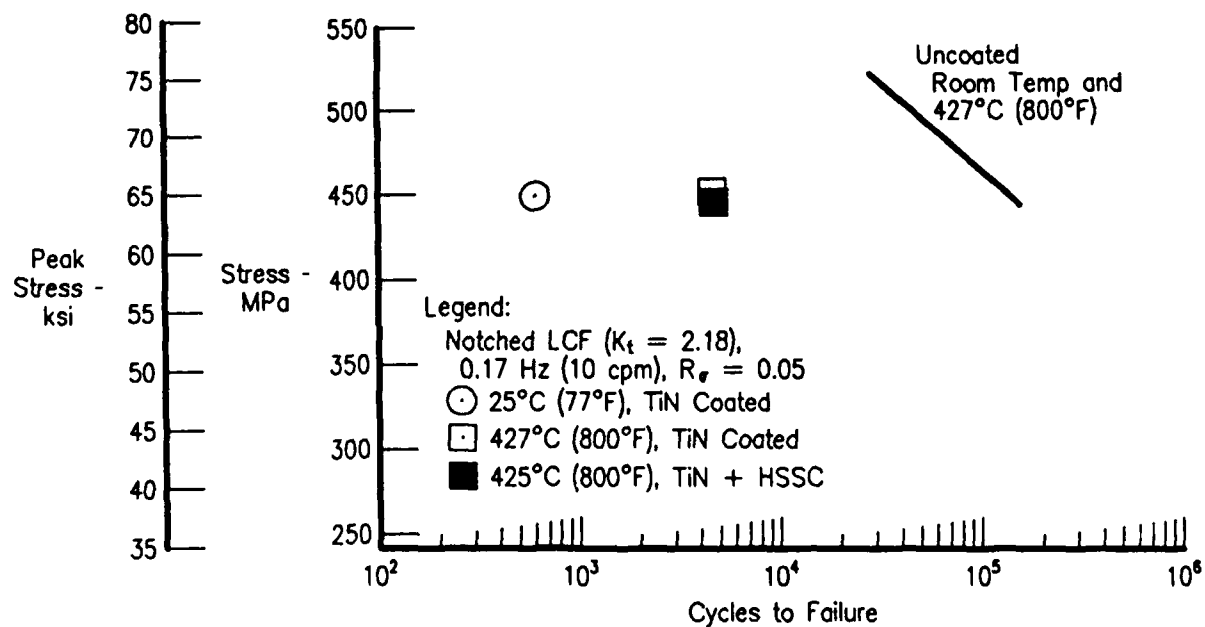


Figure 80. Ti-25Al-10Nb-3V-1Mo Notched LCF TiN Coated

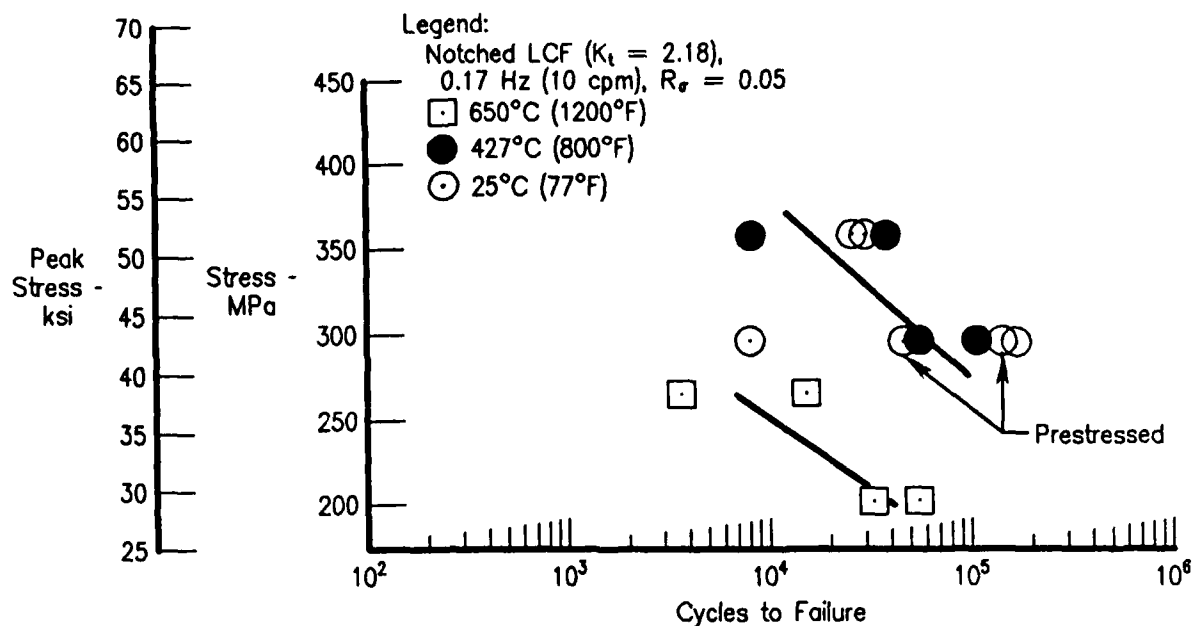


Figure 81. Ti-24Al-11Nb Notched LCF Effects of Temperature

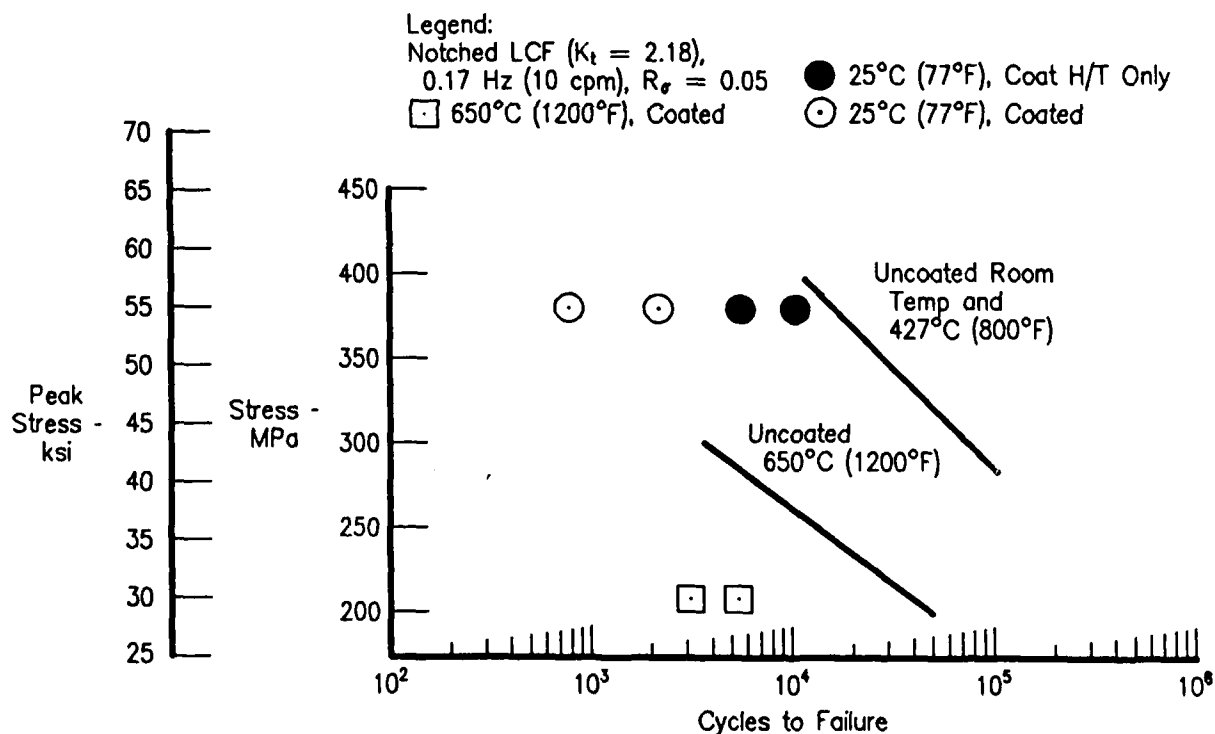


Figure 82. Ti-24Al-11Nb Notched LCF Effects of Coating

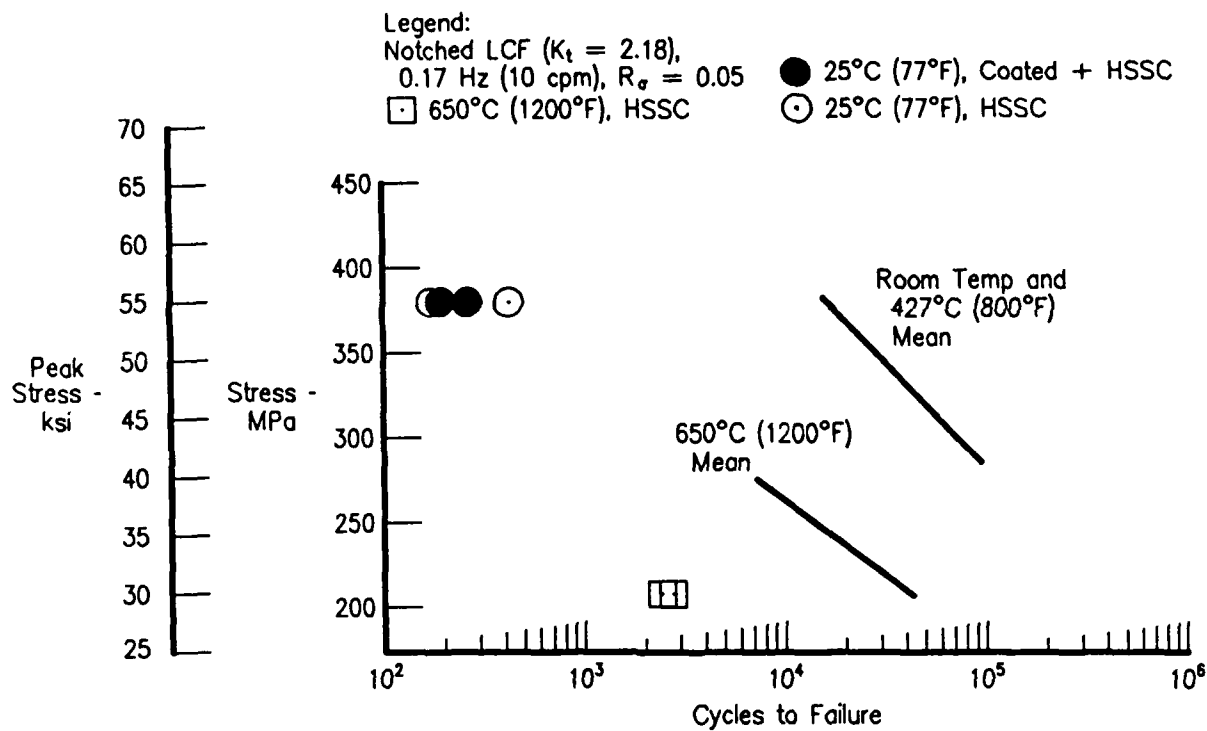


Figure 83. Ti-24Al-11Nb Notched LCF Effects of Hot Salt Stress Corrosion

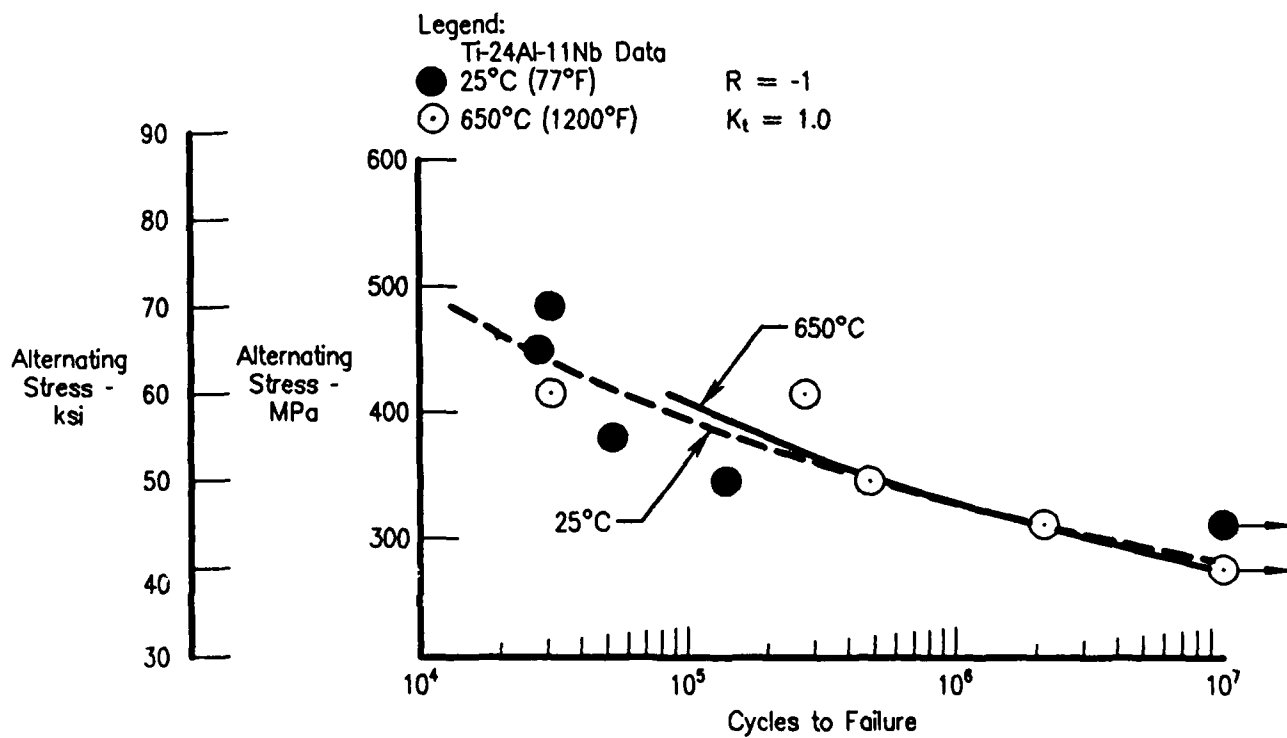


Figure 84. Effects of Temperature on Ti-24Al-11Nb, Smooth HCF at $R = -1$, $K_t = 1.0$

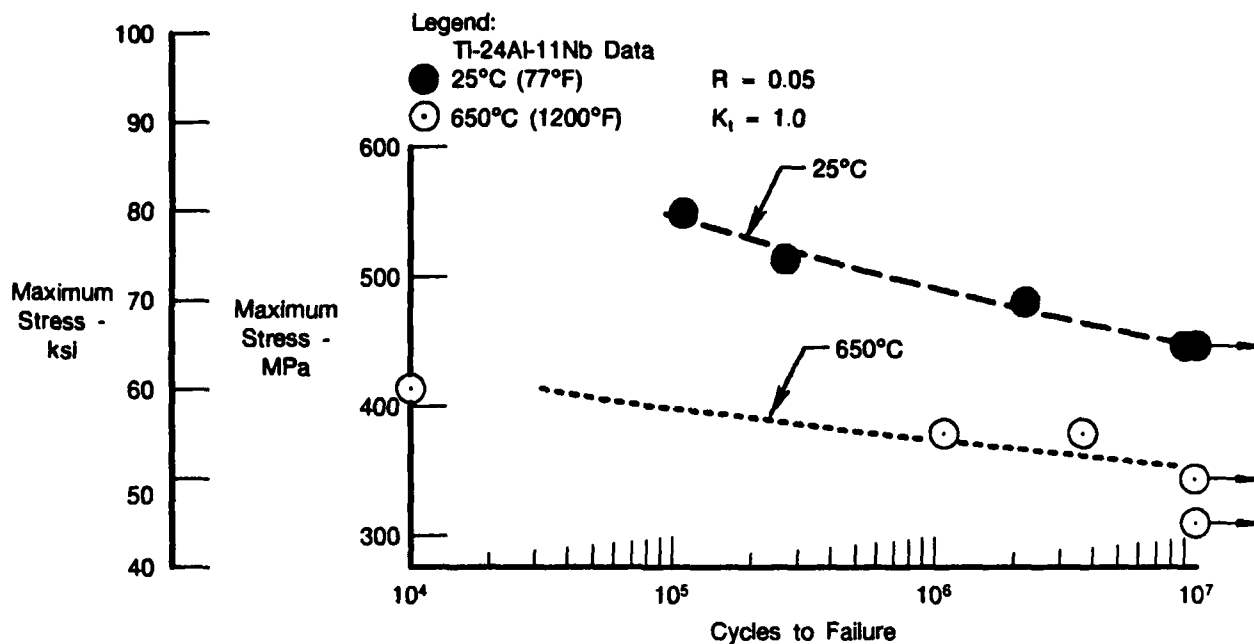


Figure 85. Effects of Temperature on Ti-24Al-11Nb, Smooth HCF at $R = 0.05$, $K_t = 1.0$

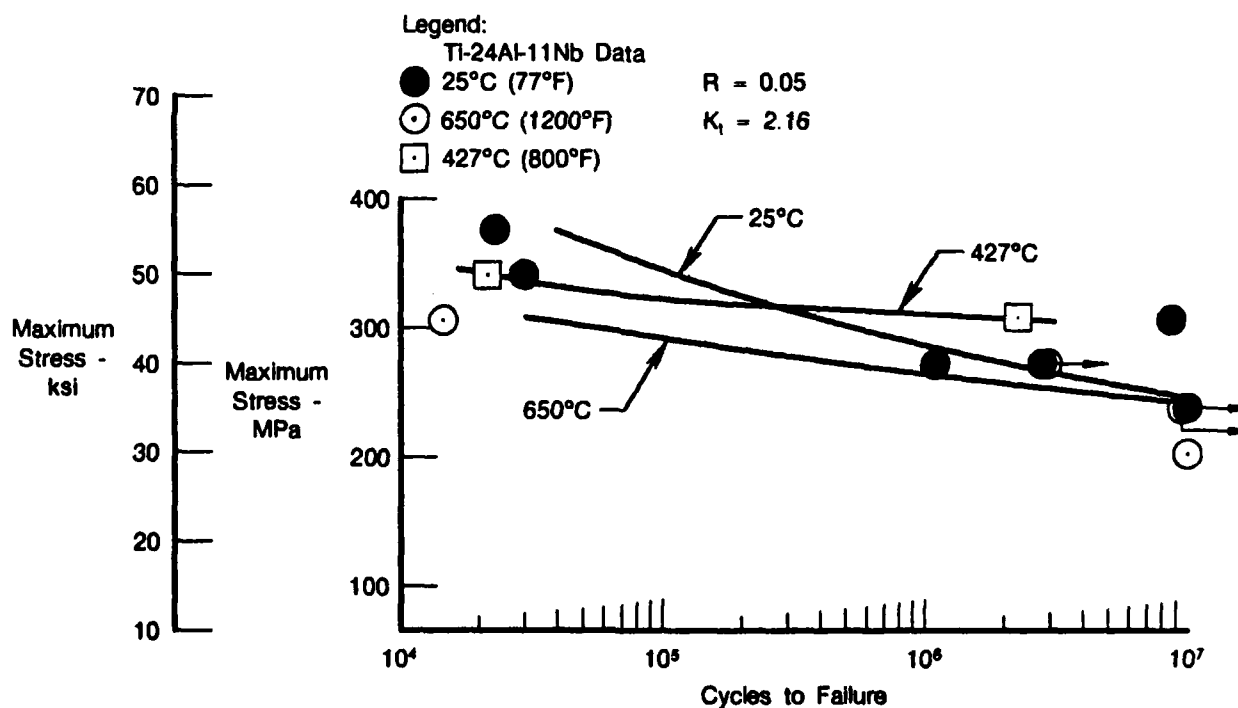


Figure 86. Effects of Temperature on Ti-24Al-11Nb, Notched HCF at $R = 0.05$, $K_t = 2.16$

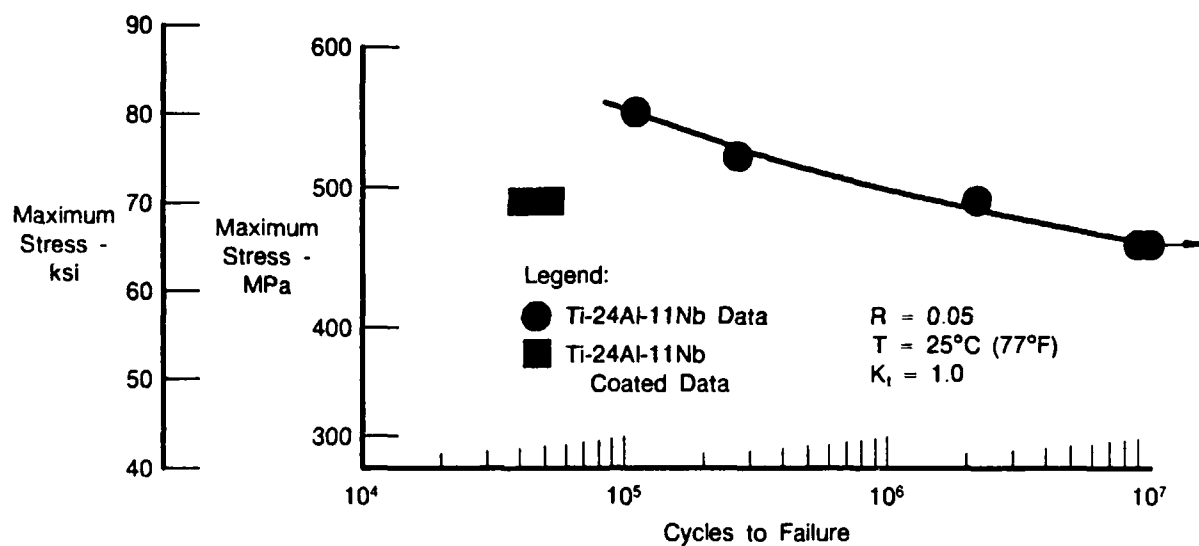


Figure 87. Effects of Coating on Ti-24Al-11Nb, Smooth HCF at $R = 0.05$, $K_t = 1.0$

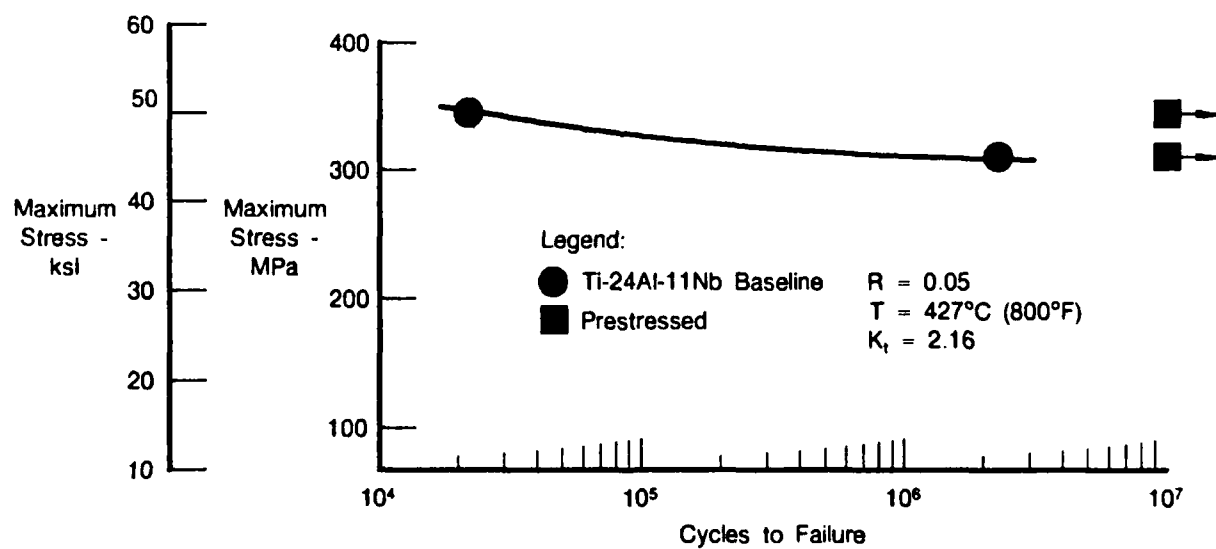


Figure 88. Effects of Prestressing on Ti-24Al-11Nb, Notched HCF at $R = 0.05$, $K_t = 2.16$

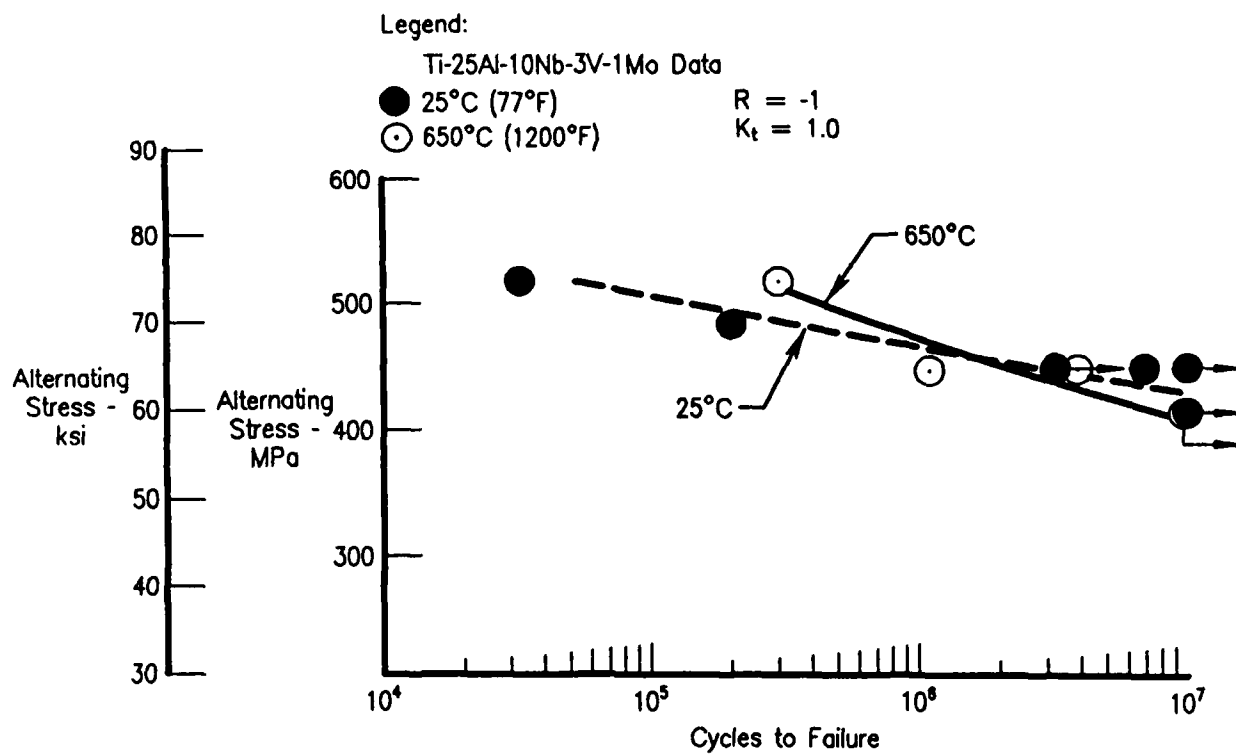


Figure 89. Effects of Temperature on Ti-25Al-10Nb-3V-1Mo, Smooth HCF at $R = -1$, $K_t = 1.0$

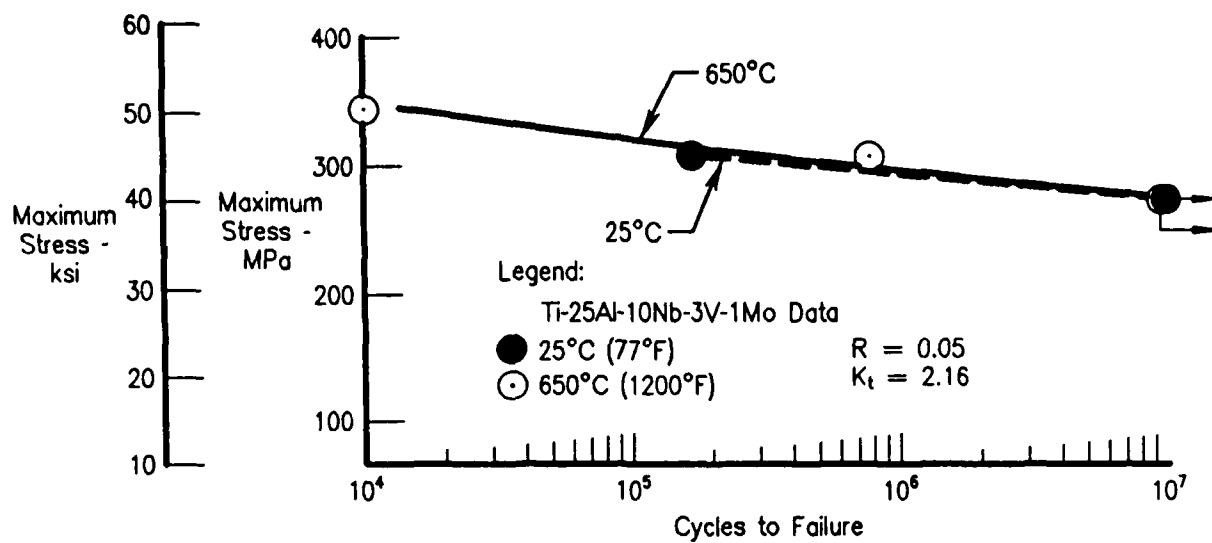


Figure 90. Effects of Temperature on Ti-25Al-10Nb-3V-1Mo, Notched HCF at $R = 0.05$, $K_t = 2.16$

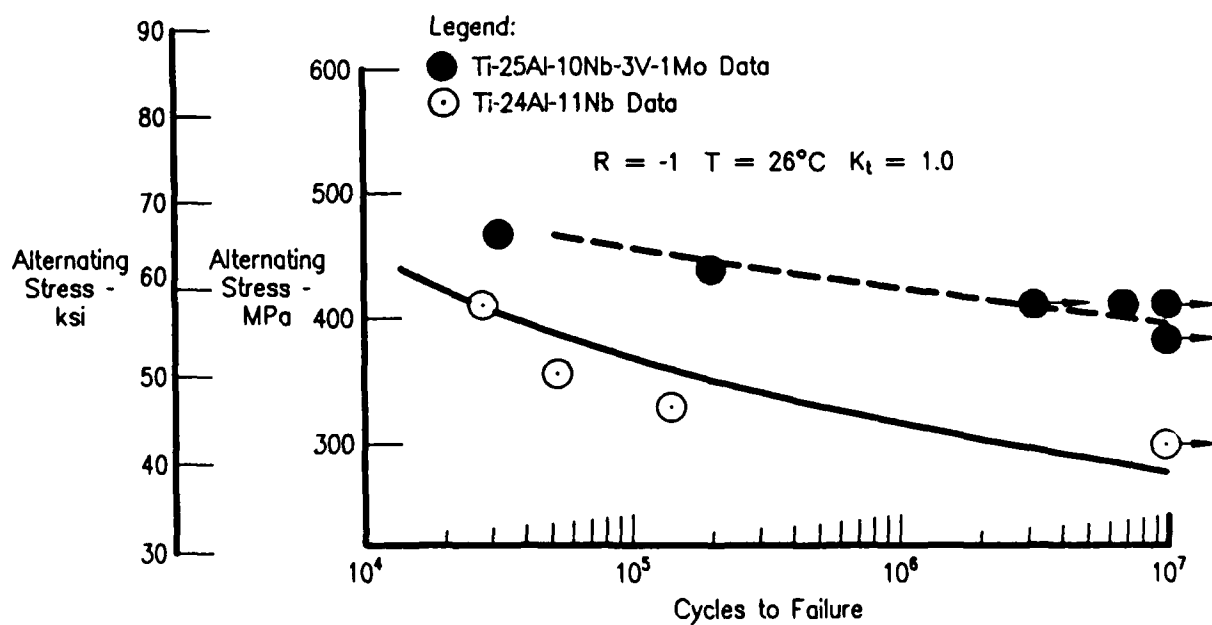


Figure 91. Smooth HCF, Ti-25Al-10Nb-3V-1Mo Versus Ti-24Al-11Nb at $R = -1$, $K_t = 1.0$

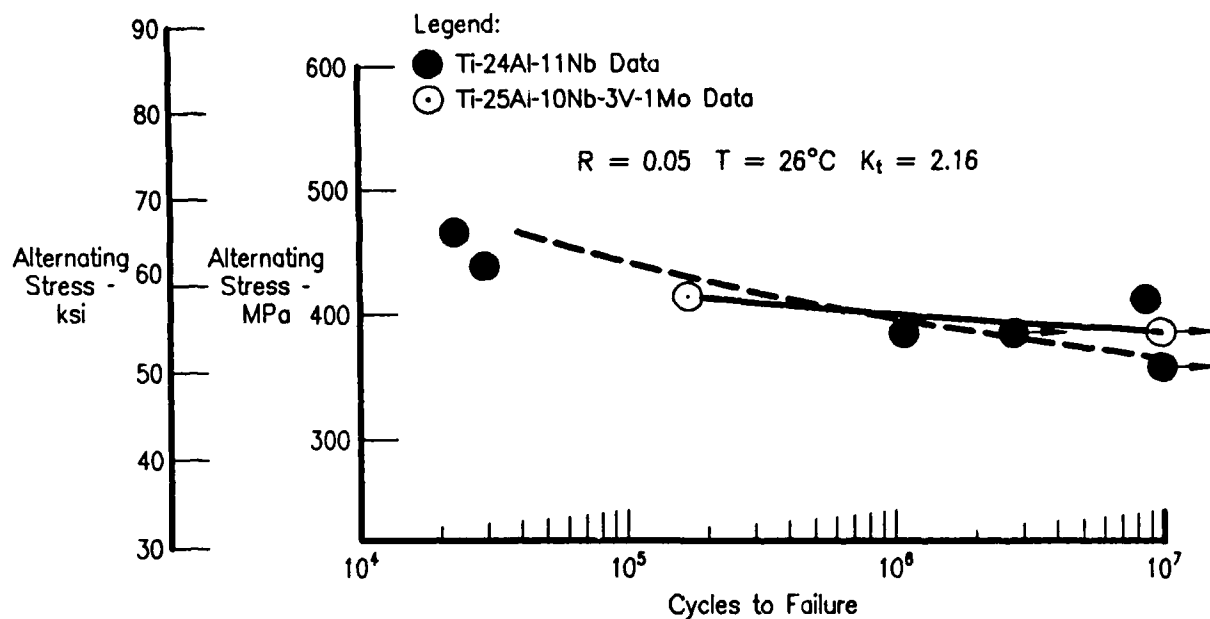


Figure 92. Notched LCF, Ti-25Al-10Nb-3V-1Mo Versus Ti-24Al-11Nb at $R = 0.05$, $K_t = 2.16$

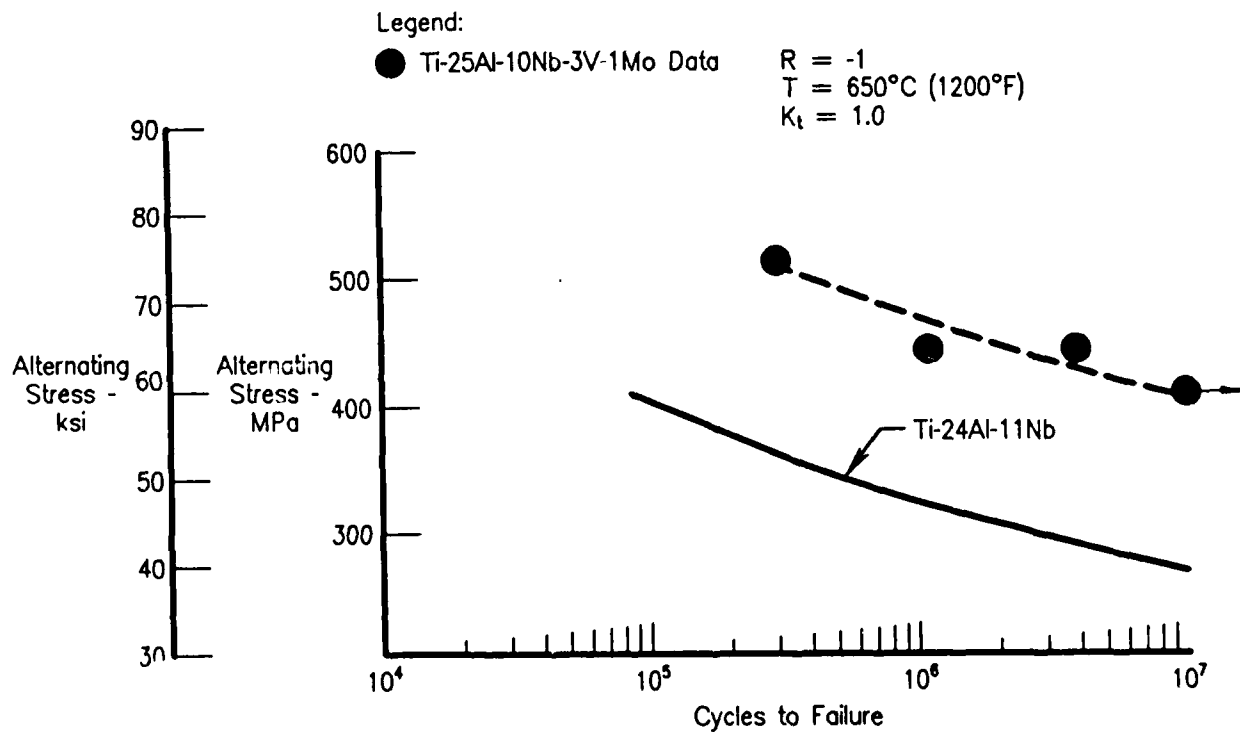


Figure 93. Smooth HCF, Ti-25Al-10Nb-3V-1Mo Versus Ti-24Al-11Nb at $R = -1$, $K_t = 1.0$

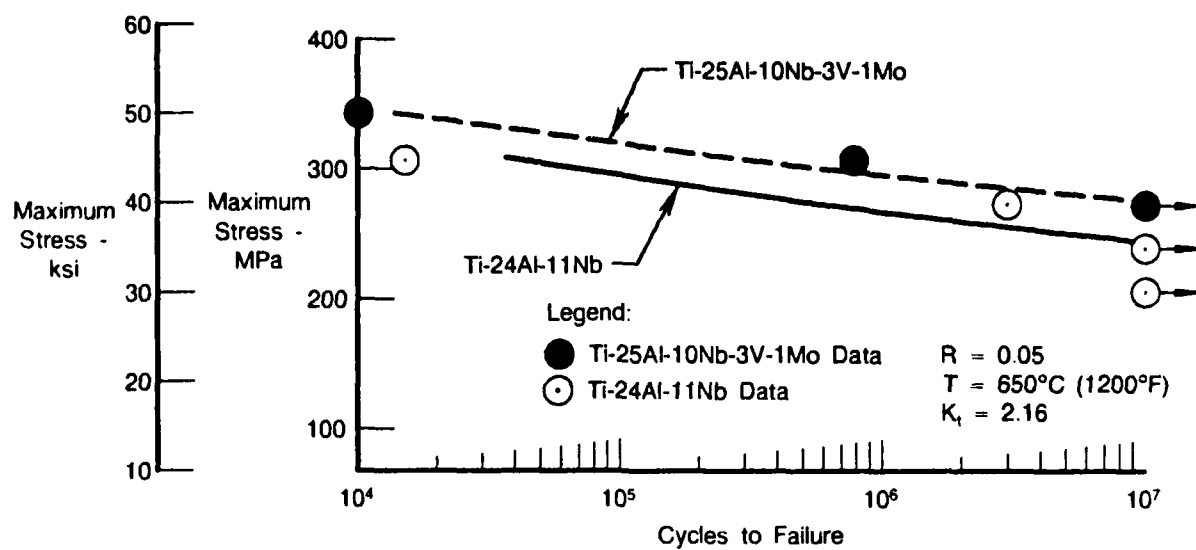


Figure 94. Notched HCF of Ti-25Al-10Nb-3V-1Mo

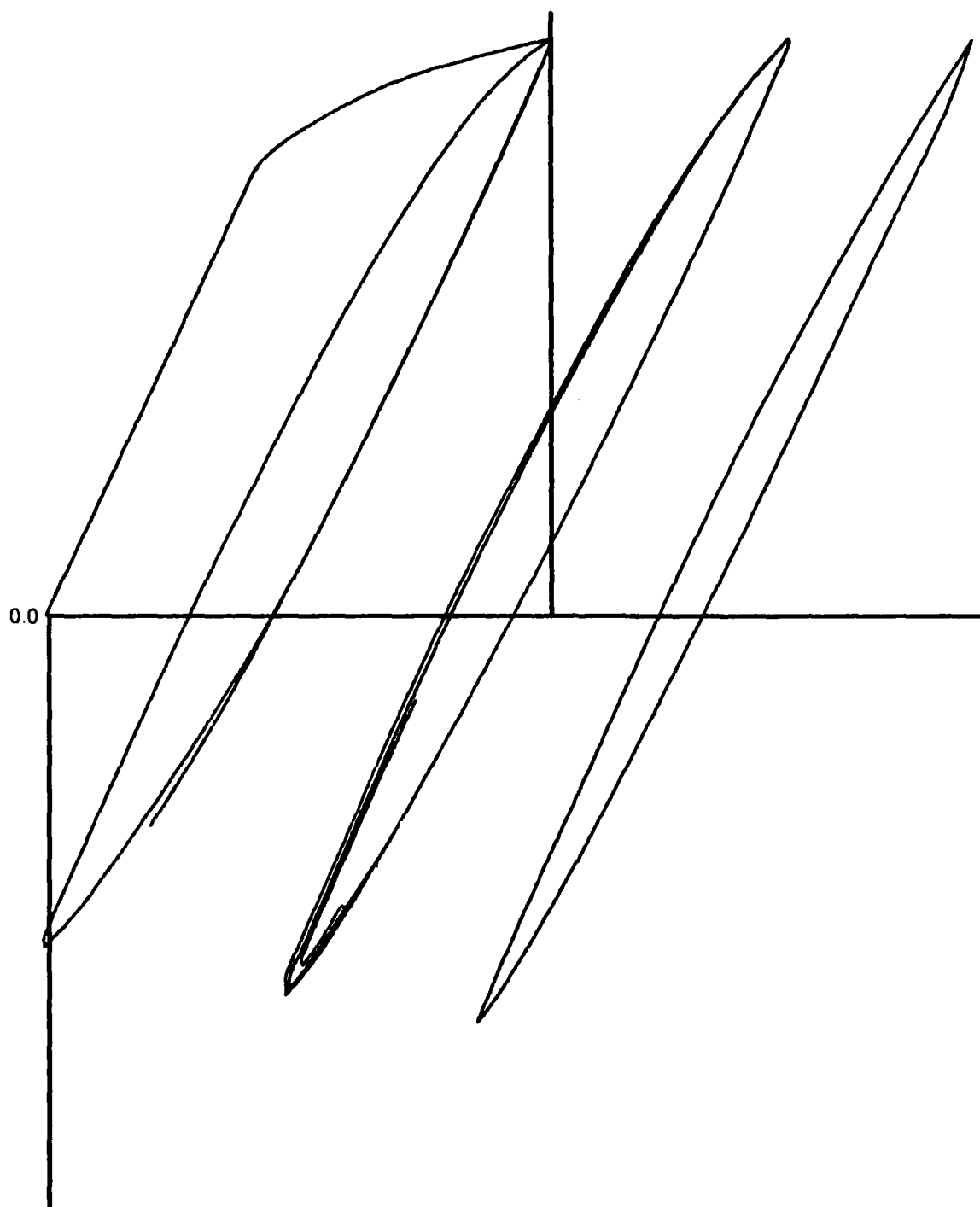


Figure 95. Significant Inelastic Strain Observed in 26°C (80°F) Ti-24Al-11Nb Strain Controlled LCF Test. Conditions: $\Delta\epsilon_t = 1.2$ Percent, Initial $\Delta\epsilon_i = 0.24$ Percent, Initial $\sigma_{max} = 627$ MPa (91 ksi)

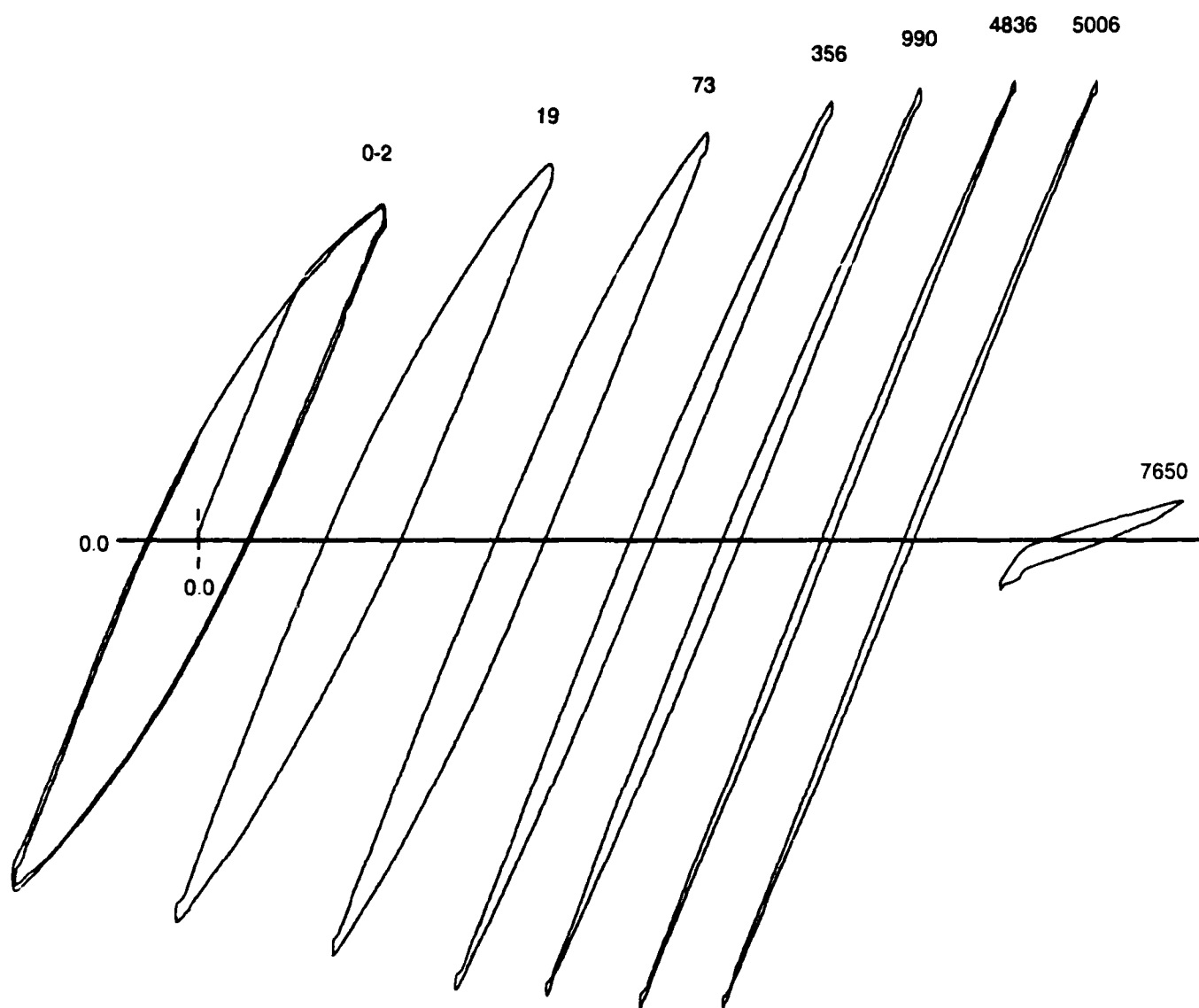


Figure 96. Cyclic Hardening Observed With Ti-24Al-11Nb at 427°C, $R = -1.0$, $\Delta\epsilon_t = 1$ Percent

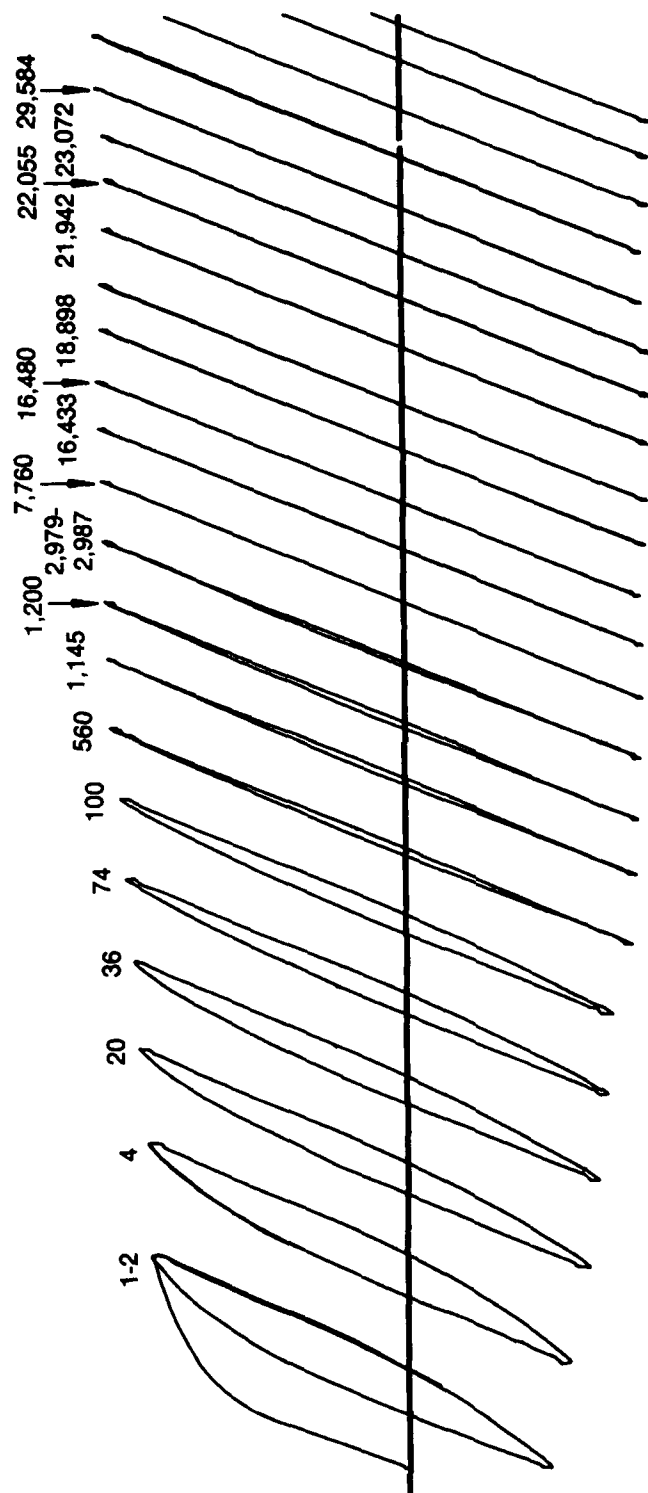
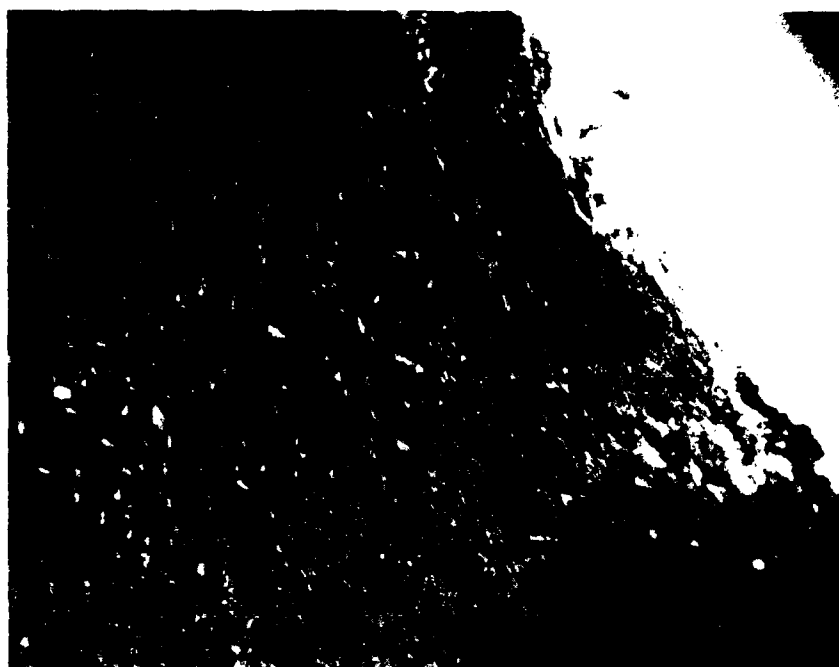
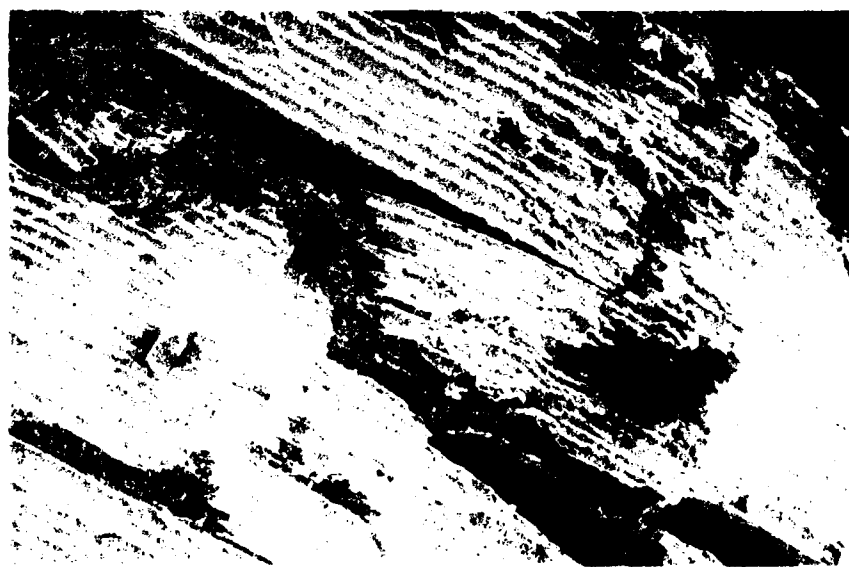


Figure 97. Mean Stress Relaxation and Cyclic Hardening Observed in Ti-24Al-11Nb at 427°C, $R = 0.0$, $\Delta\epsilon_t = 0.8$ Percent



(a)

Mag: 25X



100μm

(b)

Figure 98. Fracture Surface Edge (Upper Right in Both Photographs) of LCF Specimen Tested at 650°C (1200°F) Showing Oxide Spalling and Secondary Cracking at Scale Craze in Ti-25Al-10Nb-3V-1Mo

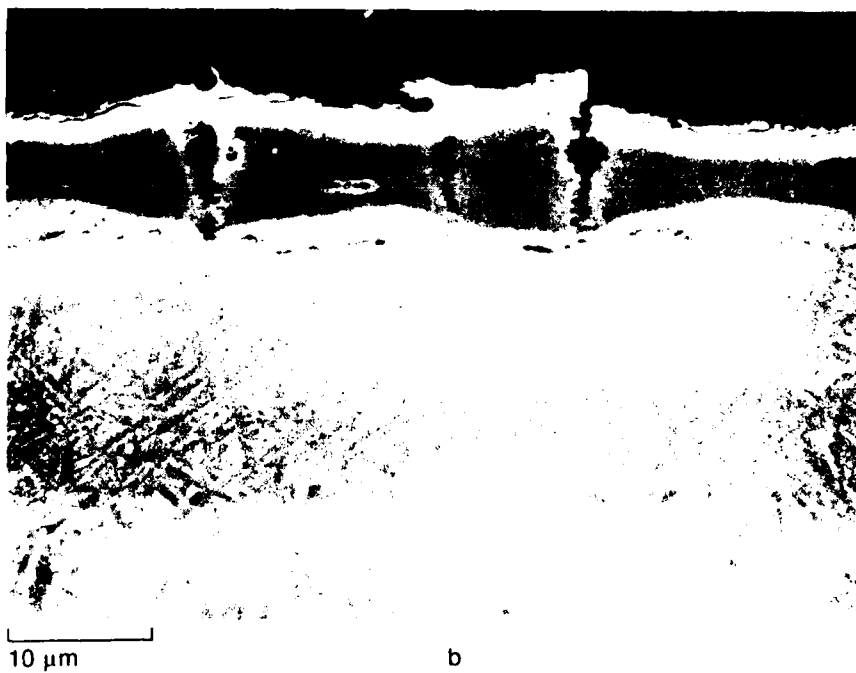
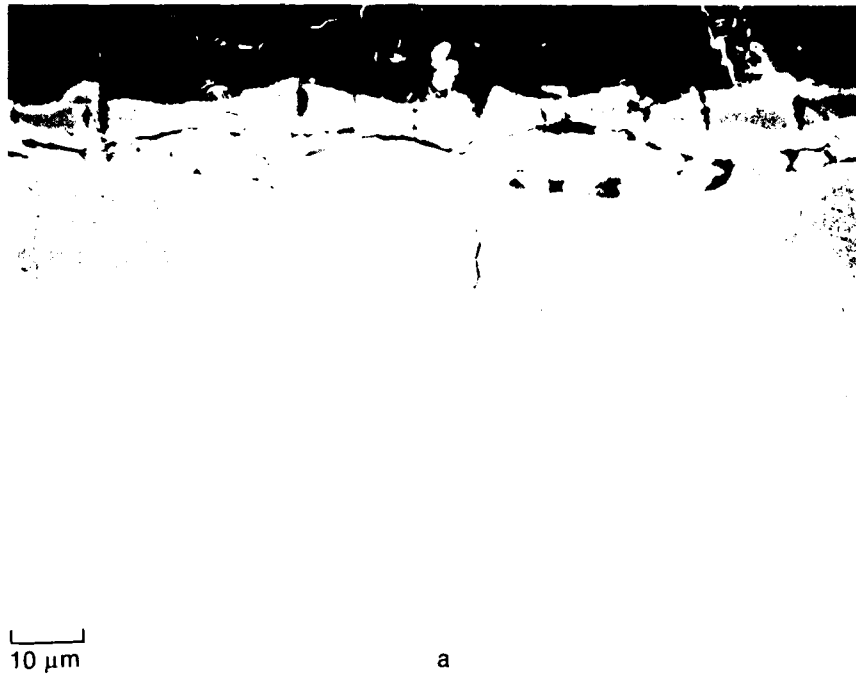
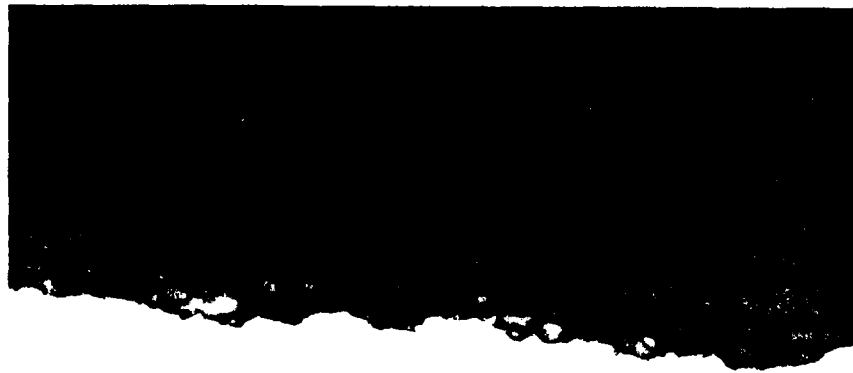


Figure 99. SEM Examination of Oxide and Sublayers (From Previous Figure) Showing Cracking Perpendicular to (a) and Parallel With (b) Stress Axis

HV 865.0 (50gm)



HV 393.3 (50gm)

Figure 100. Vickers Hardness of Oxygen Embrittled Surface Layer and Substrate Below in Ti-25Al-10Nb-3V-1Mo LCF Specimen Tested at 650°C (1200°F)

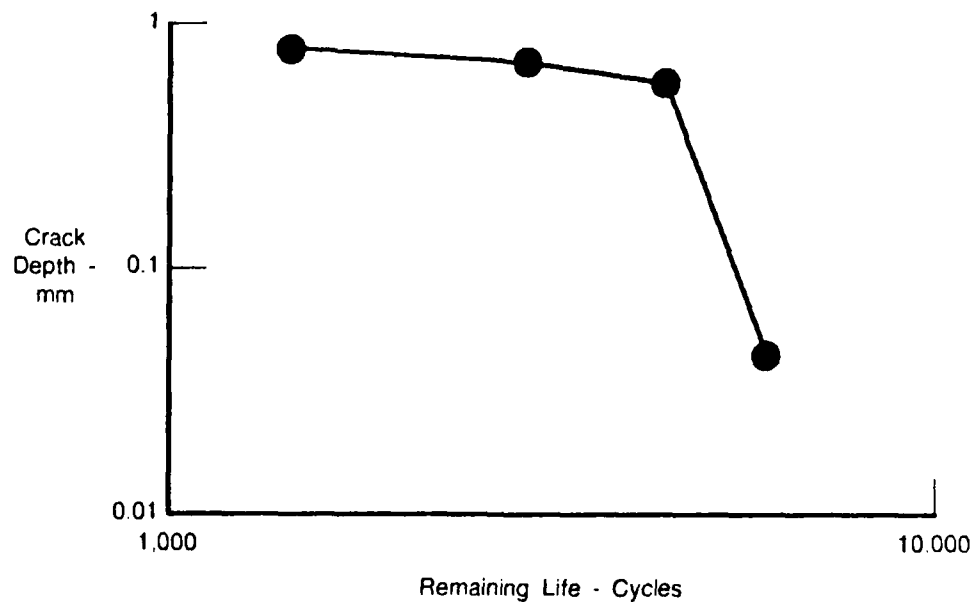


Figure 101. Remaining Life, Notched LCF Ti-24Al-11Nb at 427°C (800°F)

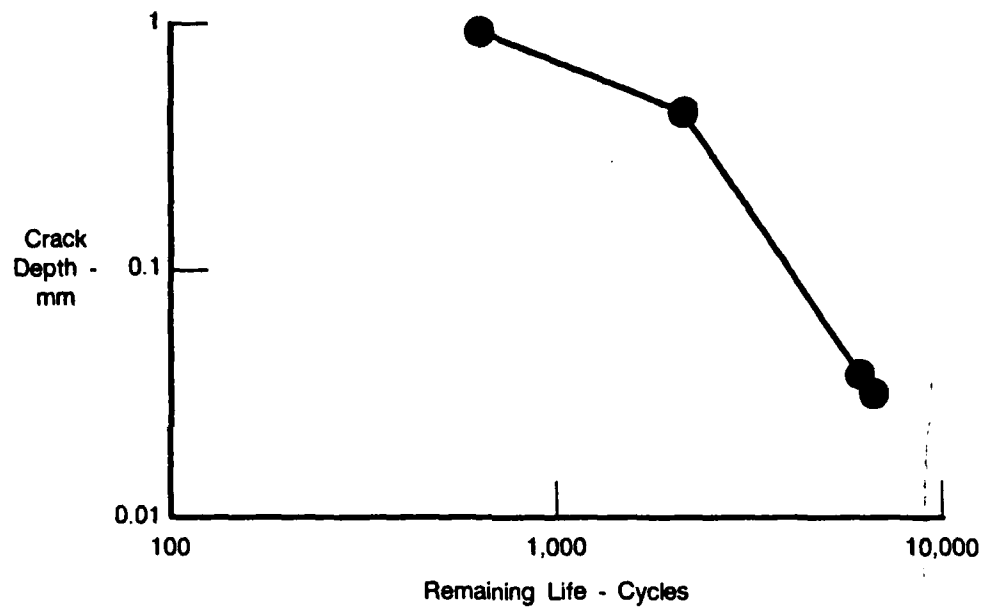


Figure 102. Remaining Life, Notched LCF Ti-25Al-10Nb-3V-1Mo at 427°C (800°F)



Figure 103. Room Temperature LCF Origin (White Arrow) and Arrest Mark (Black Arrows, Probably Critical Crack Depth) From Notched LCF Test of Ti-24Al-11Nb

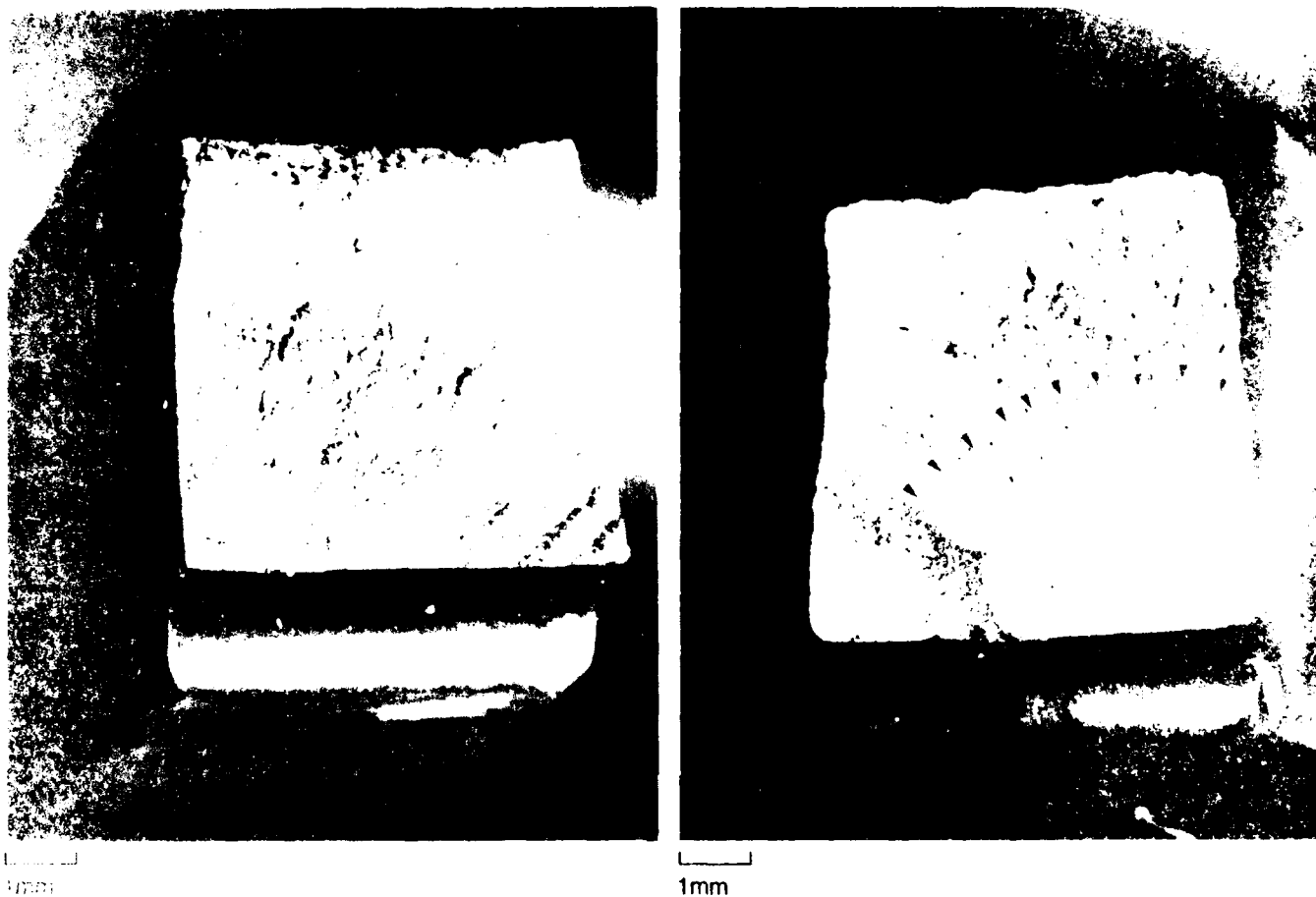


Figure 104. Critical Crack Depths are Visible in 650°C (1200°F, Left) and 427°C (800°F) Ti-24Al-11Nb Notched LCF Fractures. Dotted Line is Just Beyond Crack Front

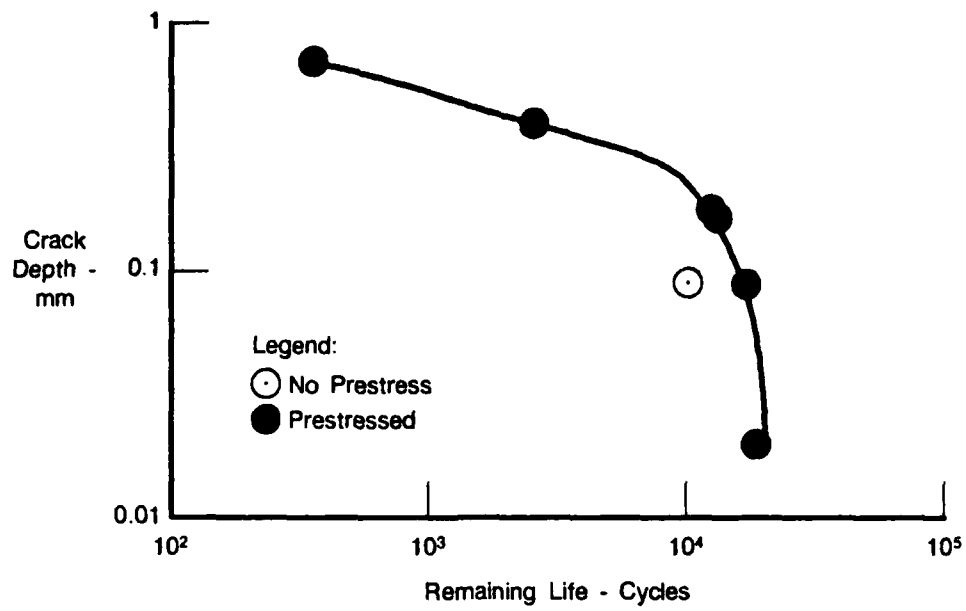
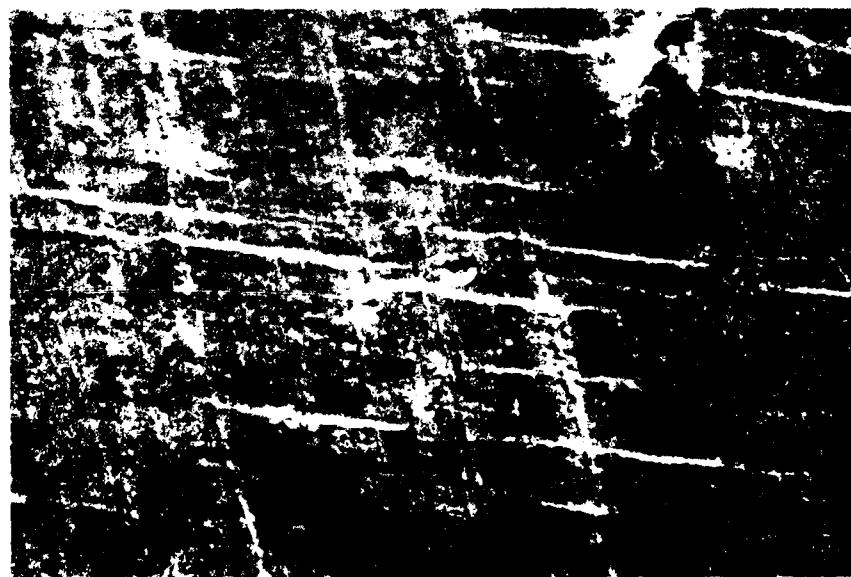


Figure 105. Remaining Life, Notched LCF Ti-24Al-11Nb at 26°C (80°F)



10µm



10µm

Figure 106 Surface Layer at Origin (Top) and Early Appearance of Oxide Scale Crazing (Bottom) on Specimen From Previous Figure

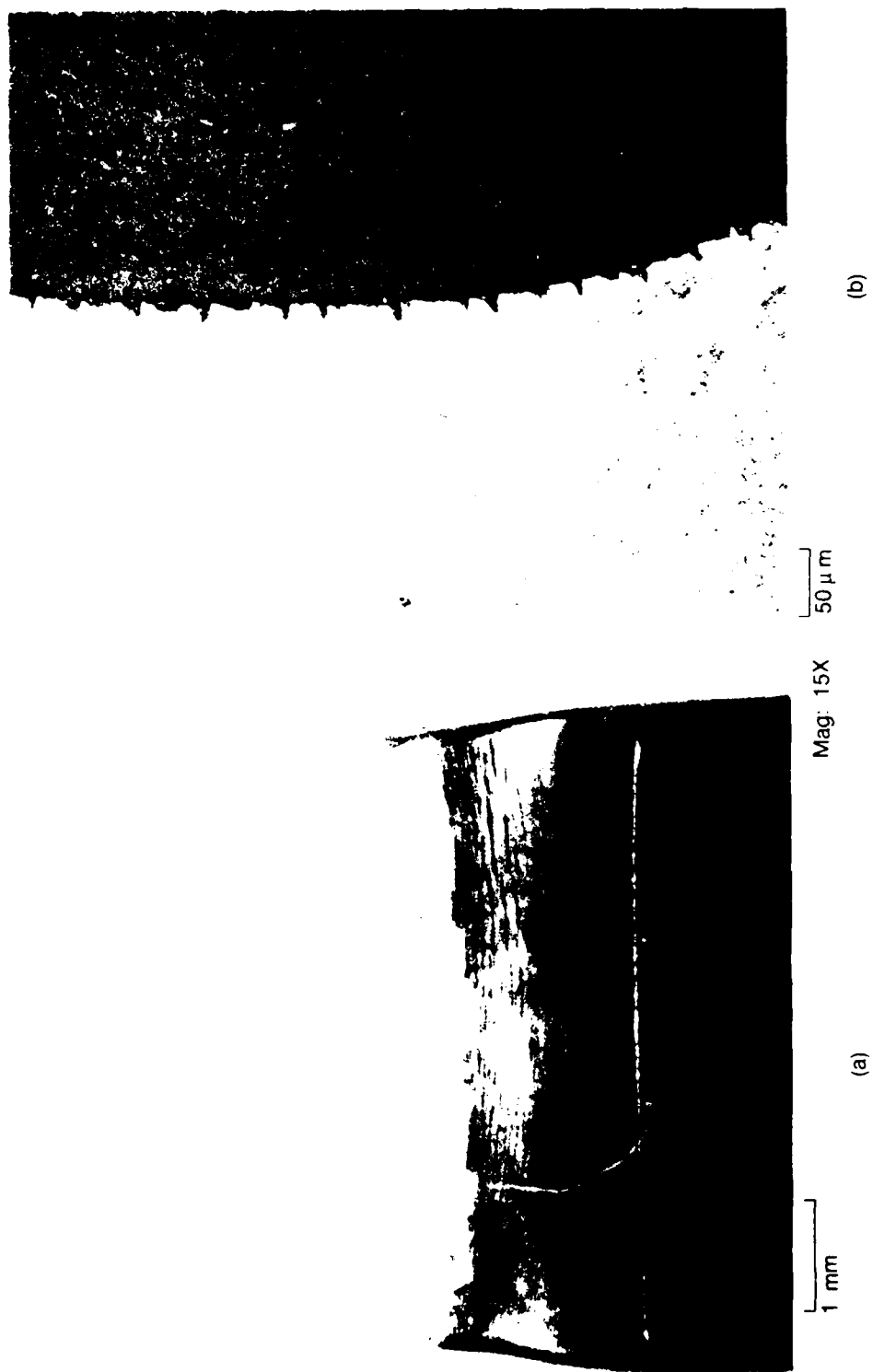


Figure 107. Notch Appearance of Specimen in Previous Figure at "Overstress" Final Failure Side Showing Brittle Cracking of Surface Layer



10 μ m

Ti-24Al-11Nb/Coated
(a)



10 μ m

Ti-25Al-10Nb-3V-1Mo/TiN
(b)

Figure 108. Notched LCF Coated Specimens



Figure 109. Ti-25Al-10Nb-3V-1Mo/TiN Coating Nodules

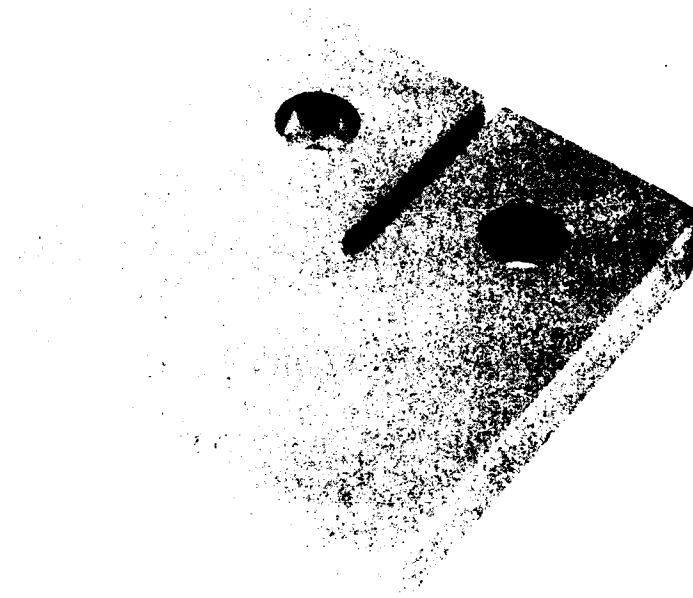


Figure 110. Compact Type (CT) Specimen

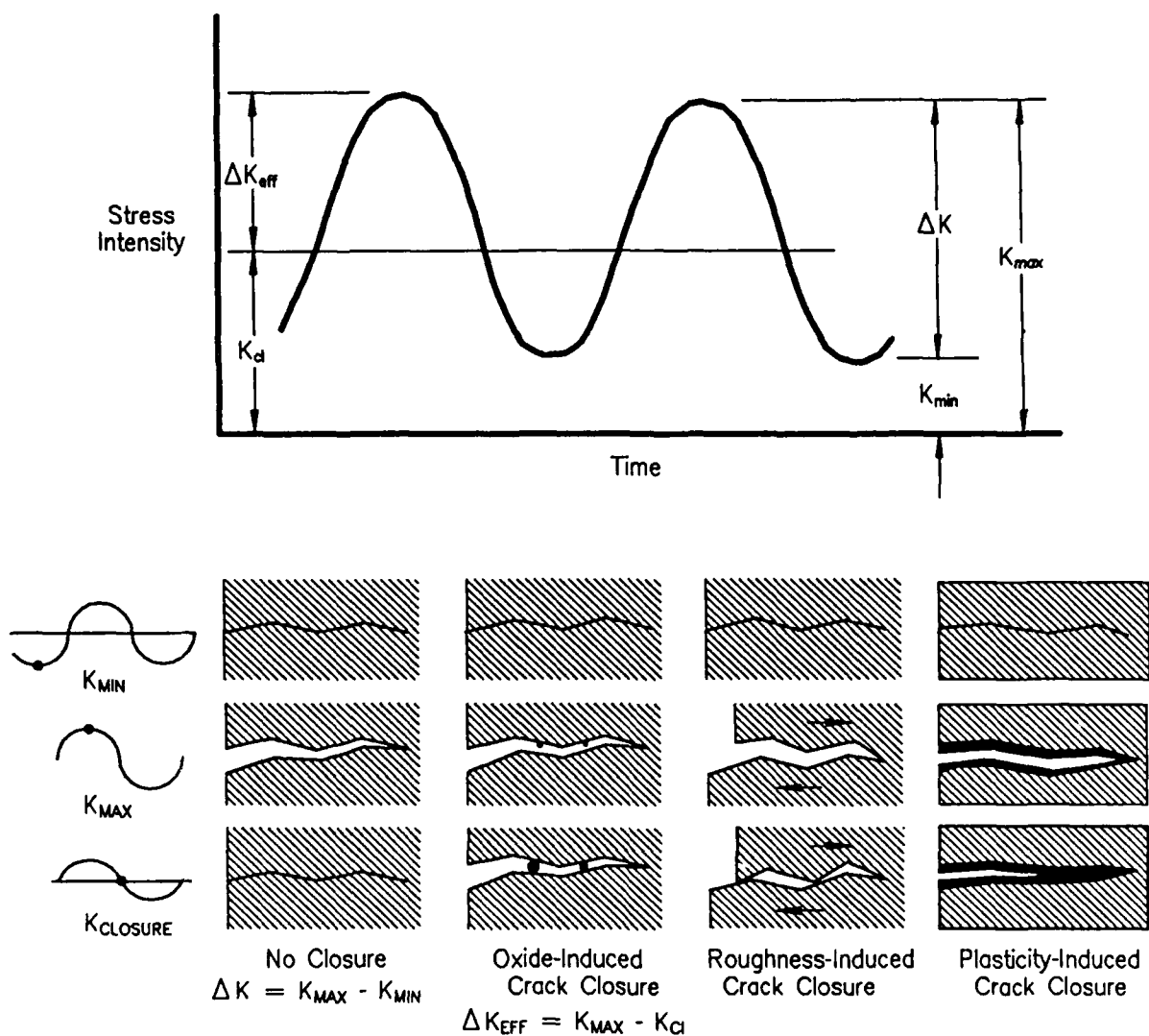
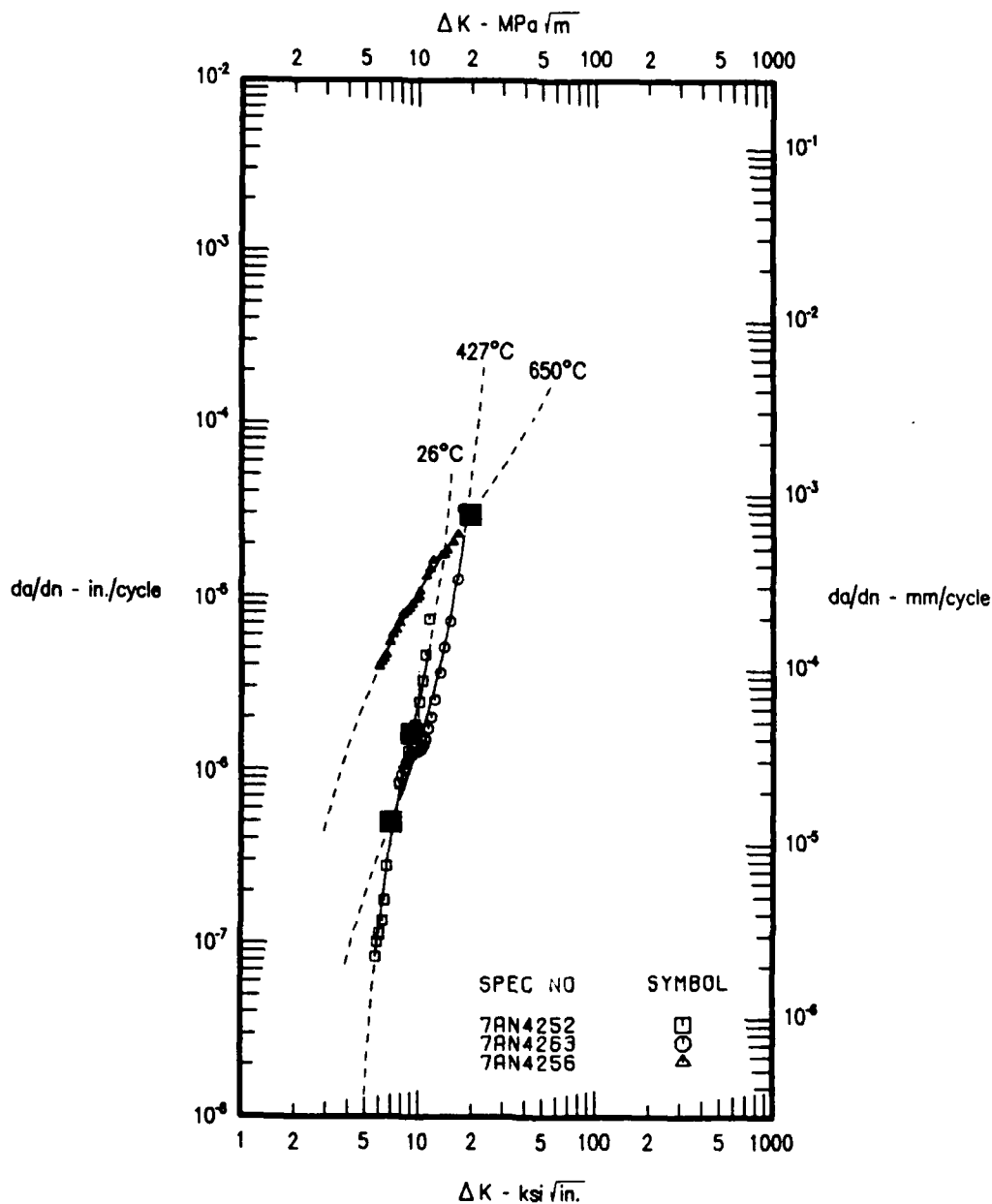


Figure 111. Effects of Closure on Stress Intensity Range and Commonly Recognized Closure Mechanisms



HYPERBOLIC SINE MODEL COEFFICIENTS

$$Y = C1 + \text{SINH}(C2 * (X + C3)) + C4$$

WHERE $Y = \text{LOG}(da/dn)$ AND $X = \text{LOG}(\Delta K)$

CURVE	SYMBOL	C1	C2	C3	C4	ΔK RANGE	NPTS	R ²	SEE
1	□	0.7000	6.4250	-0.9590	-5.7970	(5.54 , 11.57)	14	0.9926	0.0745
2	○	0.7000	3.7453	-0.8352	-6.3187	(7.67 , 18.22)	20	0.9562	0.0946
3	▲	0.7000	1.9860	-1.3030	-4.5200	(5.87 , 16.93)	23	0.9937	0.0203
TOTAL RSQRD =							0.9907	STD.ERROR.EST. =	0.0679

METRIC CONVERSIONS

C1 METRIC = C1 ENGLISH

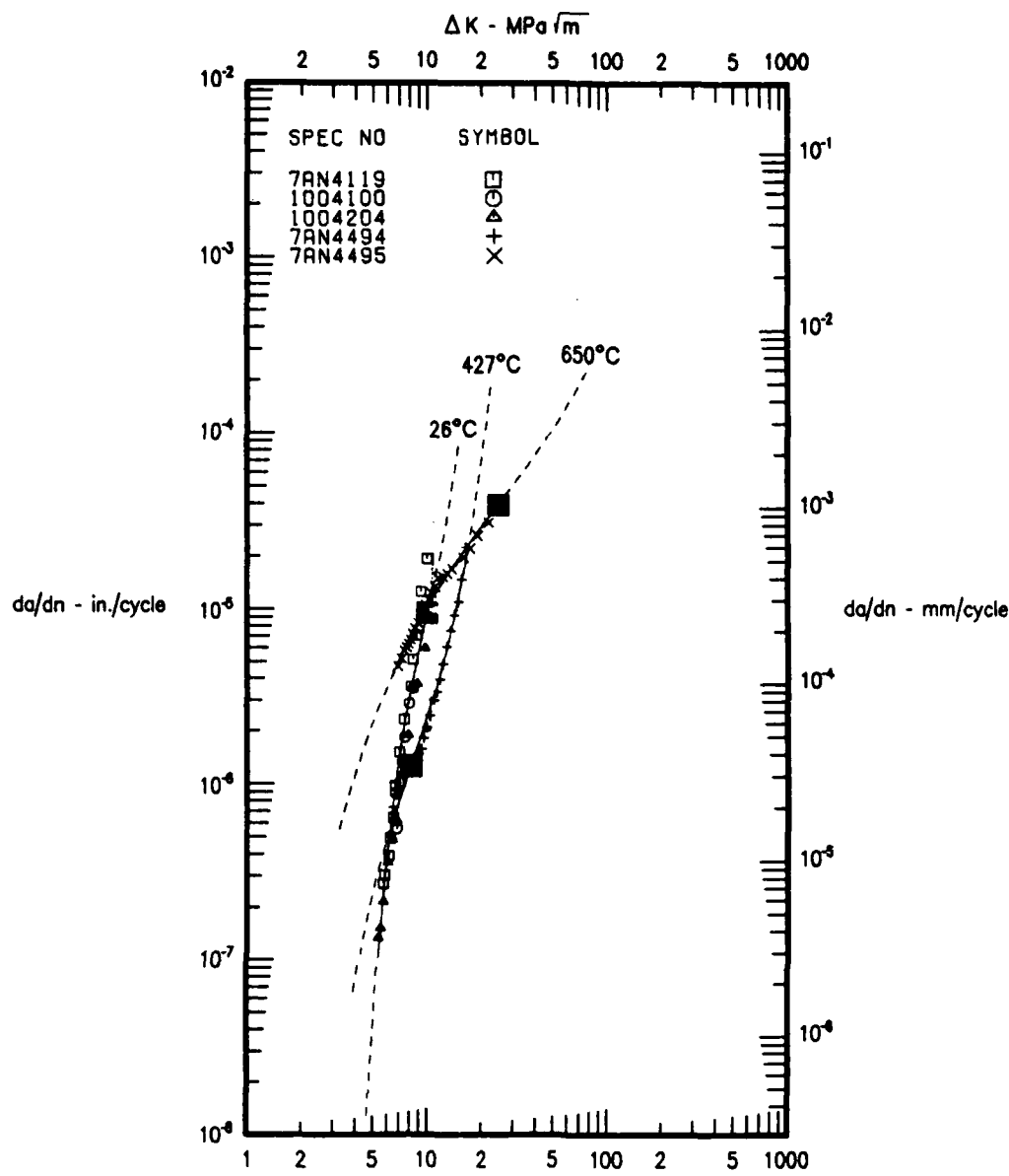
C2 METRIC = C2 ENGLISH

C3 METRIC = C3 ENGLISH * 0.040935

C4 METRIC = C4 ENGLISH * 1.40483

CURVE	SYMBOL	SPEC NO	MATERIAL	TEMP	ATM	FREQ	R	TYPE	THICK	REMARKS	P/A
1	□	7AN4252	Ti-24-11	RT	AIR	20 HZ	R=0.1	MCT	.371		0.805
2	○	7AN4263	Ti-24-11	800F	AIR	20 HZ	R=0.1	MCT	.373		0.953
3	▲	7AN4256	Ti-24-11	1200F	AIR	20 HZ	R=0.1	MCT	.375		0.981

Figure 112. Effects of Temperature, Ti-24Al-11Nb at R = 0.1, 20 Hz



HYPERBOLIC SINE MODEL COEFFICIENTS

$Y = C1 * \sinh(C2 * (X + C3)) + C4$

WHERE $Y = \log(da/dn)$ AND $X = \log(\Delta K)$

CURVE	SYMBOL	C1	C2	C3	C4	ΔK RANGE	NPTS	R ²	SEE
1	□	0.7000	6.7690	-0.9730	5.0160	5.15 - 9.23	30	0.9303	0.1629
2	△	0.7000	4.3110	-0.8910	5.0000	6.18 - 15.51	21	0.9063	0.0910
3	X	0.7000	1.9190	-1.3740	4.1870	6.19 - 20.02	21	0.9094	0.0364

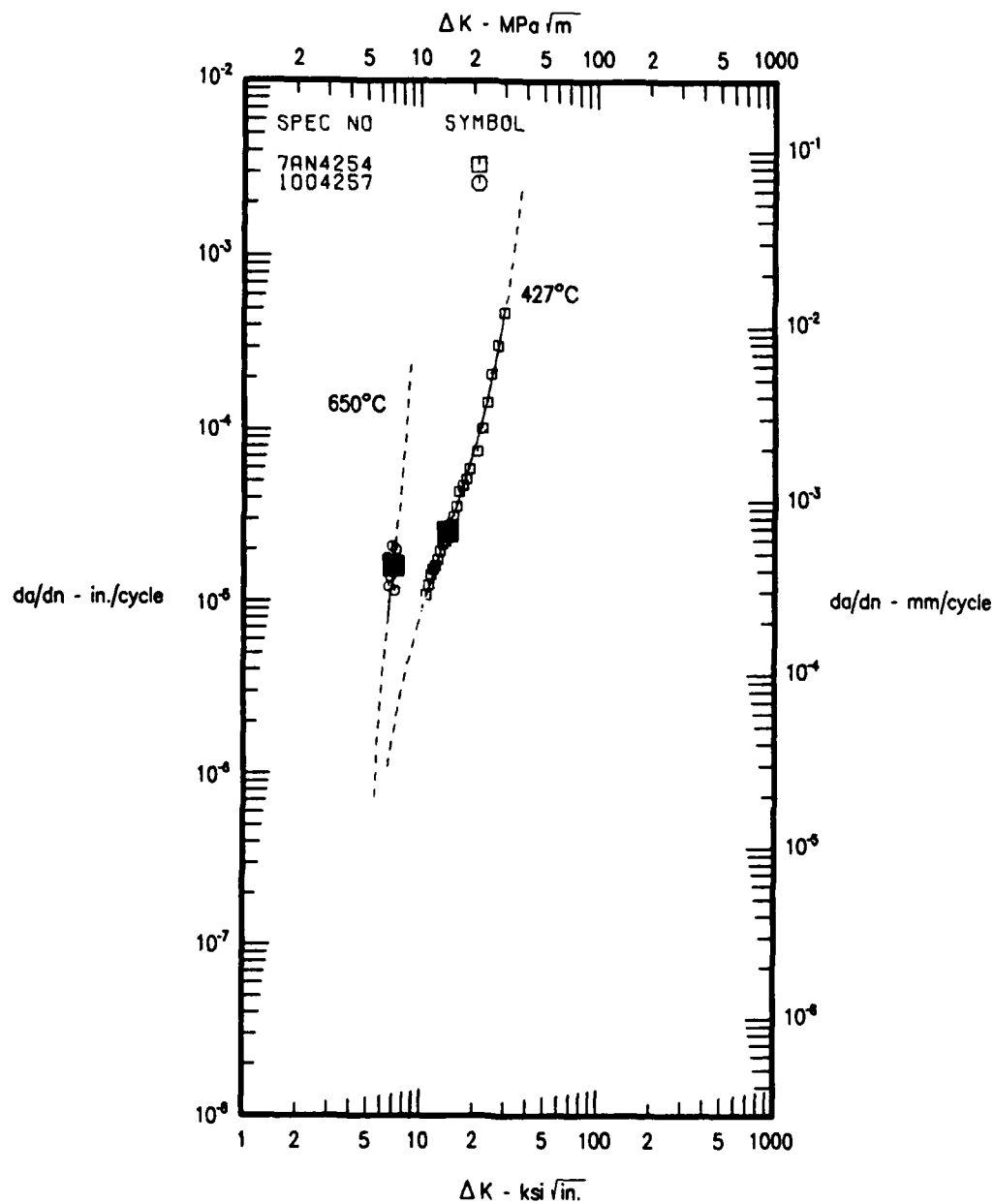
TOTAL RSQRD = 0.9721 STD.ERROR EST. = 0.1090

METRIC CONVERSIONS

C1 METRIC = C1 ENGLISH
 C2 METRIC = C2 ENGLISH
 C3 METRIC = C3 ENGLISH - 0.040935
 C4 METRIC = C4 ENGLISH + 1.40483

CURVE	SYMBOL	SPEC NO	MATERIAL	TEMP	ATM	FREQ	R	TYPE	THICK	REMARKS	P/A
1	□	7AN4119	Ti 25-10	RT	AIR	20 HZ	R=0.1	MCT	.374		1-232
1	△	1004100	Ti	RT	AIR	20 HZ	R=0.1	MCT	.370	Ti-25-10-3-1	0.683
1	△	1004204	Ti	RT	AIR	20 HZ	R=0.1	RAD MCT	.417	Ti 25-10-3-1	0.930
2	+	7AN4494		800F	AIR	20 HZ	R=0.1	MCT	.381	Ti25-10-3-1	0.987
3	X	7AN4495		1200F	AIR	20 HZ	R=0.1	MCT	.419	Ti 25-10-3-1	0.972

Figure 113. Effects of Temperature, Ti-25Al-10Nb-3V-1Mo at R = 0.1, 20 Hz



HYPERBOLIC SINE MODEL COEFFICIENTS

$$Y = C1 * \sinh(C2 * (X + C3)) + C4$$

WHERE Y = LOG10(da/dn) AND X = LOG10(K)

CURVE	SYMBOL	C1	C2	C3	C4	ΔK RANGE	NPTS	R ²	SEE
1	□	0.7000	4.1070	-1.1670	-4.5910	(10.95, 31.57)	23	0.9953	0.0332
2	○	0.7000	13.0000	-0.8500	-4.7900	(6.51, 7.38)	6	0.0415	0.2994
TOTAL RSQRD = 0.9561							STD.ERROR.EST. = 0.1125		

METRIC CONVERSIONS

$$C1 \text{ METRIC} = C1 \text{ ENGLISH}$$

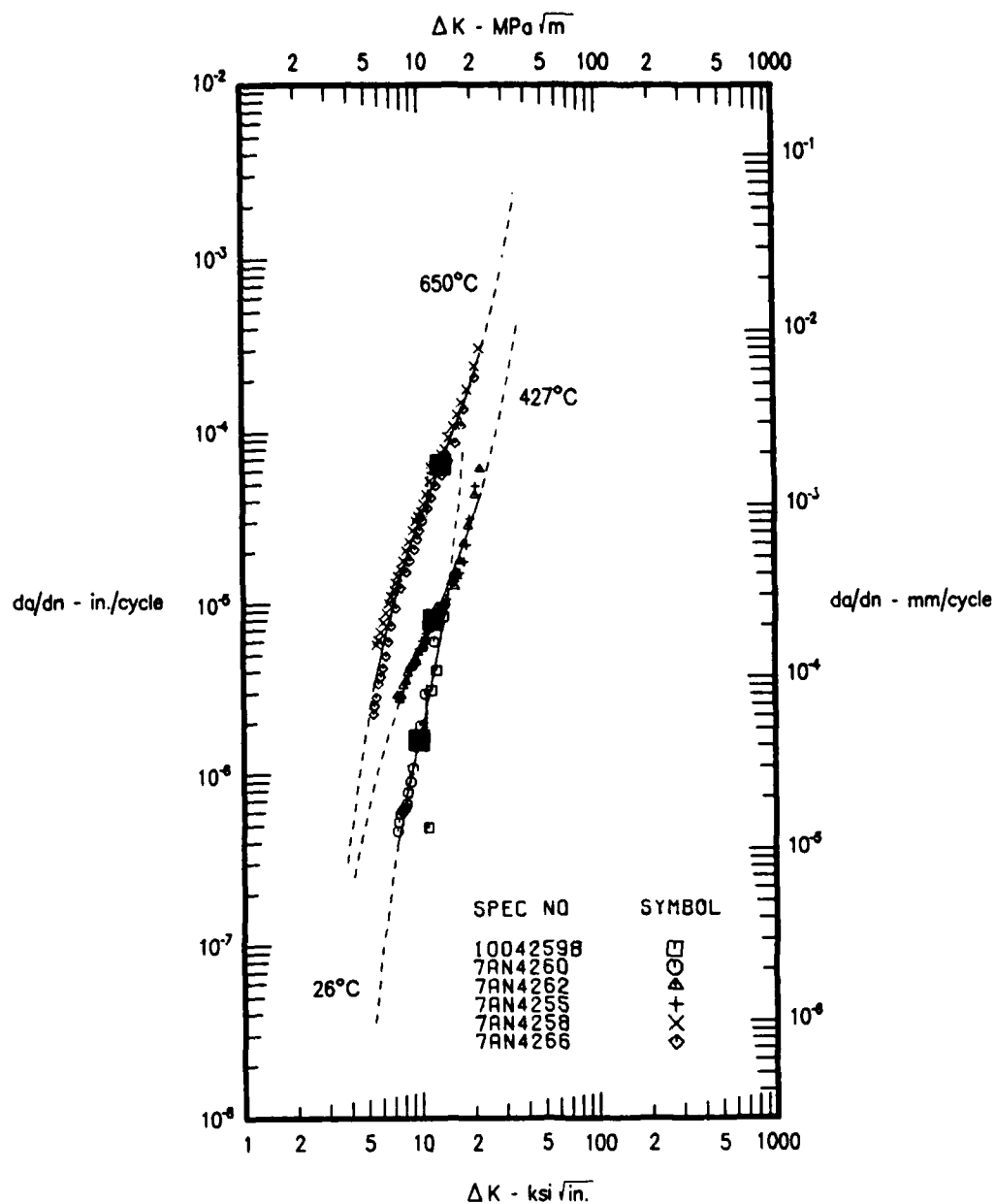
$$C2 \text{ METRIC} = C2 \text{ ENGLISH}$$

$$C3 \text{ METRIC} = C3 \text{ ENGLISH} - 0.040935$$

$$C4 \text{ METRIC} = C4 \text{ ENGLISH} + 1.40483$$

CURVE	SYMBOL	SPEC NO	MATERIAL	TEMP	ATH	FREQ	R	TYPE	THICK	REMARKS	P.R
1	□	7AN4254	11-24-11	800F	AIR	2M DNL	R=0.1	MCT	0.375	11-24-11	0.854
2	○	1004257		1200F	AIR	2 M/D	R=0.1	MCT	0.379	11-24-11	1.247

Figure 114. Effects of Temperature, Ti-24Al-11Nb at R = 0.1, 120-Second Dwell



HYPERBOLIC SINE MODEL COEFFICIENTS

$$Y = C1 * \text{SINHIC2} * (X + C3) + C4$$

WHERE Y = LOG(da/dn) AND X = LOG(ΔK)

CURVE	SYMBOL	C1	C2	C3	C4	ΔK RANGE	NPTS	R ²	SEE
1	□	0.7000	6.4250	0.9590	5.7970	1.675 - 12.360	18	0.7649	0.2119
2	△	0.7000	1.1180	1.0330	5.0990	1.670 - 20.360	44	0.9681	0.0657
3	×	0.7000	1.5670	-1.0780	-4.1840	1.484 - 20.111	59	0.9738	0.0899

TOTAL RSQRD = 0.9736

STD.ERROR.EST. = 0.1076

METRIC CONVERSIONS

C1 METRIC = C1 ENGLISH

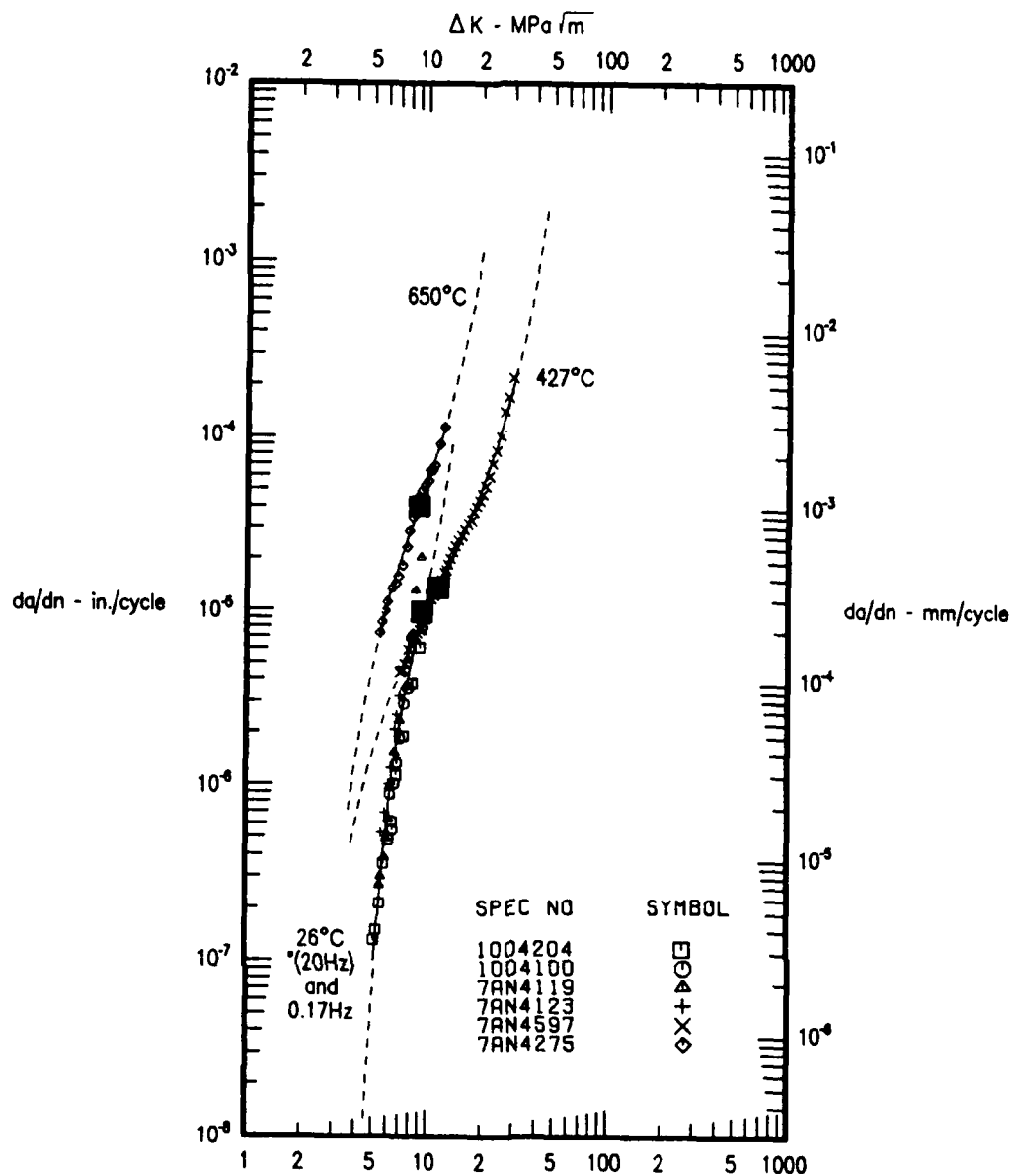
C2 METRIC = C2 ENGLISH

C3 METRIC = C3 ENGLISH - 0.040935

C4 METRIC = C4 ENGLISH + 1.40483

CURVE	SYMBOL	SPEC NO	MATERIAL	TEMP	ATM	FREQ	R	TYPE	THICK	REMARKS	P/A
1	□	10042598	TI-24-11	RT	AIR	10 CPM	R=0.1	MCT	.501		0.791
1	○	7AN4260	TI-24-11	RT	AIR	10 CPM	R=0.1	MCT	.378	TI-24-11	0.980
2	△	7AN4262		800F	AIR	10 CPM	R=0.1	MCT	.510	TI-24-11	1.013
2	+	7AN4255	TI-24-11	800F	AIR	10 CPM	R=0.1	MCT	.377		0.948
3	×	7AN4258		1200F	AIR	10 CPM	R=0.1	MCT	.377	TI-24-11	1.319
3	◇	7AN4266	TI-24-11	1200F	AIR	10 CPM	R=0.1	MCT	.511		0.733

Figure 115. Effects of Temperature, Ti-24Al-11Nb at R = 0.1, 0.17 Hz



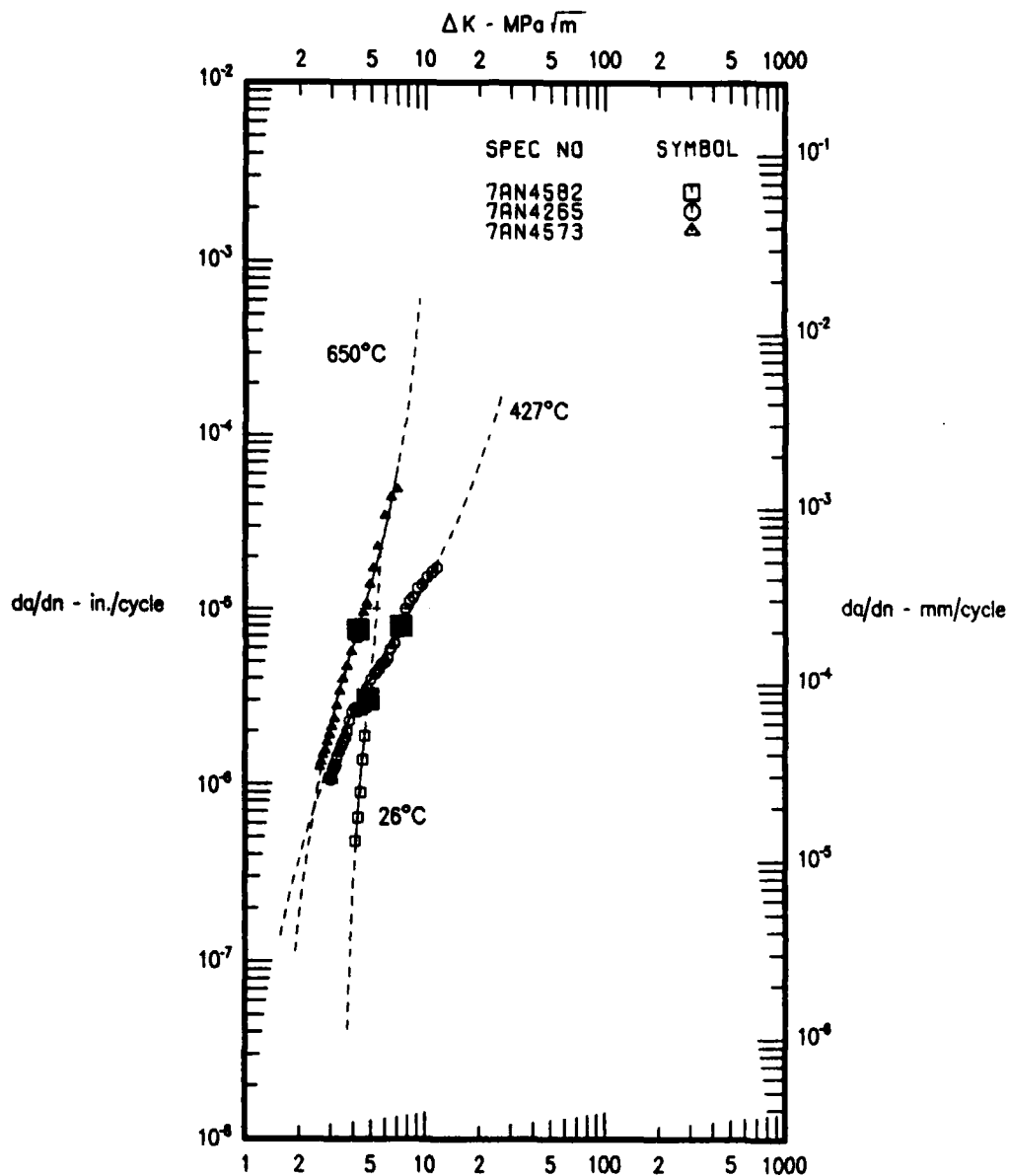
$\Delta K - \text{ksi} \sqrt{\text{in.}}$
HYPERBOLIC SINE MODEL COEFFICIENTS
 $Y = C1 + \text{SINH}(C2 * (X + C3)) + C4$
WHERE $Y = \text{LOG}(da/dn)$ AND $X = \text{LOG}(\Delta K)$

CURVE	SYMBOL	C1	C2	C3	C4	ΔK RANGE	NPIS	R ²	SIE
1	□ ○ ▲	0.7000	6.7681	0.3732	-0.0162	5.15 - 9.23	38	0.9139	0.1606
2	x	0.7000	3.0146	-1.0660	-4.8780	7.08 - 30.83	44	0.9972	0.0240
3	◇	0.7000	4.1822	-0.9530	-4.4068	5.39 - 12.54	21	0.9916	0.0358
TOTAL RSQRD = 0.9838							STD.ERROR.EST. = 0.1005		

METRIC CONVERSIONS
C1 METRIC = C1 ENGLISH
C2 METRIC = C2 ENGLISH
C3 METRIC = C3 ENGLISH - 0.040935
C4 METRIC = C4 ENGLISH + 1.40483

CURVE	SYMBOL	SPEC NO	MATERIAL	TEMP	ATM	FREQ	R	TYPE	THICK	REMARKS	P/A
1	□	1004204	TI	RT	AIR	20 HZ	R=0.1	RAD MCT	.417	TI 25-10-3-1	0.935
1	○	1004100	TI	RT	AIR	20 HZ	R=0.1	MCT	.370	TI-25-10-3-1	0.586
1	▲	7AN4119	TI 25-10	RT	AIR	20 HZ	R=0.1	MCT	.374		1.230
1	+	7AN4123	TI-25103	80F	AIR	10 CPM	R=0.1	MCT	.371	TI-25-10-3	1.428
2	x	7AN4597	TI251031	800F	AIR	10 CPM	R=0.1	MCT	.504		1.032
3	◇	7AN4275		1200F	AIR	10 CPM	R=0.1	MCT	.365	TI 25-10-3-1	0.998

Figure 116. Effects of Temperature, Ti-25Al-10Nb-3V-1Mo, at R = 0.1, 0.17 Hz



HYPERBOLIC SINE MODEL COEFFICIENTS

$$Y = C1 + \text{SINH}(C2 * (X + C3)) + C4$$

WHERE Y = LOG(da/dn) AND X = LOG(ΔK)

CURVE	SYMBOL	C1	C2	C3	C4	ΔK RANGE	NPTS	R ²	RFF
1	□	0.7000	13.2680	-0.6630	-5.5200	(4.02 , 4.65)	6	0.9435	0.0891
2	○	0.7000	2.3730	-0.6720	-6.1010	(2.88 , 12.11)	38	0.9941	0.0555
3	△	0.7000	4.6180	-0.6240	-5.1210	(2.54 , 7.19)	23	0.9936	0.0426
TOTAL RSQRD = 0.9904							STD.ERROR.EST. = 0.0538		

METRIC CONVERSIONS

C1 METRIC = C1 ENGLISH

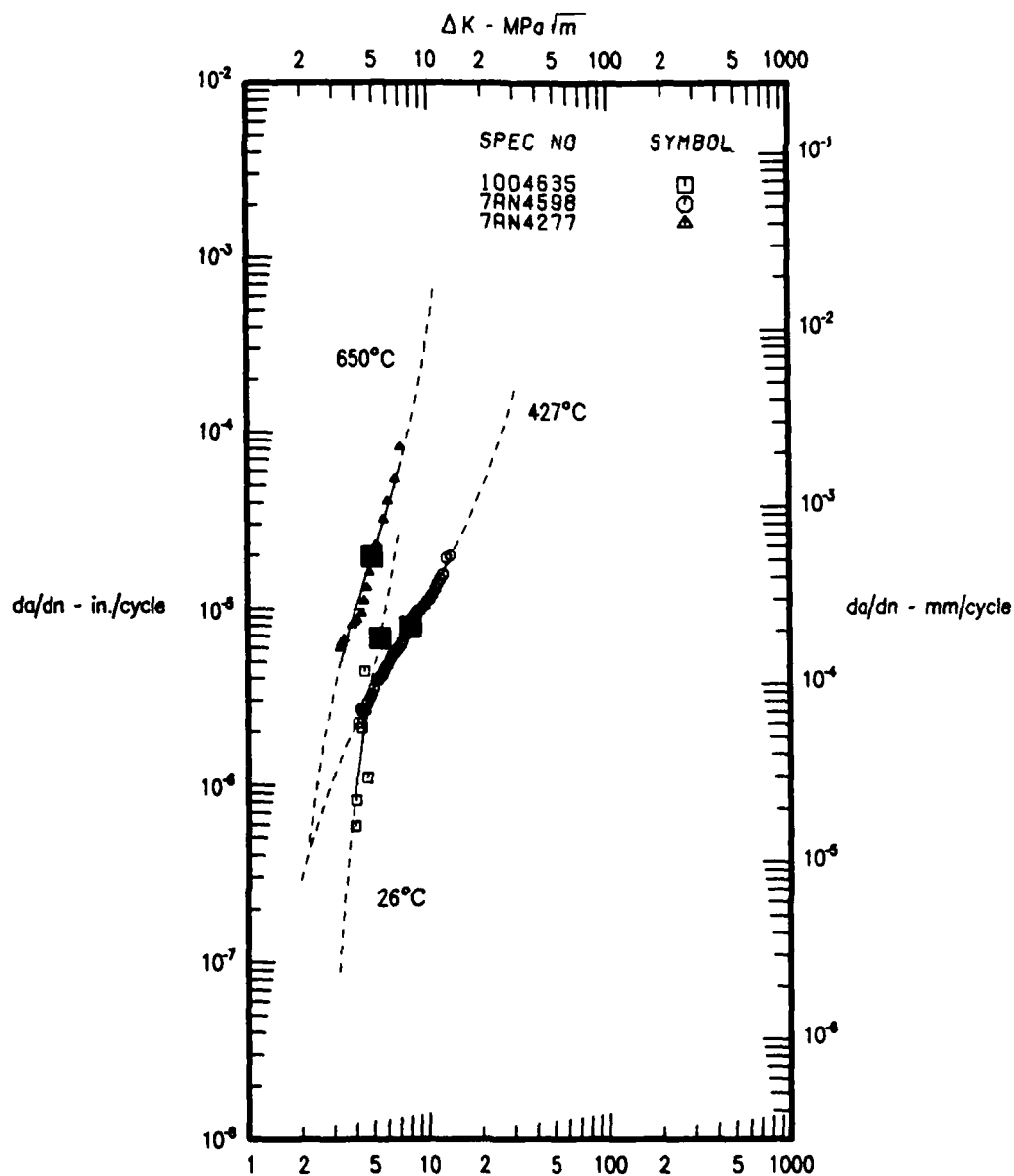
C2 METRIC = C2 ENGLISH

C3 METRIC = C3 ENGLISH - 0.040935

C4 METRIC = C4 ENGLISH + 1.40483

CURVE	SYMBOL	SPEC NO	MATERIAL	TEMP	ATM	FREQ	R	TYPE	THICK	REMARKS	P/R
1	□	7AN4582	T12411	RT	AIR	20HZ	R=0.7	MCT	.497		1.186
2	○	7AN4265	T1 24-11	800F	AIR	10 CPM	R=.7	MCT	.376		0.914
3	△	7AN4573	T1 24-11	1200F	AIR	10 CPM	R=.7	MCT	.375	T1 24-11	0.976

Figure 117. Effects of Temperature, Ti-24Al-11Nb at R = 0.7



HYPERBOLIC SINE MODEL COEFFICIENTS

$$Y = C1 \cdot \sinh(C2 \cdot (X + C3)) + C4$$

WHERE $Y = \text{LOG}(da/dn)$ AND $X = \text{LOG}(\Delta K)$

CURVE	SYMBOL	C1	C2	C3	C4	ΔK RANGE	NPTS	R ²	SII
1	□	0.7000	7.2490	-0.7360	-5.1680	(3.87 , 4.59)	6	0.9612	0.3379
2	○	0.7000	2.3250	-0.9100	-5.1000	(4.17 , 13.84)	38	0.9960	0.0161
3	△	0.7000	4.2330	-0.6930	-4.7000	(3.16 , 7.17)	16	0.9540	0.0822

TOTAL RSQRD = 0.9542 STD.ERROR.EST. = 0.0928

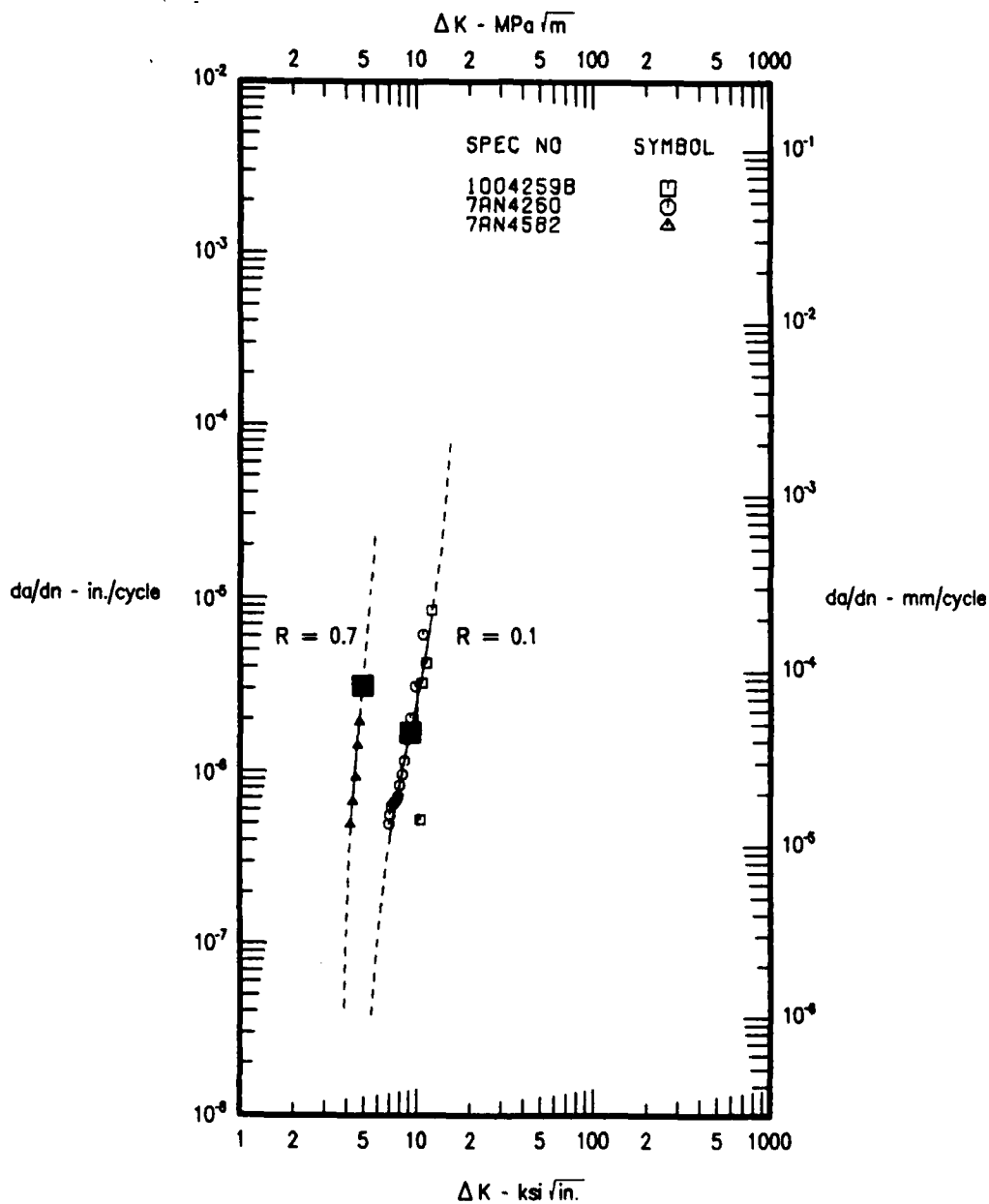
METRIC CONVERSIONS

C1 METRIC = C1 ENGLISH C2 METRIC = C2 ENGLISH

C3 METRIC = C3 ENGLISH - 0.040935 C4 METRIC = C4 ENGLISH + 1.40483

CURVE	SYMBOL	SPEC NO	MATERIAL	TEMP	ATM	FREQ	R	TYPE	THICK	REMARKS	P/A
1	□	1004635	T1	RT	AIR	10 CPM	R=0.7	MCT	.375	T1-25-10-3-1	1.908
2	○	7AN4598	T1251031	800F	AIR	10 CPM	R=0.7	MCT	.502		1.021
3	△	7AN4277		1200F	AIR	10 CPM	R=0.7	MCT	.369	T1 25-10 3-1	1.064

Figure 118. Effects of Temperature, Ti-25Al-10Nb-3V-1Mo, at R = 0.7, 0.17 Hz



HYPERBOLIC SINE MODEL COEFFICIENTS

$$Y = C1 + \text{SINH}(C2 * (X + C3)) + C4$$

WHERE $Y = \text{LOG}(da/dn)$ AND $X = \text{LOG}(\Delta K)$

CURVE	SYMBOL	C1	C2	C3	C4	ΔK RANGE	NPTS	R ²	SEE
1	□ ○	0.7000	6.4250	-0.9590	-5.7970	(6.75 , 12.36)	18	0.7649	0.2139
2	▲	0.7000	13.2660	-0.6830	-5.5200	(4.02 , 4.65)	6	0.9435	0.0891
TOTAL RSQD = 0.7872							STD.ERROR.EST. = 0.1987		

METRIC CONVERSIONS

C1 METRIC = C1 ENGLISH

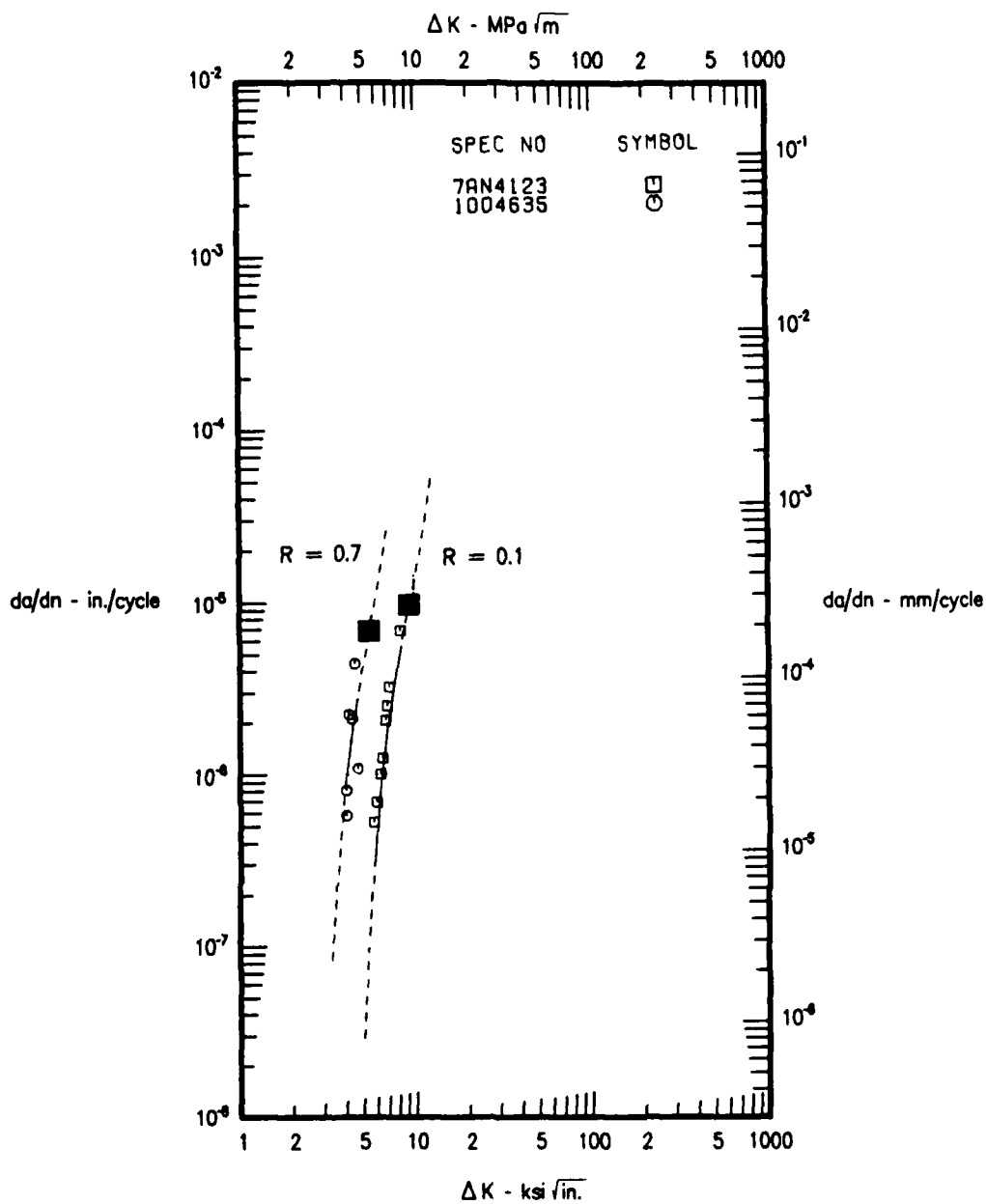
C2 METRIC = C2 ENGLISH

C3 METRIC = C3 ENGLISH - 0.040935

C4 METRIC = C4 ENGLISH + 1.40483

CURVE	SYMBOL	SPEC NO	MATERIAL	TEMP	ATM	FREQ	R	TYPE	THICK	REMARKS	P/A
1	□	10042598	Ti-24-11	RT	AIR	10 CPM	R=-1	HCT	.501		0.791
1	○	7AN4260	Ti-2411	RT	AIR	10 CPM	R=-1	HCT	.378	Ti-24-11	0.980
2	▲	7AN4582	Ti2411	RT	AIR	20HZ	R=0.7	HCT	.497		1.186

Figure 119. Effects of Stress Ratio, Ti-24Al-11Nb, 26°C (80°F)



HYPERBOLIC SINE MODEL COEFFICIENTS

$$Y = C1 * \text{SINH}(C2 * (X + C3)) + C4$$

WHERE $Y = \text{LOG}(da/dn)$ AND $X = \text{LOG}(\Delta K)$

CURVE	SYMBOL	C1	C2	C3	C4	ΔK RANGE	NPTS	R ²	SEE
1	\square	0.7000	6.7690	-0.9730	5.0160	5.60 - 8.35	9	0.9804	0.1934
2	\circ	0.7000	7.2490	-0.7360	-5.1680	3.87 - 4.59	6	0.3612	0.3379
TOTAL RSQRB = 0.7197									STD.ERROR.FST = 0.2573

METRIC CONVERSIONS

C1 METRIC = C1 ENGLISH

C2 METRIC = C2 ENGLISH

C3 METRIC = C3 ENGLISH - 0.040935

C4 METRIC = C4 ENGLISH + 1.40483

CURVE	SYMBOL	SPEC NO	MATERIAL	TEMP	ATM	FREQ	R	TYPE	THICK	REMARKS	P/R
1	\square	7AN4123	Ti-25103	80F	AIR	10 CPM	R=0.1	MCT	.371	Ti-25-10-3	1.422
2	\circ	1004635	Ti	RT	AIR	10 CPM	R=0.7	MCT	.375	Ti-25-10-3-1	1.308

Figure 120. Effects of Stress Ratio, Ti-25Al-10Nb-3V-1Mo, 26°C (80°F), 0.17 Hz

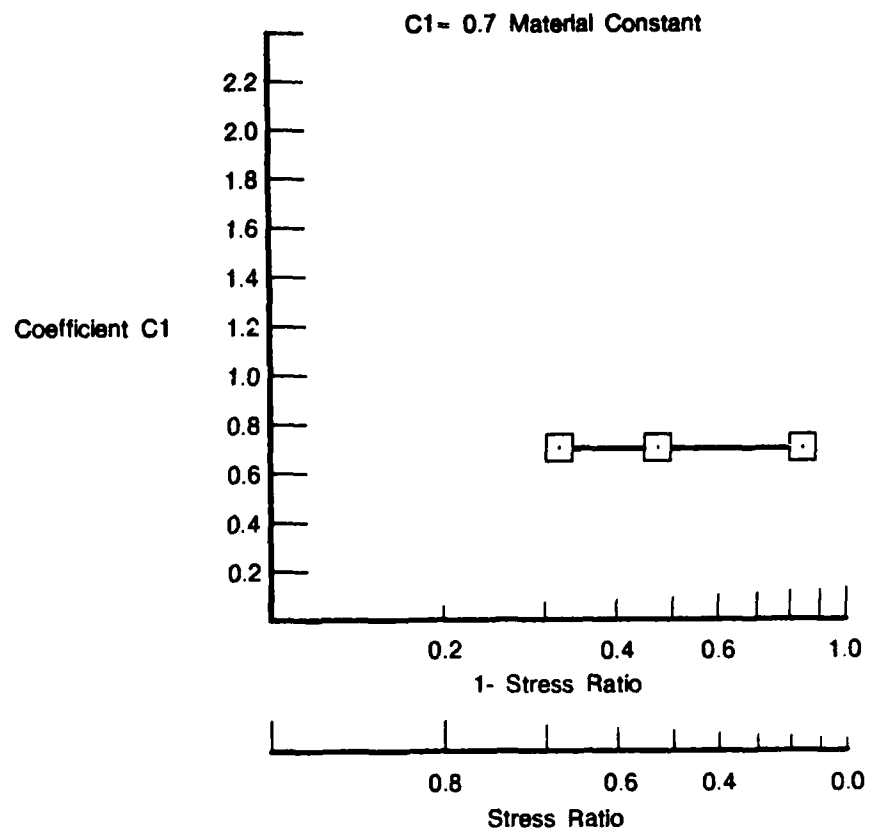


Figure 121. Stress Ratio Model Coefficient for Constant C1 Versus Stress Ratio

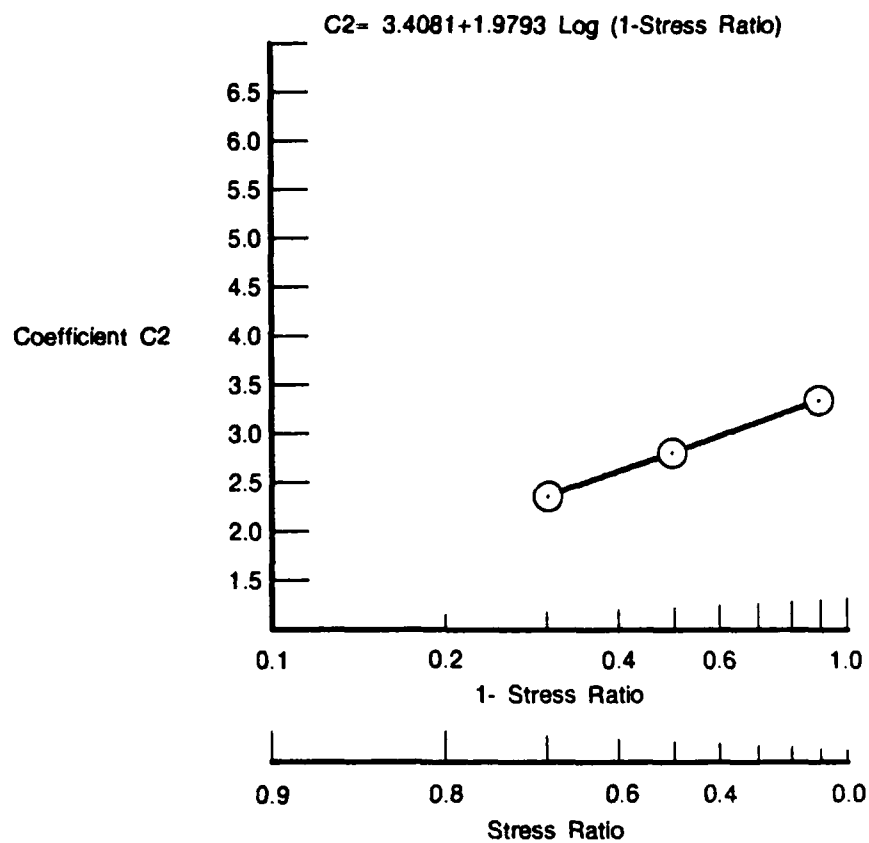


Figure 122. Stress Ratio Model Coefficient for Constant C2 Versus Stress Ratio

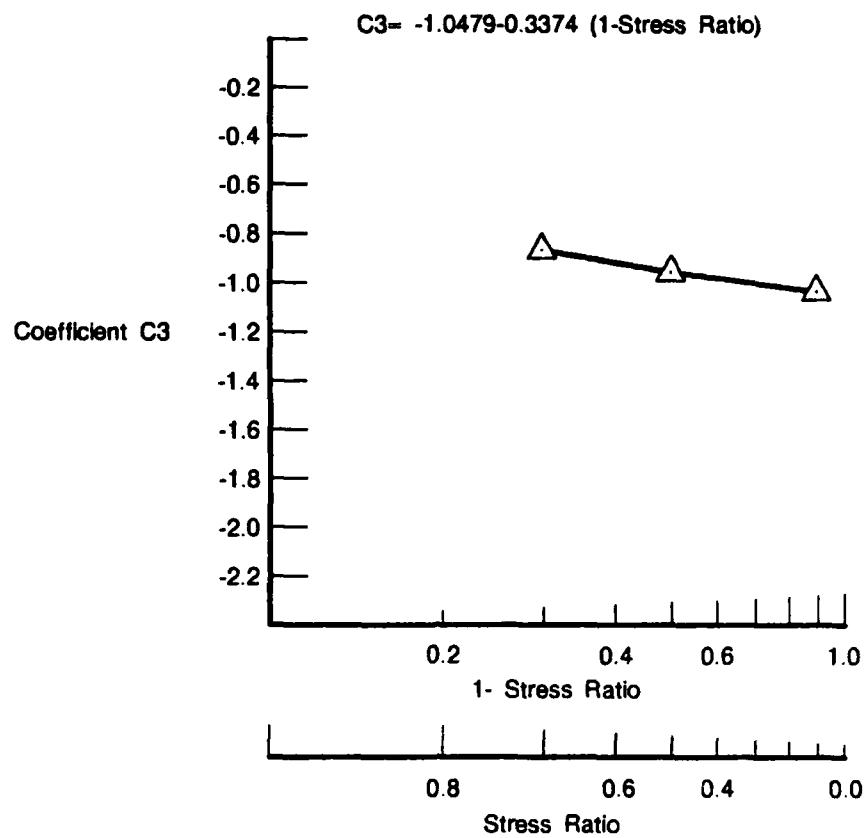


Figure 123. Stress Ratio Model Coefficient for Constant C3 Versus Stress Ratio

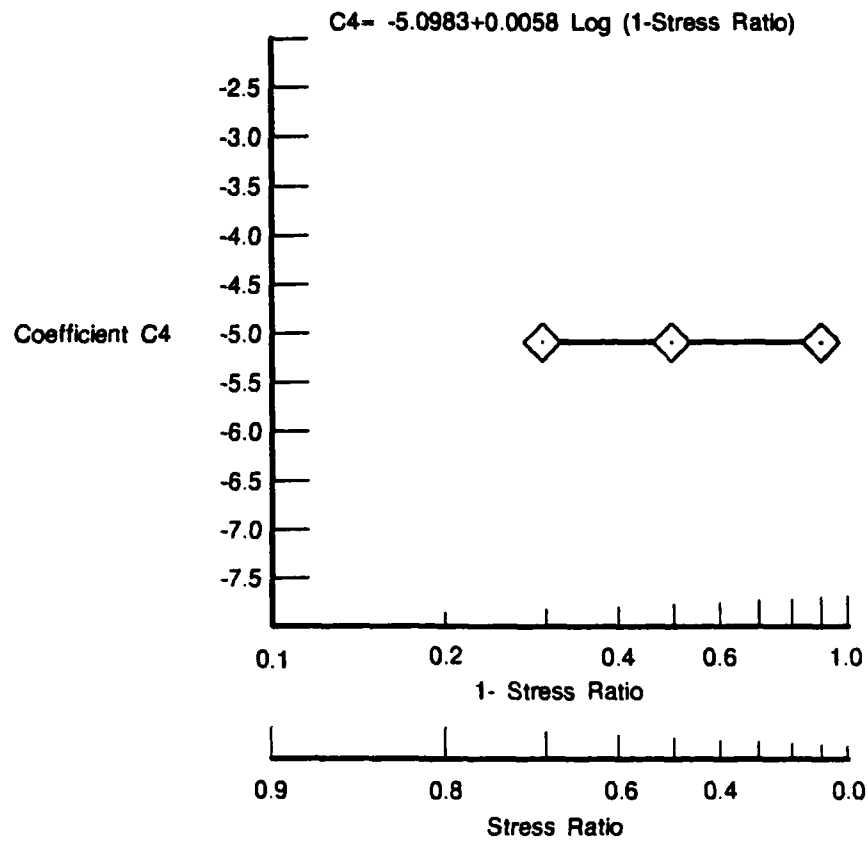
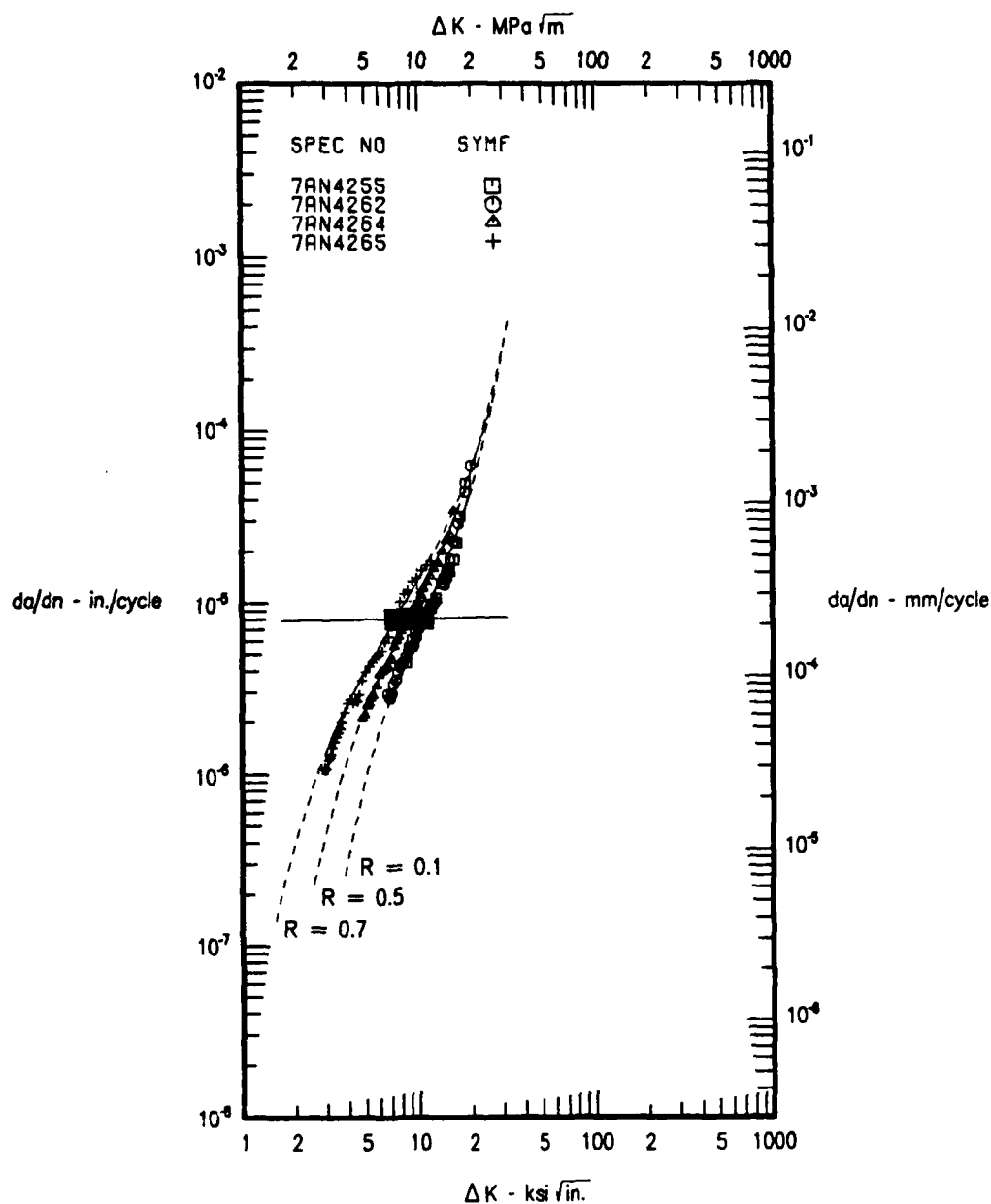


Figure 124. Stress Ratio Model Coefficient for Constant C4 Versus Stress Ratio



HYPERBOLIC SINE MODEL COEFFICIENTS

$$Y = C1 * \text{SINH}(C2 * (X + C3)) + C4$$

WHERE Y = LOG(da/dN) AND X = LOG(K)

CURVE	SYMBOL	C1	C2	C3	C4	Δ K RANGE	NPTS	R ²	SEE
1	□	0.7000	3.3175	-1.0325	-5.0986	(6.70 , 20.36)	44	0.9677	0.0623
2	▲	0.7000	2.8123	-0.9463	-5.1001	(4.78 , 16.32)	33	0.9967	0.0214
3	+	0.7000	2.3732	-0.8715	-5.1014	(2.88 , 12.11)	38	0.9937	0.0559
TOTAL RSQRD =						0.9860	STD.ERROR.EST. =		0.0516

METRIC CONVERSIONS

$$C1 \text{ METRIC} = C1 \text{ ENGLISH}$$

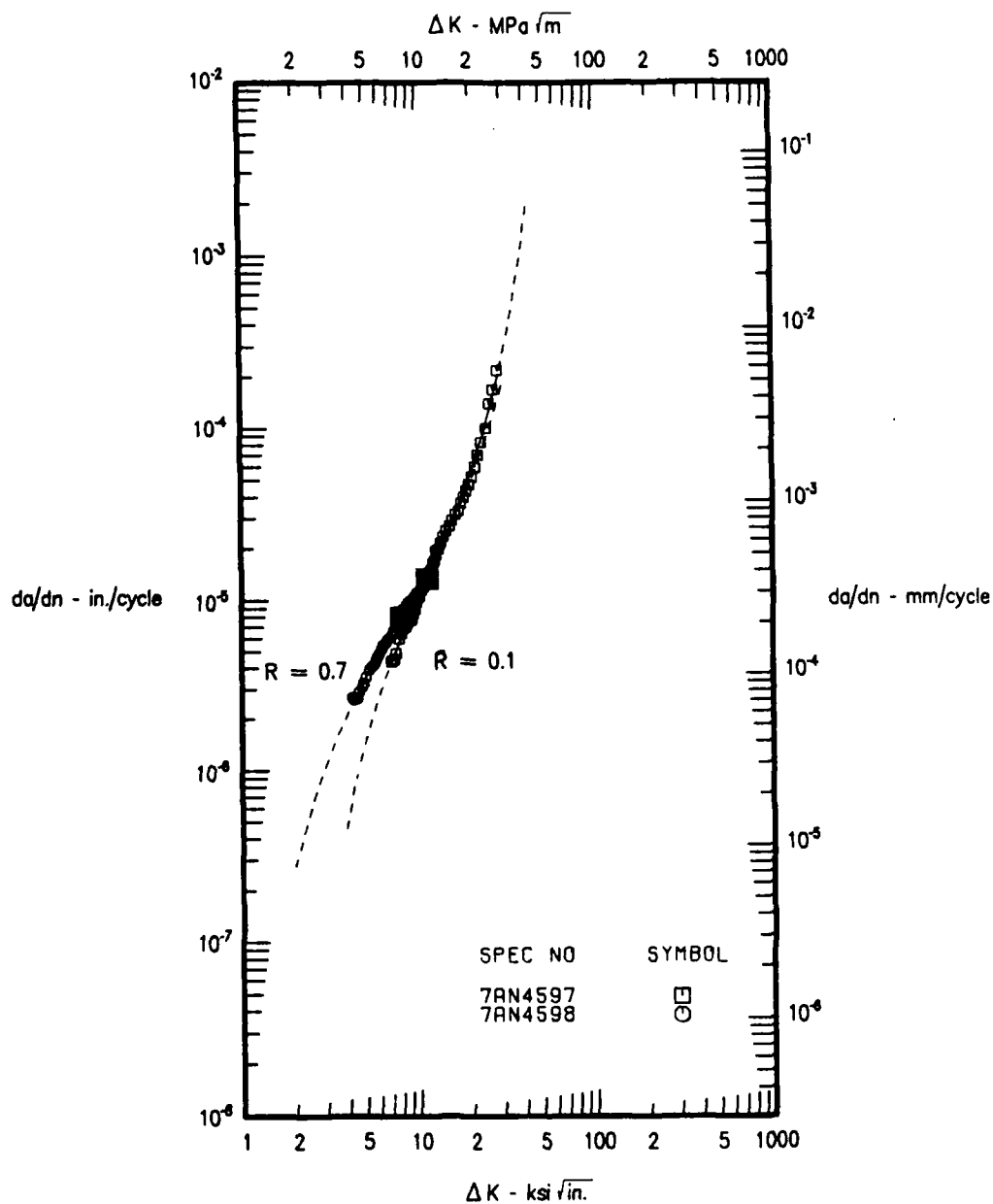
$$C2 \text{ METRIC} = C2 \text{ ENGLISH}$$

$$C3 \text{ METRIC} = C3 \text{ ENGLISH} - 0.040935$$

$$C4 \text{ METRIC} = C4 \text{ ENGLISH} + 1.40483$$

CURVE	SYMBOL	SPEC NO	MATERIAL	TEMP	ATM	FREQ	R	TYPE	THICK	REMARKS	P/R
1	□	7AN4255	TI-24-11	800F	AIR	10 CPM	R=.1	MCT	.377		0.944
1	○	7AN4262		800F	AIR	10 CPM	R=.1	MCT	.510	TI-24-11	1.009
2	△	7AN4264	TI-24-11	800F	AIR	10 CPM	R=.5	MCT	.373		0.963
3	+	7AN4265	TI 24-11	800F	AIR	10 CPM	R=.7	MCT	.376		0.913

Figure 125. Stress Ratio Model Demonstration for Ti-24Al-11Nb at 427°C (800°F) and 0.17 Hz



HYPERBOLIC SINE MODEL COEFFICIENTS

$$Y = C1 + \text{SINH}(C2 * (X + C3)) + C4$$

WHERE $Y = \text{LOG}(da/dn)$ AND $X = \text{LOG}(\Delta K)$

CURVE	SYMBOL	C1	C2	C3	C4	ΔK RANGE	NPTS	R ²	SEE
1	□	0.7000	3.0150	-1.0660	-4.8780	1 7.08 , 30.831	44	0.9971	0.0240
2	○	0.7000	2.3250	-0.9100	-5.1000	1 4.17 , 13.841	38	0.9960	0.0161
TOTAL RSQD =						0.9977	STD. ERROR EST. =		0.0208

METRIC CONVERSIONS

C1 METRIC = C1 ENGLISH

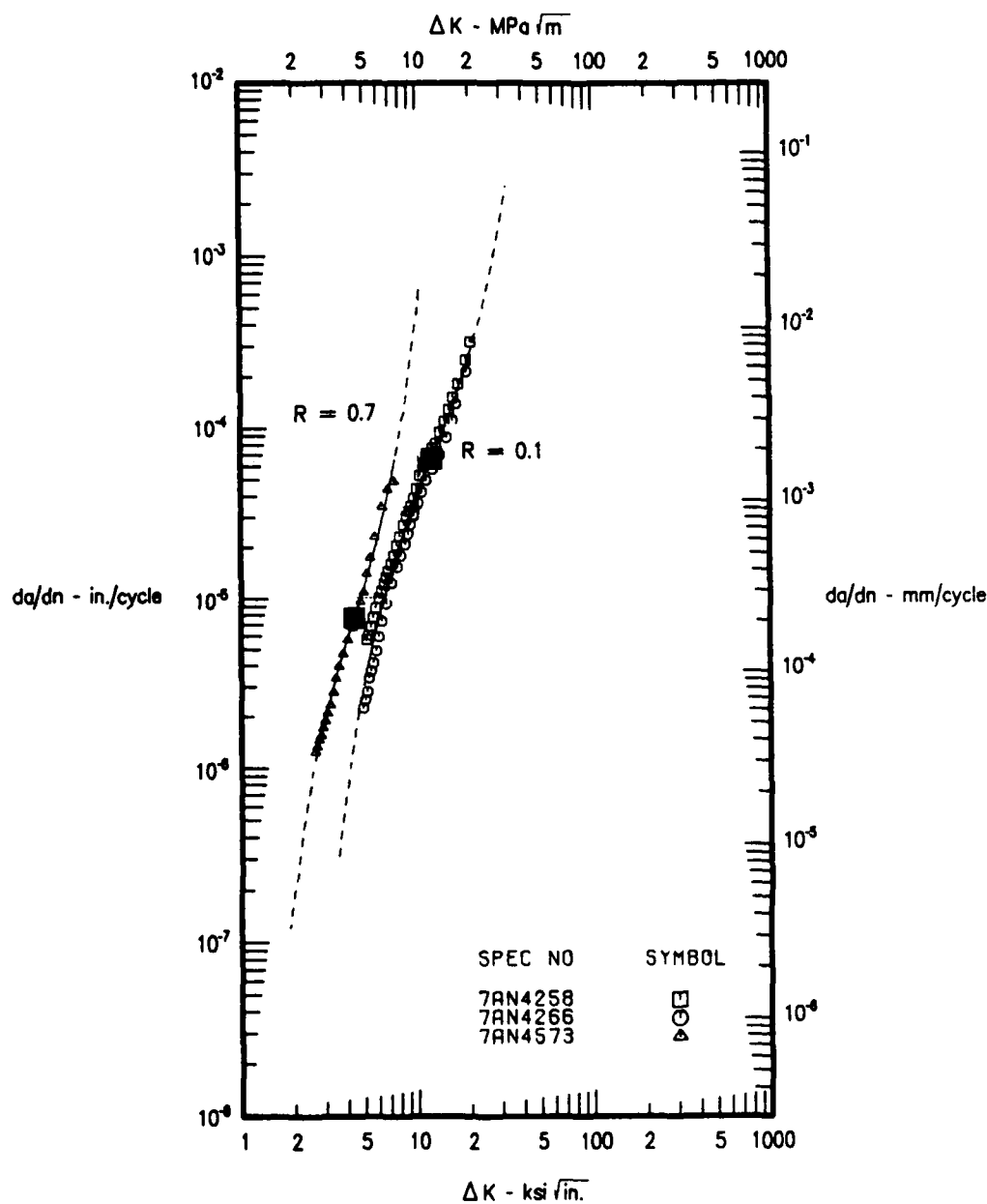
C2 METRIC = C2 ENGLISH

C3 METRIC = C3 ENGLISH - 0.040935

C4 METRIC = C4 ENGLISH + 1.40493

CURVE	SYMBOL	SPEC NO	MATERIAL	TEMP	ATM	FREQ	R	TYPE	THIN	REMARKS	P/R
1	□	7AN4597	T1251031	800F	AIR	10 CPM	R=0.1	MCT	.504		1.032
2	○	7AN4598	T1251031	800F	AIR	10 CPM	R=.7	MCT	.502		1.021

Figure 126. Effects of Stress Ratio on Ti-25Al-10Nb-3V-1Mo at 427°C (800°F) and 0.17 Hz



HYPERBOLIC SINE MODEL COEFFICIENTS

$$Y = C1 + \text{SINH}(C2 * (X + C3)) * C4$$

WHERE $Y = \text{LOG}(da/dn)$ AND $X = \text{LOG}(\Delta K)$

CURVE	SYMBOL	C1	C2	C3	C4	ΔK RANGE	NPTS	R ²	SEE
1	□	0.7000	3.5670	-1.0780	4.1840	(4.04 , 20.11)	14	0.9756	0.00994
2	△	0.7000	4.6190	-0.6240	-5.1210	(2.54 , 7.19)	23	0.9936	0.00426
TOTAL RSQD =						0.9838	STD. ERROR EST. =		
							0.0062		

METRIC CONVERSIONS

C1 METRIC = C1 ENGLISH

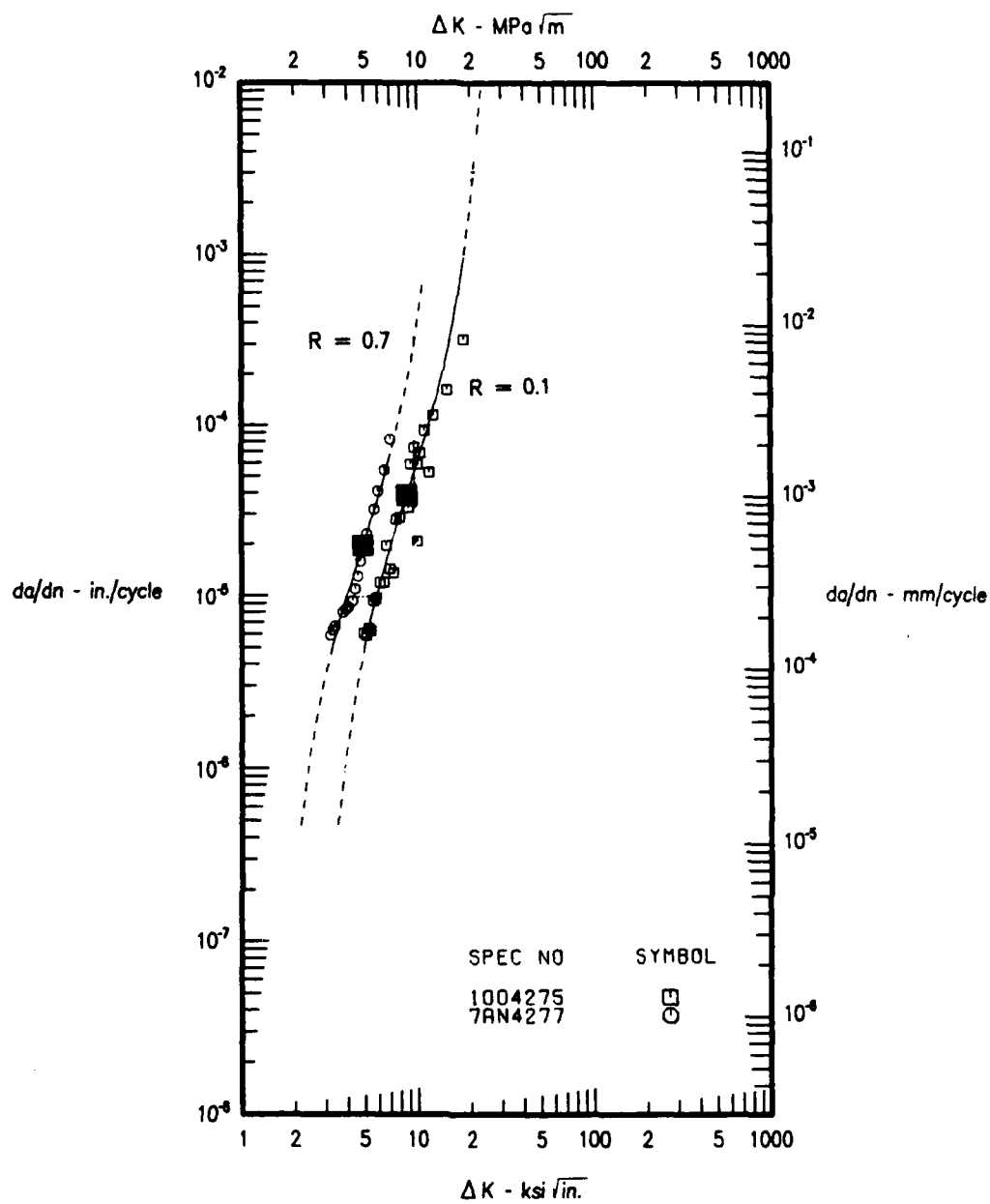
C2 METRIC = C2 ENGLISH

C3 METRIC = C3 ENGLISH - 0.040935

C4 METRIC = C4 ENGLISH * 1.40483

CURVE	SYMBOL	SPEC NO	MATERIAL	TEMP	ATM	FREQ	R	TYPE	THICK	REMARKS	P/R
1	□	7AN4258		1200F	AIR	10 CPM	R=0.1	MCT	.377	T1 24-11	1.319
1	○	7AN4266	T1-24-11	1200F	AIR	10 CPM	R=0.1	MCT	.511		0.733
2	△	7AN4573	T1 24-11	1200F	AIR	10 CPM	R=0.7	MCT	.375	T1 24-11	0.976

Figure 127. Effects of Stress Ratio on Ti-24Al-11Nb at 650°C (1200°F) and 0.17 Hz



HYPERBOLIC SINE MODEL COEFFICIENTS

$$Y = C1 + \text{SINH}(C2 * (X + C3)) + C4$$

WHERE $Y = \text{LOG}(da/dn)$ AND $X = \text{LOG}(\Delta K)$

CURVE	SYMBOL	C1	C2	C3	C4	ΔK RANGE	NPTS	R ²	SFE
1	\square	0.7000	4.1820	-0.9530	4.4070	(4.32 - 19.49)	26	0.9743	0.1502
2	\circ	0.7000	4.2330	-0.6930	4.7000	(3.16 - 7.17)	16	0.9540	0.0877
					TOTAL RSQRD =		0.9330		STD. ERROR EST. = 0.1440

METRIC CONVERSIONS

C1 METRIC = C1 ENGLISH

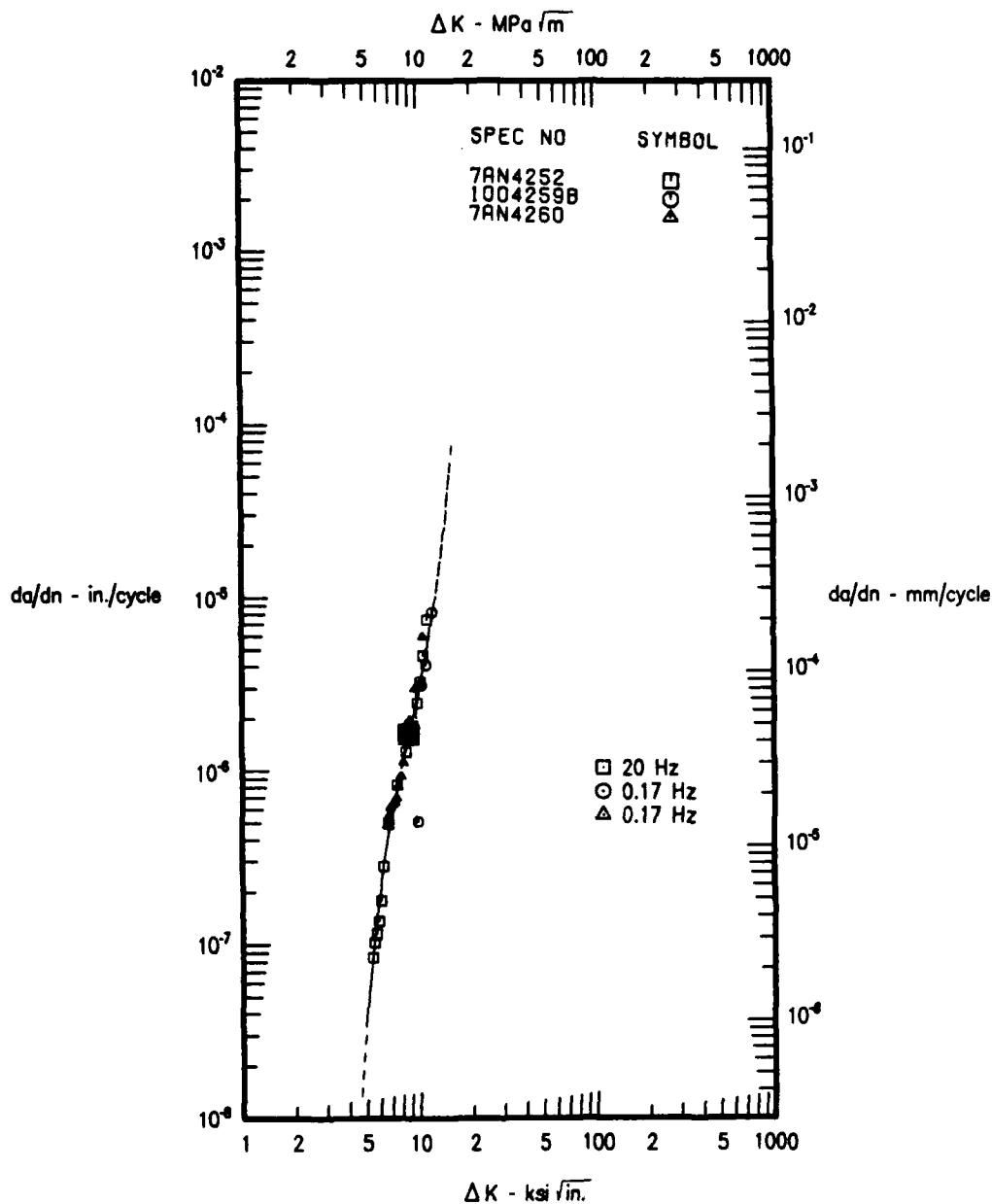
C2 METRIC = C2 ENGLISH

C3 METRIC = C3 ENGLISH - 0.040935

C4 METRIC = C4 ENGLISH + 1.40483

CURVE	SYMBOL	SPEC NO	MATERIAL	TEMP	ATH	FREQ	R	TYPE	THICK	REMARKS	P/R
1	\square	1004275		1200F	AIR	10 CPM	R=0.1	MCT	.365 TI	25-10-3-1	0.999
2	\circ	7AN4277		1200F	AIR	10 CPM	R=0.7	MCT	.369 TI	25-10-3-1	1.064

Figure 128. Effects of Stress Ratio on Ti-25Al-10Nb-3V-1Mo at 650°C (1200°F) and 0.17 Hz



HYPERBOLIC SINE MODEL COEFFICIENTS

$$Y = C1 + \text{SINH}(C2 * (X + C3)) + C4$$

WHERE $Y = \text{LOG}(da/dn)$ AND $X = \text{LOG}(\Delta K)$

CURVE	SYMBOL	C1	C2	C3	C4	ΔK RANGE	NPTS	R ²	SEE
1	□	0.7000	6.4250	-0.9590	-5.7970	(5.54 , 11.57)	14	0.9926	0.0745
2	○ ▲	0.7000	6.4250	-0.9590	-5.7970	(6.75 , 12.36)	18	0.7649	0.2139

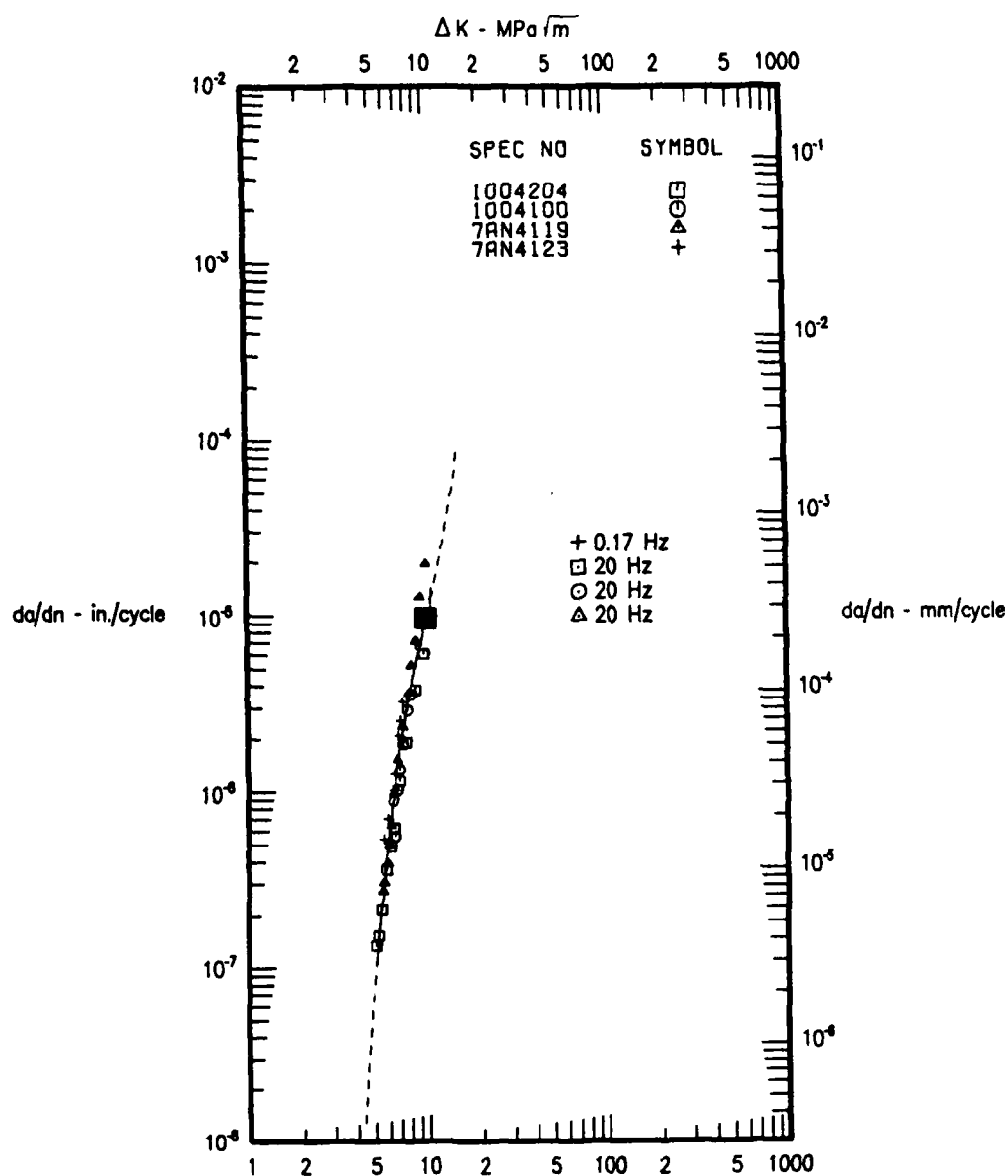
TOTAL RSQD = 0.9216 STD.ERROR.EST. = 0.1696

METRIC CONVERSIONS

C1 METRIC = C1 ENGLISH
 C2 METRIC = C2 ENGLISH
 C3 METRIC = C3 ENGLISH - 0.040935
 C4 METRIC = C4 ENGLISH + 1.40483

CURVE	SYMBOL	SPEC NO	MATERIAL	TEMP	ATM	FREQ	R	TYPE	THICK	REMARKS	P/R
1	□	7AN4252	TI-24-11	RT	AIR	20 HZ	R=0.1	MCT	.371		0.805
2	○	10042698	TI-24-11	RT	AIR	10 CPM	R=0.1	MCT	.501		0.791
2	▲	7AN4260	TI-24-11	RT	AIR	10 CPM	R=0.1	MCT	.378	TI-24-11	0.980

Figure 129. Effects of Frequency on Ti-24Al-11Nb at 26°C (80°F), R = 0.1



HYPERBOLIC SINE MODEL COEFFICIENTS

$Y = C1 * \text{SINH}(C2 * (X + C3)) + C4$
 WHERE $Y = \text{LOG}(da/dn)$ AND $X = \text{LOG}(\Delta K)$

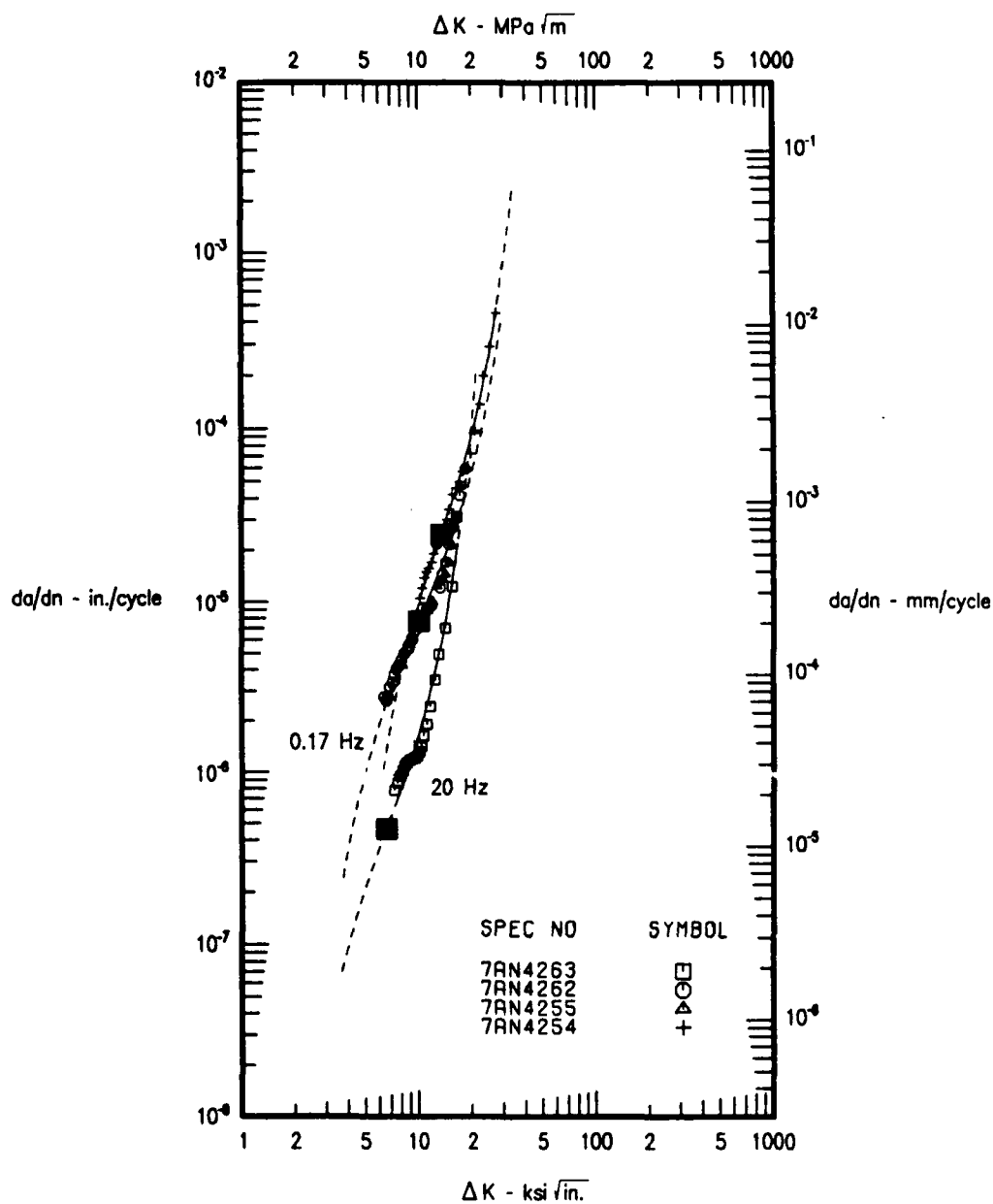
CURVE	SYMBOL	C1	C2	C3	C4	ΔK RANGE	NP'S	R ²	SEE
1	□ ○ △ +	0.7000	6.7885	-0.9732	-5.0162	(5.15 , 9.23)	38	0.9139	0.1606
TOTAL RSQRD =						0.9838	STD-ERROR-EST. =		0.1005

METRIC CONVERSIONS

C1 METRIC = C1 ENGLISH
 C2 METRIC = C2 ENGLISH
 C3 METRIC = C3 ENGLISH - 0.040935
 C4 METRIC = C4 ENGLISH + 1.40483

CURVE	SYMBOL	SPEC NO	MATERIAL	TEMP	ATH	FREQ	R	TYPE	THK	REMARKS	P/R
1	□	1004204	TI		RT AIR	20 HZ	R=0.1	RAD MCT	.417	TI-25-10-3-1	0.935
1	○	1004100	TI		RT AIR	20 HZ	R=0.1	MCT	.370	TI-25-10-3-1	0.686
1	△	7AN4119	TI-25-10		RT AIR	20 HZ	R=0.1	MCT	.374		1.238
1	+	7AN4123	TI-25103		80F AIR	10 CPM	R=0.1	MCT	.371	TI-25-10-3	1.428

Figure 130. Effects of Frequency on Ti-25Al-10Nb-3V-1Mo at 26°C (80°F), R = 0.1



HYPERBOLIC SINE MODEL COEFFICIENTS

$$Y = C1 + \text{SINH}(C2 \cdot (X + C3)) + C4$$

WHERE $Y = \text{LOG}(da/dn)$ AND $X = \text{LOG}(\Delta K)$

CURVE	SYMBOL	C1	C2	C3	C4	ΔK RANGE	NPTS	R ²	SEE
1	□	0.7000	3.7450	-0.8350	-6.3190	(7.67 , 18.22)	20	0.9544	0.0946
2	○ ▲	0.7000	3.3180	-1.0330	-5.0990	(6.70 , 20.36)	44	0.9681	0.0571
3	+	0.7000	4.1070	-1.1670	-4.5910	(10.95 , 31.57)	23	0.9453	0.0332
TOTAL RSQD = 0.9894						STD. ERROR EST. = 0.0653			

METRIC CONVERSIONS

$$C1 \text{ METRIC} = C1 \text{ ENGLISH}$$

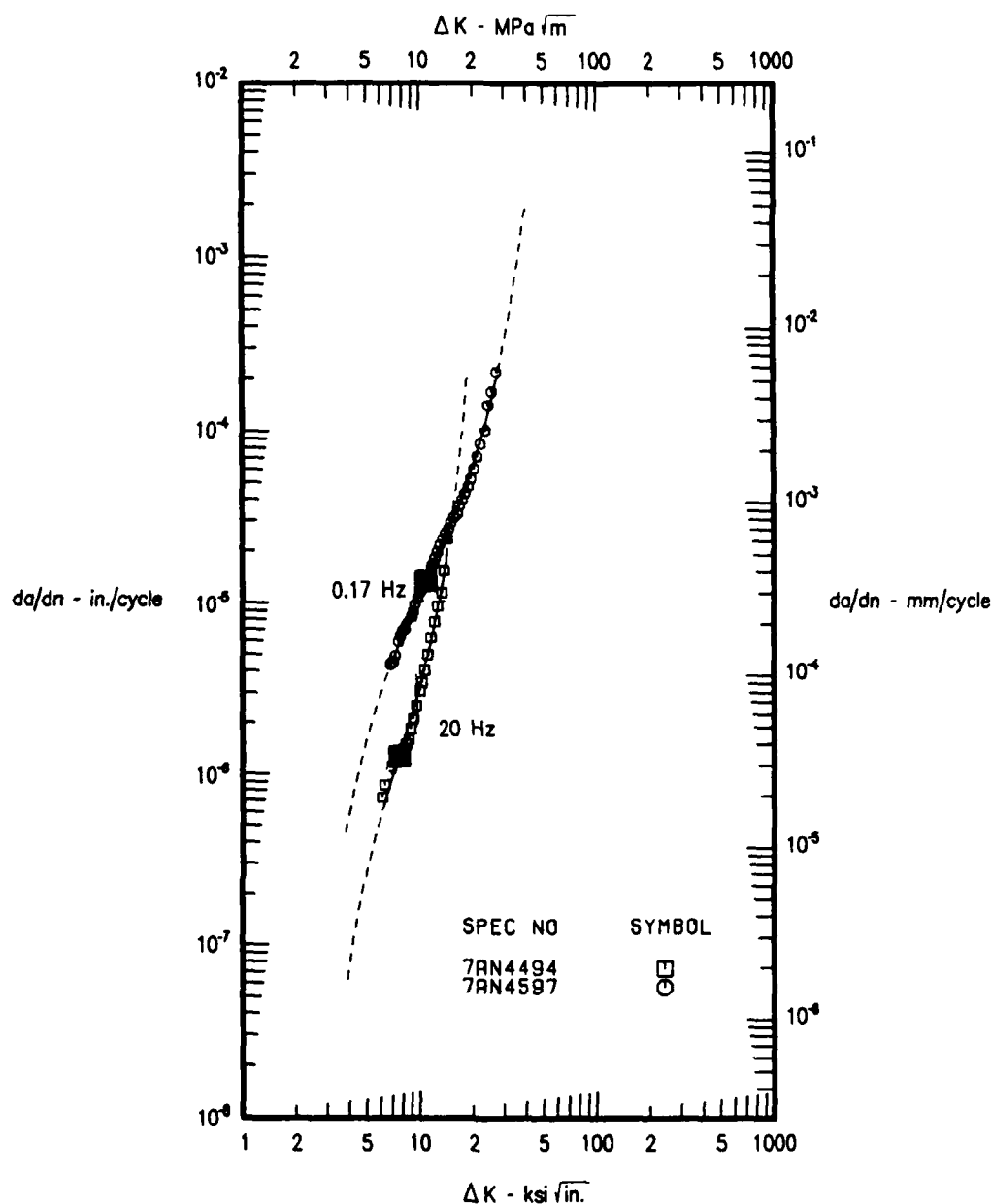
$$C2 \text{ METRIC} = C2 \text{ ENGLISH}$$

$$C3 \text{ METRIC} = C3 \text{ ENGLISH} - 0.040935$$

$$C4 \text{ METRIC} = C4 \text{ ENGLISH} + 1.40493$$

CURVE	SYMBOL	SPEC NO	MATERIAL	TEMP	ATM	FREQ	R	TYPE	THK	REMARKS	P/R
1	□	7AN4263	TI-24-11	800F	AIR	20 HZ	R=.1	MCT	.373		0.952
2	○	7AN4262	800F	AIR	10 CPM	R=.1	MCT	.510	TI-24-11		1.013
2	▲	7AN4255	TI-24-11	800F	AIR	10 CPM	R=.1	MCT	.377		0.948
3	+	7AN4254	TI-24-11	800F	AIR	2M DWL	R=.1	MCT	.375	TI-24-11	0.854

Figure 131. Effects of Frequency on Ti-24Al-11Nb at 427°C (800°F), R = 0.1



HYPERBOLIC SINE MODEL COEFFICIENTS

$$Y = C1 + \text{SINH}(C2 * (X + C3)) + C4$$

WHERE Y = LOG₁₀ (da/dn) AND X = LOG₁₀ (ΔK)

CURVE	SYMBOL	C1	C2	C3	C4	ΔK RANGE	NPTS	R ²	SEE
1	□	0.7000	4.3310	-0.8910	-5.9000	(6.18 - 15.51)	23	0.9863	0.0519
2	○	0.7000	3.0160	-1.0660	-4.8780	(7.08 - 30.83)	44	0.9971	0.0240

TOTAL RSQRD = 0.9966 STD. ERROR EST. 0.0357

METRIC CONVERSIONS

C1 METRIC = C1 ENGLISH

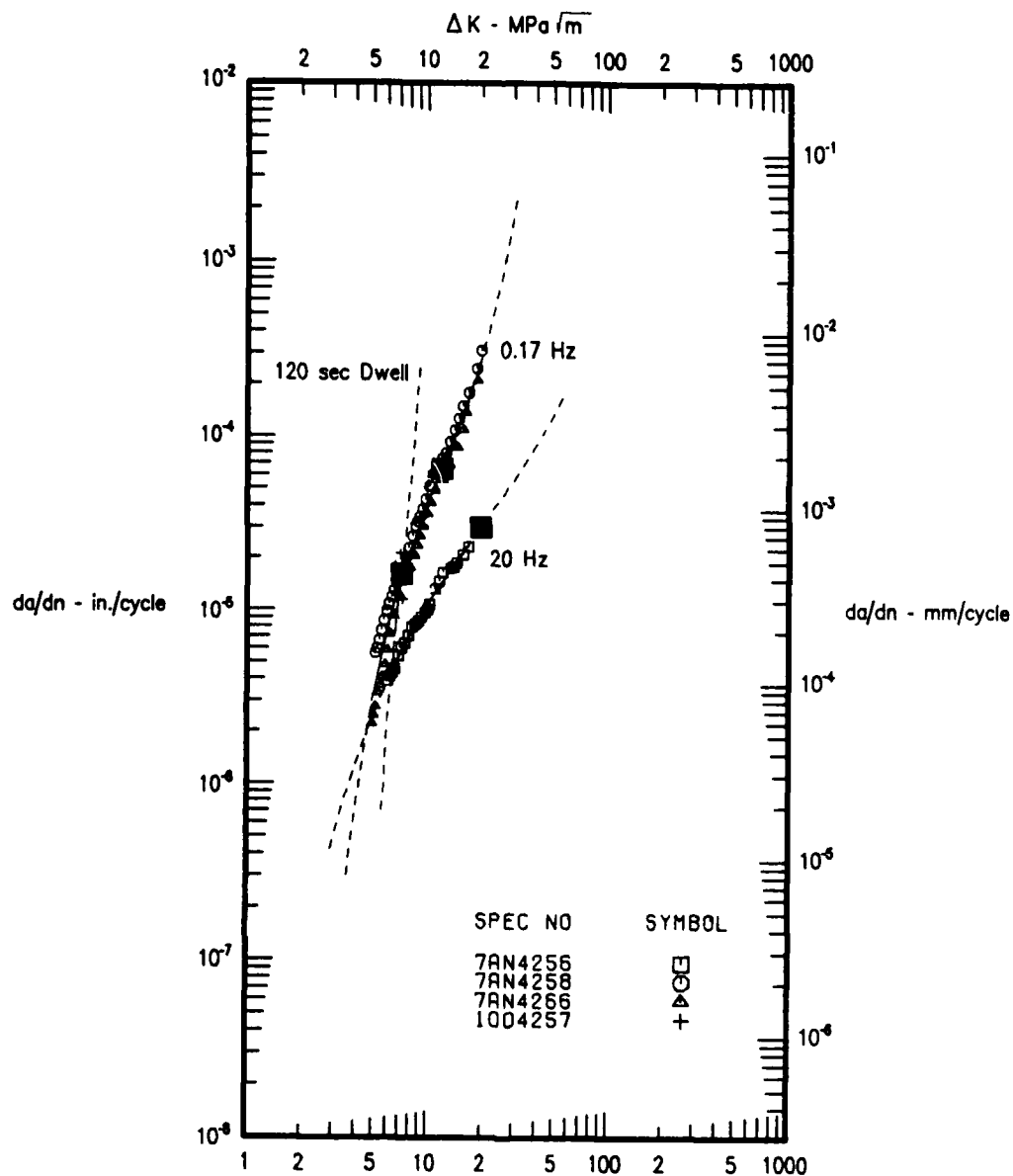
C2 METRIC = C2 ENGLISH

C3 METRIC = C3 ENGLISH - 0.040935

C4 METRIC = C4 ENGLISH + 1.40483

CURVE	SYMBOL	SPEC NO	MATERIAL	TEMP	ATM	FREQ	R	TYPE	THICK	REMARKS	P/R
1	□	7AN4494		800F	AIR	20 HZ.	R=-1	MCT	.381	T125-10-3-1	0.987
2	○	7AN4597	T1251031	800F	AIR	10 CPM	R=0.1	MCT	.504		1.032

Figure 132. Effects of Frequency on Ti-25Al-10Nb-3V-1Mo at 427°C (800°F), R = 0.1



$\Delta K - \text{ksi} \sqrt{\text{in.}}$
 HYPERBOLIC SINE MODEL COEFFICIENTS
 $Y = C1 + \text{SINH}(C2 * (X + C3)) + C4$
 WHERE $Y = \text{LOG}(da/dn)$ AND $X = \text{LOG}(\Delta K)$

CURVE	SYMBOL	C1	C2	C3	C4	ΔK RANGE	NPTS	R ²	SEE
1	□	0.7000	1.9860	-1.3030	-4.5200	5.87 - 16.93	23	0.9937	0.0203
2	○	0.7000	3.5670	-1.0780	-4.1840	4.84 - 20.11	59	0.9718	0.00899
3	+	0.7000	13.0000	-0.8500	-4.7900	6.51 - 7.18	5	0.0415	0.2704

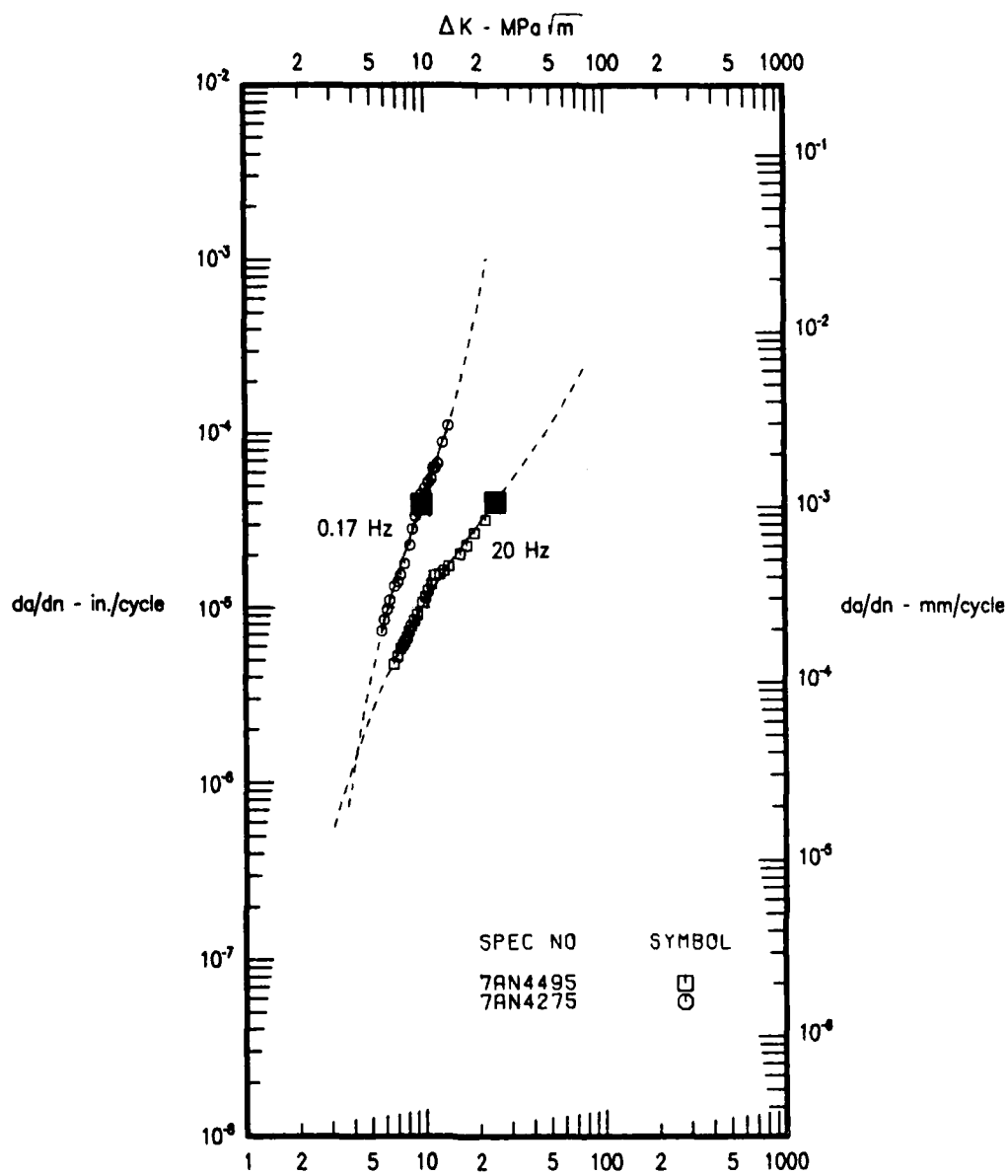
TOTAL RSQRD = 0.9667 STD.ERROR.EST. 0.0361

METRIC CONVERSIONS

$C1 \text{ METRIC} = C1 \text{ ENGLISH}$
 $C2 \text{ METRIC} = C2 \text{ ENGLISH}$
 $C3 \text{ METRIC} = C3 \text{ ENGLISH} - 0.040935$
 $C4 \text{ METRIC} = C4 \text{ ENGLISH} + 1.40483$

CURVE	SYMBOL	SPEC NO	MATERIAL	TEMP	ATM	FREQ	R	TYPE	THICK	REMARKS	P/A
1	□	7AN4256	TI-24-11	1200F	AIR	20 HZ	R=0.1	MCT	.375		0.981
2	○	7AN4258	TI-24-11	1200F	AIR	10 CPM	R=0.1	MCT	.377	TI 24-11	1.319
2	△	7AN4266	TI-24-11	1200F	AIR	10 CPM	R=0.1	MCT	.511		0.733
3	+	1004257	TI-24-11	1200F	AIR	2 M/D	R=0.1	MCT	.379	TI-24-11	1.247

Figure 133. Effects of Frequency on Ti-24Al-11Nb at 650°C (1200°F), R = 0.1



HYPERBOLIC SINE MODEL COEFFICIENTS
 $Y = C1 + \text{SINH}(C2 * (X + C3)) + C4$
 WHERE $Y = \text{LOG}(da/dn)$ AND $X = \text{LOG}(\Delta K)$

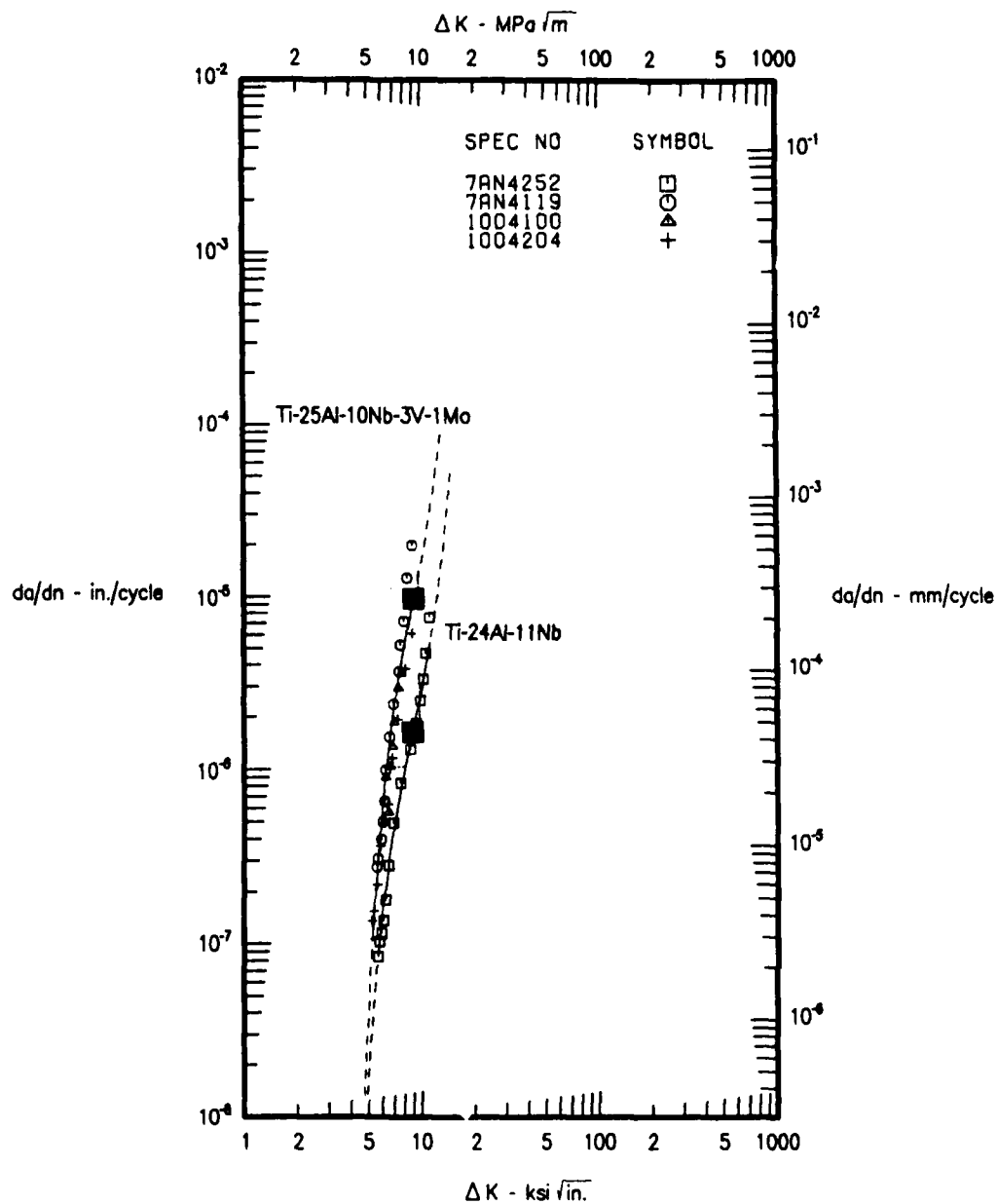
CURVE	SYMBOL	C1	C2	C3	C4	ΔK RANGE	NPTS	R ²	SEE
1	□	0.7000	1.9190	-1.3740	-4.3870	6.39 - 20.92	24	0.9894	0.0264
2	○	0.7000	4.1020	-0.9530	-4.4070	6.39 - 12.54	21	0.9915	0.0159
TOTAL RSQRD =						0.9937	STD. ERROR F=1		

METRIC CONVERSIONS

C1 METRIC = C1 ENGLISH
 C2 METRIC = C2 ENGLISH
 C3 METRIC = C3 ENGLISH - 0.040935
 C4 METRIC = C4 ENGLISH + 1.40483

CURVE	SYMBOL	SPEC NO	MATERIAL	TEMP	ATM	FREQ	R	TYPE	THICK	REMARKS	P/R
1	□	7AN4495		1200F	AIR	20 HZ.	R=0.1	MCT	.419 TI	25-10-3-1	0.972
2	○	7AN4275		1200F	AIR	10 CPM	R=0.1	MCT	.365 TI	25-10-3-1	0.999

Figure 134. Effects of Frequency on Ti-25Al-10Nb-3V-1Mo at 650°C (1200°F), R = 0.1



HYPERBOLIC SINE MODEL COEFFICIENTS

$$Y = C1 * \text{SINH}(C2 * (X + C3)) + C4$$

WHERE Y = LOG(da/dn) AND X = LOG(ΔK)

CURVE	SYMBOL	C1	C2	C3	C4	ΔK RANGE	NPTS	R ²	EFF
1	□	0.7000	6.4250	-0.9590	-5.7970	(5.54 , 11.57)	14	0.9926	0.074%
2	○ ▲ +	0.7000	6.7690	-0.9730	-5.0160	(5.15 , 9.23)	30	0.9901	0.134%
TOTAL RSQRD =						0.9554	STD ERROR (Y) =		0.1461

METRIC CONVERSIONS

C1 METRIC = C1 ENGLISH

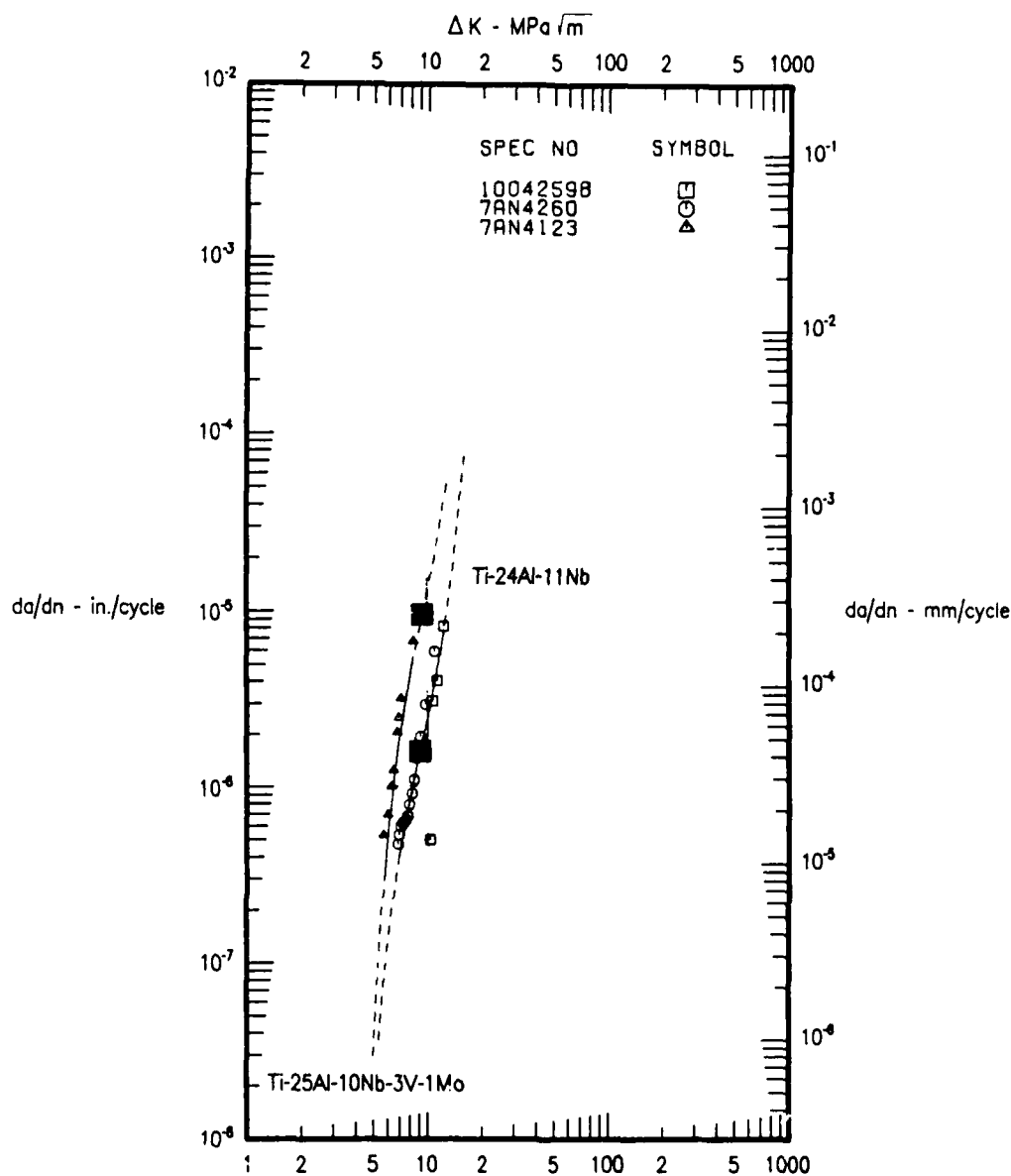
C2 METRIC = C2 ENGLISH

C3 METRIC = C3 ENGLISH - 0.040935

C4 METRIC = C4 ENGLISH + 1.40483

CURVE	SYMBOL	SPEC NO	MATERIAL	TEMP	ATM	FREQ	R	TYPE	THICK	REMARKS	R ²
1	□	7AN4252	Ti 24-11	RT	AIR	20 HZ	R=-1	MCT	.371		0.805
2	○	7AN4119	Ti 25-10	RT	AIR	20 HZ	R=-1	MCT	.374		1.232
2	▲	1004100	TI	RT	AIR	20 HZ	R=-1	MCT	.370	TI-25-10-3-1	0.683
2	+	1004204	TI	RT	AIR	20 HZ	R=-1	RND MCT	.417	TI 25-10 3-1	0.930

Figure 135. Alloy Comparison at R = 0.1, 20 Hz, and 26°C (80°F)



HYPERBOLIC SINE MODEL COEFFICIENTS

$$Y = C1 + \text{SINH}(C2 * (X + C3)) + C4$$

WHERE Y = LOG(da/dn) AND X = LOG(ΔK)

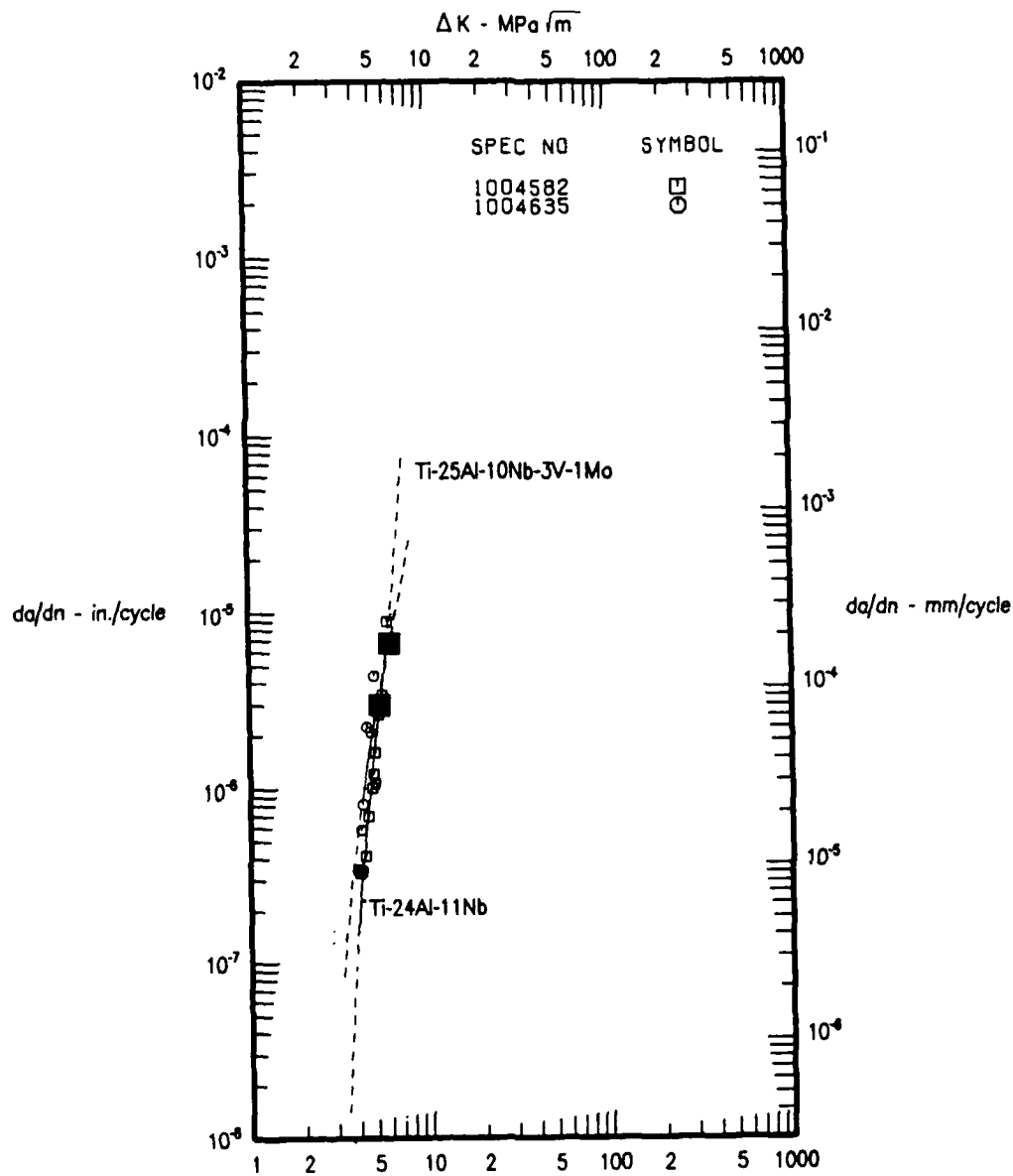
CURVE	SYMBOL	C1	C2	C3	C4	ΔK RANGE	NPTS	R ²	SEE
1	□ ○	0.7000	6.4250	-0.9590	-5.7970	1.675 - 12.361	18	0.7649	0.2139
2	▲	0.7000	6.7690	-0.9730	-5.0160	1.560 - 8.31	8	0.9804	0.1114
TOTAL RSQRD = 0.7957							STD. ERROR EST. = 0.2090		

METRIC CONVERSIONS

C1 METRIC = C1 ENGLISH
 C2 METRIC = C2 ENGLISH
 C3 METRIC = C3 ENGLISH - 0.040935
 C4 METRIC = C4 ENGLISH + 1.40493

CURVE	SYMBOL	SPEC NO	MATERIAL	TEMP	ATM	FREQ	R	TYPE	THICK	REMARKS	P-4
1	□	10042598	TI-24-11	RT	AIR	10 CPM	R=0.1	MCT	.501		0.791
1	○	7AN4260	TI-2411	RT	AIR	10 CPM	R=0.1	MCT	.378	TI-24-11	0.980
2	▲	7AN4123	TI-25103	BDP	AIR	10 CPM	R=0.1	MCT	.371	TI-25-10.3	1.422

Figure 136. Alloy Comparison at R = 0.1, 0.17 Hz, and 26°C (80°F)



HYPERBOLIC SINE MODEL COEFFICIENTS

$$Y = C1 * \text{SINH}(C2 * (X + C3)) + C4$$

WHERE Y = LOG(da/dn) AND X = LOG(ΔK)

CURVE	SYMBOL	C1	C2	C3	C4	ΔK RANGE	NPT	R ²	SEE
1	□	0.7000	13.2560	-0.6830	-5.5200	3.78 - 5.29	11	0.9289	0.1706
2	○	0.7000	7.2490	-0.7360	-5.1680	3.87 - 4.59	6	0.3612	0.3379
TOTAL RSQD = 0.8259									STD. ERROR EST. = 0.2287

METRIC CONVERSIONS

C1 METRIC = C1 ENGLISH

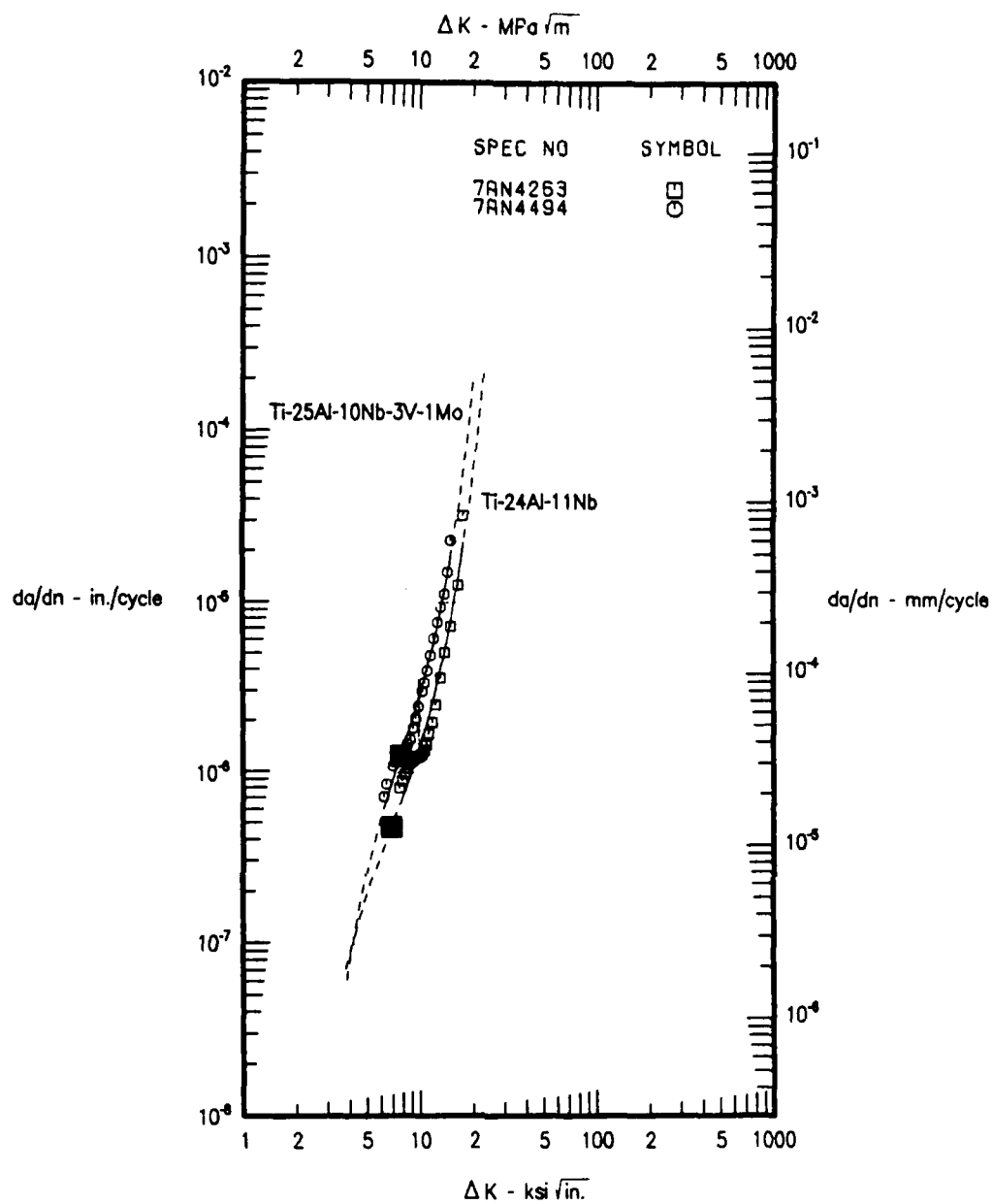
C2 METRIC = C2 ENGLISH

C3 METRIC = C3 ENGLISH - 0.040935

C4 METRIC = C4 ENGLISH + 1.40493

CURVE	SYMBOL	SPEC NO	MATERIAL	TEMP	ATM	FREQ	R	TYPE	THK	REMARKS	P/R
1	□	1004582	Ti-24Al	RT	AIR	20HZ	P=0.7	MCT	.497		1.186
2	○	1004635	Ti	RT	AIR	10 CPM	R=0.7	MCT	.375	Ti-25-10-3-1	1.308

Figure 137. Alloy Comparison at R = 0.7 and 26°C (80°F)



HYPERBOLIC SINE MODEL COEFFICIENTS

$$Y = C1 \cdot \sinh(C2 \cdot (X + C3)) + C4$$

WHERE Y = LOG(da/dn) AND X = LOG(ΔK)

CURVE	SYMBOL	C1	C2	C3	C4	ΔK RANGE	NPTS	R ²	SEE
1	□	0.7000	3.7450	-0.8350	-6.3190	(7.67 , 18.22)	20	0.9564	0.0946
2	○	0.7000	4.3310	-0.8910	-6.9000	(6.18 , 15.51)	23	0.9863	0.0519
TOTAL RSQRD = 0.9729							STD. ERROR EST. = 0.0746		

METRIC CONVERSIONS

C1 METRIC = C1 ENGLISH

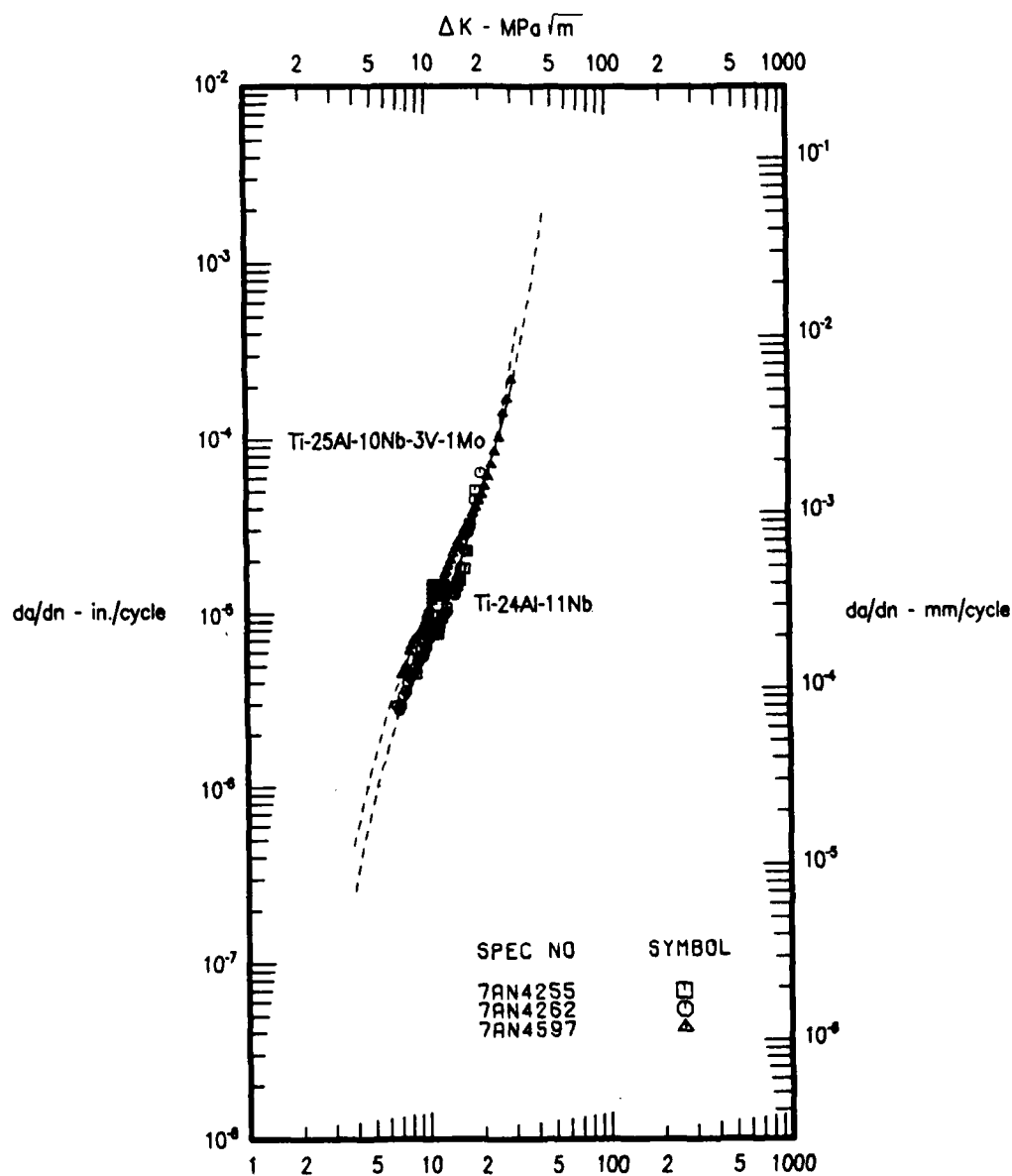
C2 METRIC = C2 ENGLISH

C3 METRIC = C3 ENGLISH - 0.040935

C4 METRIC = C4 ENGLISH + 1.40483

CURVE	SYMBOL	SPEC NO	MATERIAL	TEMP	ATM	FREQ	R	TYPE	THIN	REMARKS	P/R
1	□	7AN4263	Ti-24-11	800F	RIR	20 HZ	R=0.1	MLT	0.174		0.957
2	○	7AN4494		800F	RIR	20 HZ	R=0.1	MLT	0.381	1125, 10, 1, 1	0.987

Figure 138. Alloy Comparison at R = 0.1, 20 Hz, and 427°C (800°F)



HYPERBOLIC SINE MODEL COEFFICIENTS

$$Y = C1 * \text{SINHIC2} * (X + C3) + C4$$

WHERE Y = LOG(da/dn) AND X = LOG(ΔK)

CURVE	SYMBOL	C1	C2	C3	C4	ΔK RANGE	NP	W ²	SEE
1	□ ○	0.7000	3.3180	-1.0330	-6.0990	(6.70 , 20.36)	44	0.1582	0.0622
2	▲	0.7000	3.0150	-1.0660	-4.8780	(7.08 , 30.83)	44	0.9371	0.0240
TOTAL RSQD =						0.9885	STD.ERROR. EST. = 0.0471		

METRIC CONVERSIONS

C1 METRIC = C1 ENGLISH

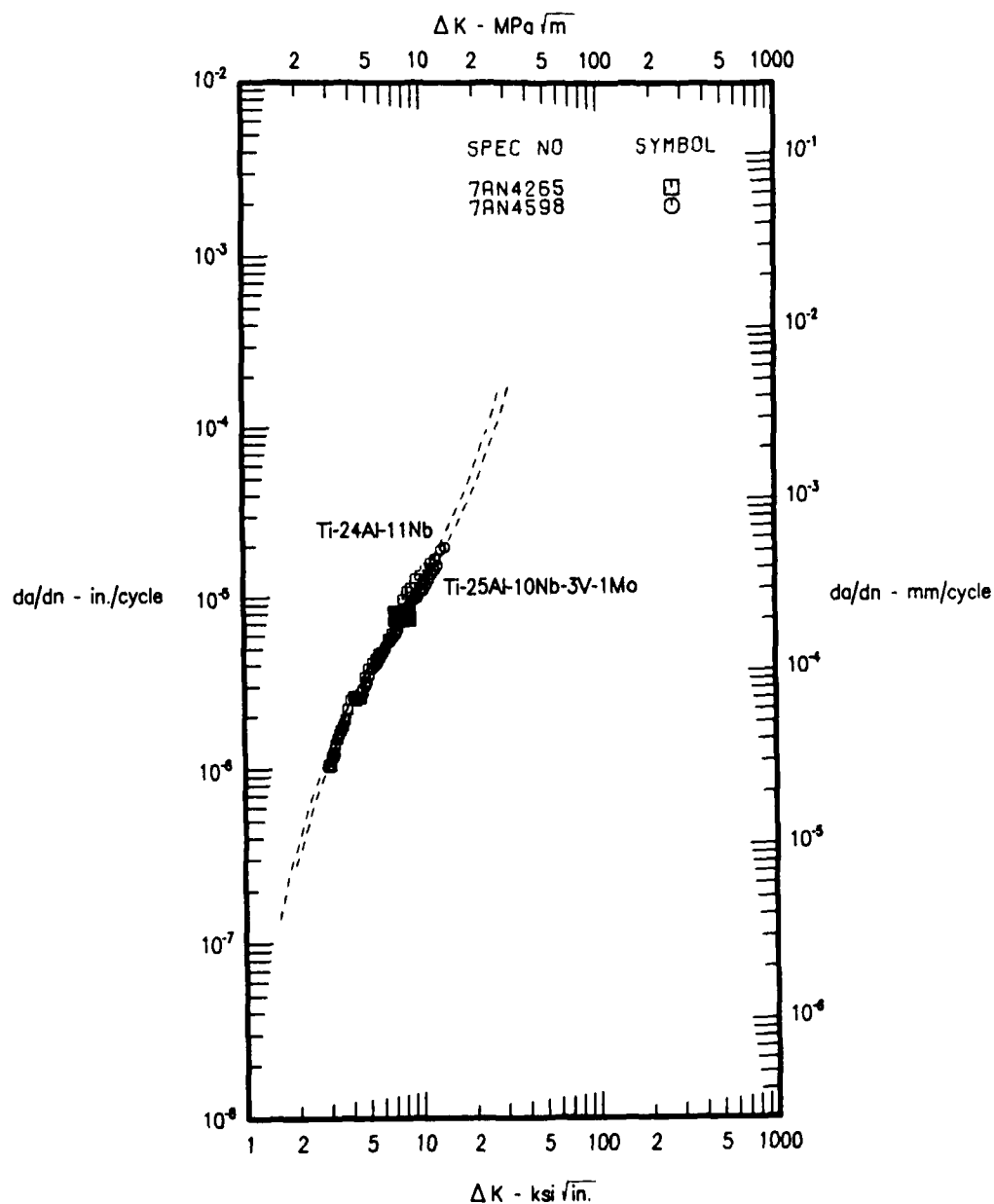
C2 METRIC = C2 ENGLISH

C3 METRIC = C3 ENGLISH - 0.040935

C4 METRIC = C4 ENGLISH + 1.40483

CURVE	SYMBOL	SPEC NO	MATERIAL	TEMP	ATH	FREQ	R	TYPE	THICK	REMARKS	P/R
1	□	7AN4255	Ti-24-11	800F	R/R	10 CPM	R=-1	MCT	.377		0.948
1	○	7AN4262	800F	R/R	10 CPM	R=-1	MCT	.610	Ti-24-11		1.013
2	▲	7AN4597	T1251031	800F	R/R	10 CPM	R=0.1	MCT	.504		1.032

Figure 139. Alloy Comparison at R = 0.1, 0.17 Hz, and 427°C (800°F)



HYPERBOLIC SINE MODEL COEFFICIENTS

$$Y = C1 * \sinh(C2 * (X + C3)) + C4$$

WHERE Y = LOG(da/dn) AND X = LOG(ΔK)

CURVE	SYMBOL	C1	C2	C3	C4	ΔK RANGE	NPTS	R ²	SEE
1	□	0.7000	2.3730	-0.6720	-5.1010	1.288 - 12.111	38	0.9941	0.0555
2	○	0.7000	2.3250	-0.9100	-5.1000	1.417 - 13.841	38	0.9960	0.0161
TOTAL RSQD =						0.9933	STD. ERROR EST. =		0.0409

METRIC CONVERSIONS

C1 METRIC = C1 ENGLISH

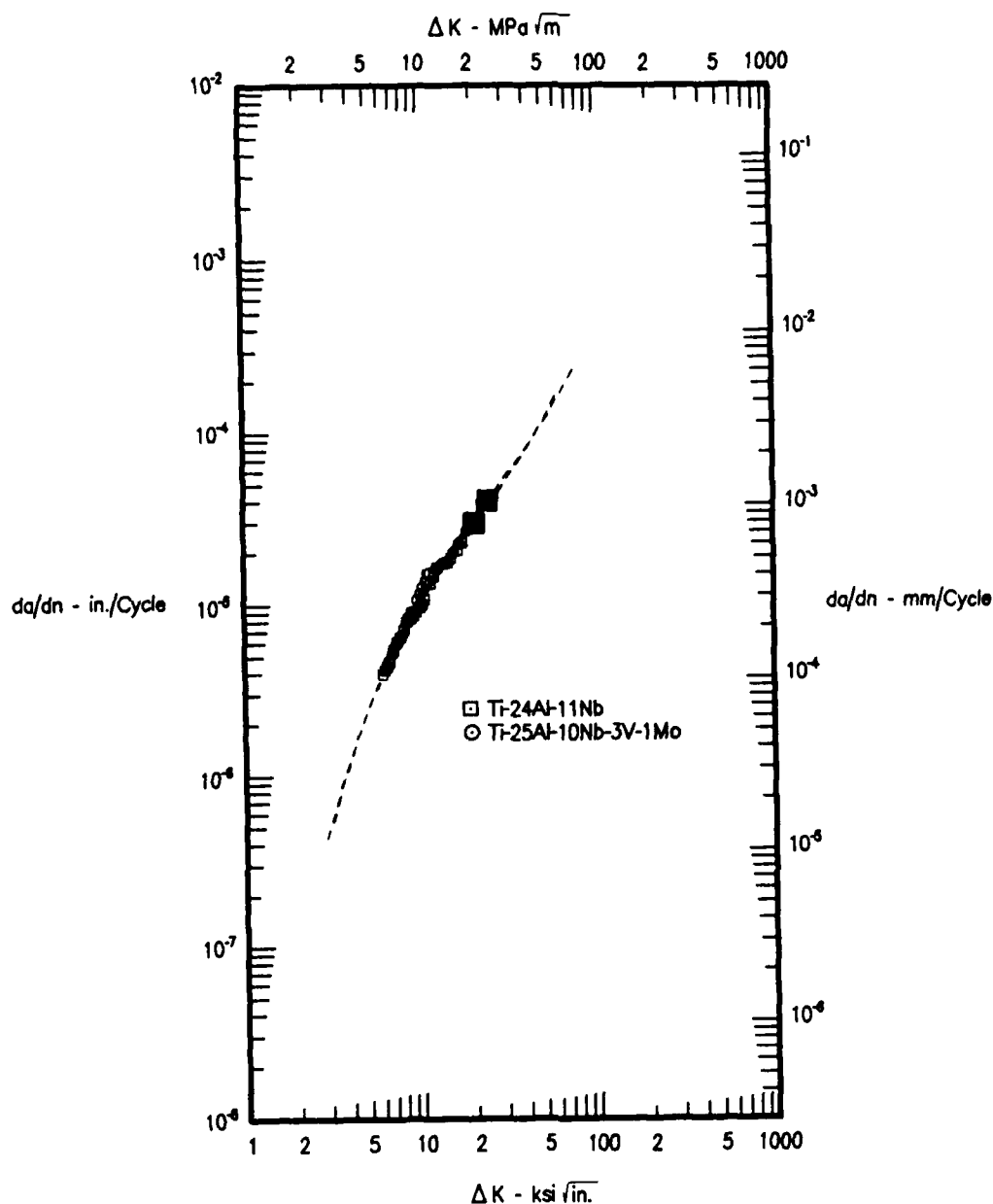
C2 METRIC = C2 ENGLISH

C3 METRIC = C3 ENGLISH * 0.040935

C4 METRIC = C4 ENGLISH * 1.40483

CURVE	SYMBOL	SPEC NO	MATERIAL	TEMP	ATM	FREQ	R	TYPE	THICK	REMARKS	P/R
1	□	7AN4265	TI 24-11	800F	HR	10 LPM	R=0.7	ML	0.175		0.914
2	○	7AN4598	TI 25-10-3	800F	HR	10 LPM	R=0.7	ML	0.175		1.021

Figure 140. Alloy Comparison at R = 0.7, 0.17 Hz, and 427°C (800°F)



HYPERBOLIC SINE MODEL COEFFICIENTS

$$Y = C1 + \text{SINH}(C2 * (X + C3)) + C4$$

WHERE $Y = \text{LOG}(da/dN)$ AND $X = \text{LOG}(\Delta K)$

CURVE	SYMBOL	C1	C2	C3	C4	ΔK RANGE	NPTS	R ²	SEE
1	□	0.7000	1.9860	-1.3030	-4.5200	(5.87 , 16.93)	23	0.9937	0.0203
2	○	0.7000	1.9190	-1.3740	-4.3870	(6.39 , 20.92)	22	0.9894	0.0264

TOTAL RSQRD = 0.9919 STD.ERROR.EST. = 0.0435

METRIC CONVERSIONS

C1 METRIC = C1 ENGLISH

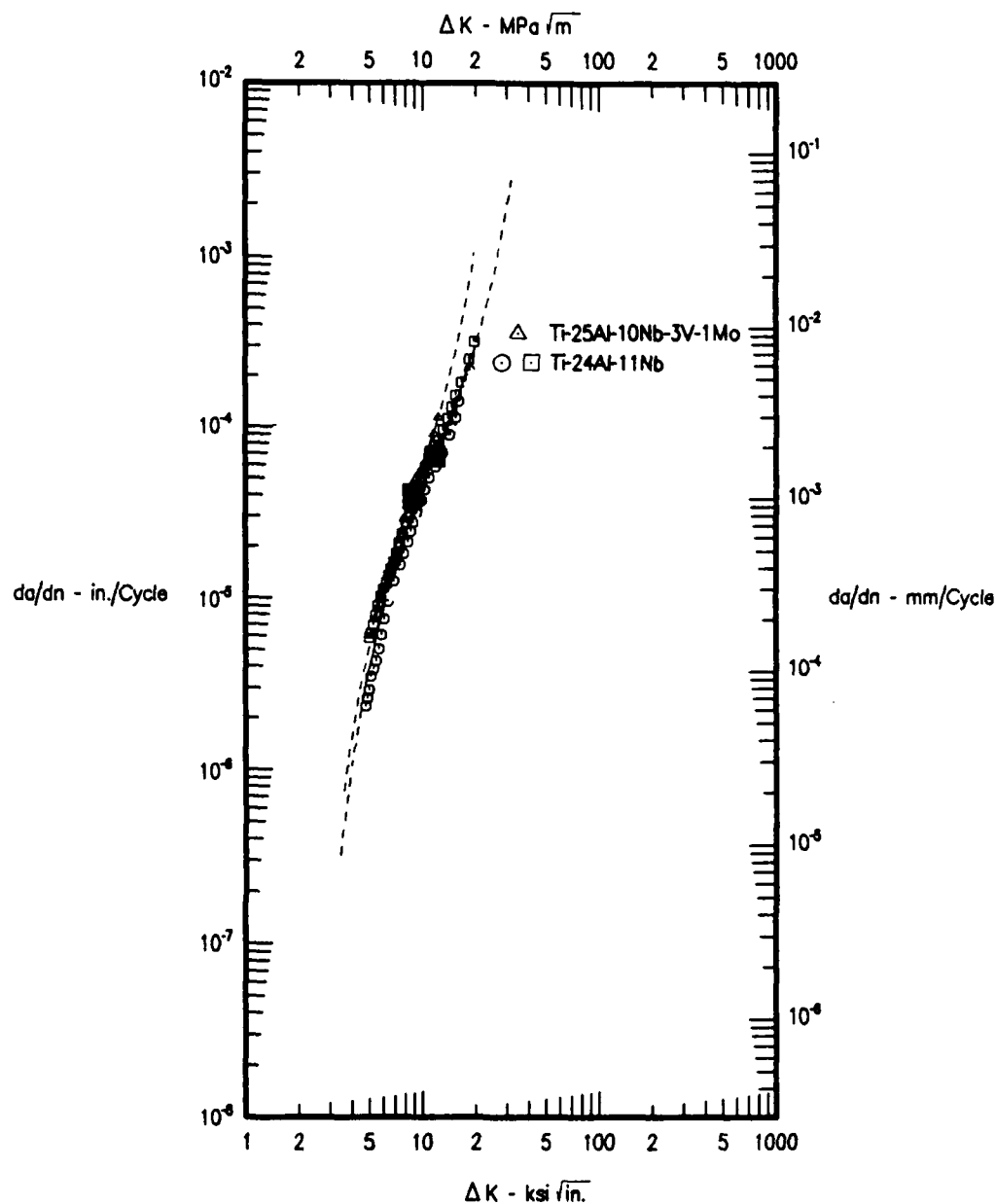
C2 METRIC = C2 ENGLISH

C3 METRIC = C3 ENGLISH - 0.040935

C4 METRIC = C4 ENGLISH + 1.40483

CURVE	SYMBOL	SPEC NO	MATERIAL	TEMP	ATH	FREQ	R	TYPE	THICK	REMARKS	P/R
1	□	7AN4256	TI-24-11	1200F	AIR	20 HZ	R=-1	MCT	.375		0.981
2	○	7AN4495		1200F	AIR	20 HZ	R=-1	MCT	.419	TI 25-10-3-1	0.972

Figure 141. Alloy Comparison at R = 0.1, 20 Hz, and 650°C (1200°F)



HYPERBOLIC SINE MODEL COEFFICIENTS

$$Y = C1 + \text{SINH}(C2 * (X + C3)) + C4$$

WHERE $Y = \text{LOG}(da/dn)$ AND $X = \text{LOG}(\Delta K)$

CURVE	SYMBOL	C1	C2	C3	C4	ΔK RANGE	NPTS	R ²	SEE
1	□ ○	0.7000	3.5670	-1.0780	-4.1840	(4.84 , 20.11)	54	0.9733	0.0899
2	▲	0.7000	4.1820	-0.9530	-4.4070	(5.39 , 12.54)	21	0.9915	0.0358

TOTAL RSQRD = 0.9762

STD. ERROR EST. = 0.0807

METRIC CONVERSIONS

C1 METRIC = C1 ENGLISH

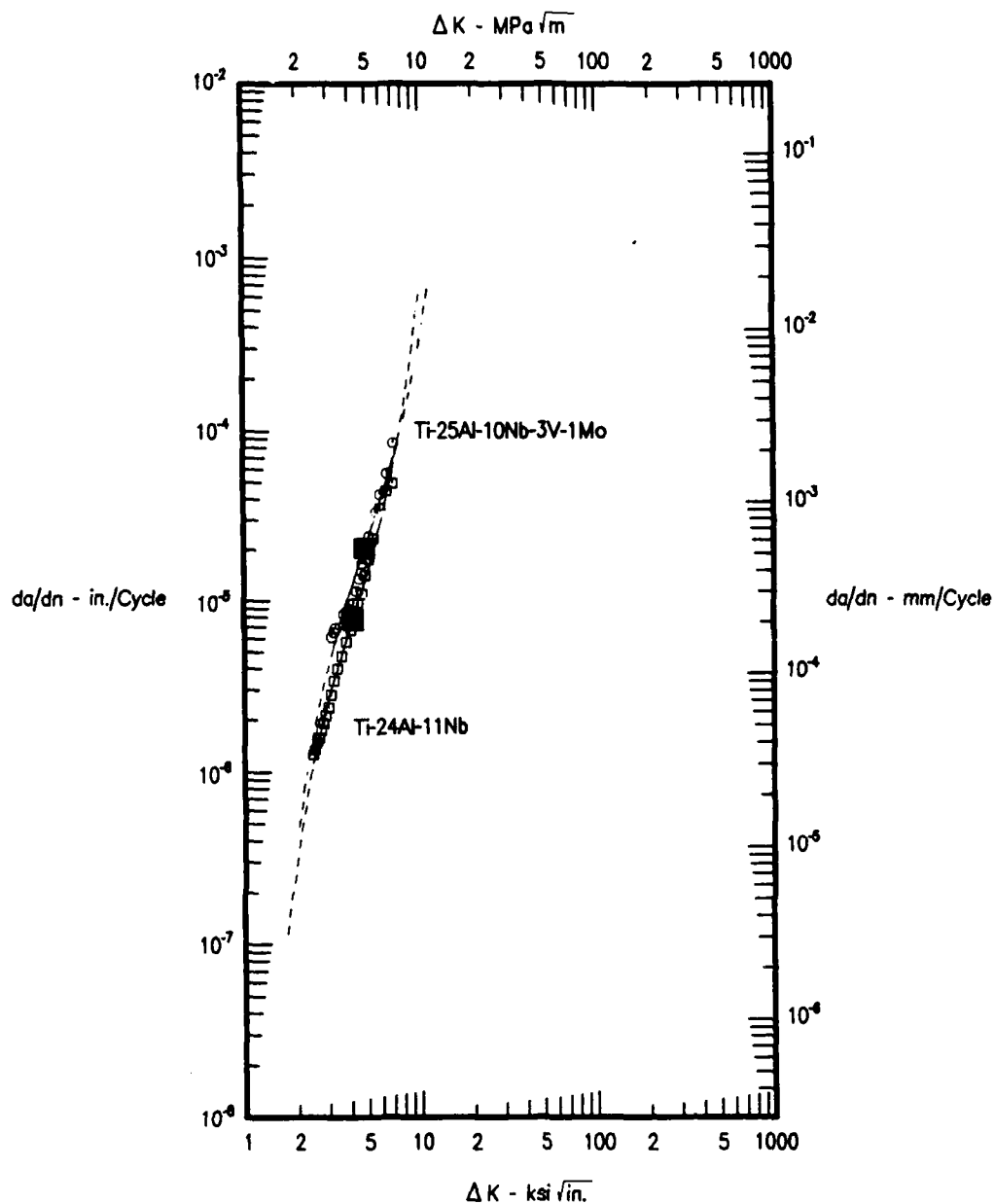
C2 METRIC = C2 ENGLISH

C3 METRIC = C3 ENGLISH - 0.040935

C4 METRIC = C4 ENGLISH + 1.40483

CURVE	SYMBOL	SPEC NO	MATERIAL	TEMP	ATM	FREQ	R	TYPE	IN/A	REMARKS	P/W
1	□	7AN4258		1200F	AIR	10 CPM	R=-1	MCT	.377	TI 24-11	1.319
1	○	7AN4266	TI-24-11	1200F	AIR	10 CPM	R=-1	MCT	.511		0.733
2	▲	7AN4275		1200F	AIR	10 CPM	R=-1	MCT	.365	TI 25-10-3-1	0.999

Figure 142. Alloy Comparison at $R = 0.1$, 20 Hz, and 650°C (1200°F)



HYPERBOLIC SINE MODEL COEFFICIENTS

$$Y = C1 * \text{SINH}(C2 * (X + C3)) + C4$$

WHERE Y = LOG(da/dn) AND X = LOG(ΔK)

CURVE	SYMBOL	C1	C2	C3	C4	ΔK RANGE	NPTS	R ²	SEE
1	□	0.7000	4.6190	-0.6240	-5.1210	(2.54 , 7.19)	23	0.9936	0.0426
2	○	0.7000	4.2330	-0.6930	-4.7000	(3.16 , 7.17)	16	0.9540	0.0822

TOTAL RSQRD = 0.9870 STD.ERROR.EST. = 0.0613

METRIC CONVERSIONS

C1 METRIC = C1 ENGLISH

C2 METRIC = C2 ENGLISH

C3 METRIC = C3 ENGLISH - 0.040935

C4 METRIC = C4 ENGLISH + 1.40483

CURVE	SYMBOL	SPEC NO	MATERIAL	TEMP	R/R	FREQ	R	TYPE	THICK	REMARKS	POR
1	□	7AN4673	TI 24-11	1200F AIR	10 LPM	R=0.7	MCT	.375	TI 24-11		0.976
2	○	7AN4277		1200F AIR	10 CPM	R=0.7	MCT	.389	TI 25-10-3-1		1.064

Figure 143. Alloy Comparison at R = 0.7, 0.17 Hz, and 650°C (1200°F)

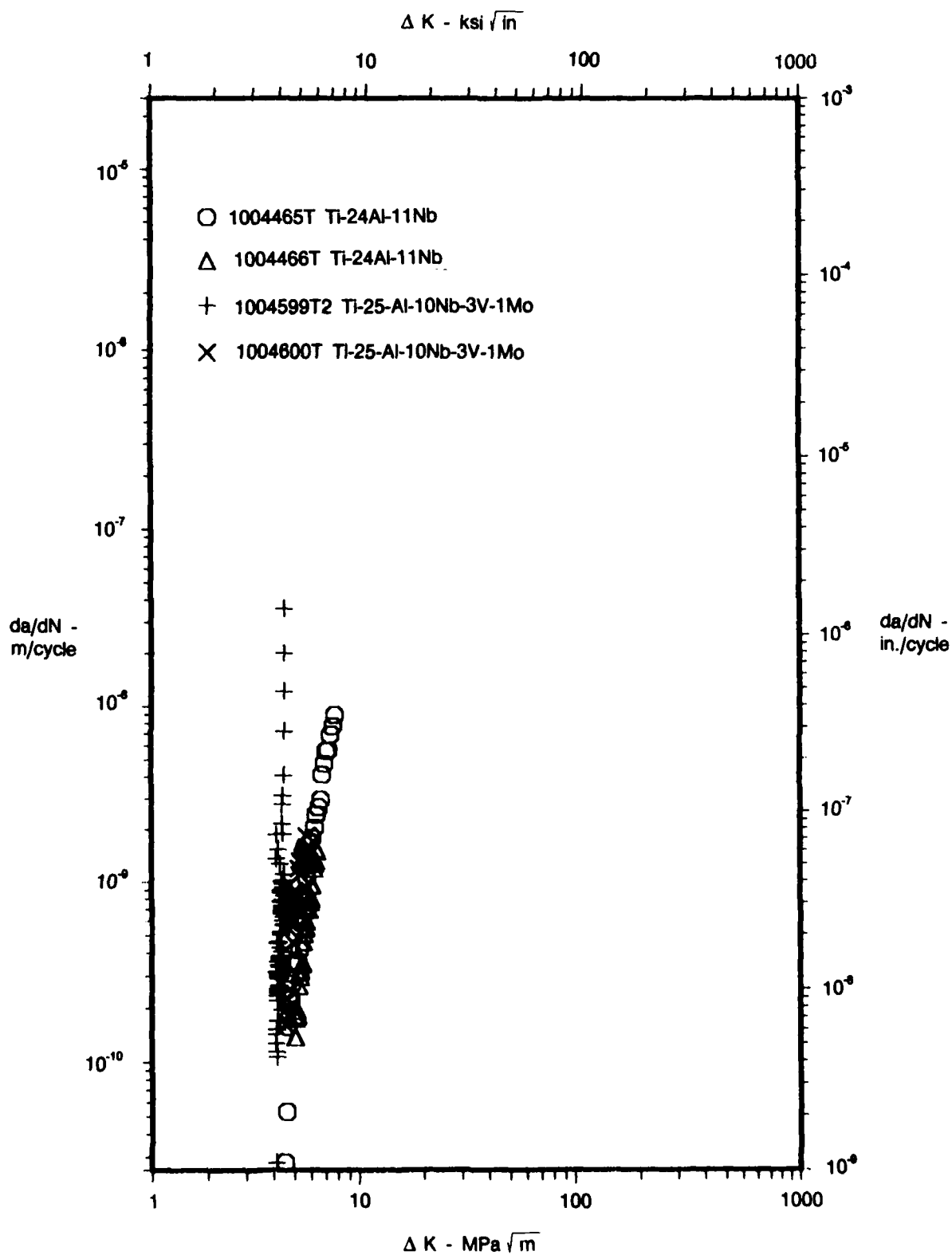


Figure 144. Threshold Crack Growth Rate Material Comparison, Ti-24Al-11Nb Versus Ti-25Al-10Nb-3V-1Mo at 26°C (80°F), $R = 0.1$, and 20 Hz

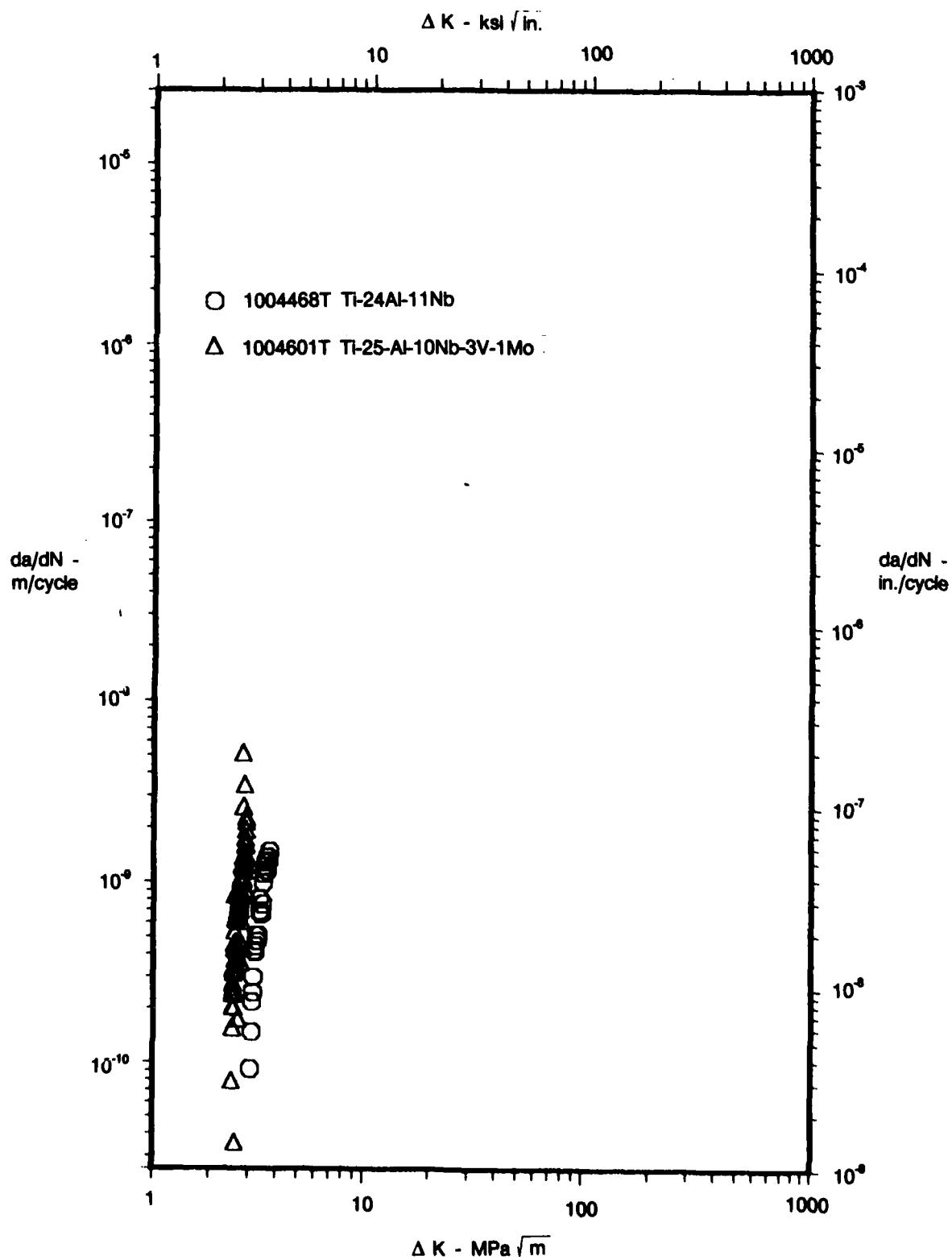
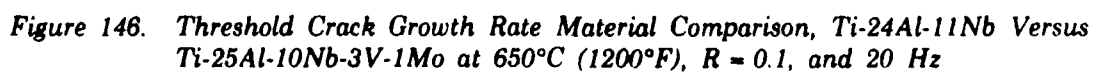
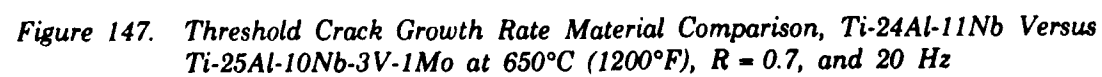


Figure 145. Threshold Crack Growth Rate Material Comparison, Ti-24Al-11Nb Versus Ti-25Al-10Nb-3V-1Mo at 26°C (80°F), $R = 0.7$, and 20 Hz





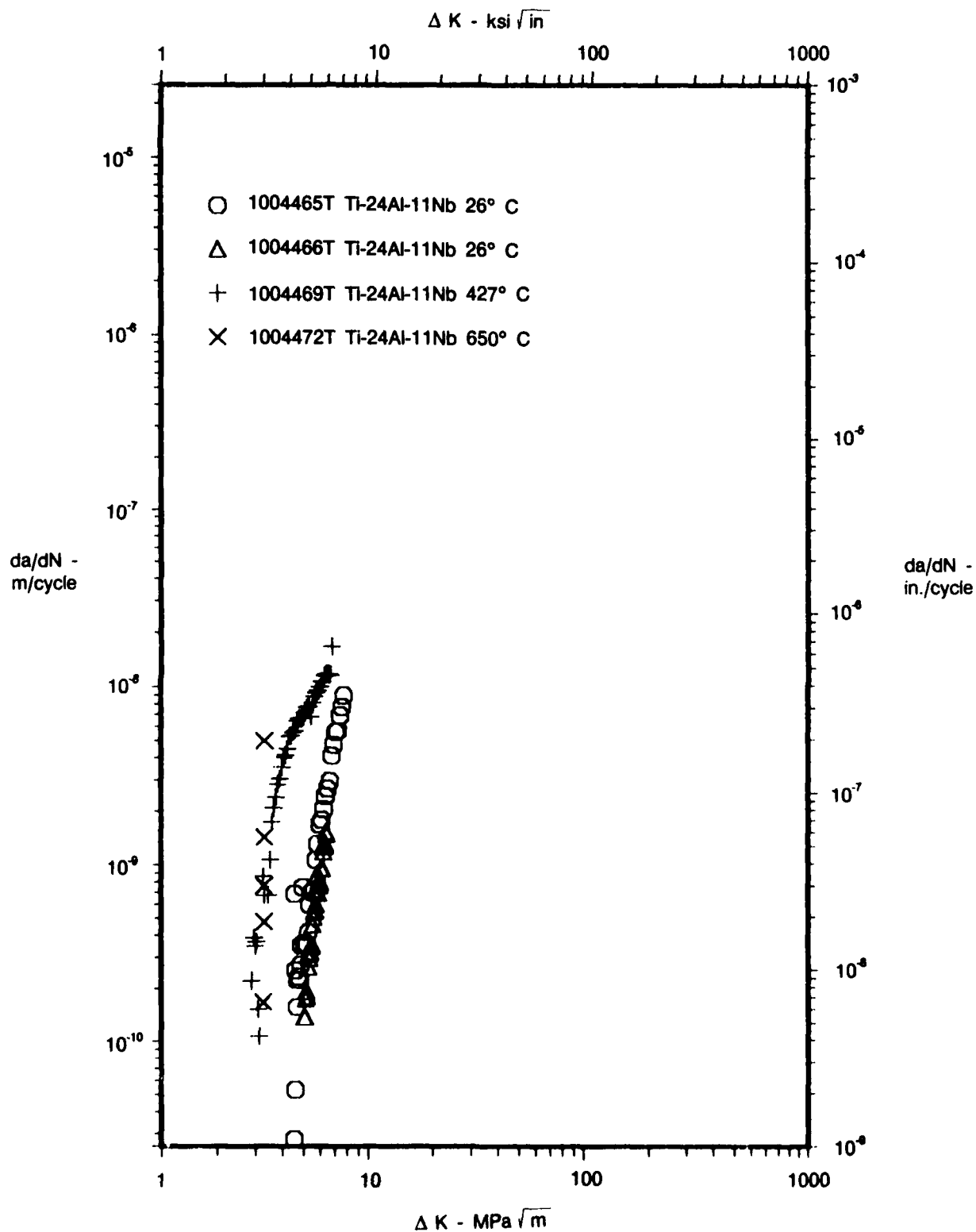


Figure 148. Threshold Crack Growth Rate Temperature Comparison, Ti-24Al-11Nb at $R = 0.1$ and 20 Hz

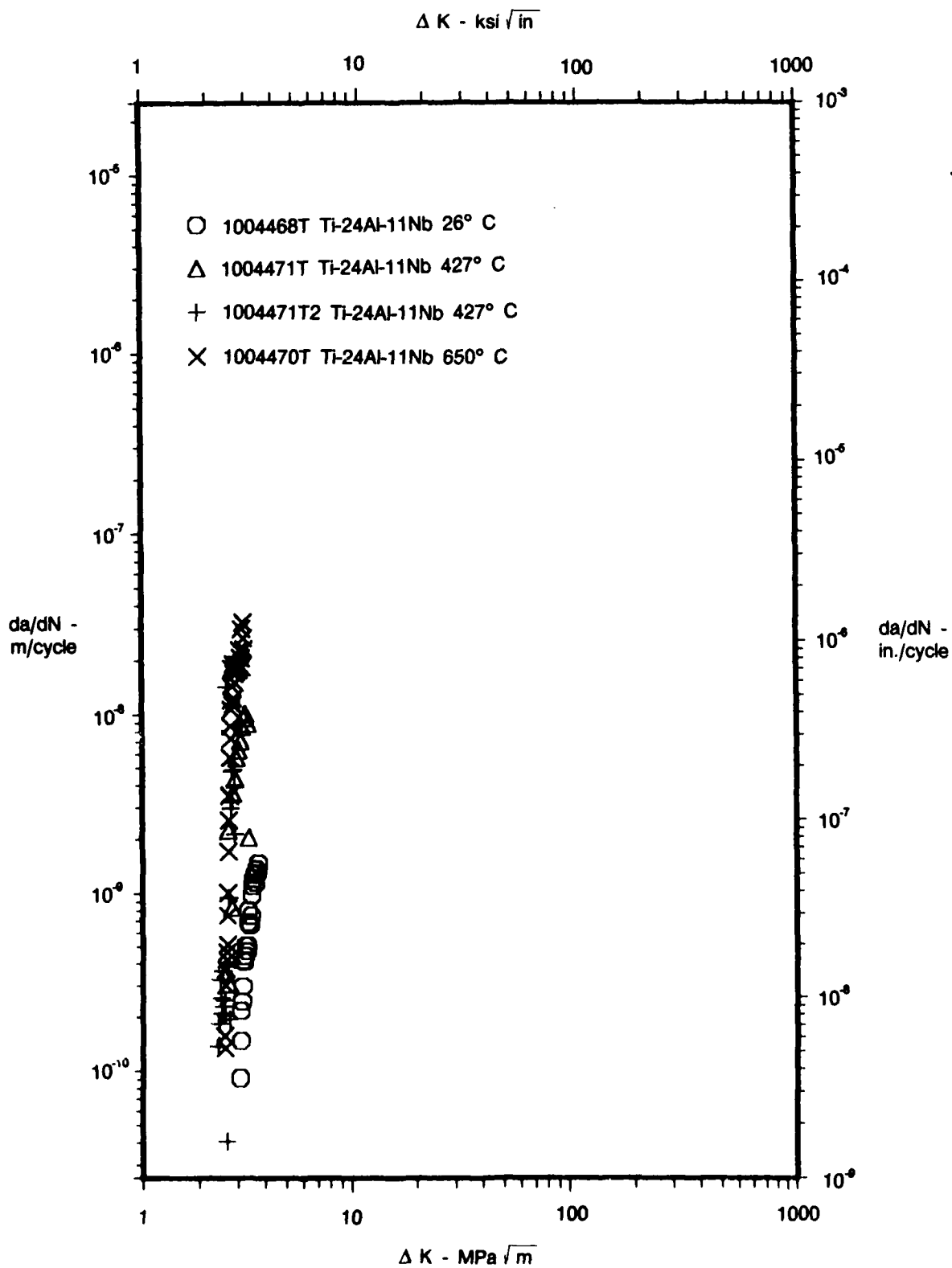


Figure 149. Threshold Crack Growth Rate Temperature Comparison, Ti-24Al-11Nb at $R = 0.7$ and 20 Hz

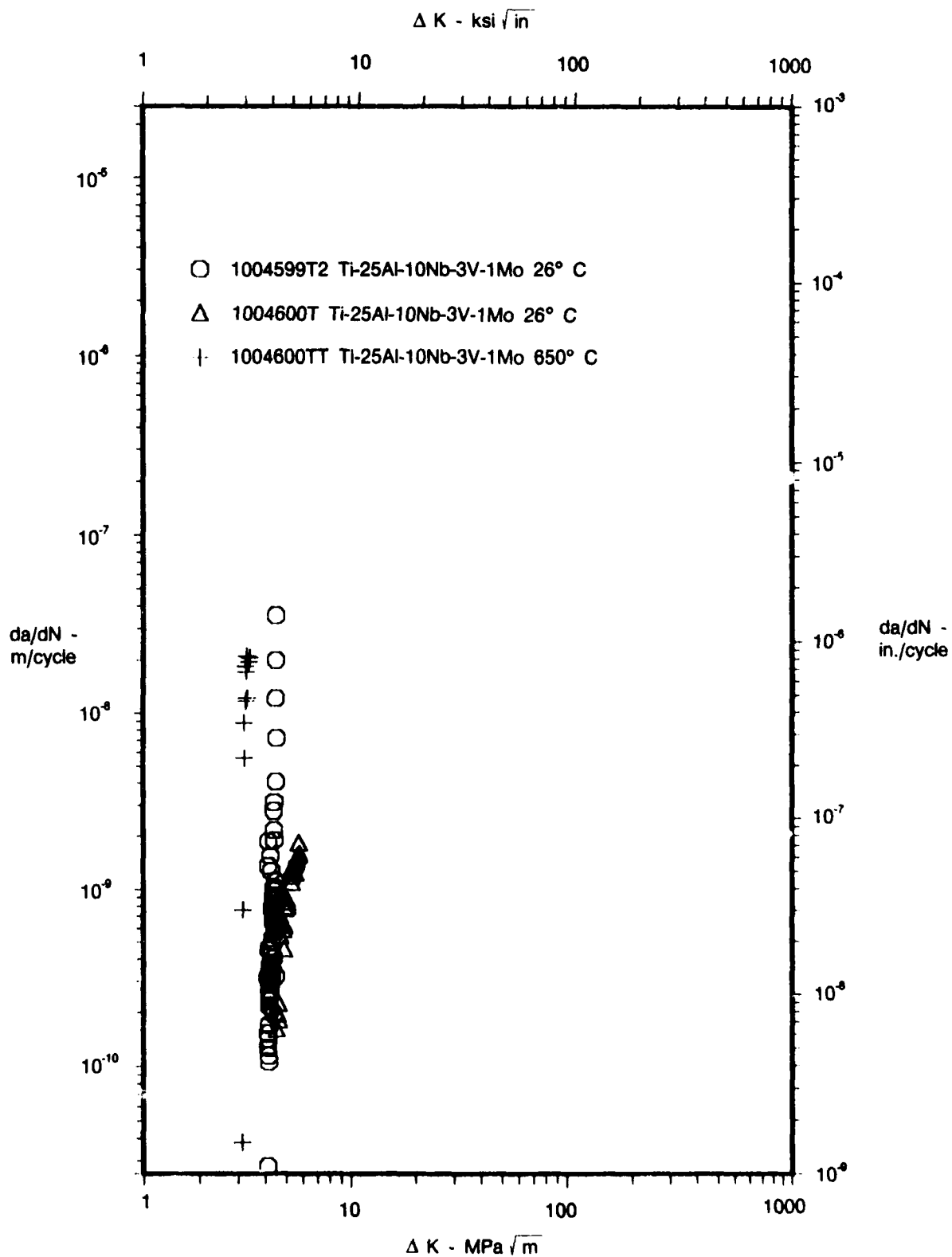


Figure 150. Threshold Crack Growth Rate Temperature Comparison, Ti-25Al-10Nb-3V-1Mo at $R = 0.1$ and 20 Hz

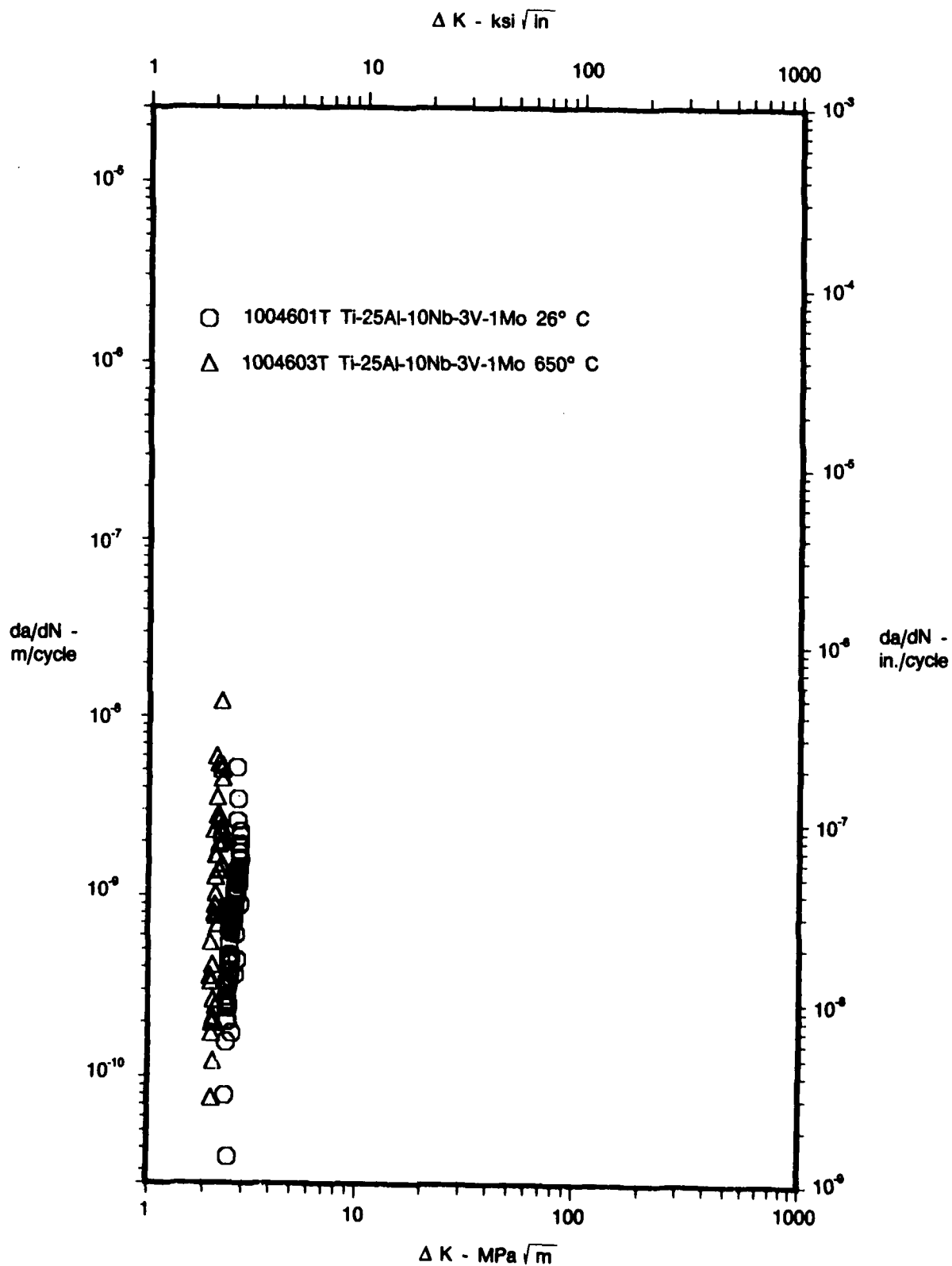


Figure 151. Threshold Crack Growth Rate Temperature Comparison, Ti-25Al-10Nb-3V-1Mo at $R = 0.7$ and 20 Hz

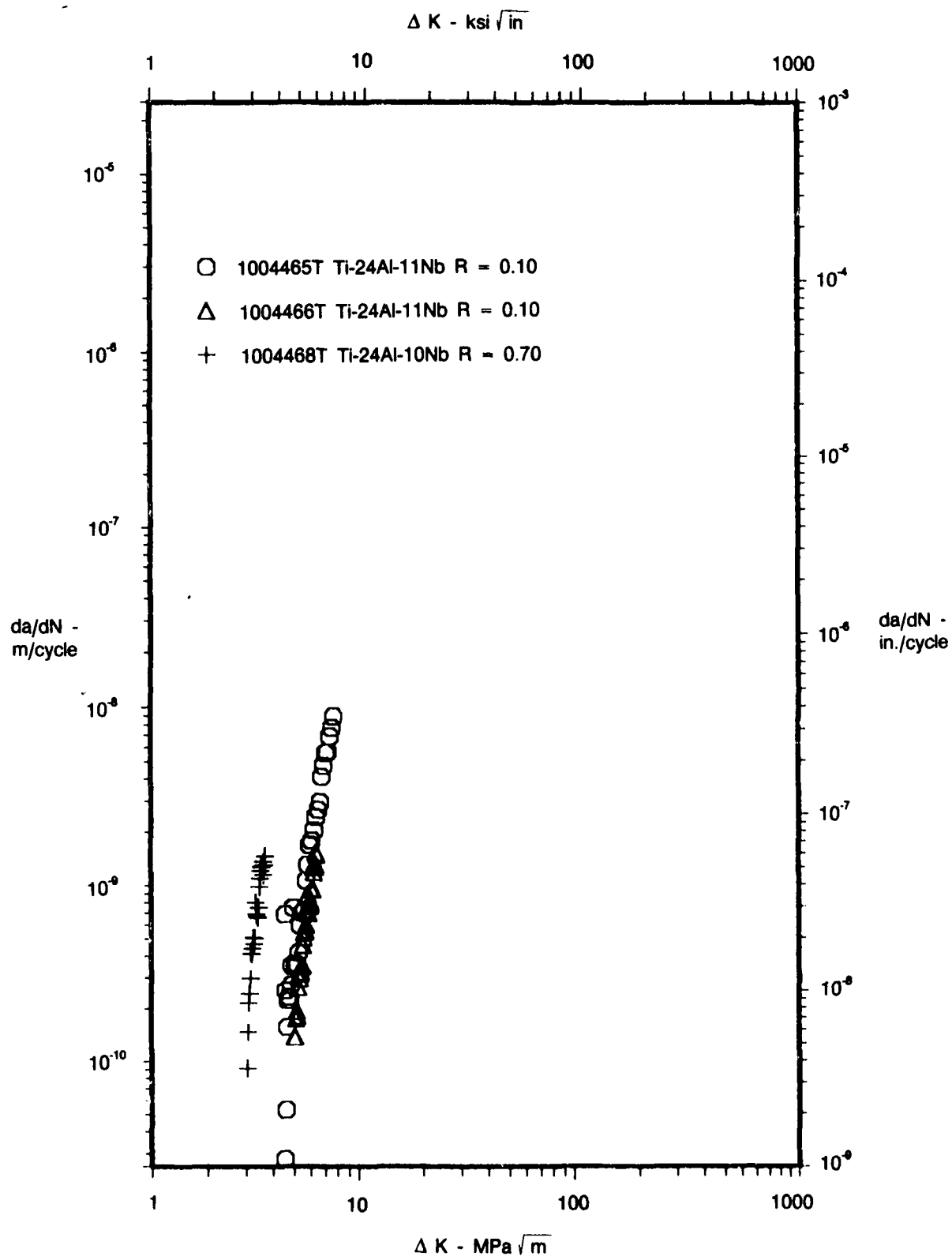


Figure 152. Threshold Crack Growth Rate Stress Ratio Effect, Ti-24Al-11Nb at 26°C (80°F) and 20 Hz

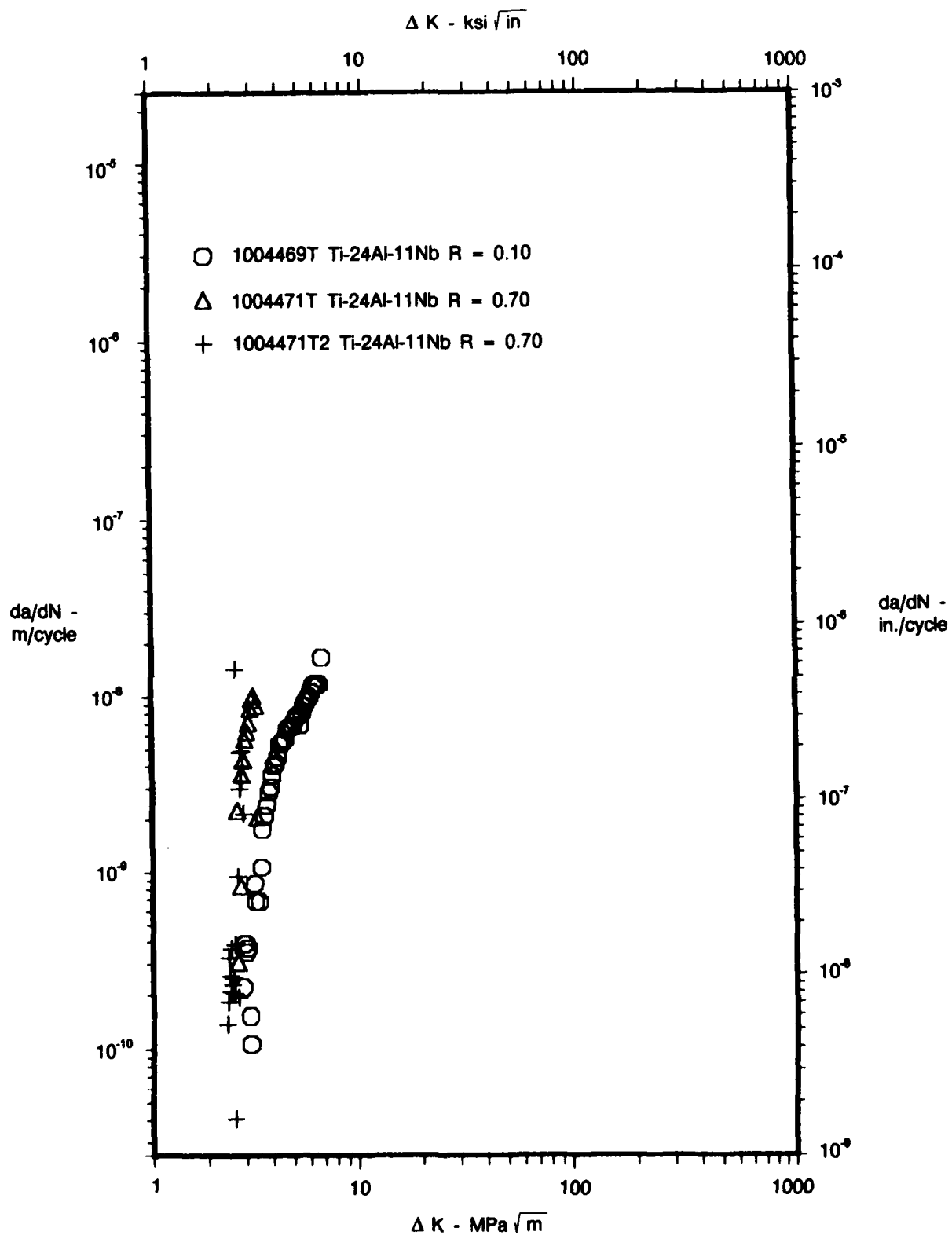


Figure 153. Threshold Crack Growth Rate Stress Ratio Effect, Ti-24Al-11Nb at 427°C (800°F) and 20 Hz

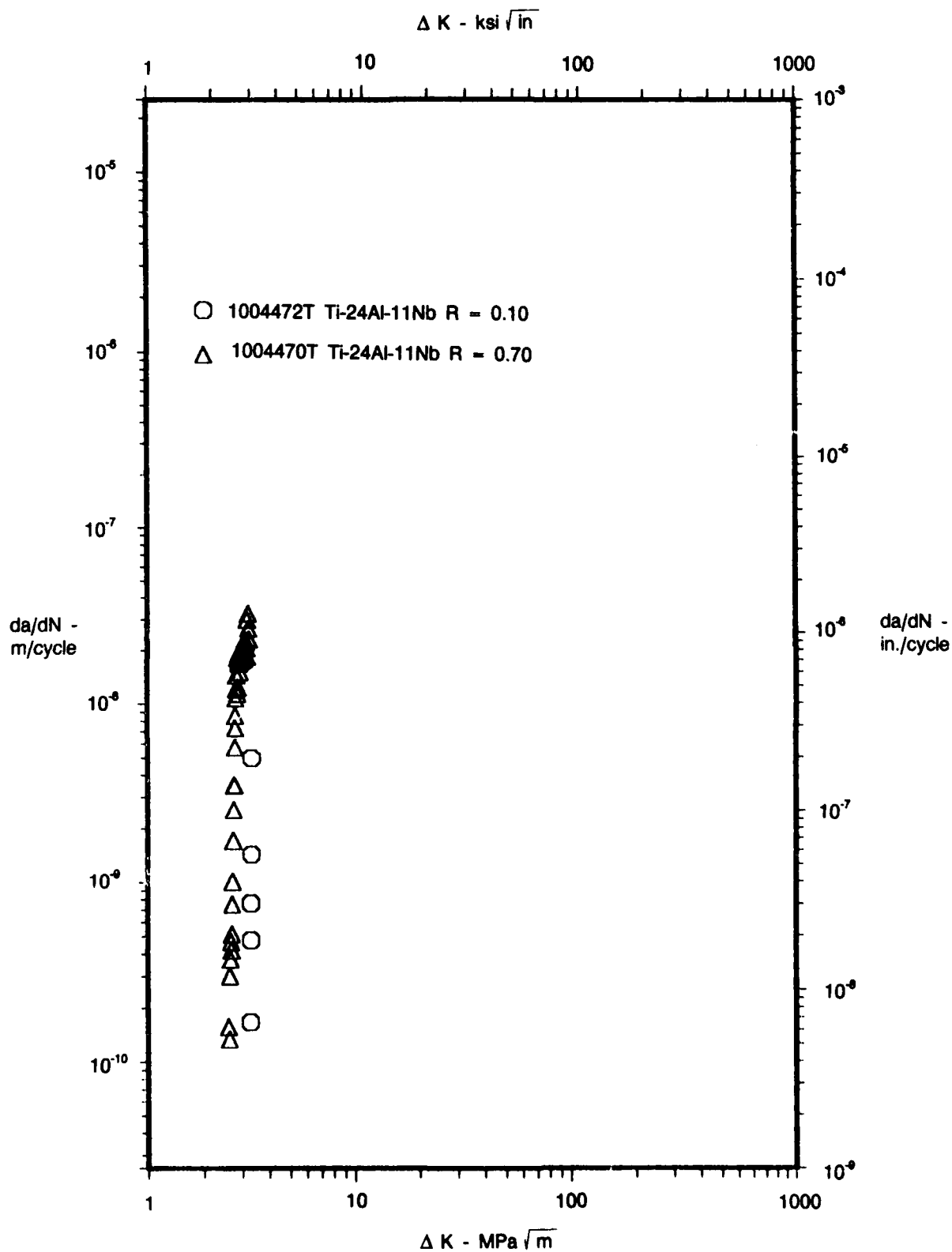


Figure 154. Threshold Crack Growth Rate Stress Ratio Effect, Ti-24Al-11Nb at 650°C (1200°F) and 20 Hz

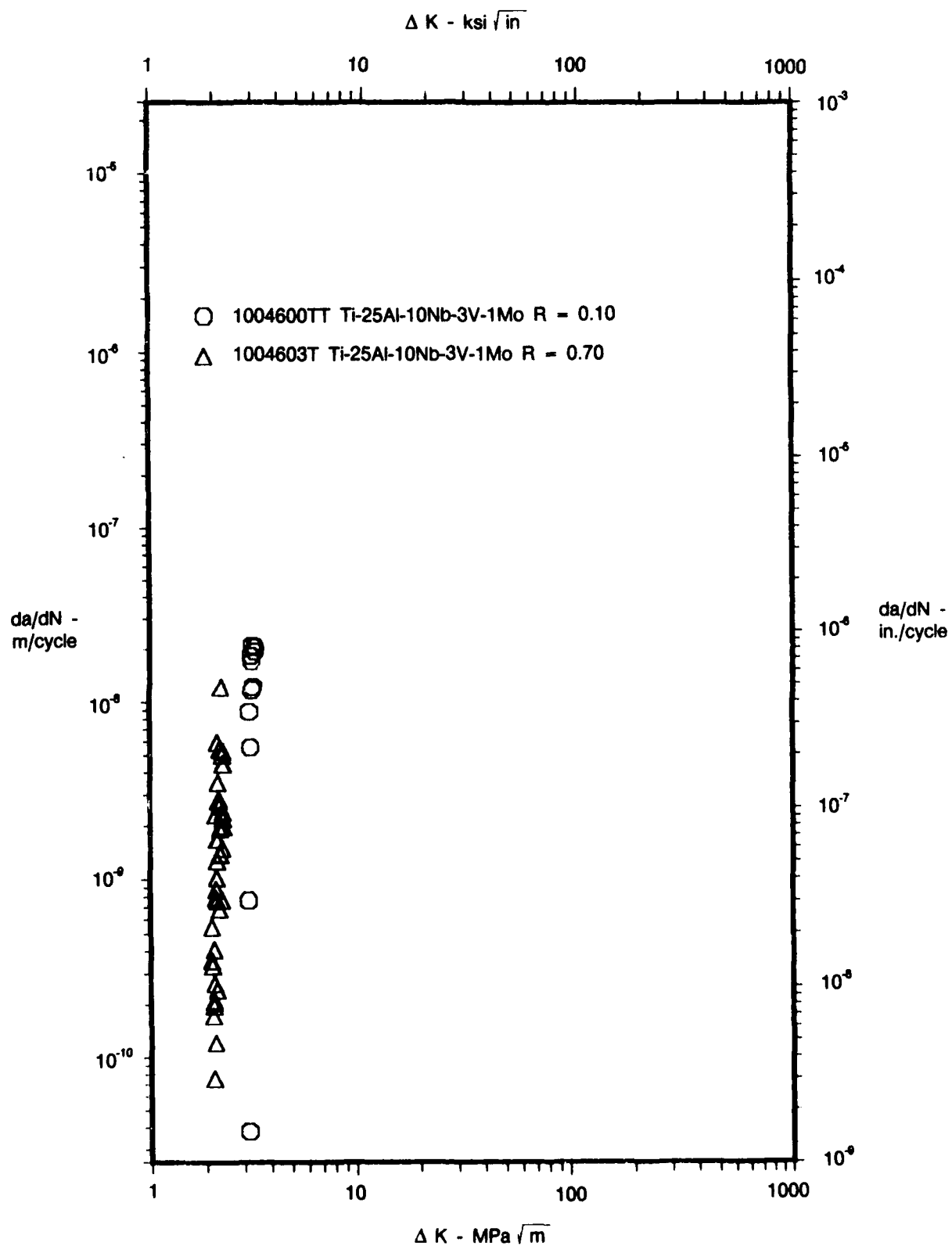


Figure 156. Threshold Crack Growth Rate Stress Ratio Effect, Ti-25Al-10Nb-3V-1Mo at 650°C (1200°F) and 20 Hz

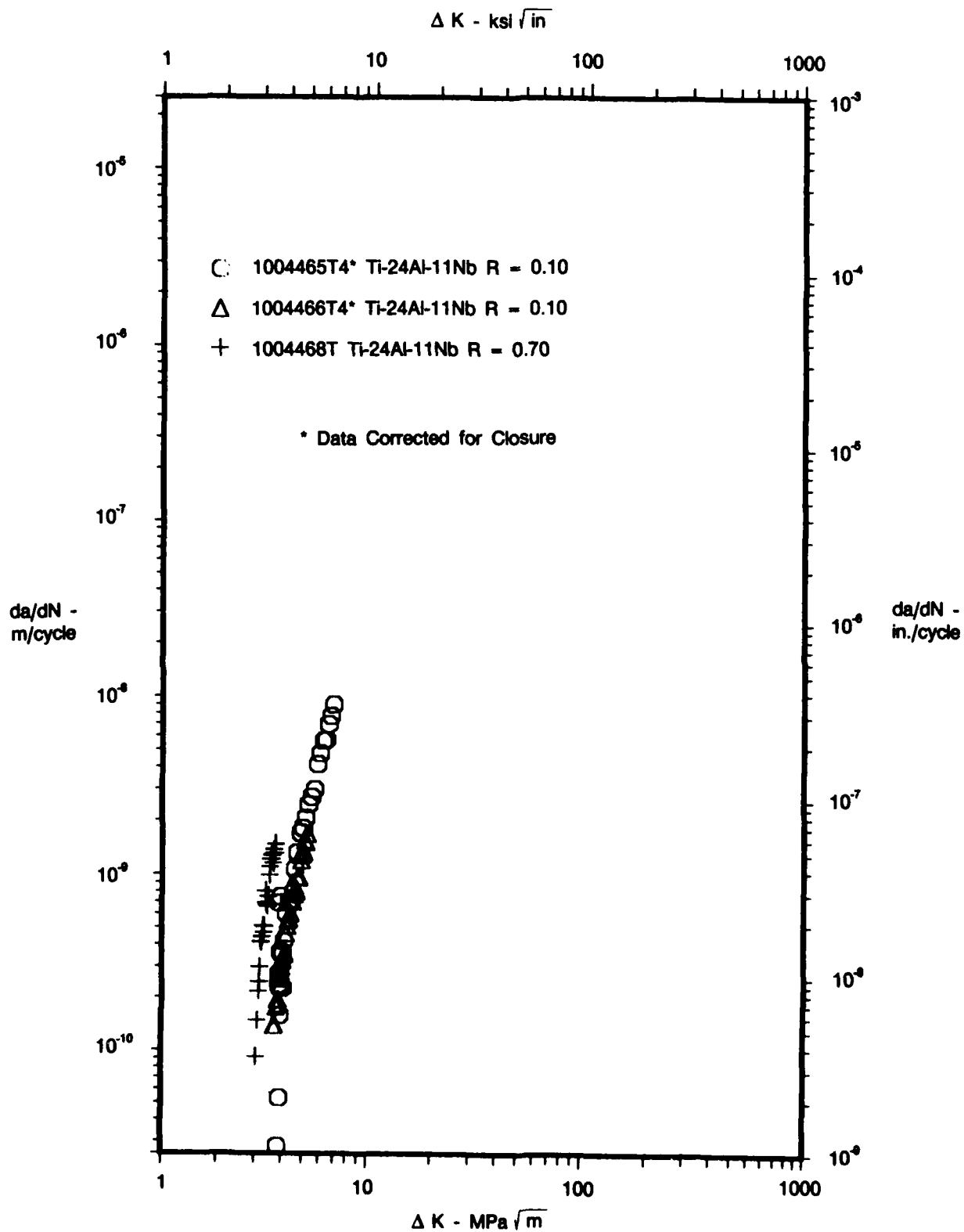


Figure 157. Threshold Crack Growth Rate Stress Ratio Comparison After Closure Correction, Ti-24Al-11Nb at 26°C (80°F) and 20 Hz

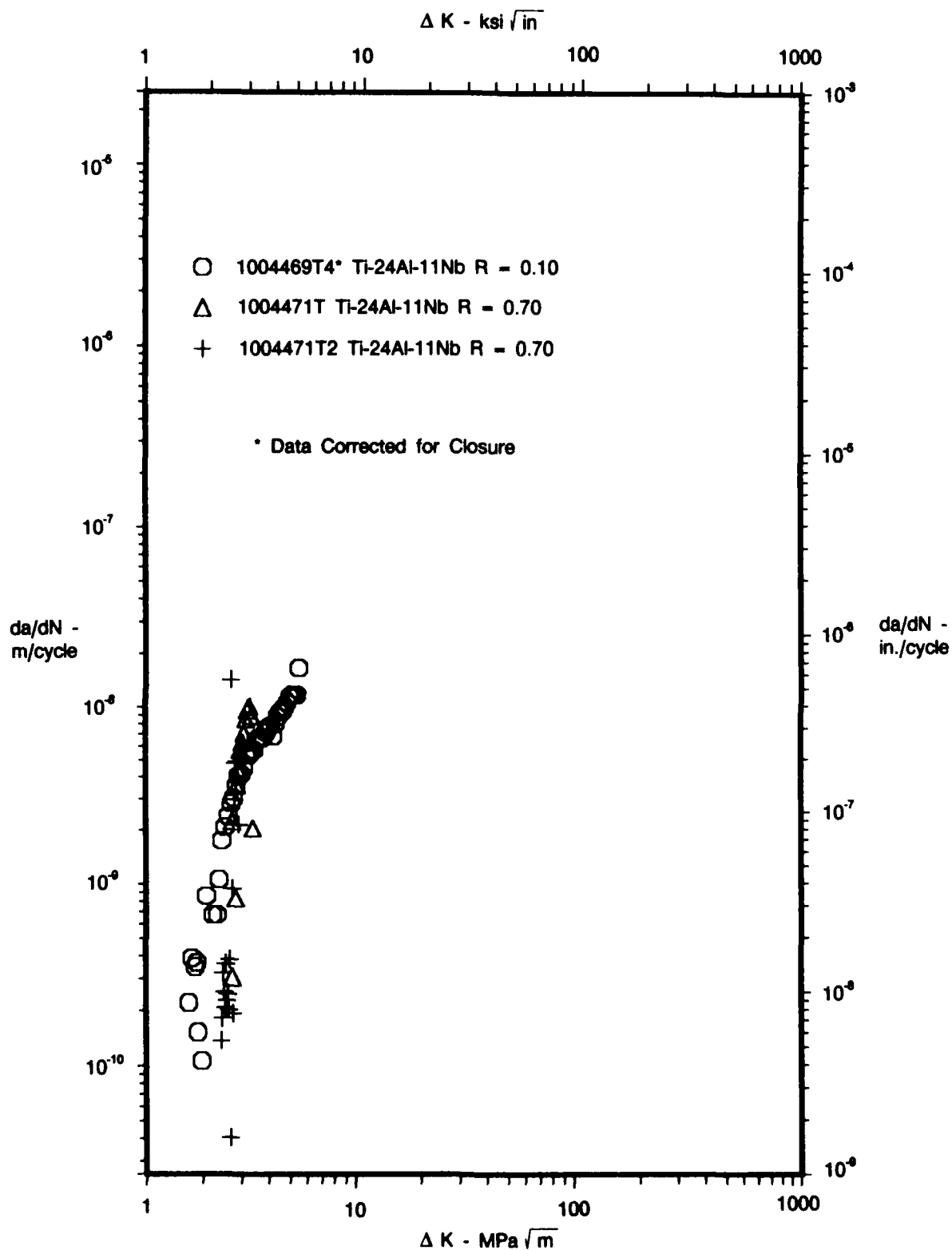


Figure 158. Threshold Crack Growth Rate Stress Ratio Comparison After Closure Correction, Ti-24Al-11Nb at 427°C (800°F) and 20 Hz

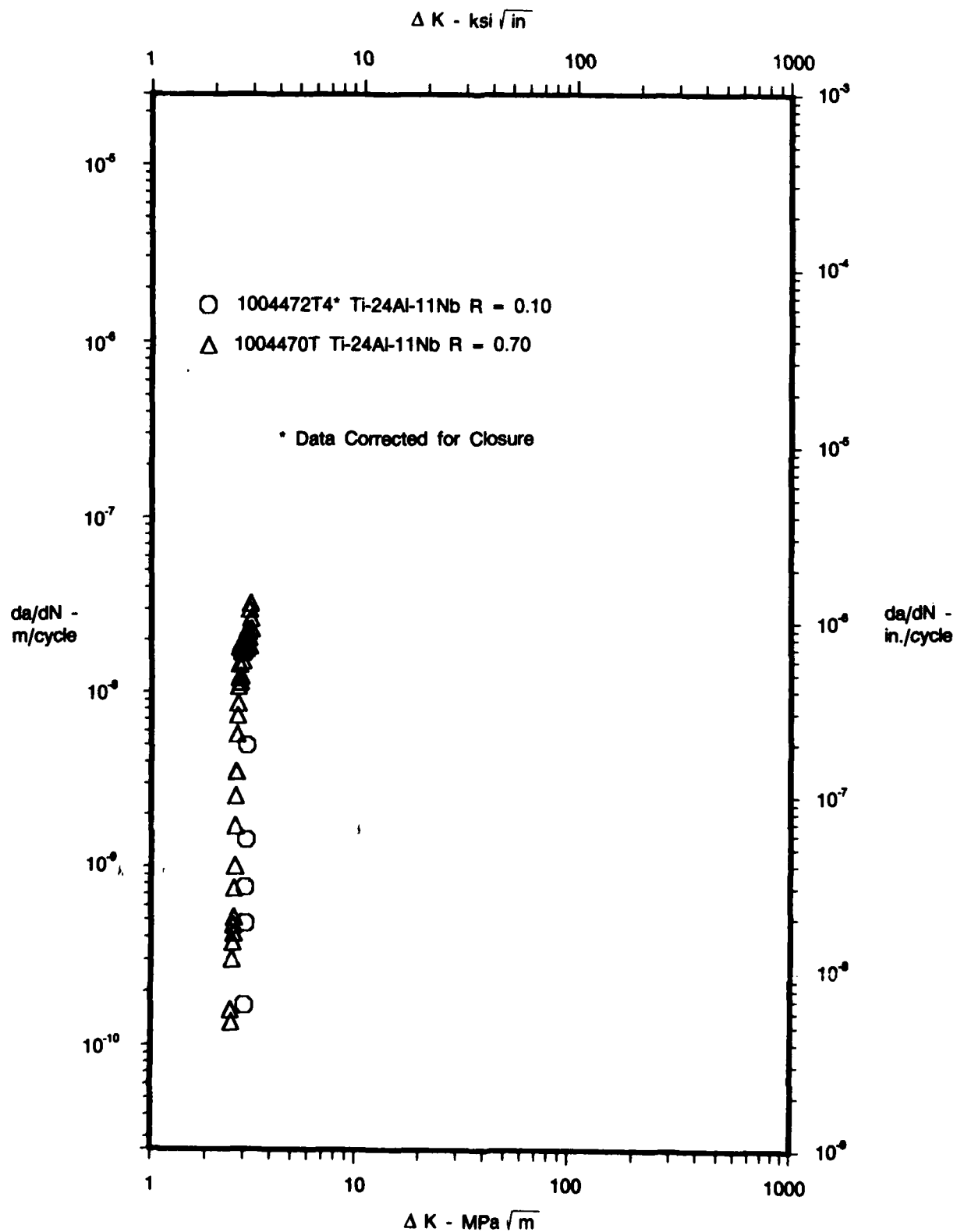


Figure 159. Threshold Crack Growth Rate Stress Ratio Comparison After Closure Correction, Ti-24Al-11Nb at 650°C (1200°F) and 20 Hz

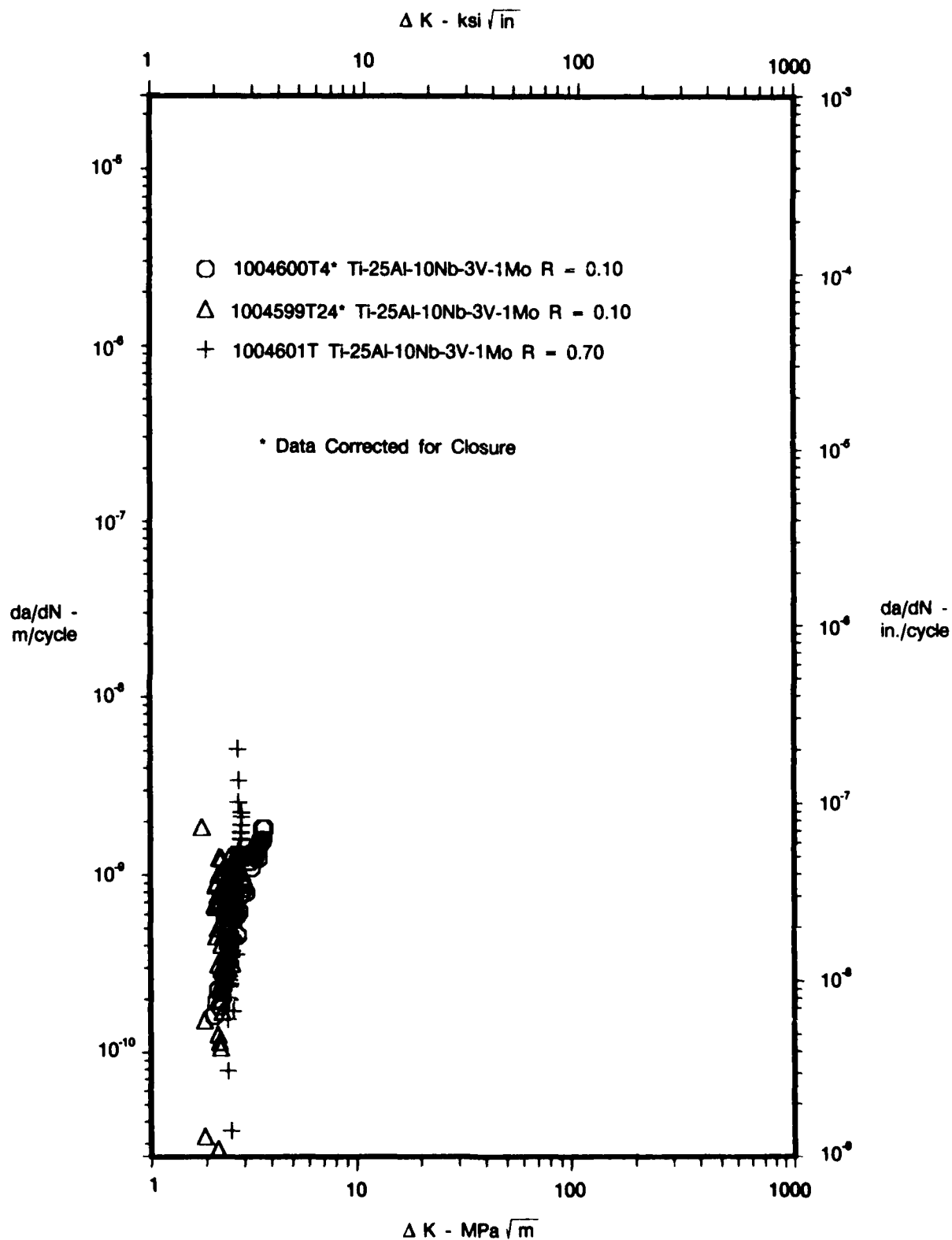


Figure 160. Threshold Crack Growth Rate Stress Ratio Comparison After Closure, Ti-25Al-10Nb-3V-1Mo at 26°C (80°F) and 20 Hz

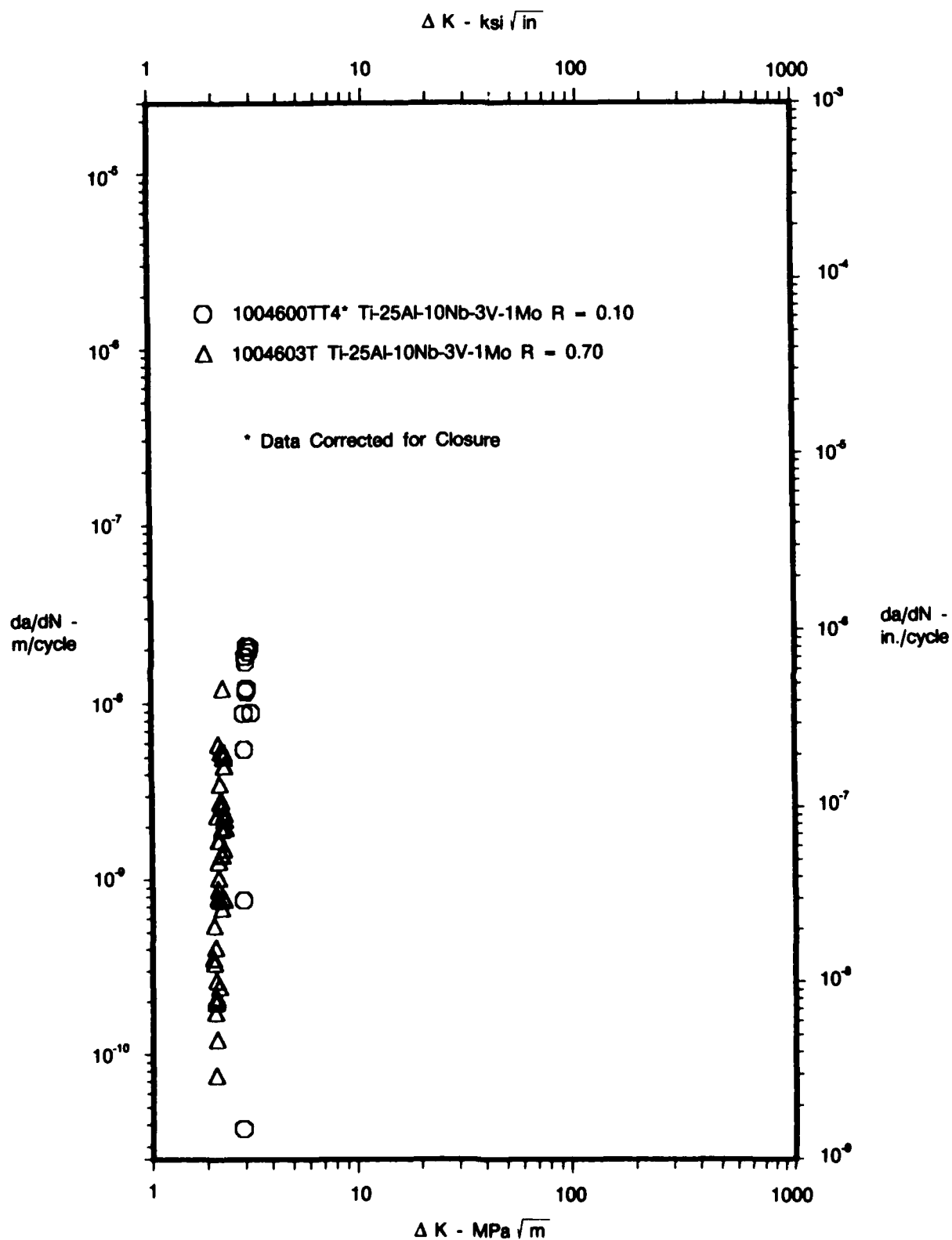


Figure 161. Threshold Crack Growth Rate Stress Ratio Comparison After Closure, Ti-25Al-10Nb-3V-1Mo at 650°C (1200°F) and 20 Hz

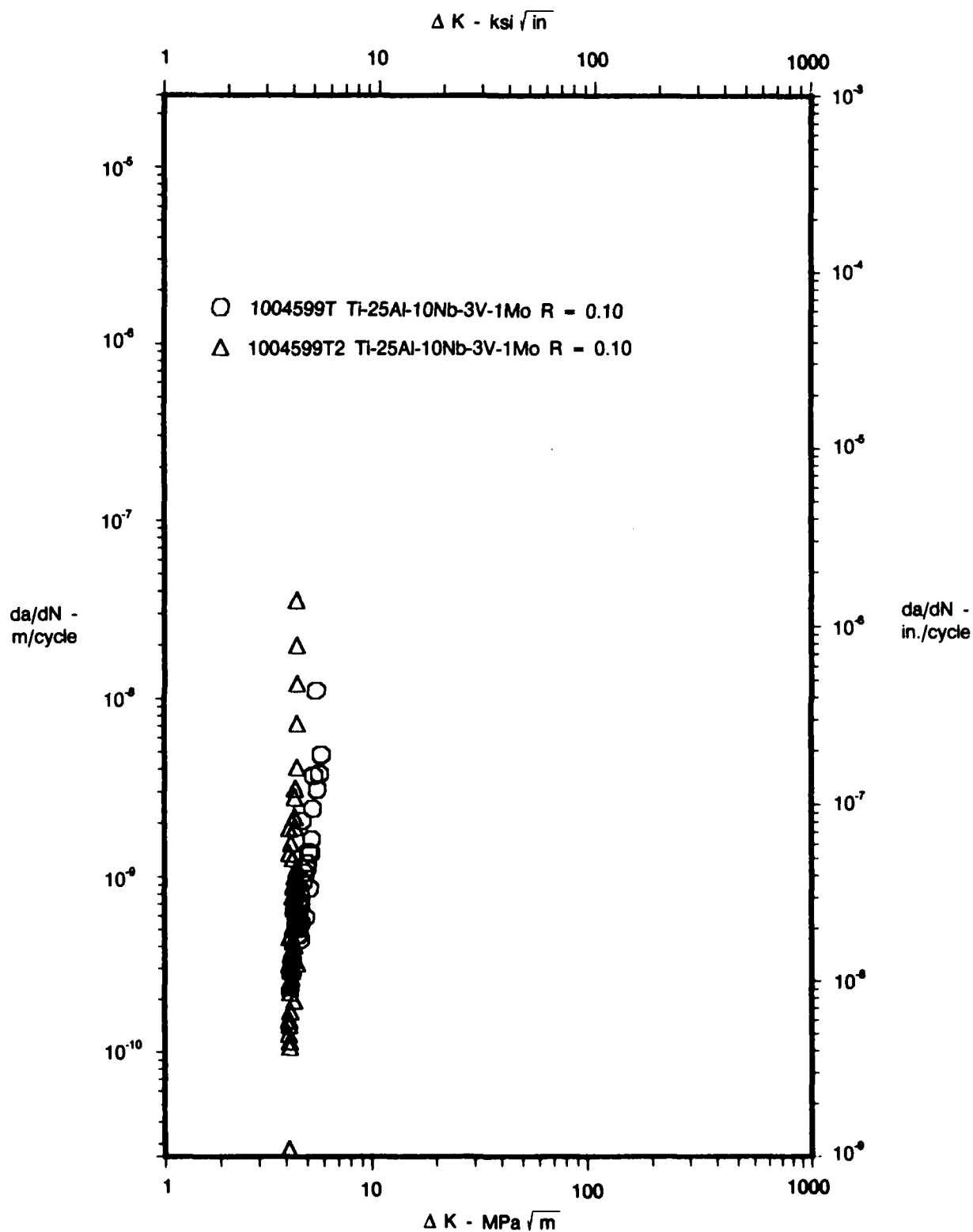
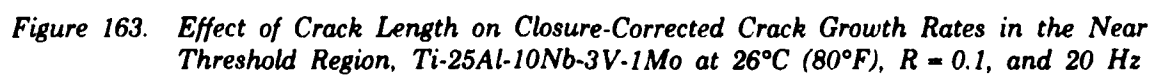
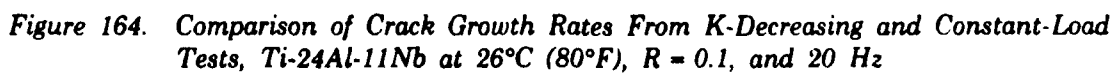


Figure 162. Effect of Crack Length on Near Threshold Crack Growth Rates, Ti-25Al-10Nb-3V-1Mo at 26°C (80°F) and 20 Hz





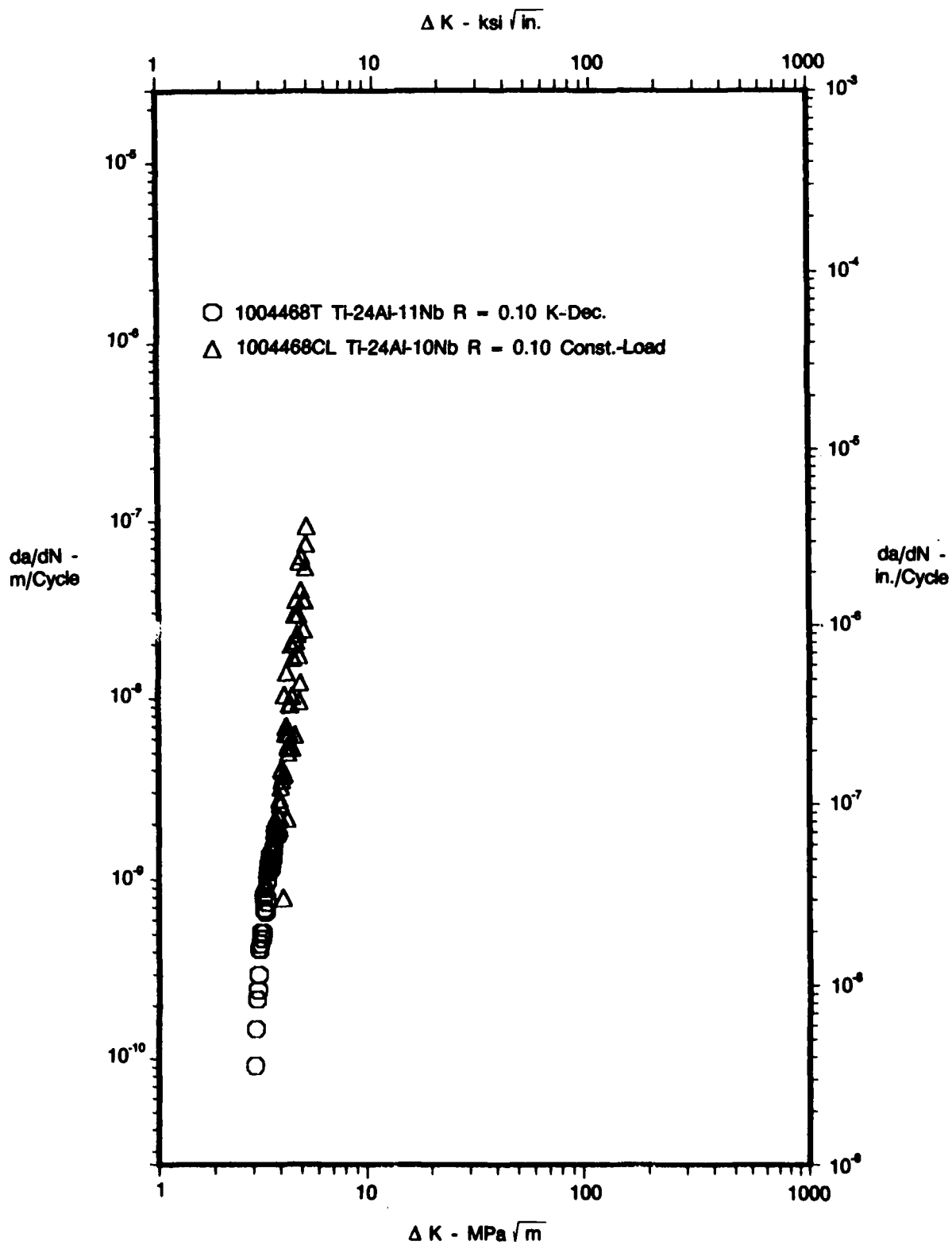


Figure 165. Comparison of Crack Growth Rates From K-Decreasing and Constant-Load Tests, Ti-24Al-11Nb at 26°C (80°F), R = 0.7, and 20 Hz

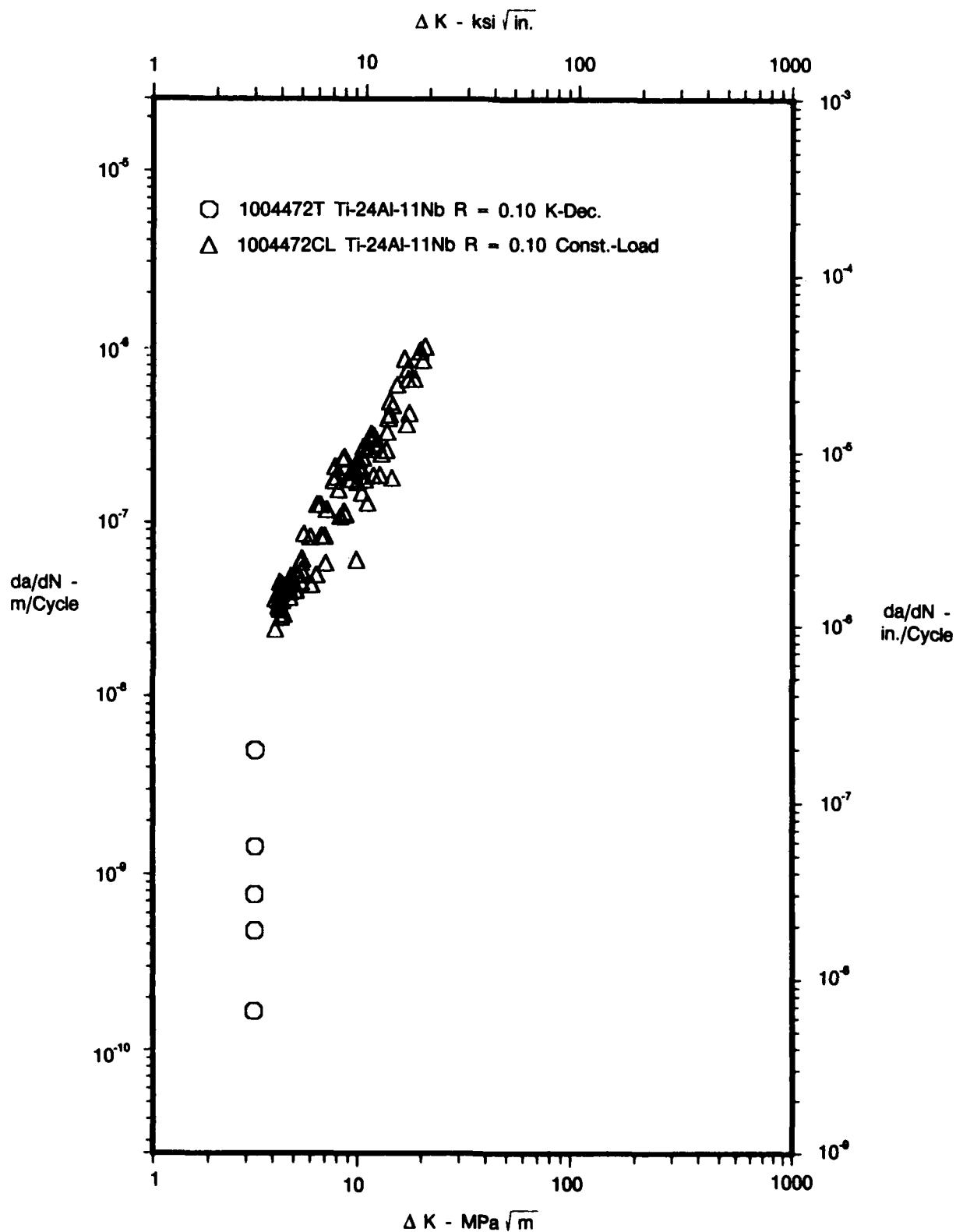


Figure 166. Comparison of Crack Growth Rates From K-Decreasing and Constant-Load Tests, Ti-24Al-11Nb at 650°C (1200°F), R = 0.1, and 20 Hz

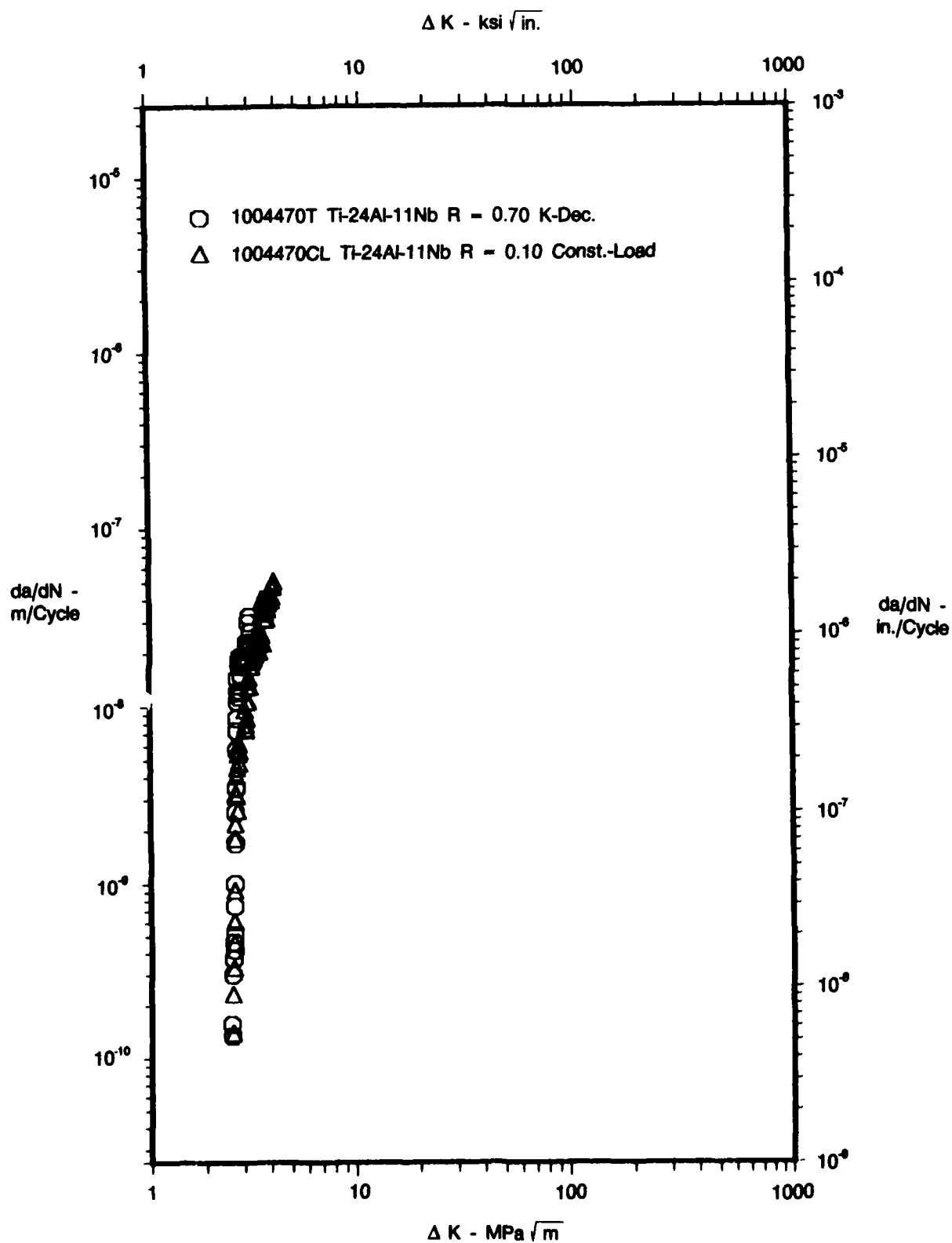


Figure 167. Comparison of Crack Growth Rates From K-Decreasing and Constant Load Tests, Ti-24Al-11Nb at 650°C (1200°F), R = 0.7, and 20 Hz

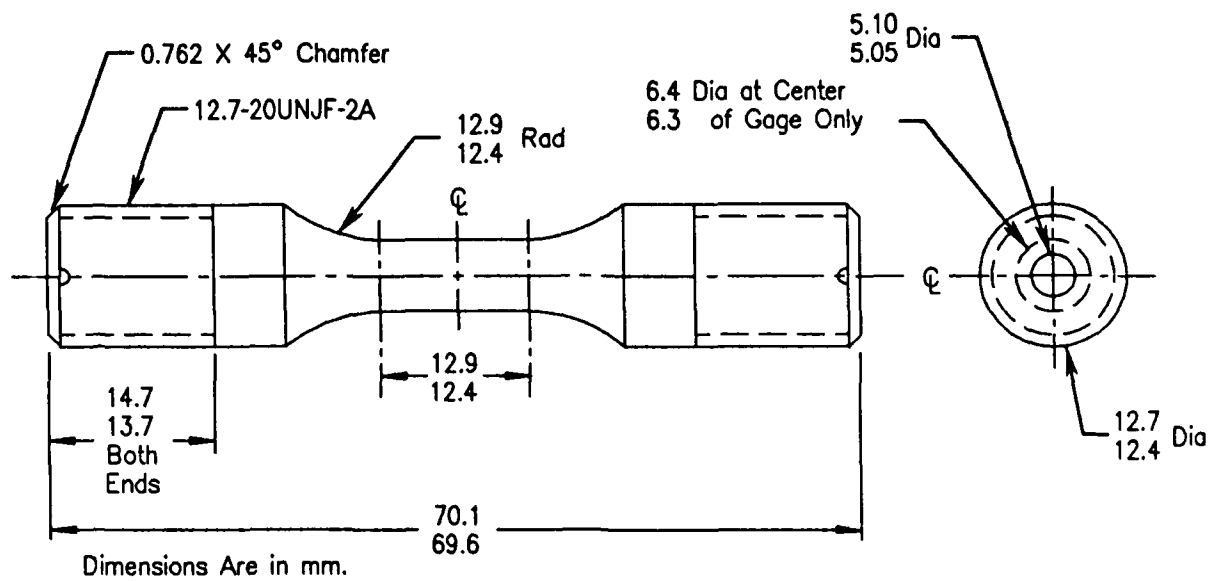


Figure 168. Load Control TMF Specimen

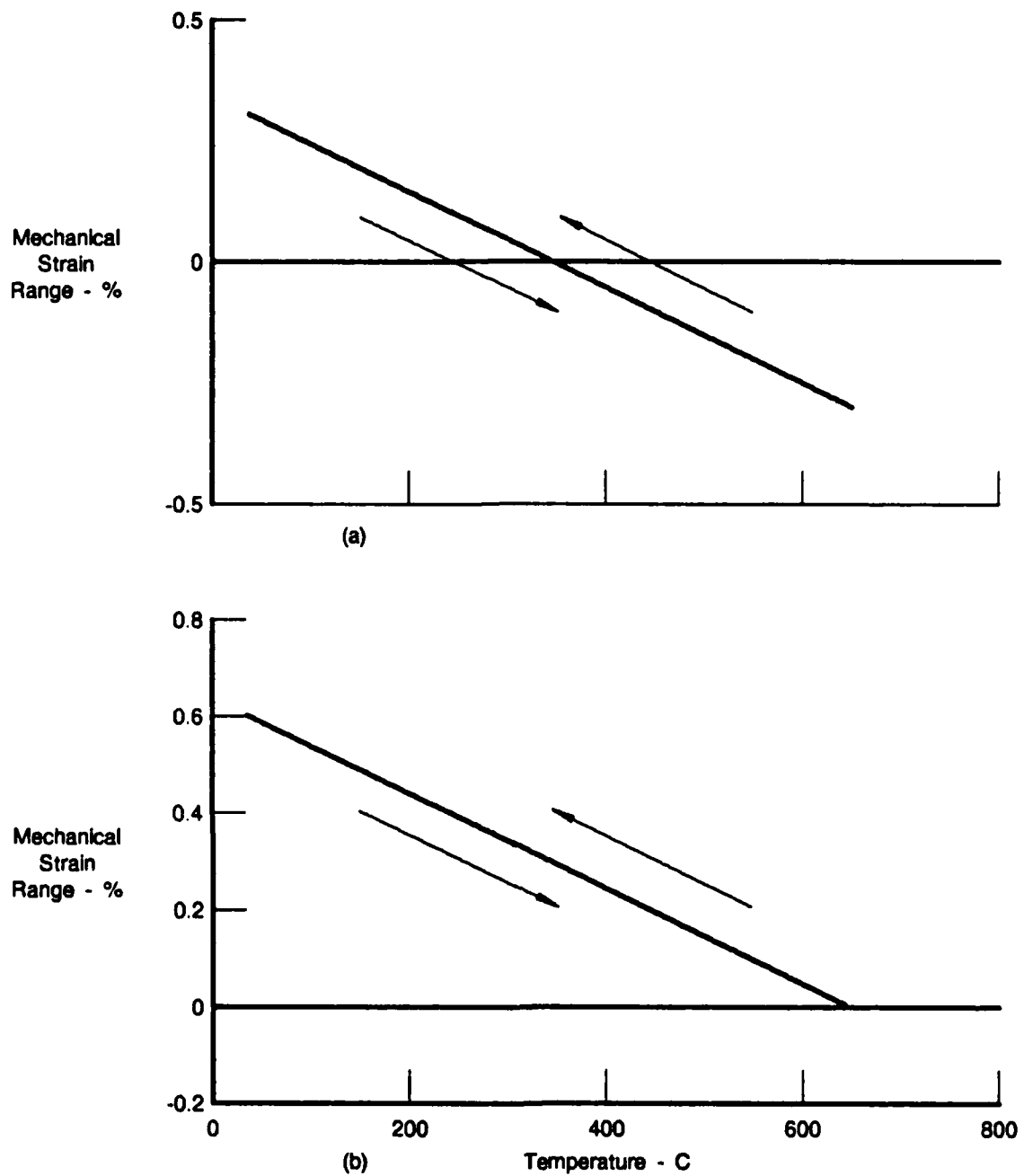
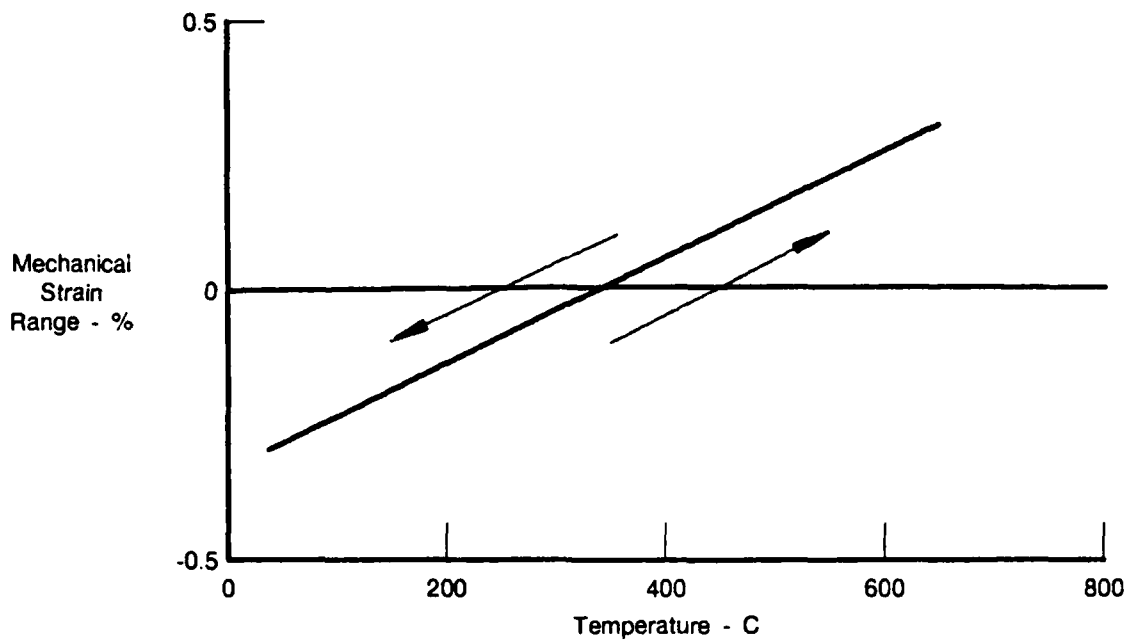


Figure 169. Out-of-Phase Cycle (Type I) with (a) $R = -1.0$ and (b) $R = 0.0$



FDA 369704

Figure 170. In-Phase Cycle (Type II) with $R = -1.0$

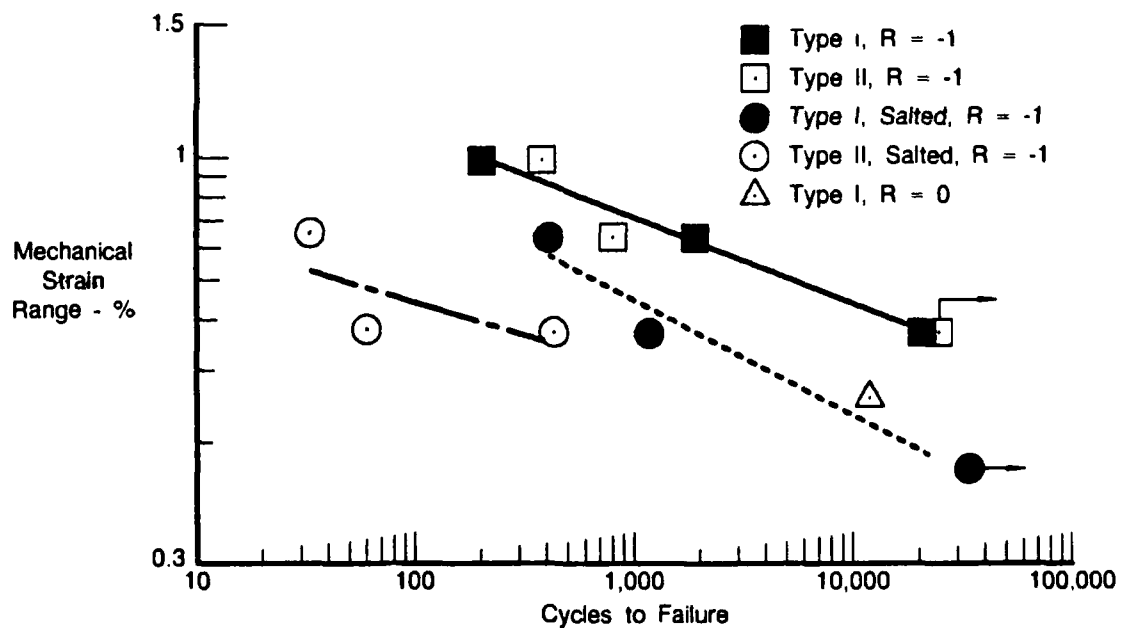
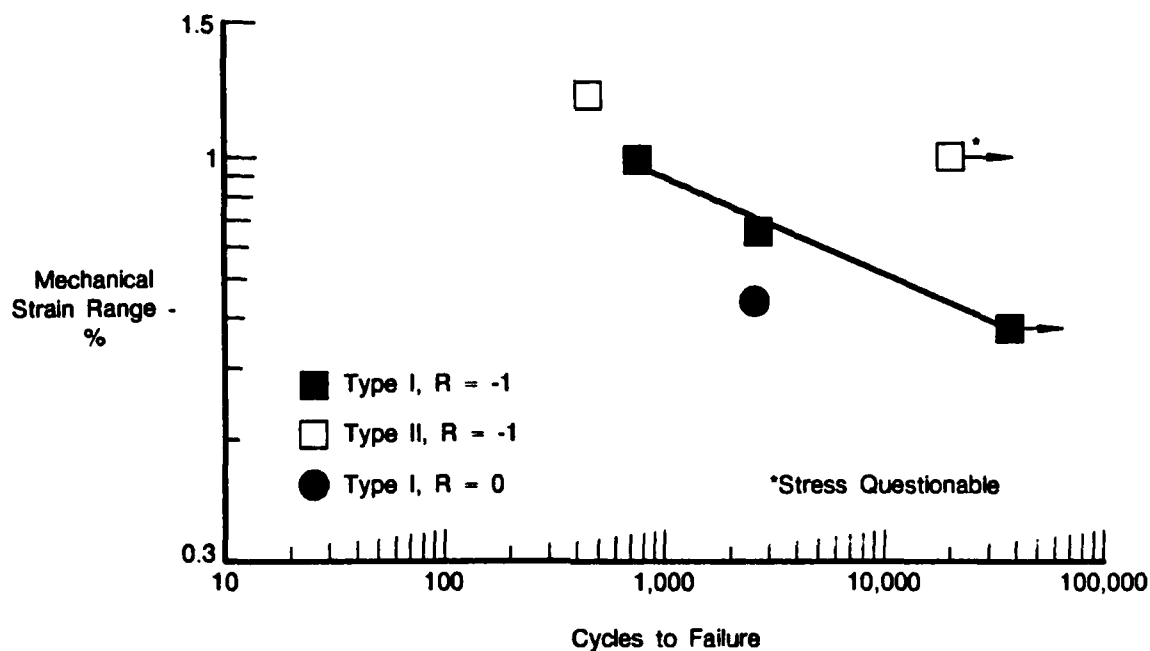


Figure 171. Load Control TMF Results of Ti-24Al-11Nb at 0.5 cpm and 38° to 650°C (Strain Ratio = R and Salted = Hot Salt Stress Corrosion Test)



FDA 369706

Figure 172. Load Control TMF Results of Ti-25Al-10Nb-3V-1Mo at 0.5 cpm and 38° to 650°C (Strain Ratio = R)

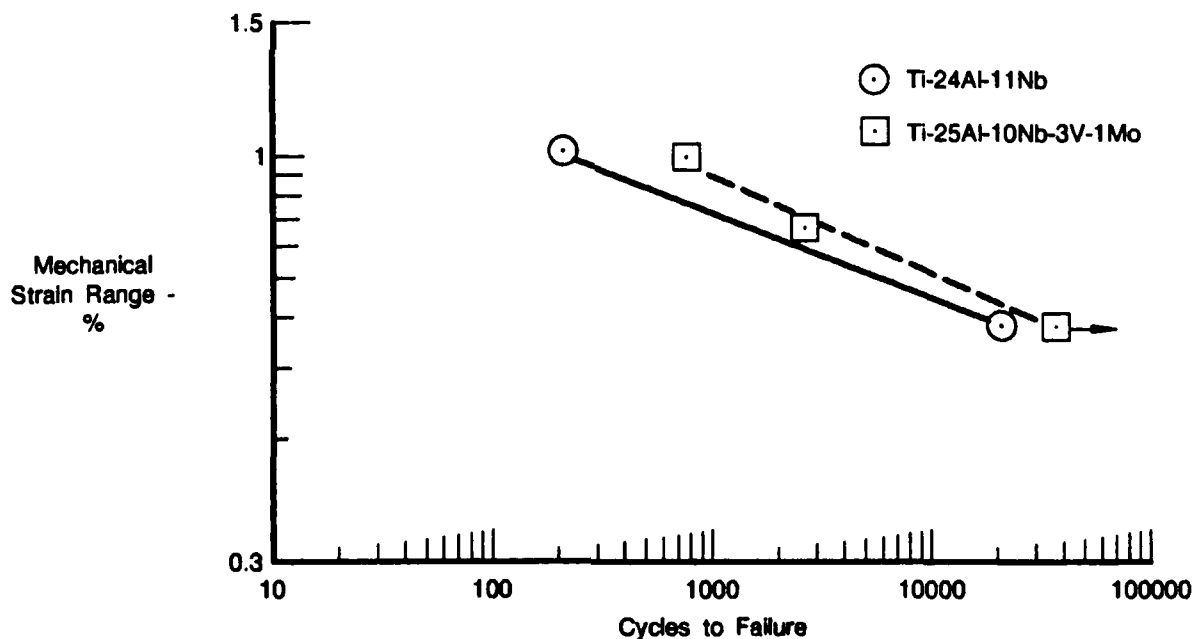


Figure 173. Ti-24Al-11Nb Versus Ti-25Al-10Nb-3V-1Mo, Load Control TMF Results (Type I Cycle, 0.5 cpm, 38° to 650°C, and Strain Ratio = -1.0)

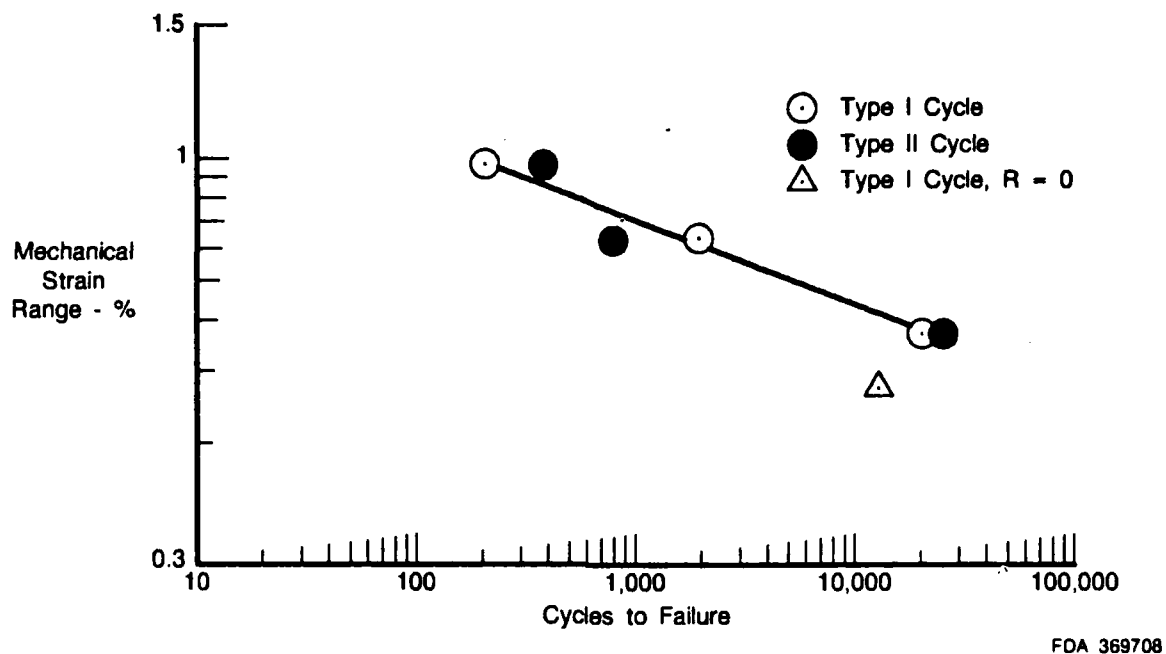


Figure 174. Load Control TMF Results of Ti-24Al-11Nb for Type I Cycle Versus Type II Cycle (0.5 cpm, 38° to 650°C, and Strain Ratio = -1.0)

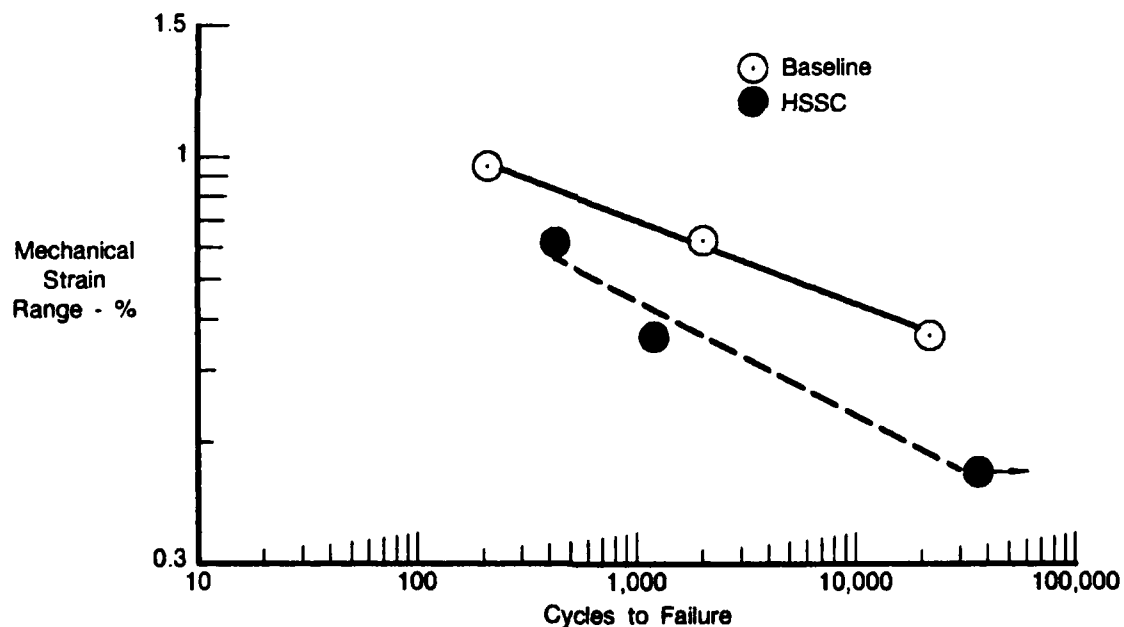


Figure 175. Effects of HSSC on Ti-24Al-11Nb for Type I Cycle (0.5 cpm, 38° to 650°C, and Strain Ratio = -1.0)

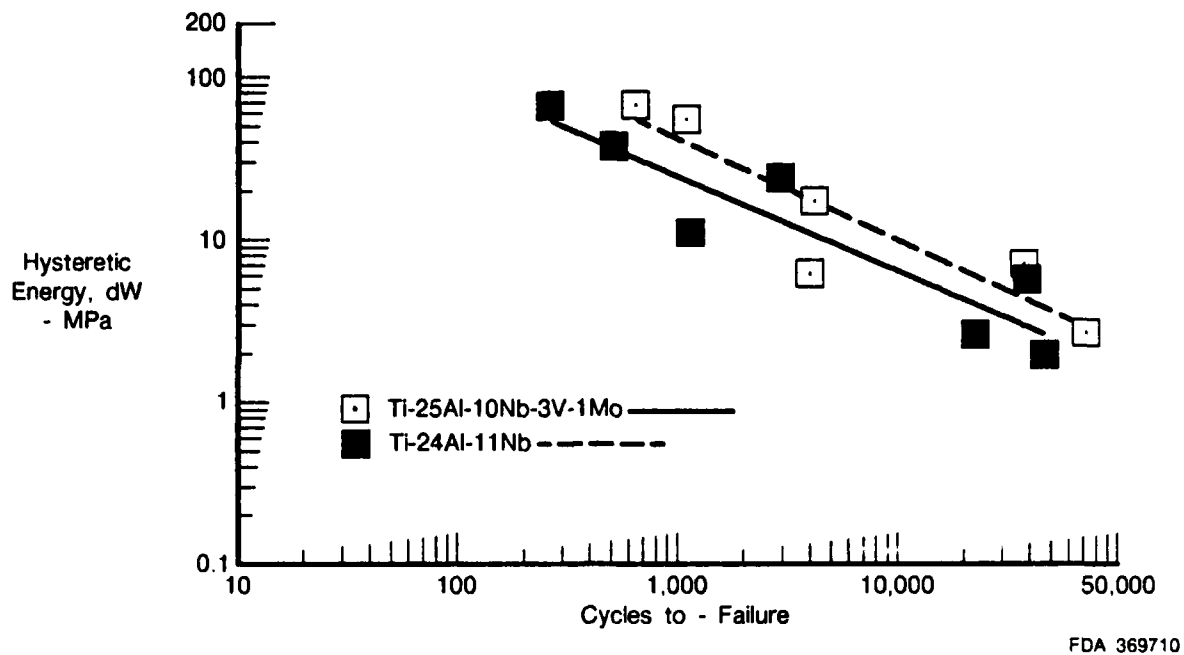


Figure 176. Hysteretic Energy Versus Cycles to Failure for Type I Cycle (0.5 cpm, 38° to 650°C, and Strain Ratio Varied)

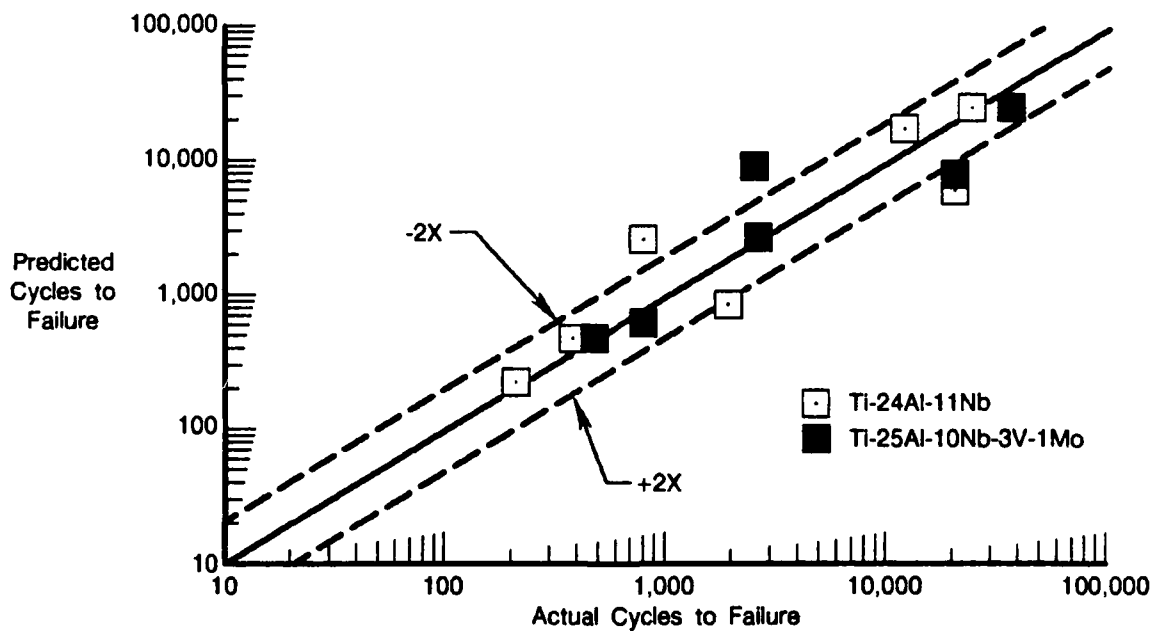


Figure 177. Actual Life Versus Predicted Life

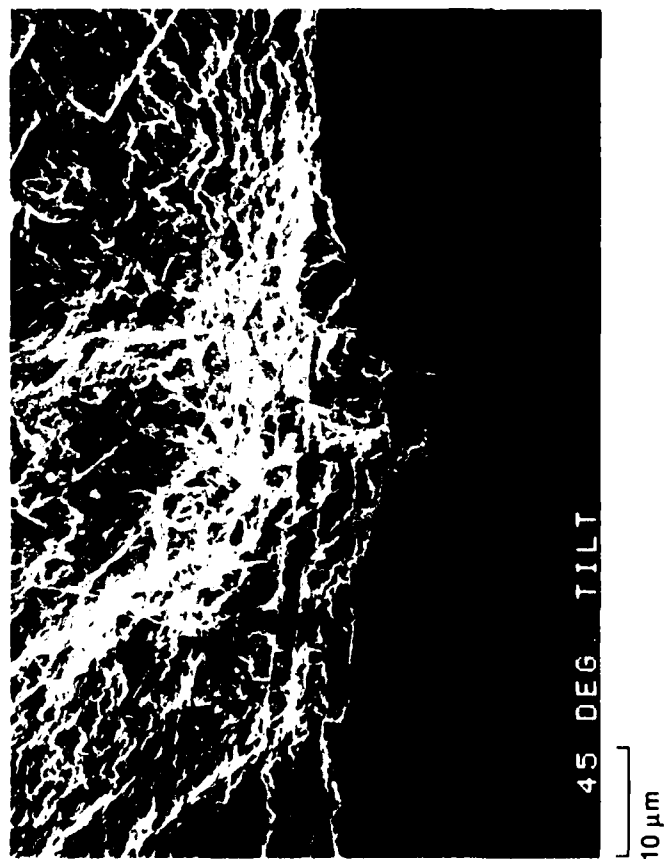


Figure 178. Detail of HSSC Fracture from Ti-24Al-11Nb TMF. Note Secondary Cracking on Gage Section Sides in Photograph at Left.

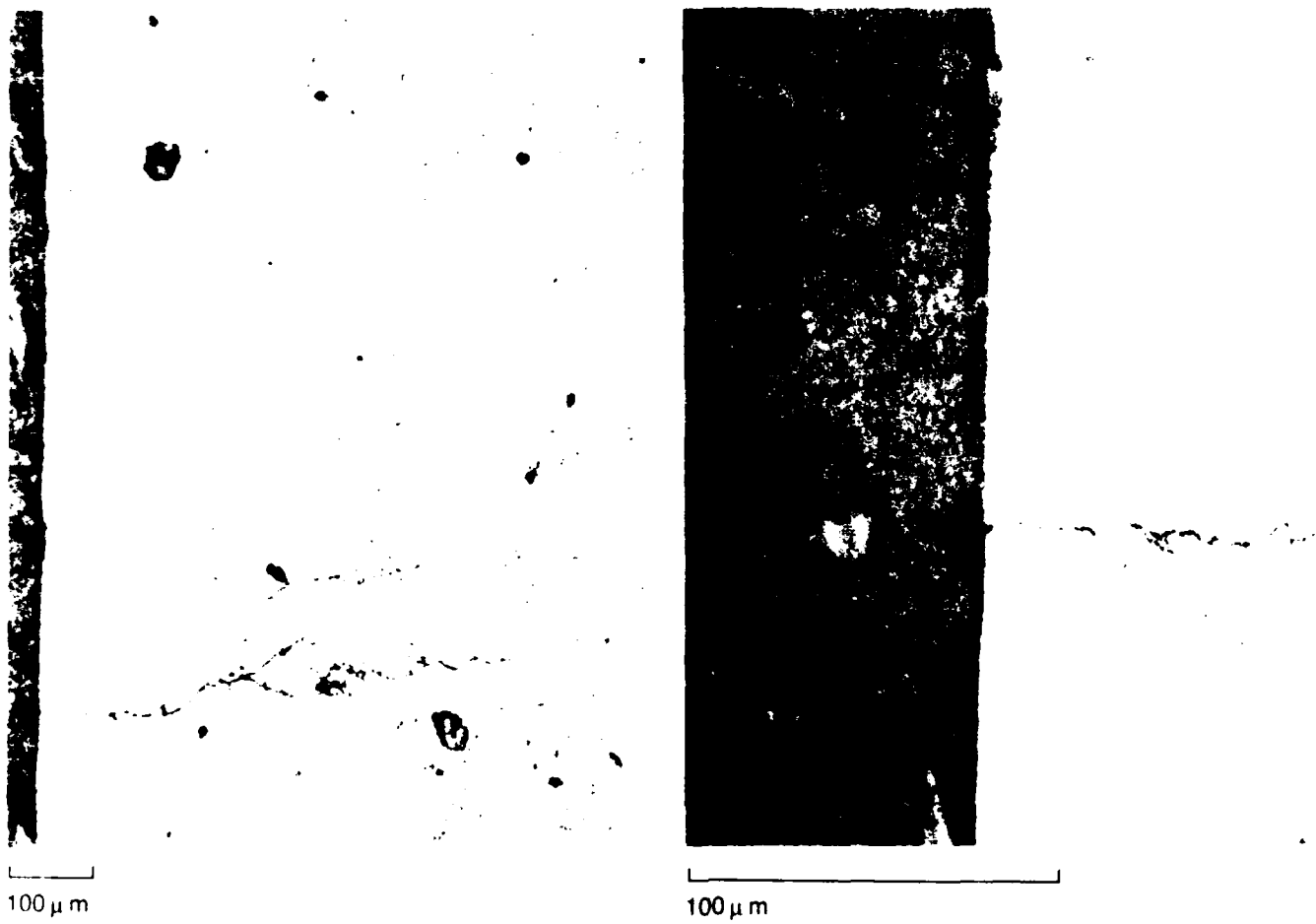


Figure 179. Oxygen Embrittlement Layer (Arrows) After 0.5 Hours at 650°C (1200°F) in Ti-24Al-11Nb LCF Test. Note Secondary Cracking

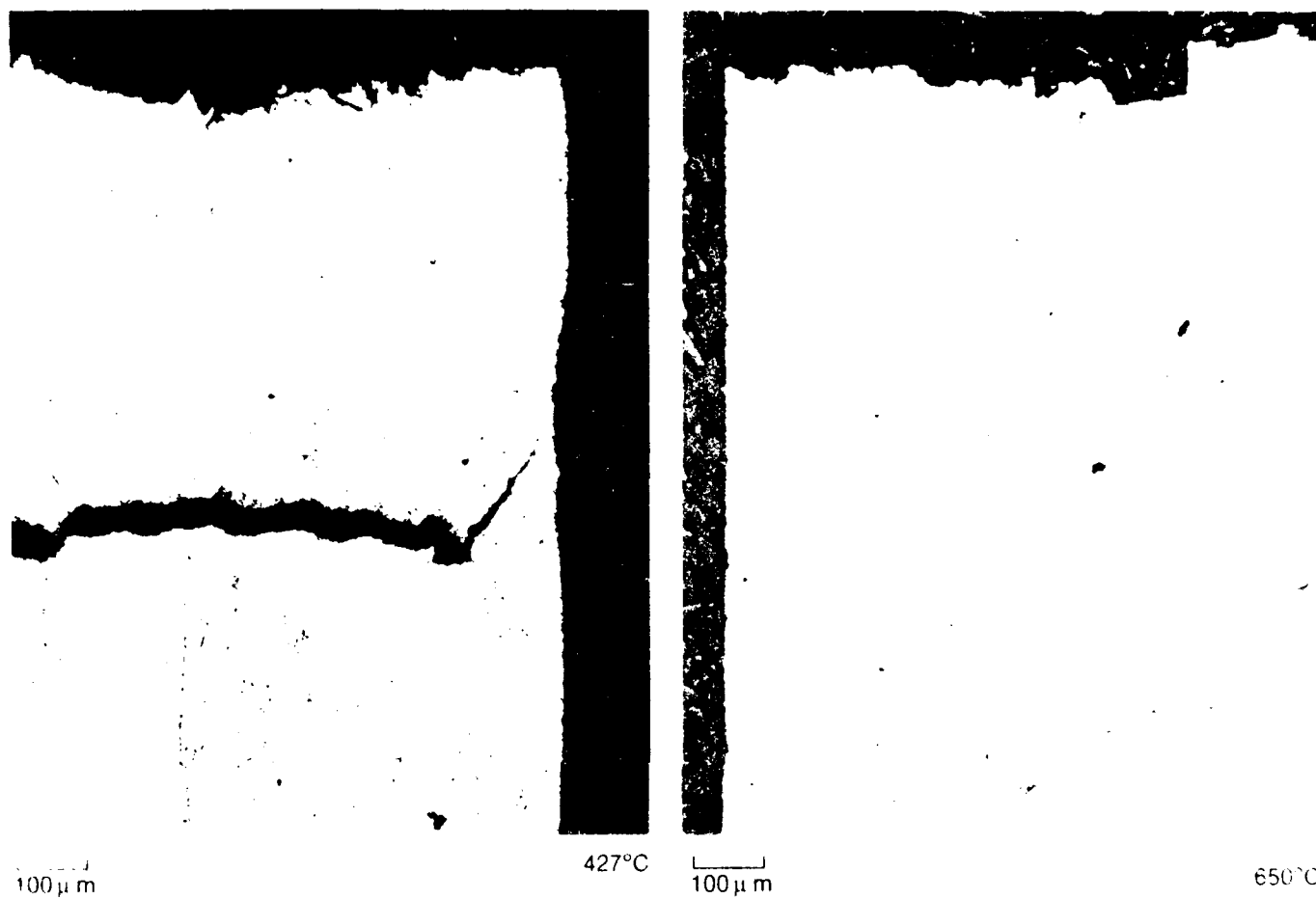


Figure 180. Secondary LCF Cracks in Ti-24Al-11Nb Seen in Cross Section Near Origin (Top). Left is 427°C (800°F), Right is 650°C (1200°F).

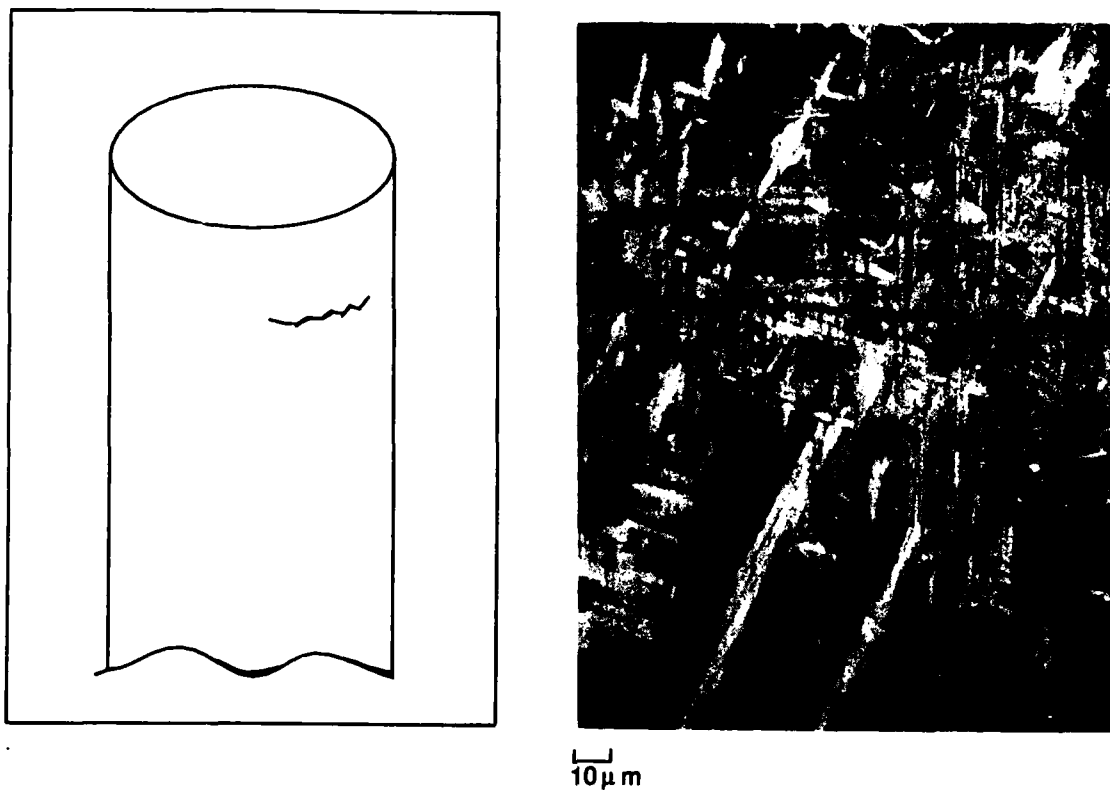


Figure 181. Secondary Crack on Outer Diameter of Gage Section, Ti-24Al-11Nb, LCF. Structure Revealed by Test Environment, 427°C (800°F) Air. There Seems to be No Obvious Relationship Between Crack and Microstructure

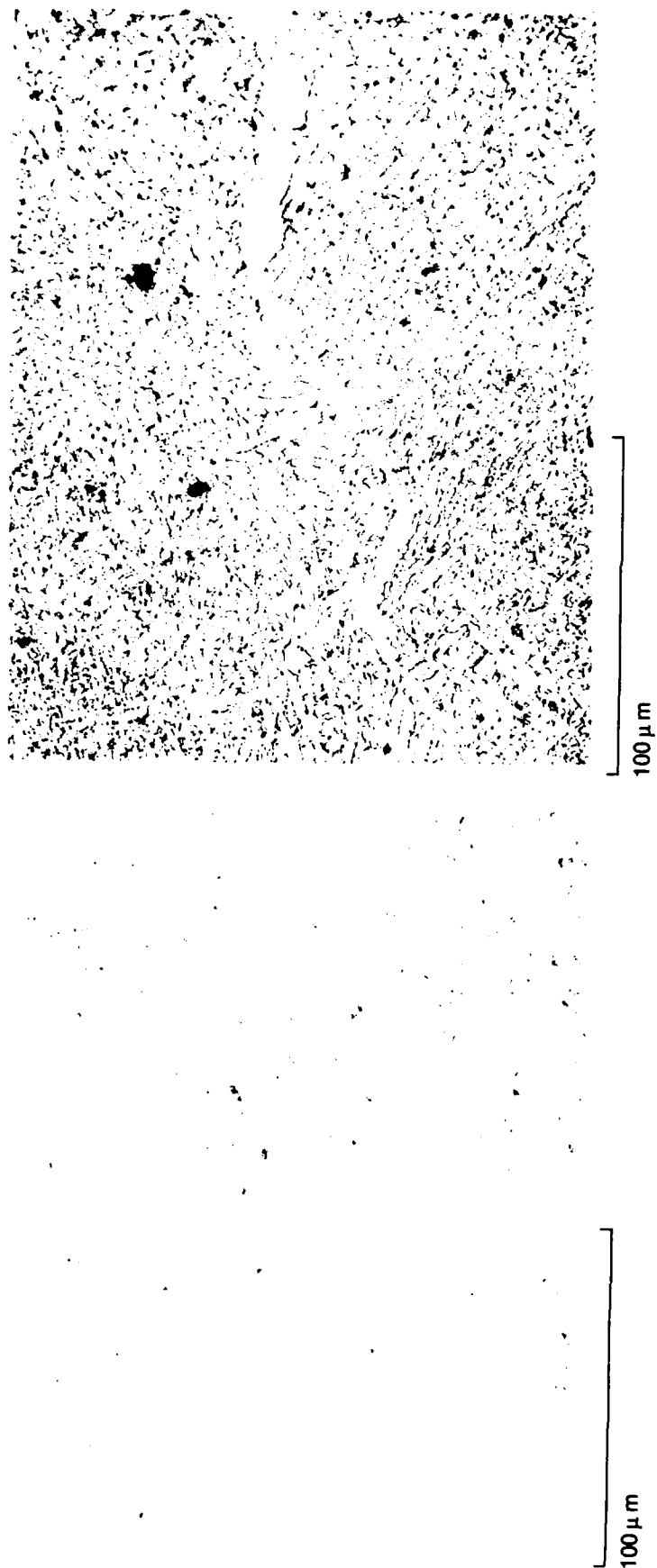
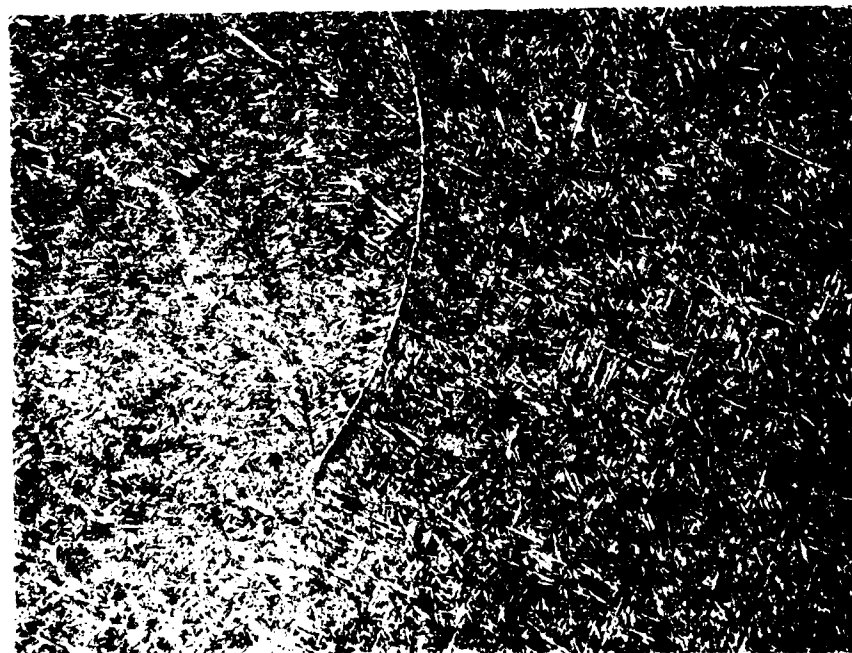


Figure 182. Isolated Heavy Concentrations of Grain Boundary Alpha-2 in Ti-24Al-11Nb



FC 99865
Mag: 200X



FC 99866
Mag: 500X

Figure 183. Microstructure of Ti-25Al-10Nb-3V-1Mo. Showing Grain Boundary, Alpha-2 and Preferential Alignment of Widmanstatten Structure Along Prior Beta Grain Boundary



100μm

(a)

FC 103966



100μm

(b)

FC 103967

Figure 184. (a) Fractographic Appearance of Preferentially Aligned Widmanstatten Structure Along Prior Beta Grain Boundary With Probable Grain Boundary Alpha-2 (b) Enlargement of (a) Showing Cracked Oxide Scale and Sublayer Beneath for Ti-25Al-10Nb-3V-1Mo

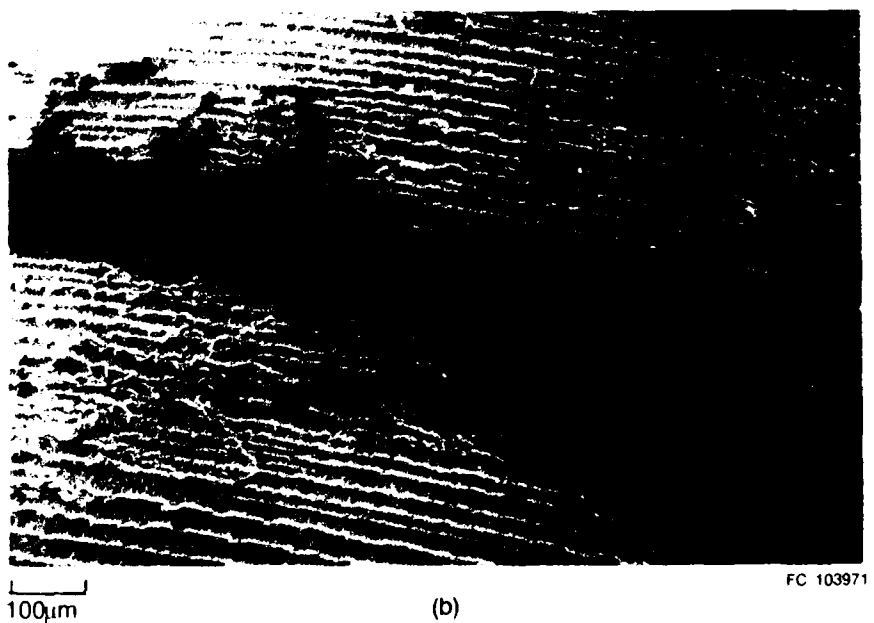
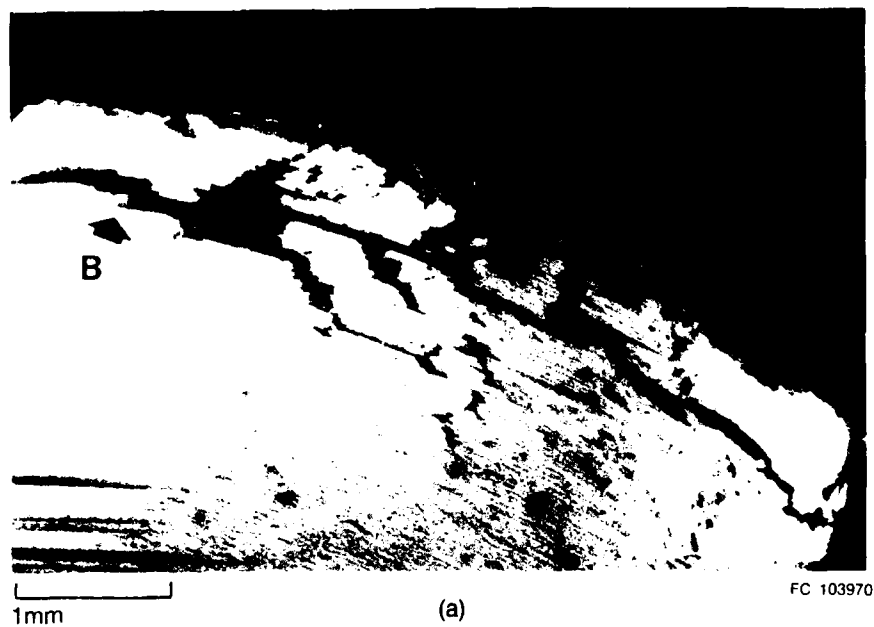


Figure 185. *Pronounced Linear Oxide Cracking and Associated Multiple Secondary Cracks Perpendicular to Strain Axis on Ti-25Al-10Nb-3V-1Mo Smooth LCF Specimen Seen in Previous Figure*

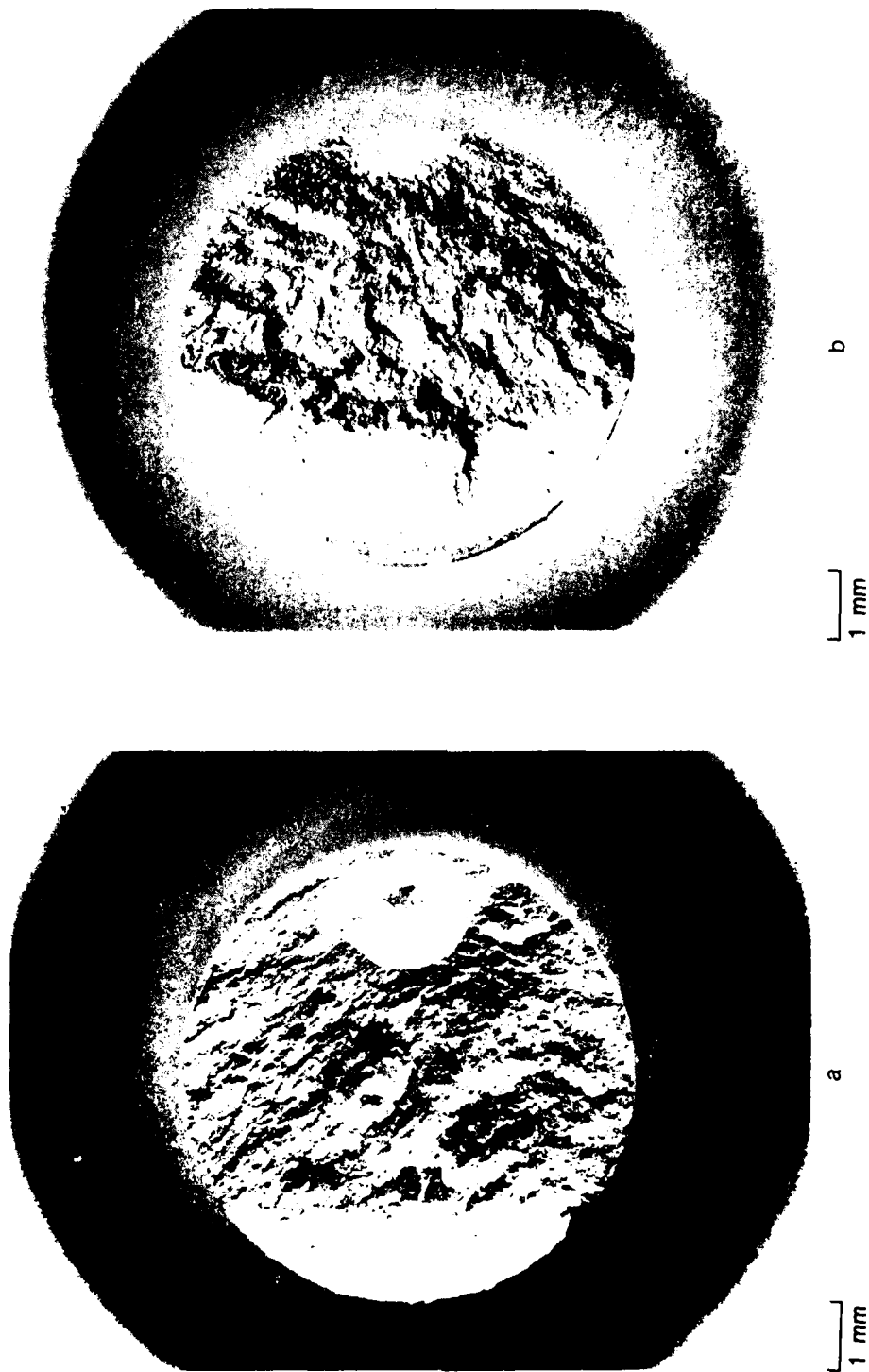
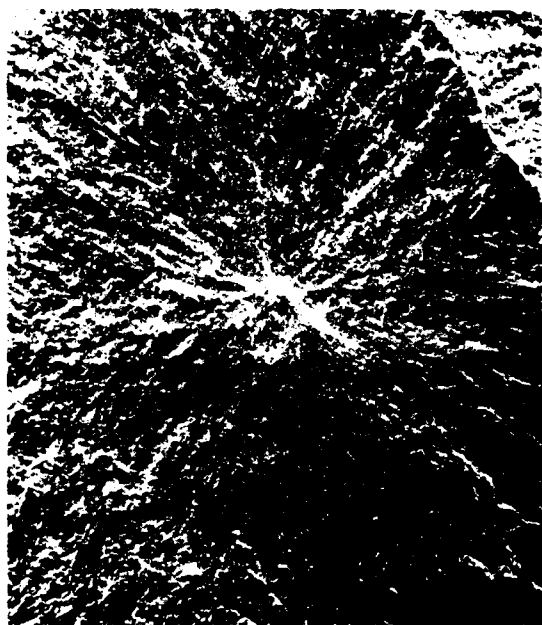
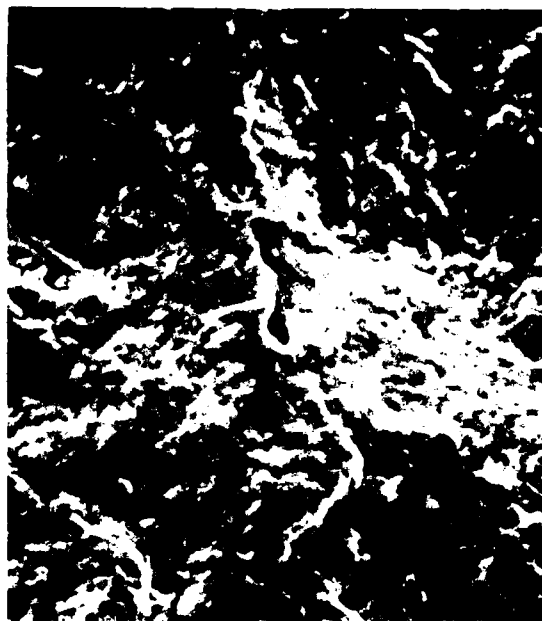


Figure 186 Low Cycle Fatigue (LCF) Fractures Produced at 650°C (1200°F) Exhibiting Internal (a) and Surface (b) Fatigue Origins for Ti-25Al-10Nb-3V-1Mo



100μm



10μm

Figure 187. Void at Fatigue Origin in Ti-25Al-10Nb-3V-1Mo Smooth LCF Specimen Tested at 650°C (1200°F)



1mm

427°C (800°F)



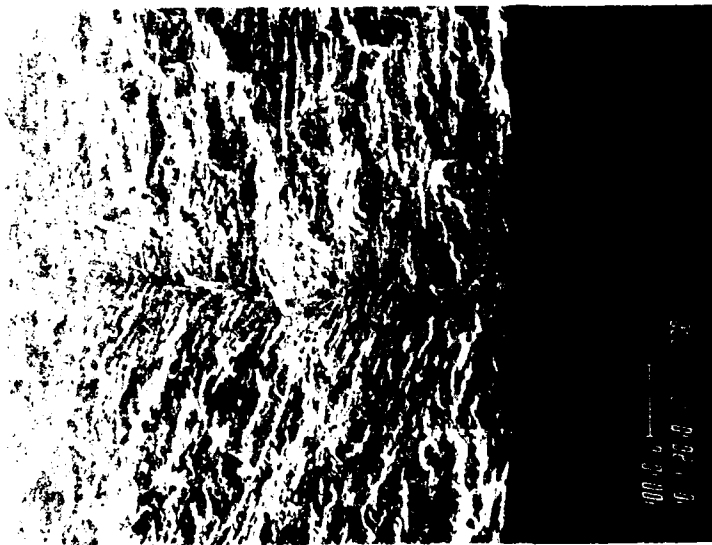
1mm

650°C (1200°F)

Figure 188. Ti-24Al-11Nb LCF Origins at Grain Boundary Alpha-2



FC 105623 H



FC 105624 H

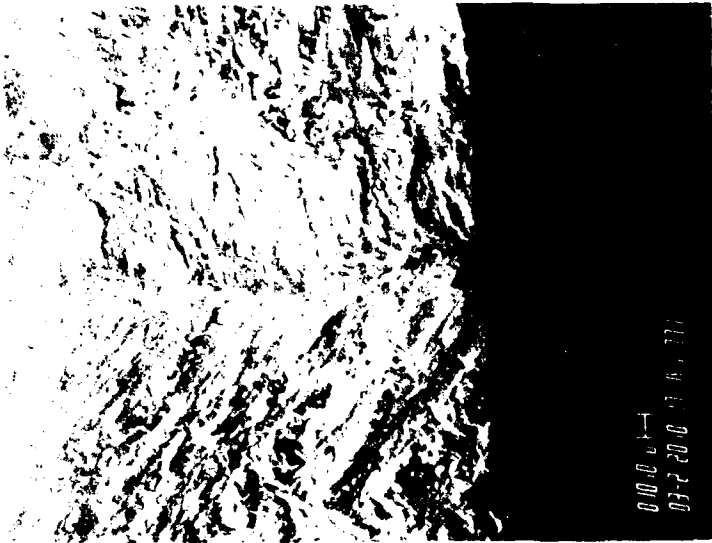
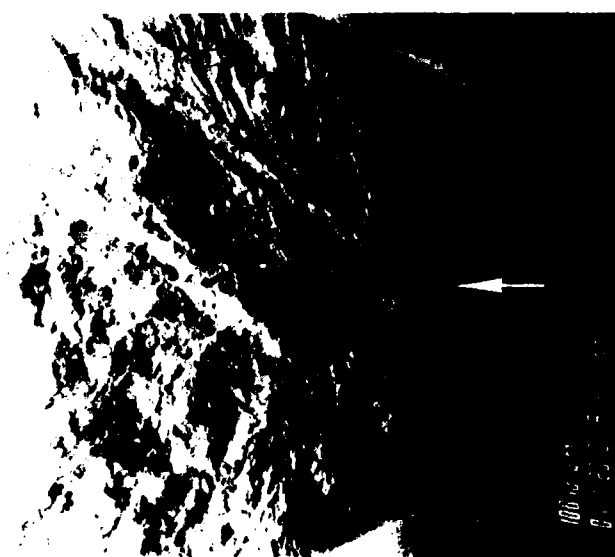
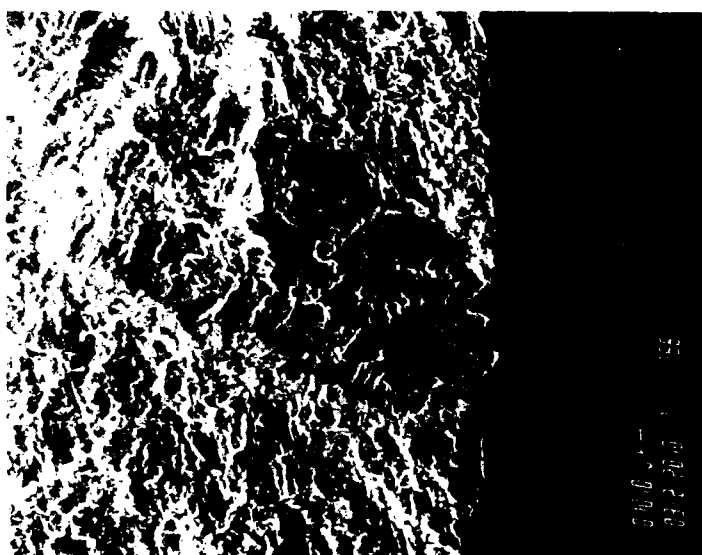


Figure 189 Room Temperature Strain Control LCF Origin in Ti-25Al-10Nb-3V-1Mo at a Prior Beta Grain Boundary



FC 105627 H

FC 105626 H

Figure 190. 427°C (800°F) Strain Control LCF Origin at Prior Beta Grain Boundary in Ti-24Al-11Nb



Figure 191 650°C (1200°F) Strain Control LCF Origin at Probable Alpha-2 Platelets in Ti-24Al-11Nb

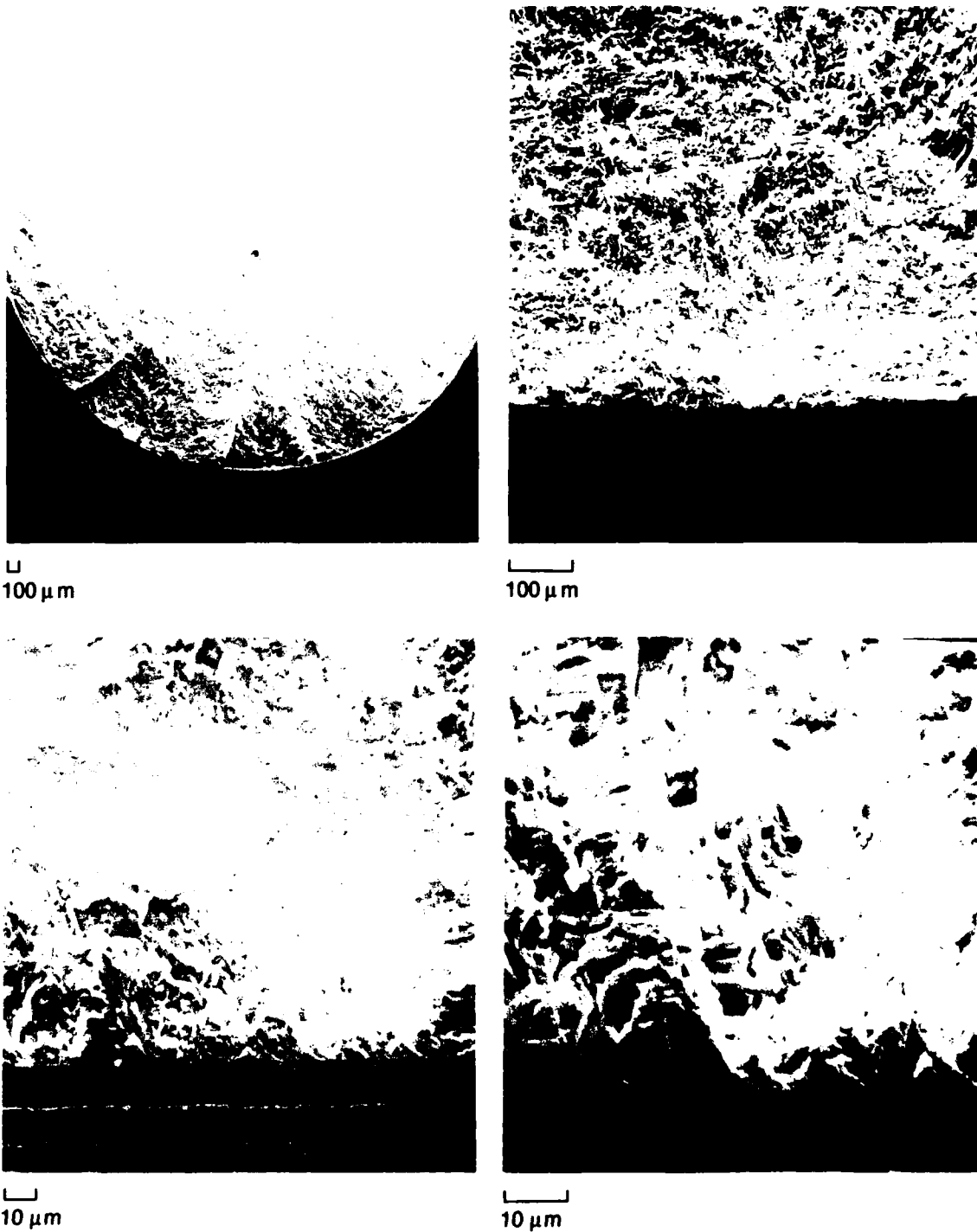
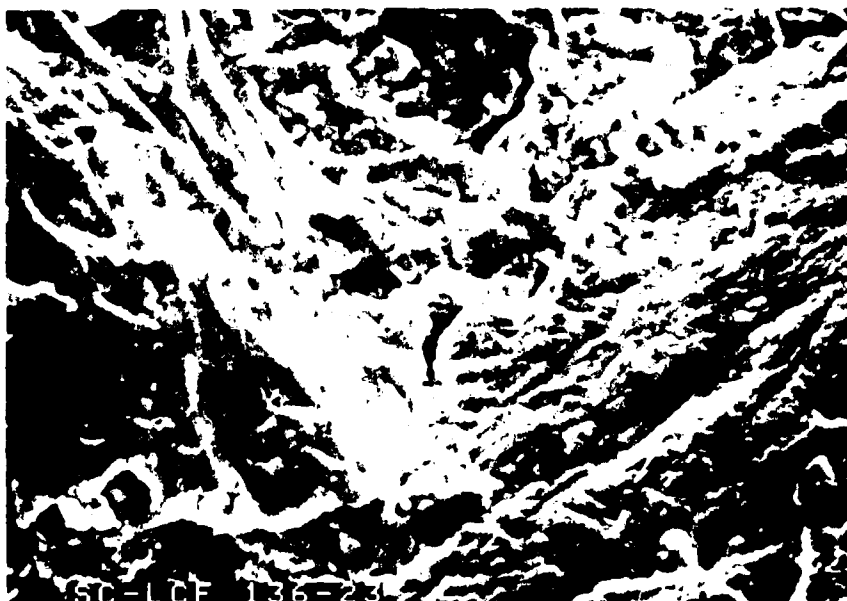


Figure 192. High Cycle Fatigue (HCF) Origin in 427°C (800°F) Notched Ti-24Al-11Nb Specimen



100 μ m



10 μ m

Figure 193. Subsurface LCF Origin in Ti-24Al-11Nb 650°C (1200°F) Duell Test. There Appears to be Fine Porosity Present

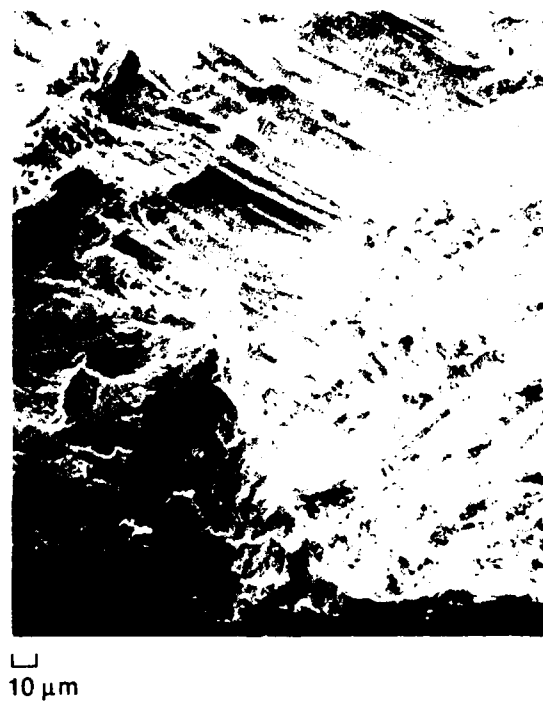


Figure 194. Fatigue Striations on Ti-24Al-11Nb LCF Specimens at 427°C (800°F). Left is 0.17 Hz, $R = -1.0$; Right is $R = 0$, 120 Second Peak Strain Dwell Cycle



(a)

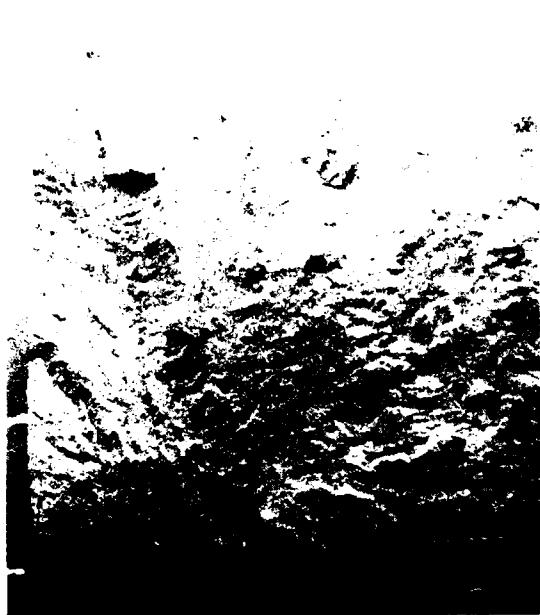
FC103974
Mag: 10X



(b)

FC103975
Mag: 15X

Figure 195. Notched LCF Fracture Surface (a) and Notch Appearance (b) at Origin, Ti-25Al-10Nb-3V-1Mo Tested at 650°C (1200°F)



□
100 μm



□
100 μm

Figure 196. Documentation of Crack Aspect Ratio in Ti-24Al-11Nb 427°C (800°F) Notched LCF Test

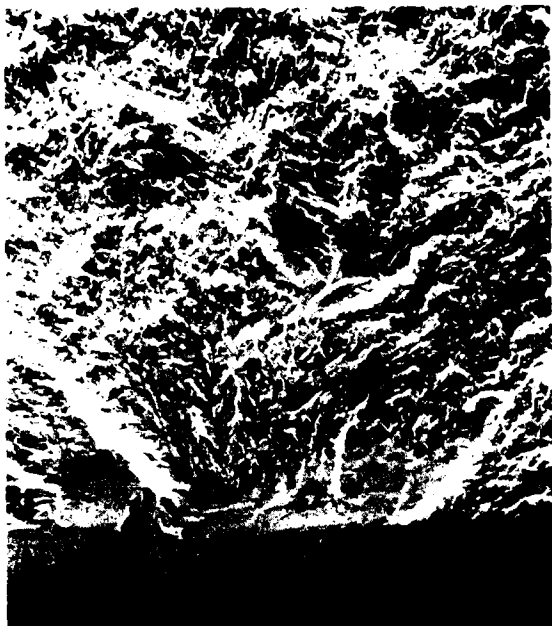


0.5 mm



0.5 mm

Figure 197. Prestressed Ti-24Al-11Nb Notched LCF 26°C (80°F) Test ($N_f = 46,524$ cycles). Photographs Show Material Flaking From Surface and Critical Crack Depth



10 μ m



10 μ m

Figure 198. Ti-24Al-11Nb Notched LCF Origin, 650°C (1200°F). Unusual Texture at Notch May Be Alpha-2 Platelet



Figure 199. Left, Multiple Surface Crack Initiations in Coated Ti-24Al-11Nb 650°C (1200/F) Notched LCF. Center, Same as Left But With HSSC From ASTM Sea Salt Visible in Notches. Right, Ti-25Al-10Nb (Al-Mo Notched LCF, Titanium Nitride Coated P/S HSSC) Surface Cracks in 427°C (800°F) LCF Test

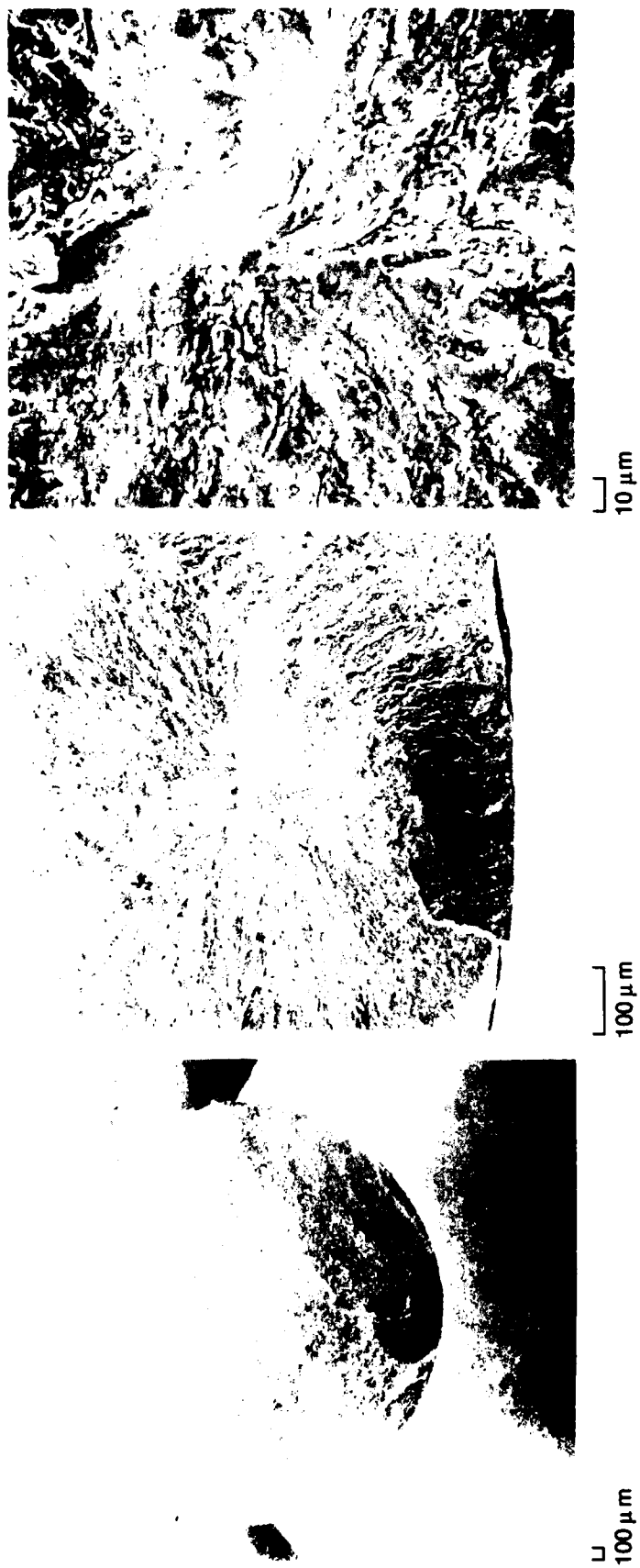
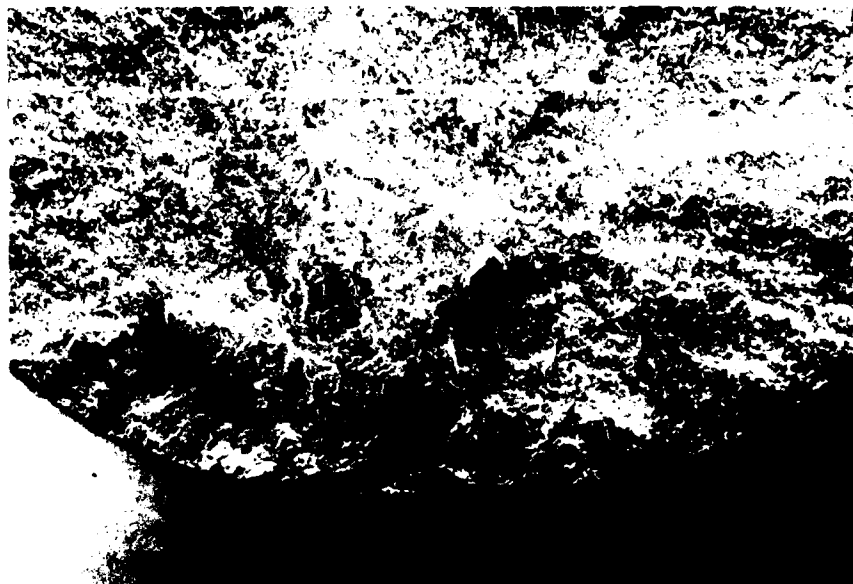


Figure 200. Subsurface HCF Origin in Ti-25Al-10Nb-3V-1Mo at 650°C (1200°F), $R = -1.0$ at Possible Void

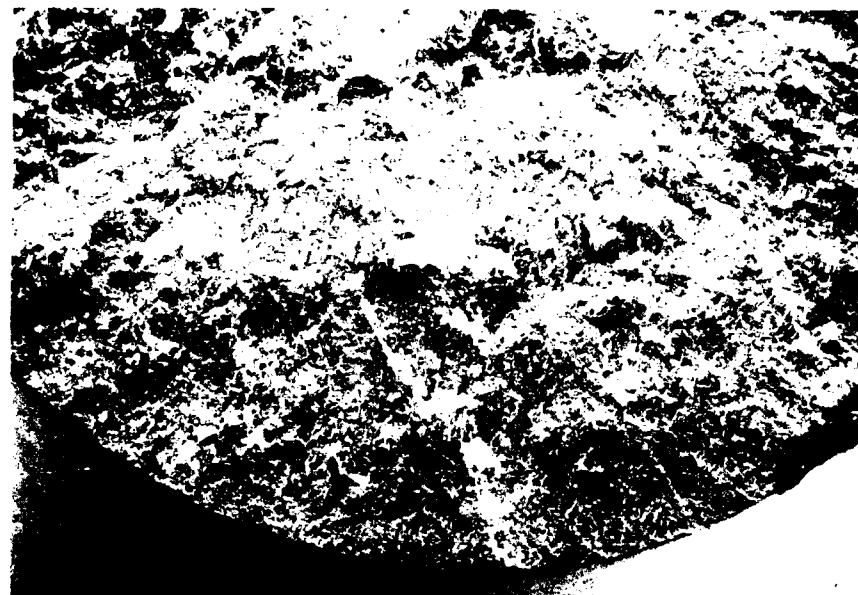


1mm



100 μ m

Figure 201 Room Temperature HCF Origin at Surface Connected Prior Beta Grain Boundary in Ti-24Al-11Nb. Edge is Smeared



1mm

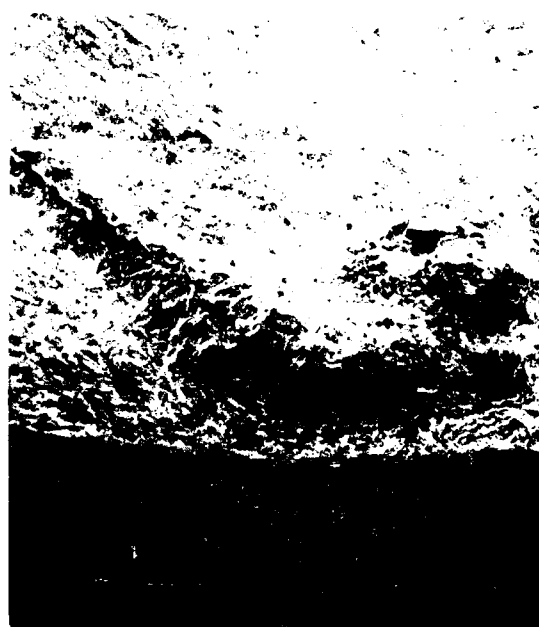


100 μ m

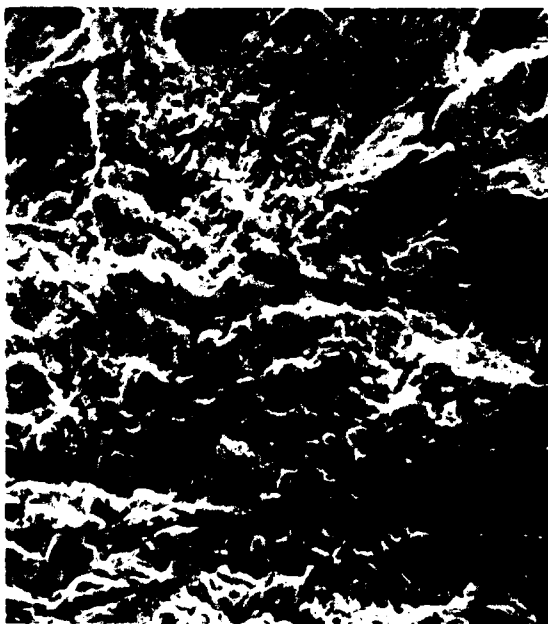
Figure 202. Room Temperature HCF Origin in Ti-24Al-11Nb. Streaks are Probably Prior Beta Grain Boundaries



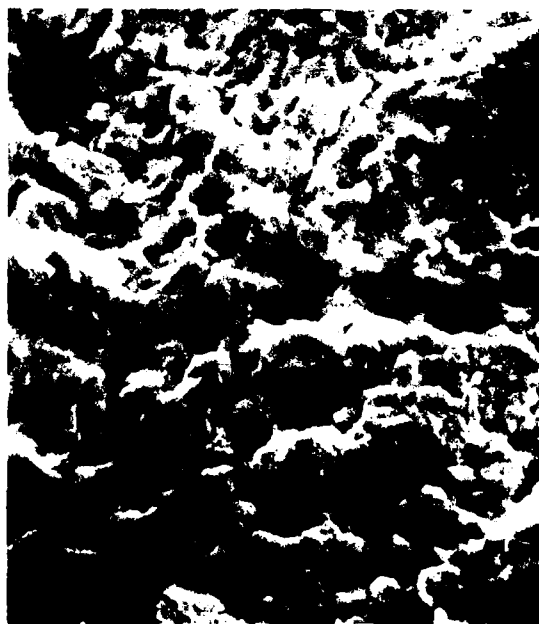
100 μm



100 μm



10 μm

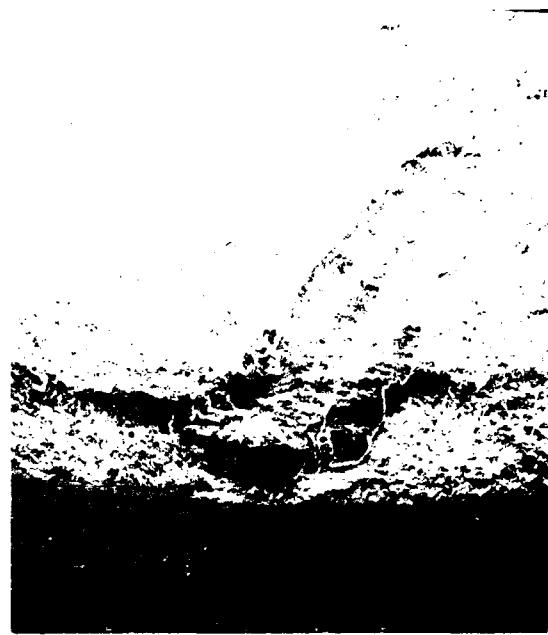


10 μm

Figure 203. Subsurface HCF Origin in Ti-24Al-11Nb at 650°C (1200°F)



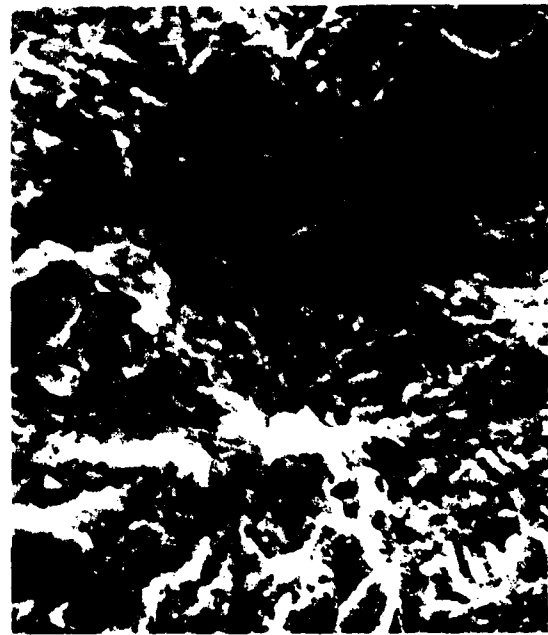
100 μ m



100 μ m

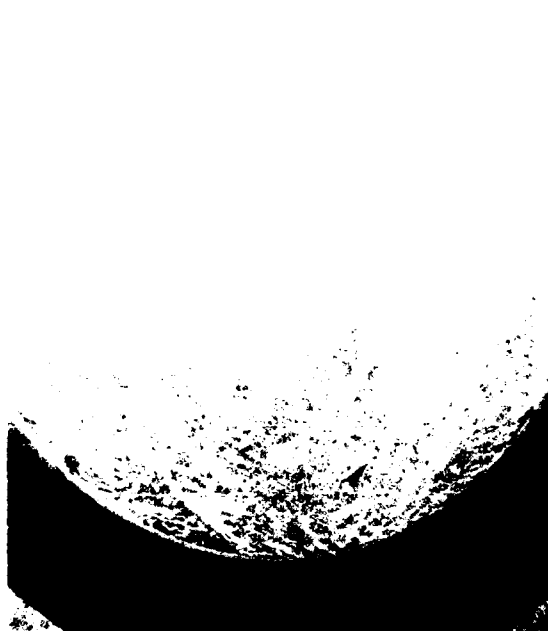


10 μ m

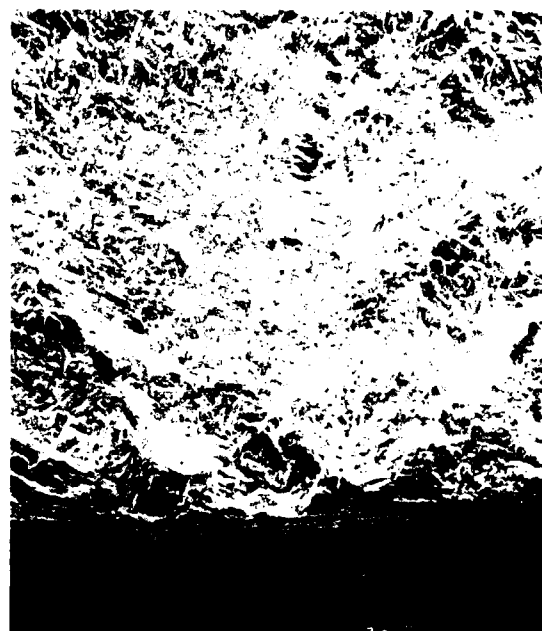


10 μ m

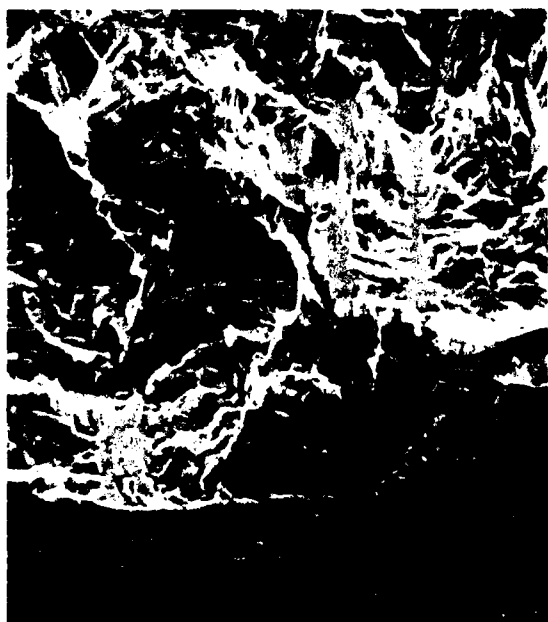
Figure 204. Near Surface HCF Origin in Ti-25Al-10Nb-3V-1Mo at 650°C (1200°F) Appears to be Prior Beta Grain Boundary Junction



□
100 μm



□
100 μm



□
10 μm



□
10 μm

Figure 205. Notched HCF Origin at Alpha Platelet in 427°C (800°F) Ti-24Al-11Nb Specimen



Figure 206 From Left, Macro Views of Room Temperature, 427°C (800°F) and 650°C (1200°F) Fracture Surfaces From Ti-24Al-11Nb 20 Hz Crack Growth Tests



#4204

FC 105609
2X



#4100

FC 105610
2X

Figure 207. Ti-25Al-10Nb-3V-1Mo Room Temperature Crack Growth Fractures -- Orientations "c" (Left) and "h" (Right) Described in Figure 29

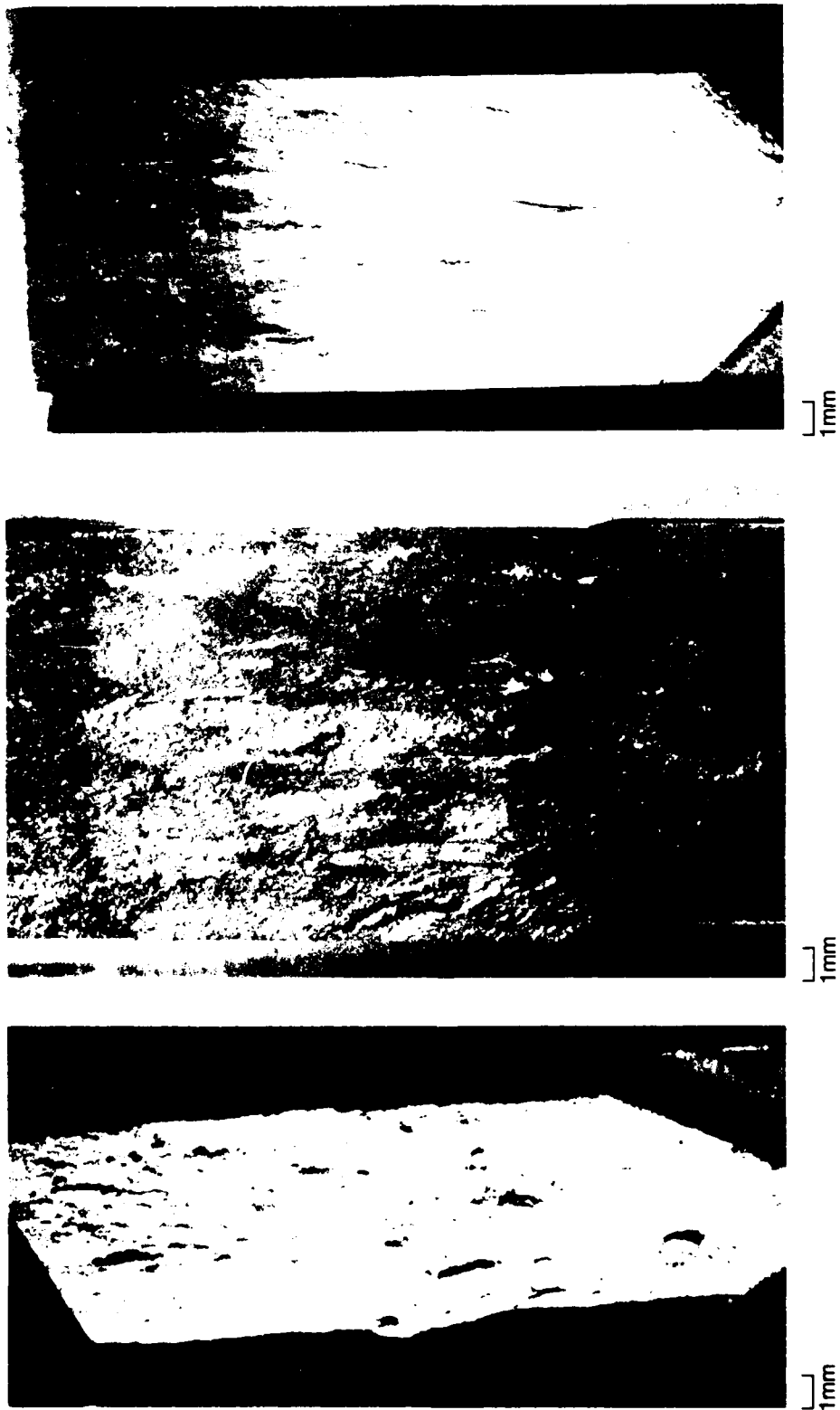
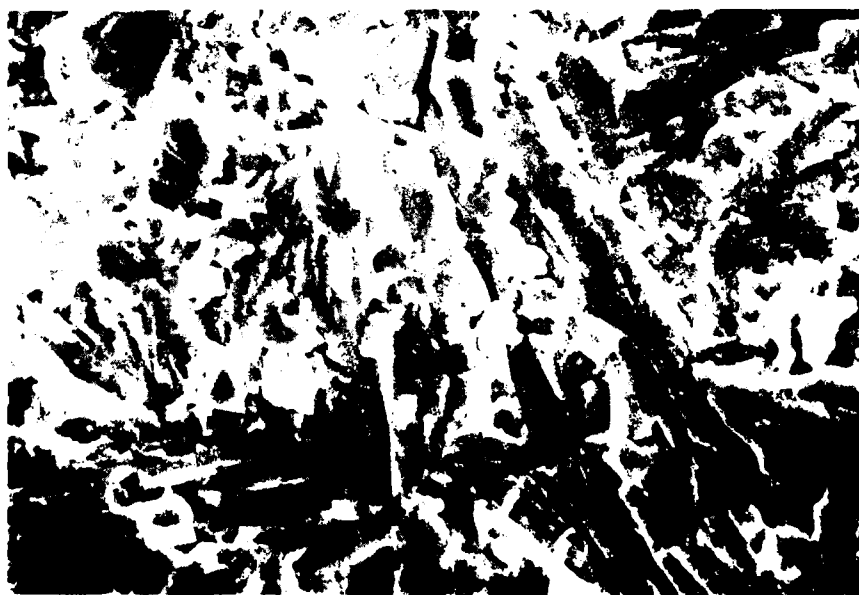
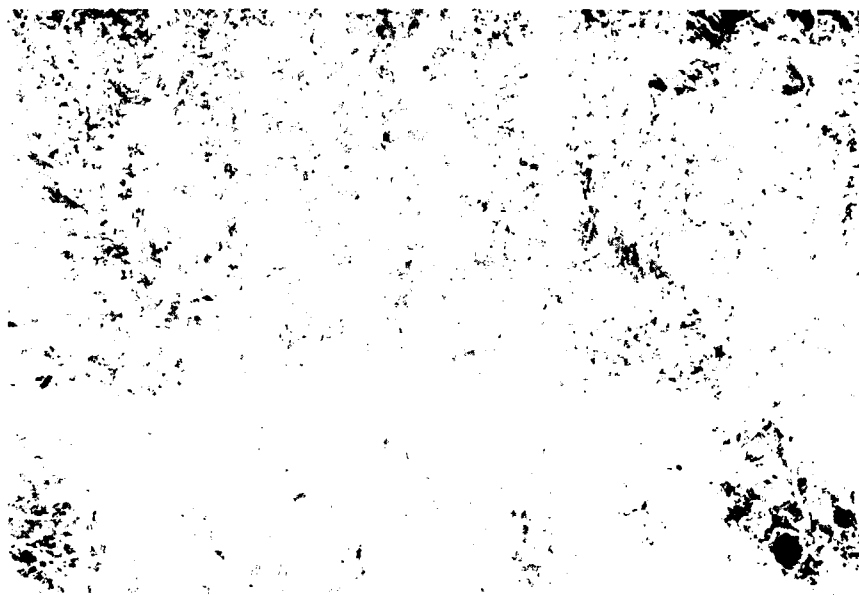
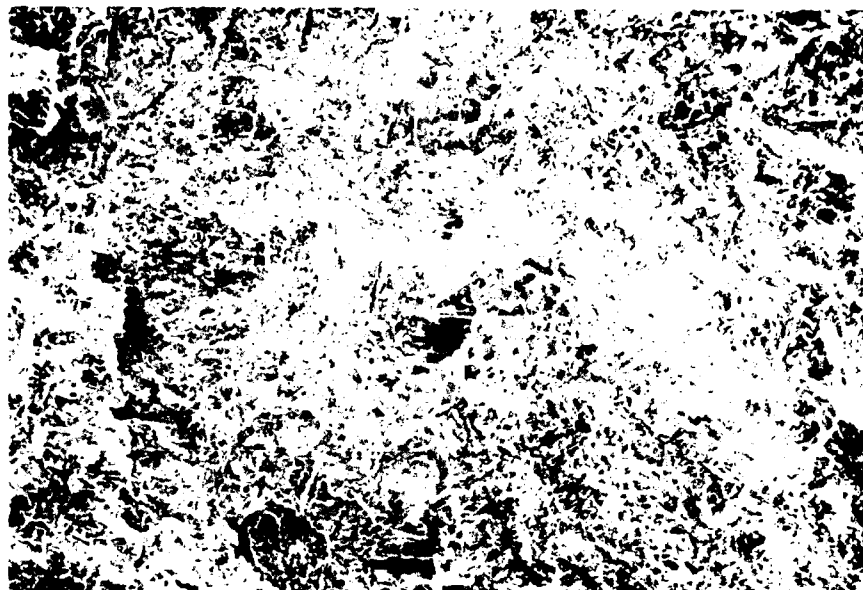


Figure 208. Macro View, of 0.17 Hz Crack Growth Test Specimens (Ti-24Al-11Nb). From Left: Room Temperature, 427°C (800°F), and 650°C (1200°F). Grain Pullout Decreases as Temperature Increases



10 μm

Figure 209. Room Temperature 20 Hz Crack Growth Surface of Ti-24Al-11Nb at Low and High Magnifications

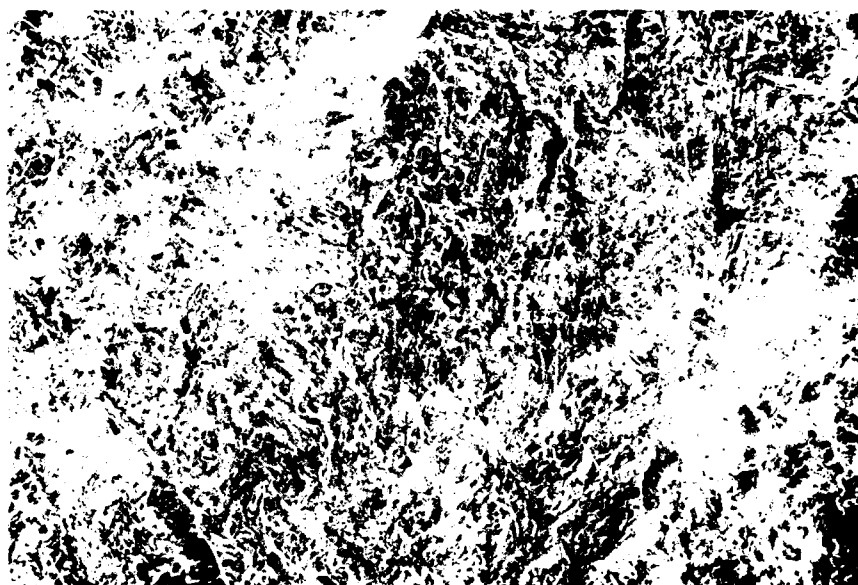


100 μm

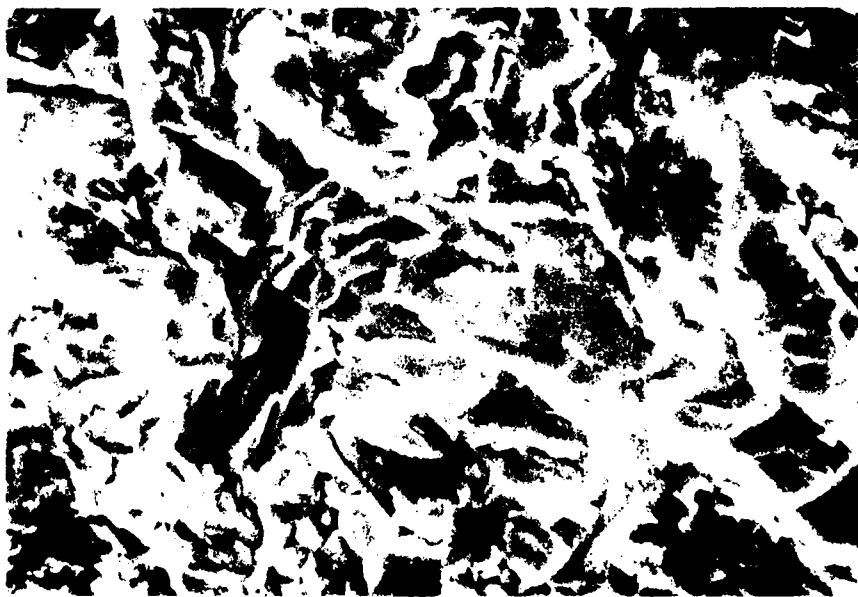


10 μm

Figure 210. Room Temperature 0.17 Hz Crack Growth Surface of Ti-24Al-11Nb at Low and High Magnifications

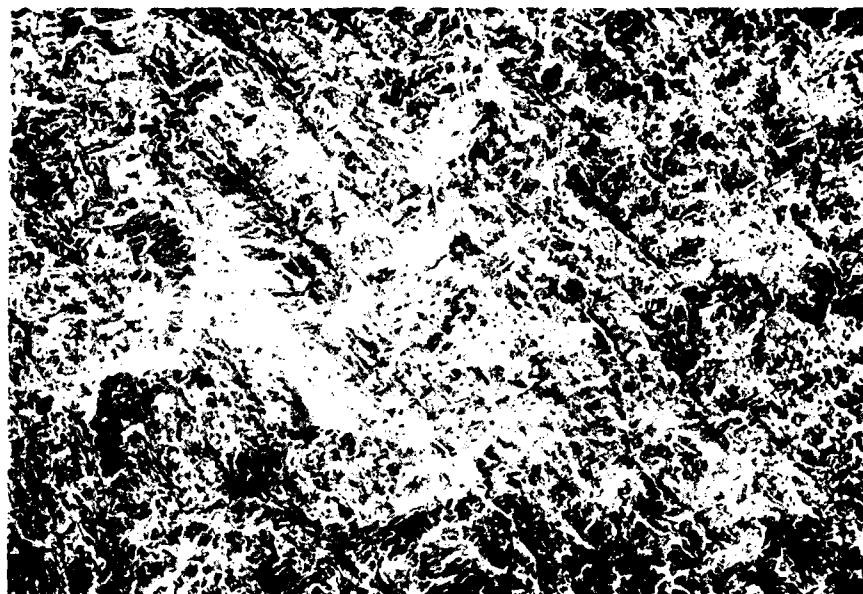


100 μm

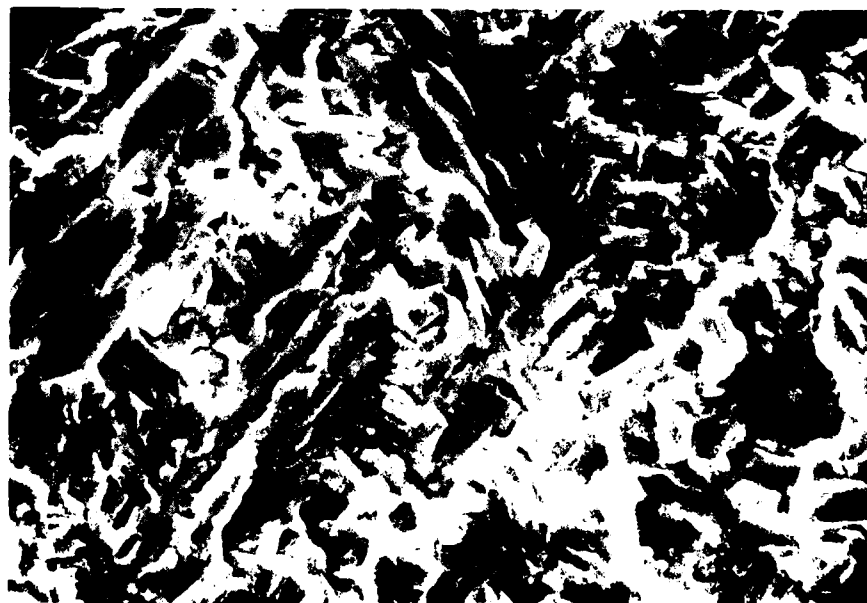


10 μm

Figure 211. 427°C (800°F) Crack Growth Surface of Ti-24Al-11Nb at 20 Hz

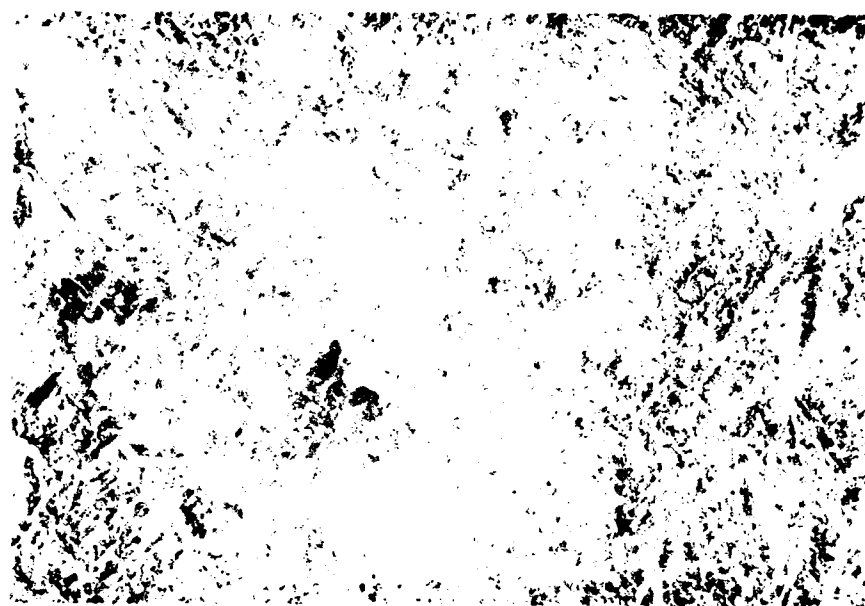


100 μm

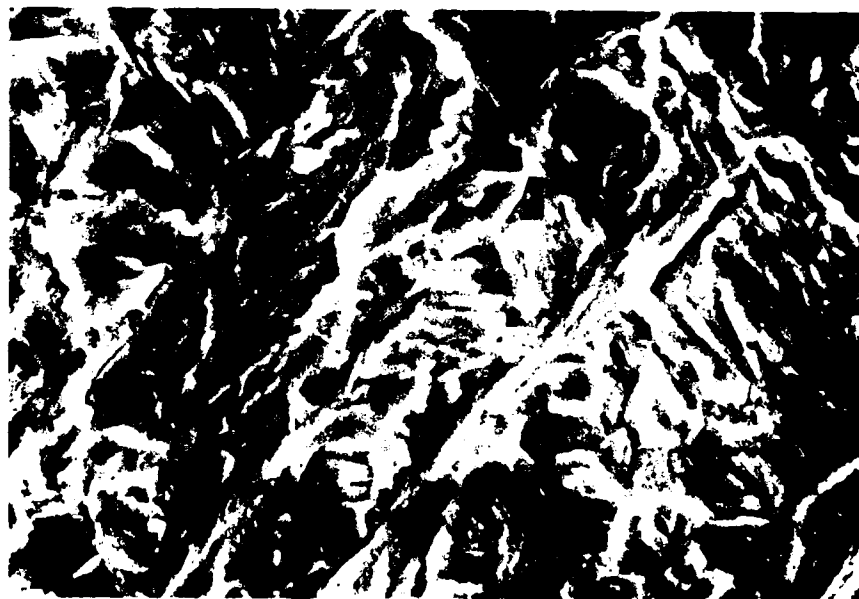


10 μm

Figure 212. 427°C (800°F) Crack Growth Surface of Ti-24Al-11Nb at 0.17 Hz

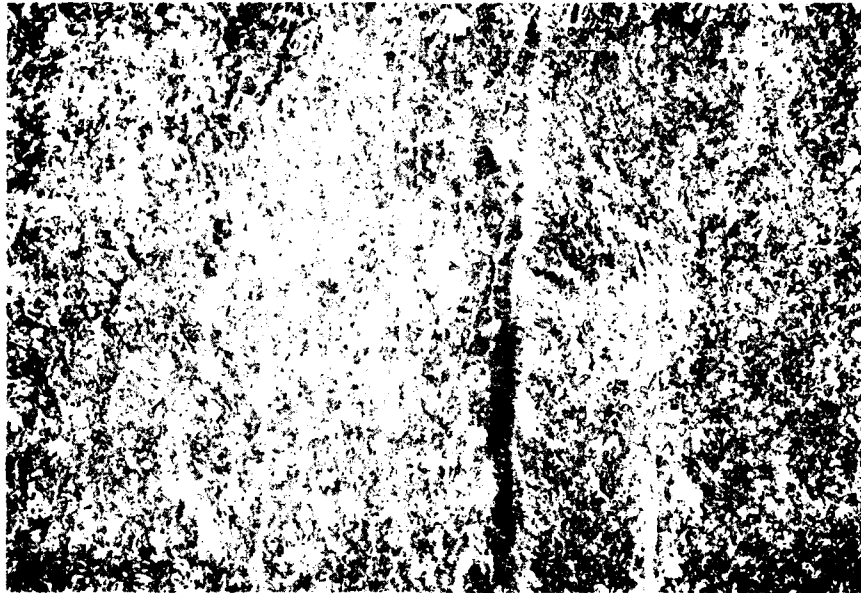


100 μ m



10 μ m

Figure 213. Low and High Magnifications of 650°C (1200°F) Ti-24Al-11Nb Crack Growth Surface at 20 Hz



100 μm



10 μm

Figure 214. Crack Growth Fracture Surface of Ti-24Al-11Nb at 650°C (1200°F) and 0.17 Hz

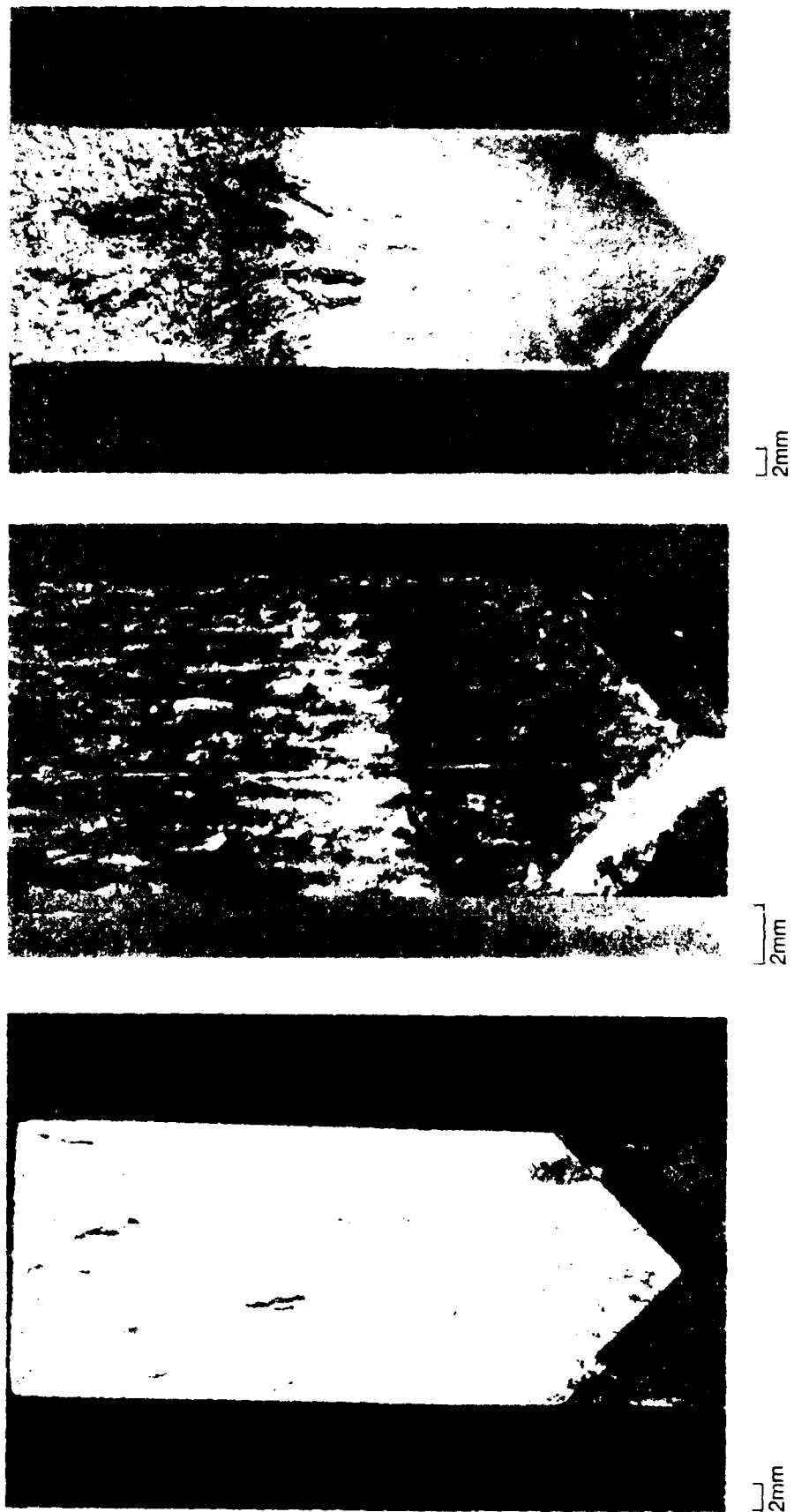
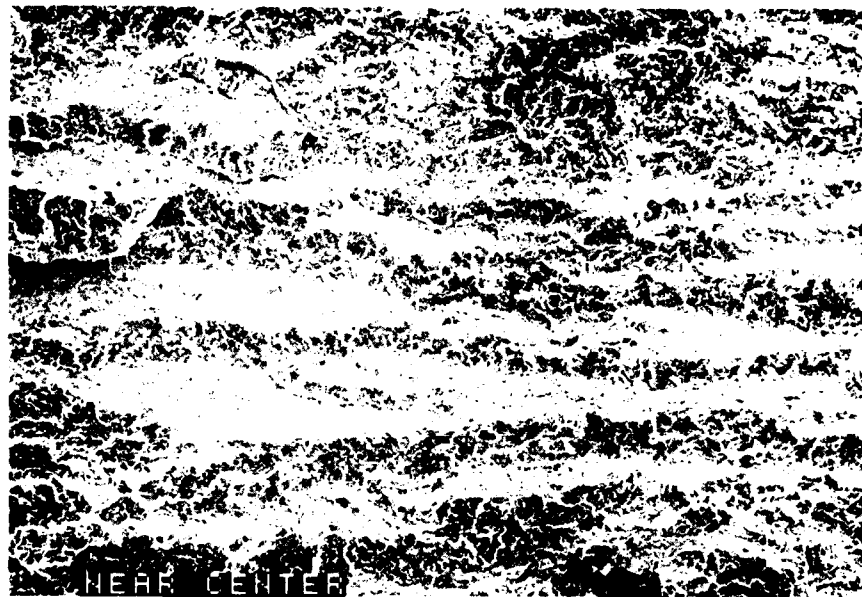
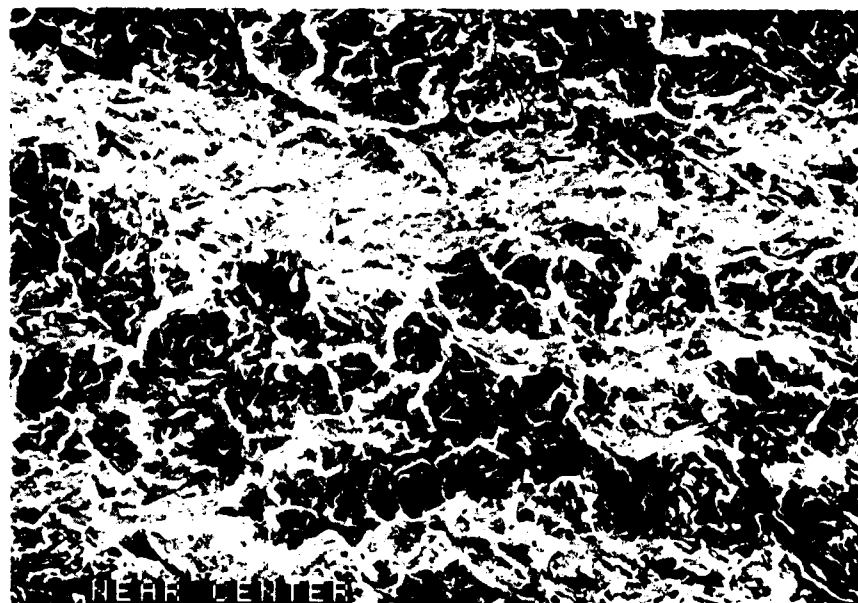


Figure 215 Macro Views of Ti-5Al-0.5Nb-3V-1Mo Crack Growth Specimen Surfaces From Left to Right: Room Temperature, 425°C (800°F), and 530°C (990°F)



100 μ m



100 μ m

Figure 216. Furrowed Crack Propagation Surface on Ti-25Al-10Nb-3V-1Mo Compact Tension Specimen Tested at Room Temperature and 20 Hz. Feathery Cleavage Predominates

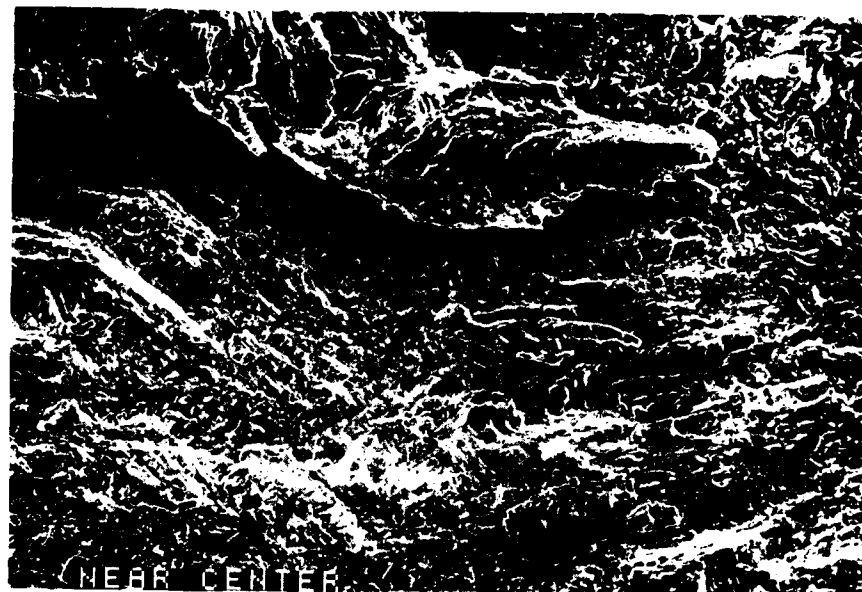


100 μ m

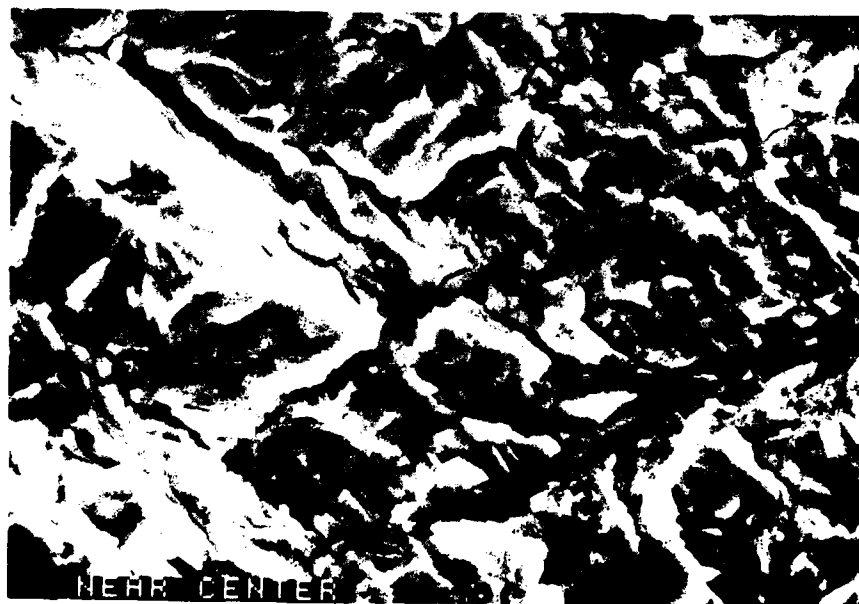


10 μ m

Figure 217. Ti-25Al-10Nb-3V-1Mo at 427°C (800°F) Crack Growth Specimen Exhibits Deep Furrowing Resulting From Branching Crack Front and Resultant Material Ejection



100 μ m



10 μ m

Figure 218. Ti-25Al-10Nb-3V-1Mo Crack Growth Specimen Tested at 650°C (1200°F) and 0.17 Hz. Extensive Secondary Cracking Results in Exfoliation of Large Pieces of Material



Mag: 10X



Mag: 10X

Figure 219. Fracture Faces From Ti-25Al-10Nb-3V-1Mo TMF Specimens. Left is Type I (Out-of-Phase). Right is Type II (In-Phase)

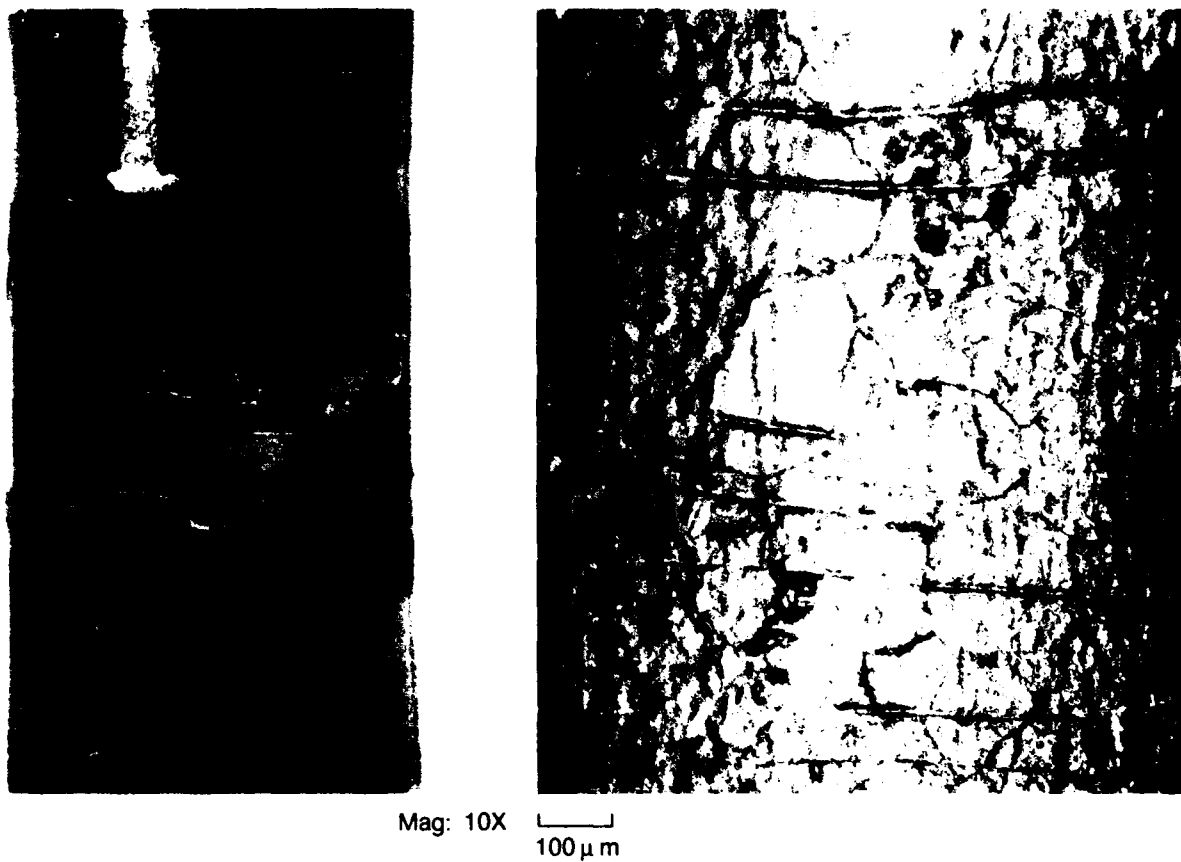


Figure 220 Ti-25Al-10Nb-3V-1Mo In-Phase TMF Test Showing Extensive Oxide Scale Spalling and Rumpling

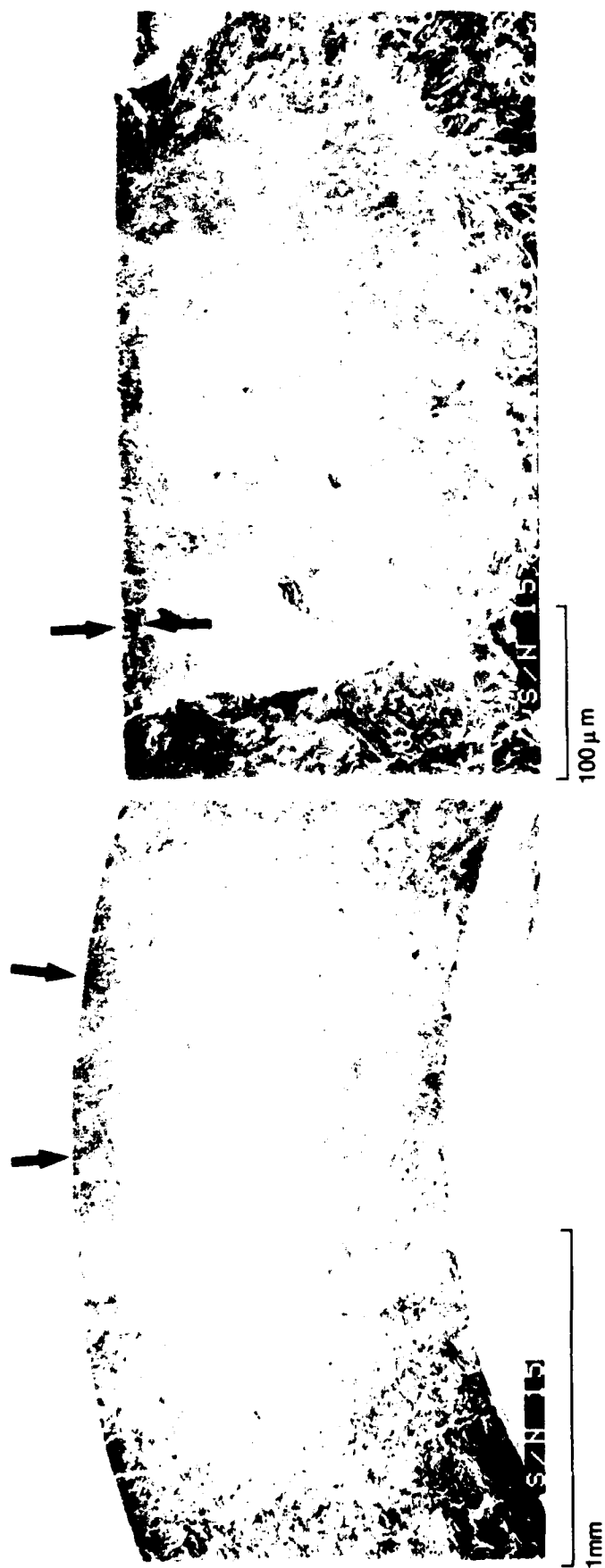


Figure 221. Ti-24Al-11Nb In-Phase TMF Fracture at Outside of Gage Surface (Left). Dark Surface Layer is Oxygen Diffusion (Right)

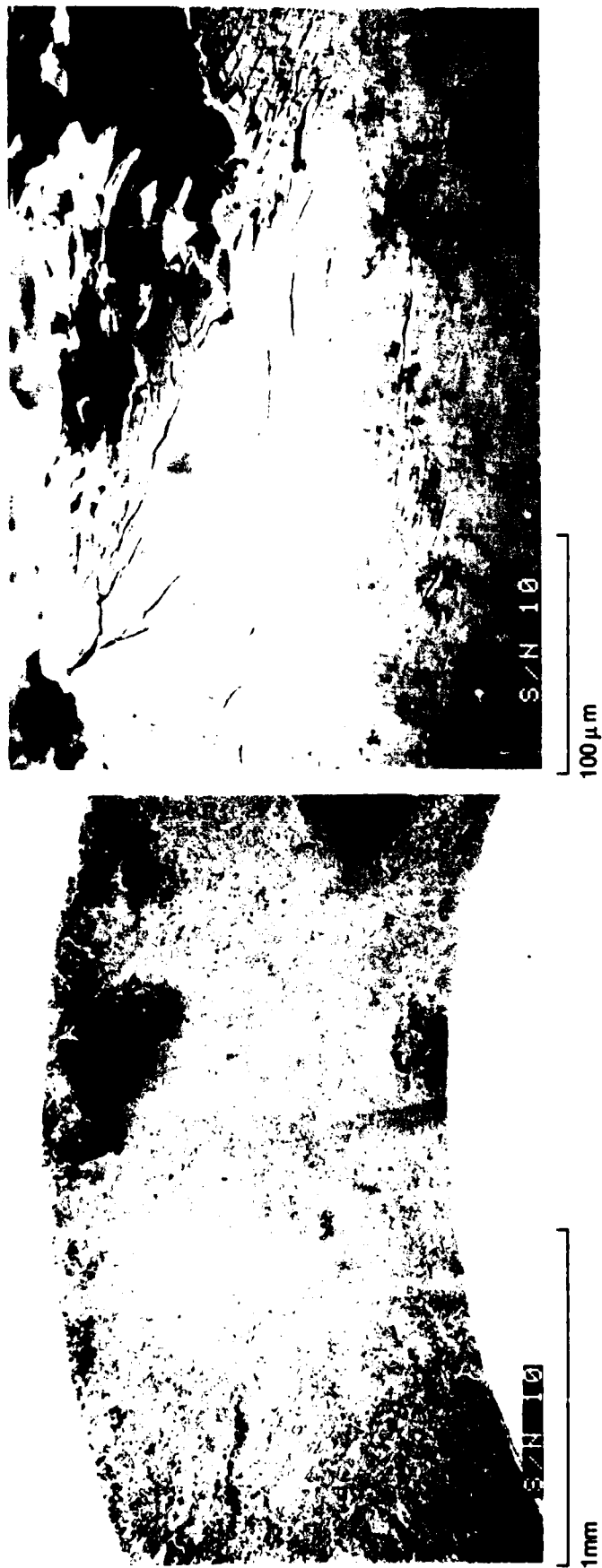
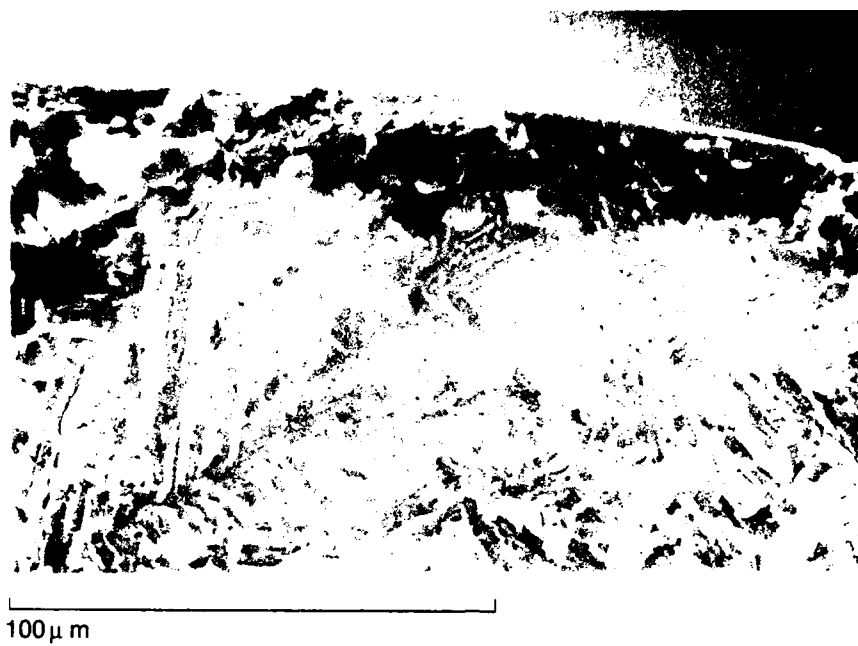
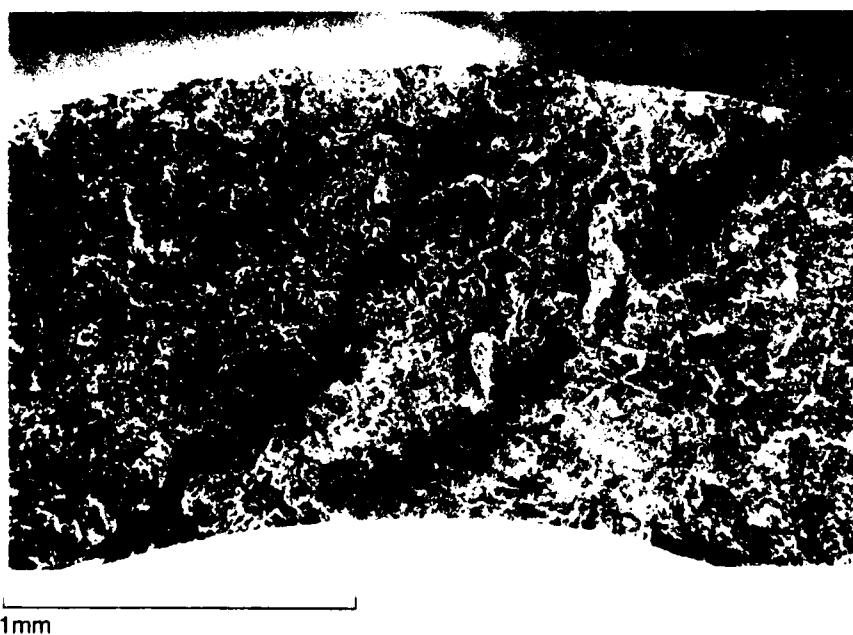


Figure 222. Ti-24Al-11Nb Out-of-Phase TMF Fracture Surface and Side of Gage Showing Secondary Cracking Near Origin



(a)



(b)

Figure 223. Ti-24Al-11Nb In-Phase Thermal Mechanical Fatigue Fracture Surfaces Showing Surface Connected Prior Beta Grain Boundary and Oxygen Diffused Surface Layer



Figure 224. Ti-24Al-11Nb TMF Type II HSSC Showing Multiple Surface Origins

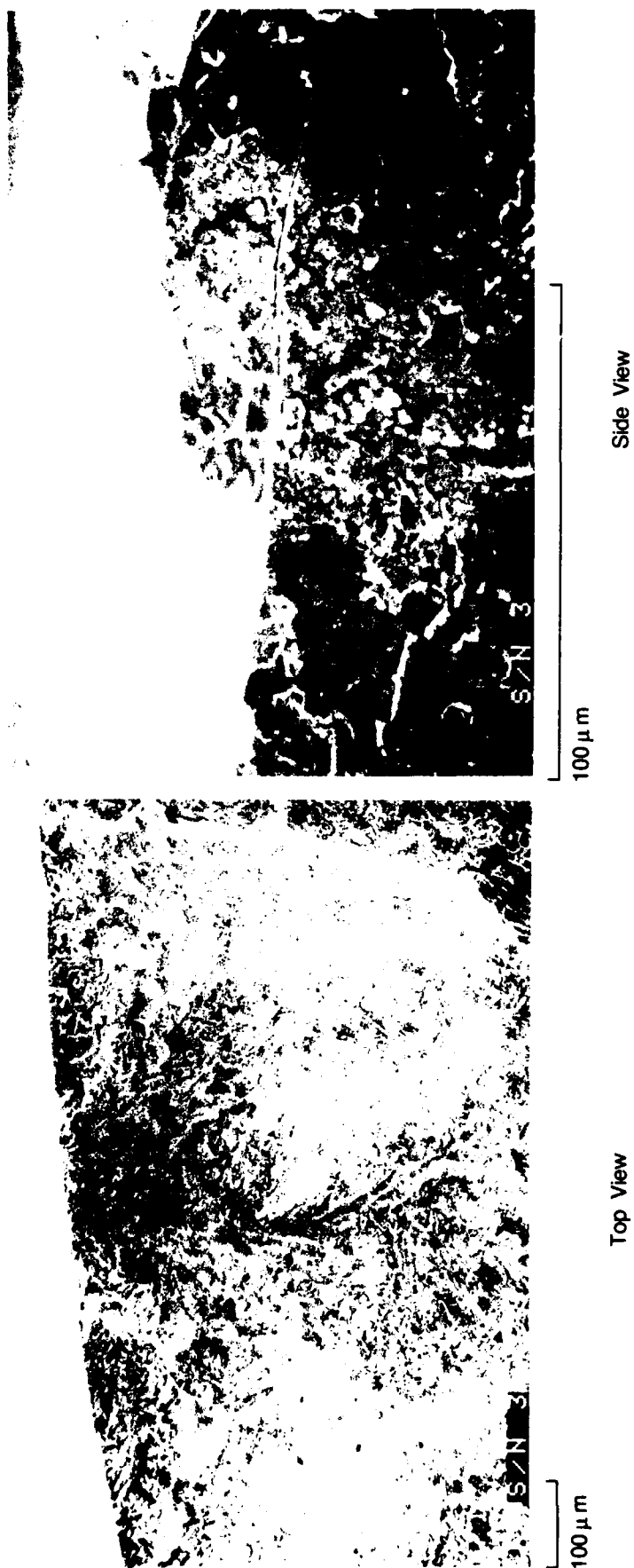
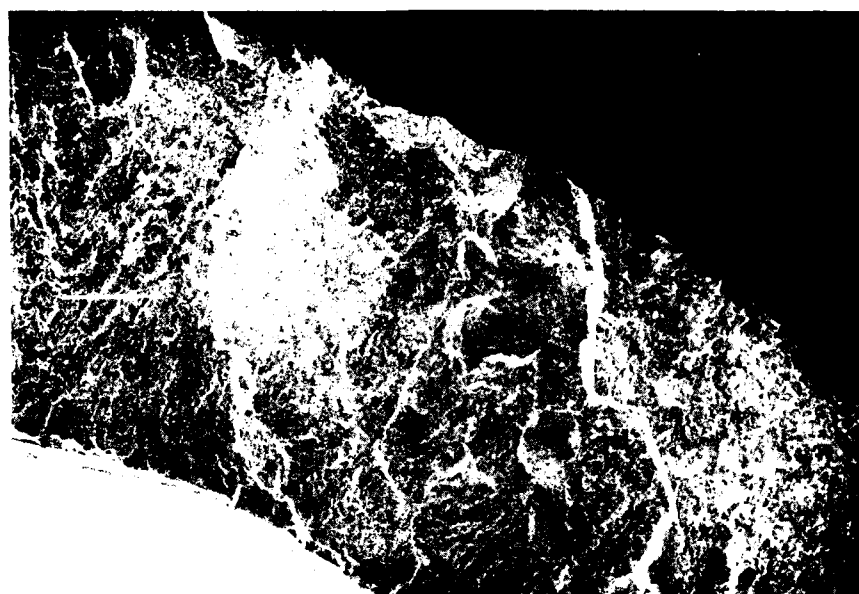
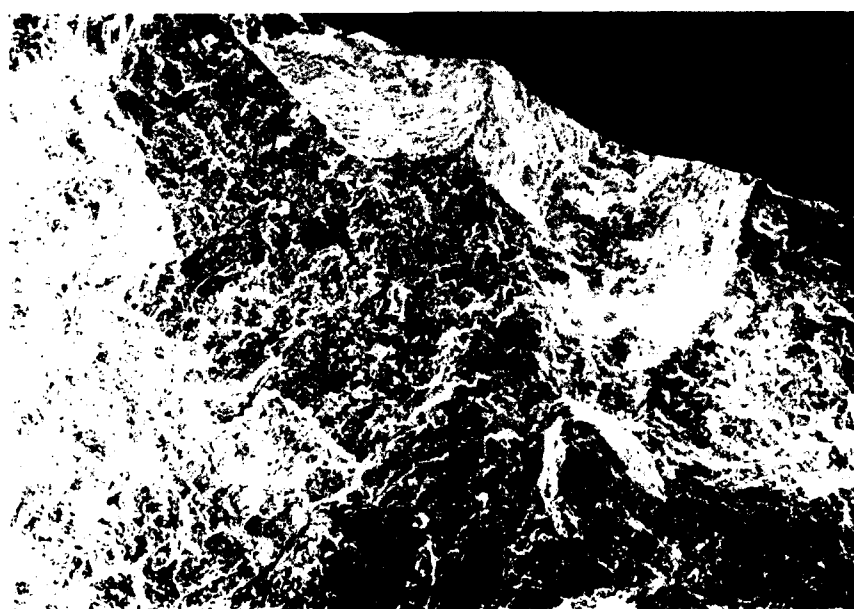


Figure 225. Ti-24Al-11Nb Out-of-Phase TMF Fracture Resulting From HSSC



1mm



100 μ m

Figure 226. Hot Salt Stress Corrosion (HSSC) TMF Origin in Ti-24Al-11Nb (In-Phase Cycle)

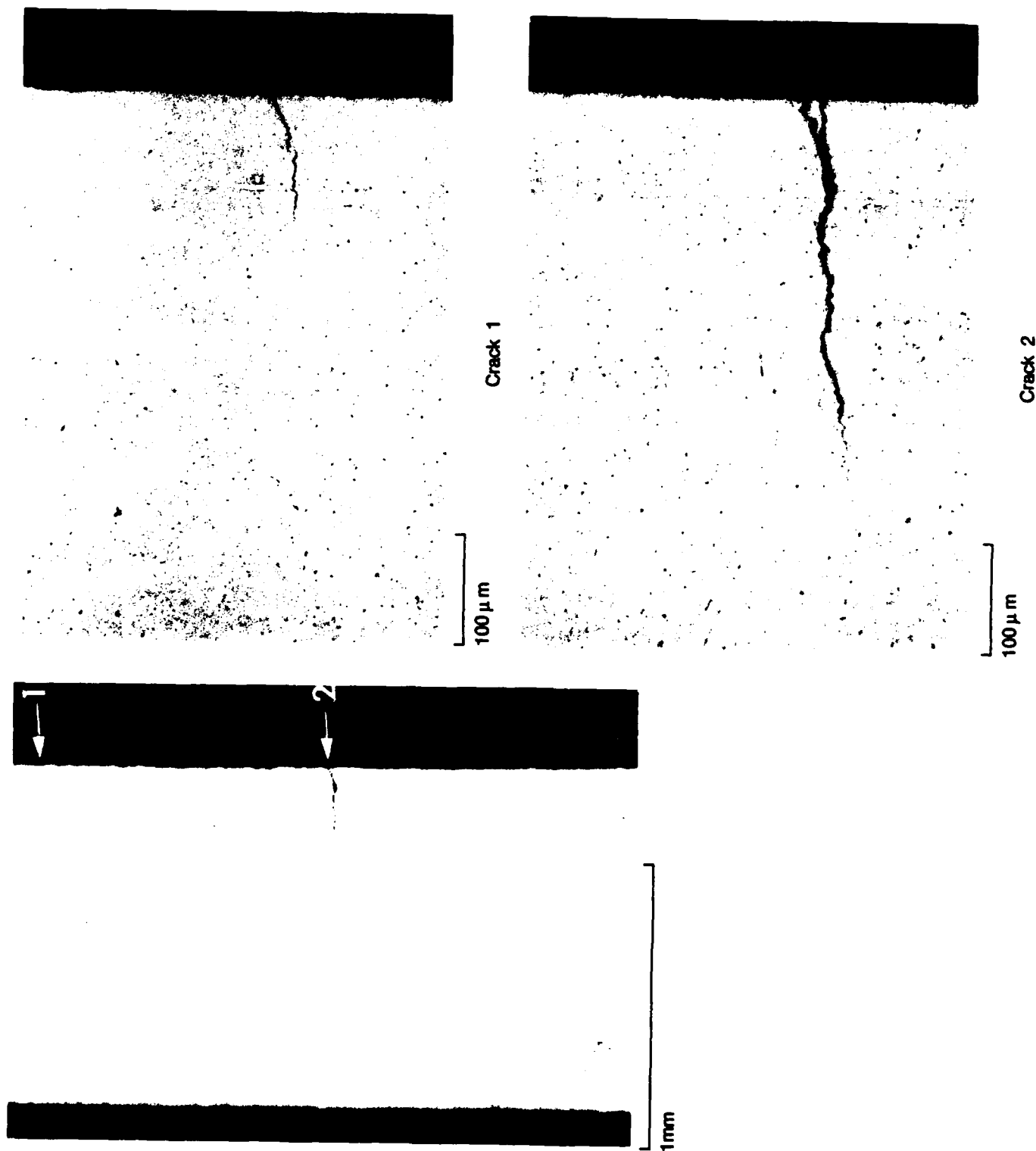


Figure 227. Section Through HSSC TMF of Ti-24Al-11Nb Showing Secondary Cracking

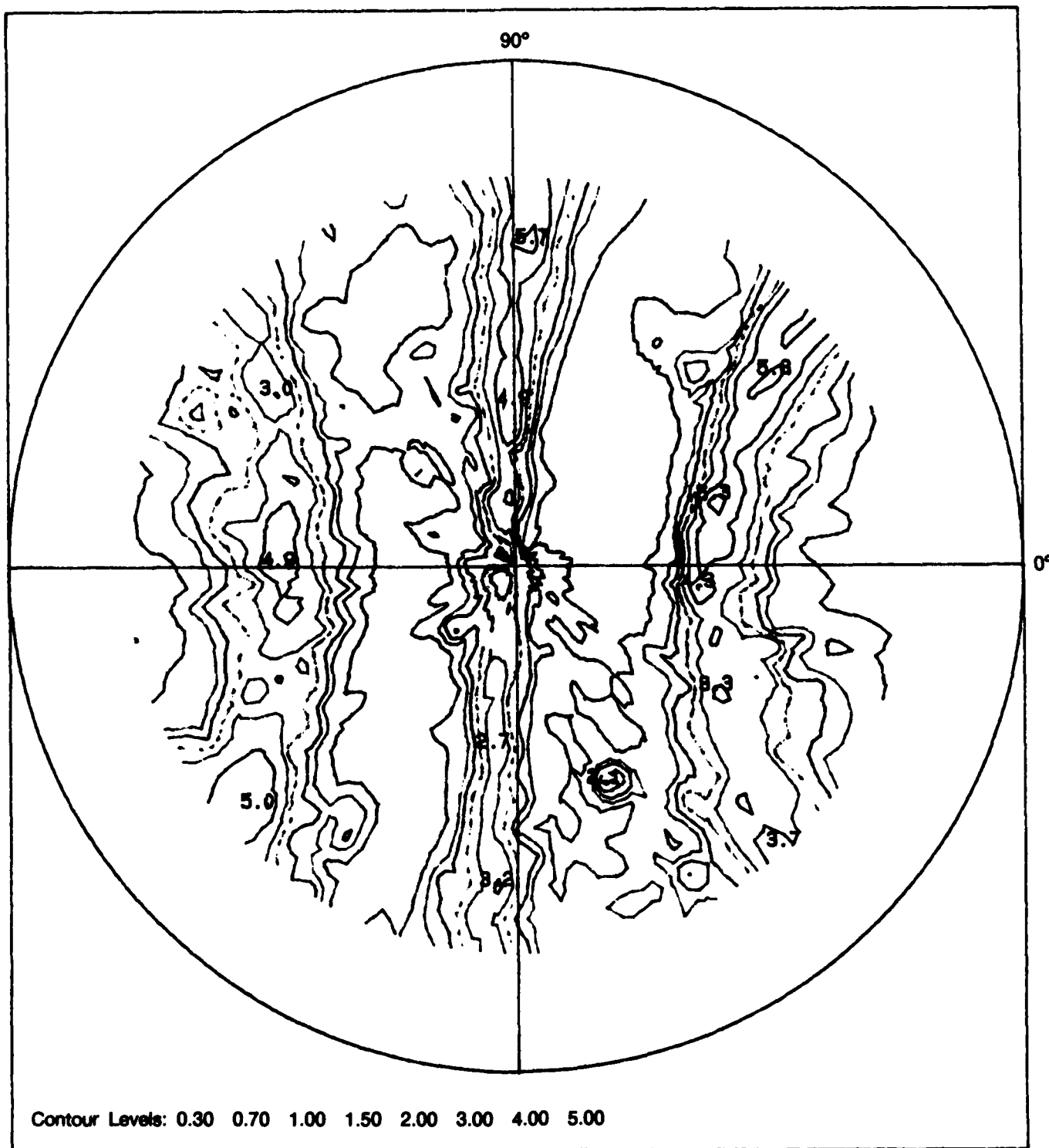


Figure 228. (110) Pole Figure for Beta Phase of Ti-25Al-10Nb-3V-1Mo Pancake in Radial Direction

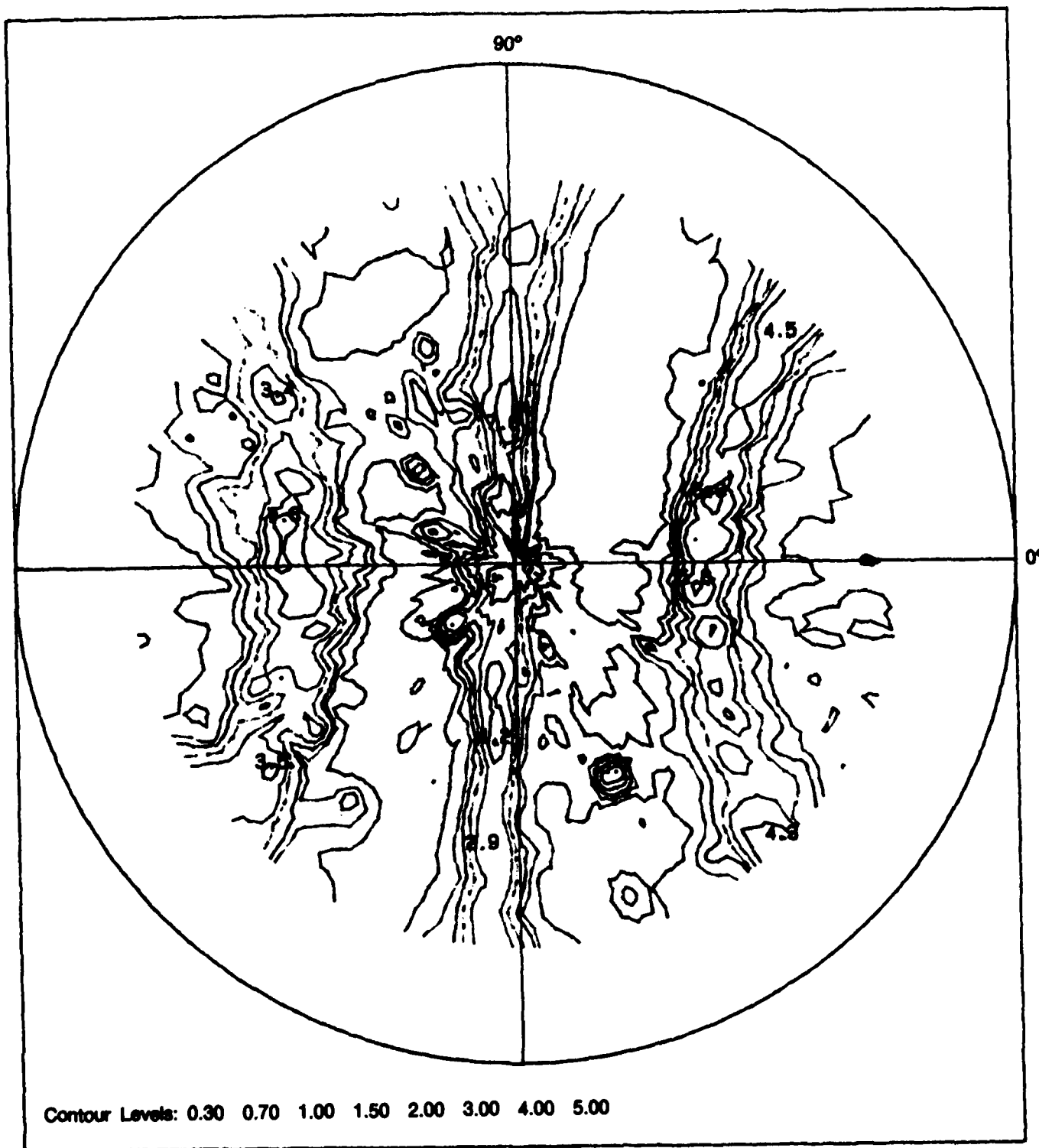


Figure 229. (0002) Pole Figure for Alpha-2 Phase of Ti-25Al-10Nb-3V-1Mo Pancake in Radial Direction

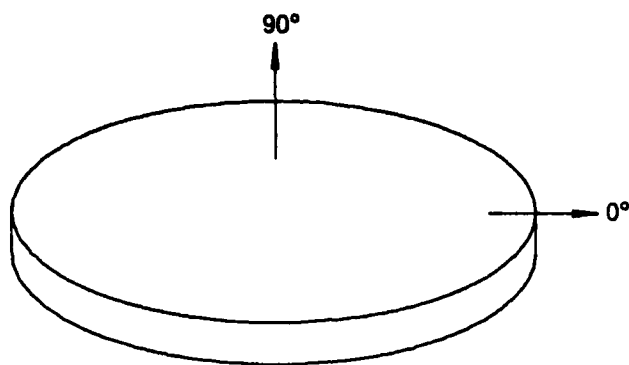


Figure 230. Relationship of Pancake to Pole Figures

REFERENCES

1. Blackburn, M.J., M.P. Smith, "R&D on Composition and Processing of Titanium Aluminide Alloys for Turbine Engines," Interim Technical Report, FR-16259, AFWAL/MMLM contract F33615-80-C-5163, June 1982.
2. Box, G.E.P., N. Draper, "Empirical Model-Building and Response Surfaces," John Wiley and Sons, 1987.
3. Teer, D.G., F.B. Salem, "The Formation of Low Friction, Wear Resistant Surfaces on Titanium by Ion Plating," Conference on Ion Plating & Allied Techniques, *Proceedings*, 1977, pp. 126-134.
4. Ostergren, W.J. "A Damage Function and Associated Failure Equations for Predicting Hold Time and Frequency Effects in Elevated Temperature, Low Cycle Fatigue," *Journal of Testing and Evaluation*, No. 5, September 1976.
5. Pejsa, P.N. and B.A. Cowles, "Thermal Mechanical Fatigue Life Prediction for Advanced Anisotropic Turbine Alloys," Transactions of the ASME, *Journal of Engineering for Gas Turbine and Power*, Vol. 108, July 1986, pp. 504-506.
6. Annis, C.G., Jr., R.M. Wallace, and D.L. Sims, "An Interpolative Model for Elevated Temperature Fatigue Crack Propagation," AFML-TR-76-176, Part I, November 1976, presented at 1977 SESA Spring Meeting, Dallas, Texas, May 1977.
7. Wallace, R.M., C.G. Annis, Jr., and D.L. Sims, "Application of Fracture Mechanics at Elevated Temperatures," AFML-TR-76-176, Part II, November 1976, presented to Air Force Materials Laboratory, WPAFB, Ohio, May 1977.
8. Standard Test Method for Measurement of Fatigue Crack Growth Rates, E647-88, *Annual Book of ASTM Standards*, Vol. 03.01, Metals-Mechanical Testing; Elevated and Low Temperature Tests; *Metallography*; American Society for Testing and Materials, pp. 636-654, 1988.
9. Saxena, A., S. J. Hudak, Jr., J. K. Donald, and D. W. Schmidt, "Computer Controlled Decreasing Stress Intensity Technique for Low Rate Fatigue Crack Growth Testing," *Journal of Testing and Evaluation*, JTEVA, Vol. 6, No. 3, pp. 167-174, 1978.
10. Donald, J. K., "A Procedure for Standardizing Crack Closure Levels," *Mechanics of Fatigue Crack Closure*, ASTM STP 982, J. C. Newman, Jr., and W. Elber, Eds., American Society for Testing and Materials, Philadelphia, 1988, pp. 222-229.
11. Ostergren, W.J., "A Damage Function and Associated Failure Equations for Predicting Hold Time and Frequency Effects in Elevated Temperature, Low Cycle Fatigue," *Journal of Testing and Evaluation*, JTEVA, Vol. 4, No. 5, September 1976, pp 327-339.

12. Morrow, J.D., "Cyclic Plastic Strain Energy and Fatigue of Metals," *Internal Friction, Damping, and Cyclic Plasticity*, ASTM STP No. 378 American Society for Testing and Materials, 1965.
13. Heine, J.E., J.R. Warren and B.A. Cowles, "Thermal Mechanical Fatigue of Coated Blade Materials," Draft Final Report, FR-20505, AFWAL/MLLN Contract F33615-84-C-5027, December 1988.
14. Venkataraman, S., "Elevated Temperature Crack Growth Studies of Advanced Ti_3Al ," Final Technical Report, AFWAL-TR-87-4103, AFWAL/MLLN Contract F33615-86-C-5142, September 1987.